The Auroral Large Imaging System
—Design, operation and scientific results

Akademisk avhandling

som med vederbörligt tillstånd av rektorsämbetet vid Umeå universitet för avläggande av filosofie doktorsexamen i rymdfysik framlägges till offentligt försvar i IRF:s aula, fredagen den 13 juni 2003, kl.9' (09.15.00). Disputationsakten kommer att äga rum på engelska.

av

Urban Brändström, Institutet för rymdfysik, Kiruna

Fakultetsopponent

Dr. Kirsti Kauristie, Meteorologiska institutet, Helsingfors, Finland.

Sammanfattning: Ett gemensamt skandinaviskt markbaserat nät av automatiserade stationer för avbildande norrskensstudier föreslogs 1989 av Åke Steen. Systemet gavs namnet ALIS efter engelskans "Auroral Large Imaging System". De huvudsakliga vetenskapliga motiven för detta återfanns inom norrskensfysiken, men möjligheten att använda ALIS för andra ändamål som tex. studier av polära stratosfärsmoln, meteorer och liknande fenomen insågs tidigt.

Denna avhandling fokuserar på konstruktion och drift av en svensk prototyp till ALIS bestående av sex obemannade fjärrstyrda stationer i norra Sverige som är inplacerade i ett rutnät med ungefär fem mils sida. Vidare ges en sammanfattning av de vetenskapliga resultaten.

Varje station är utrustad med en känslig, högupplösande (1024×1024 bildelement) icke-bildförstärkt avbildande monokromatisk CCD detektor. Ett filterhjul med plats för sex smalbandiga interferensfilter möjliggör avbildande spektroskopiska absolutmätningar av tex. norrskensemissioner. Stationernas inbördes avstånd (ca. 50 km) och synfält (ca. 50°–60°) är anpassade så att synfälten överlappar varandra. Detta gör det möjligt att använda triangulering och tomografiska metoder för att ta fram höjdinformation för de observerade fenomenen.

ALIS var troligen ett av de första instrumenten som utnyttjade icke-bildförstärkta högkvalitativa CCD detektorer för spektroskopiska avbildande flerstationsstudier av ljussvaga fenomen som tex. norrskensemissioner. Därvid är absolutkalibrering av de avbildande instrumenten ett lika viktigt som svårt problem.

Även om ALIS huvudsakligen byggdes för norrskensstudier, så kom, helt oväntat, merparten av de vetenskapliga resultaten från ett annat näraliggande område, nämligen radio-inducerade optiska emissioner. ALIS gjorde de första otvetydiga observationerna av detta fenomen på hög latitud samt den första inversionen (med tomografiliknande metoder) av höjdprofiler från dessa data. Övriga vetenskapliga resultat inkluderar uppskattningar av norrskenets elektronspektra med tomografiska metoder, resultat från koordinerade mätningar med satelliter och radarsystem samt studier av polära stratosfärsmoln. En ALIS-detektor användes vidare i ett samarbetsprojekt som resulterade i de första markbaserade norrskensbilderna tagna under dagtid. Nyligen gjorde ALIS observationer av ett meteorspår från en Leonid där en preliminär studie ger vissa belägg för att vatten observerats i meteorspåret.

Nyckelord: Flerstationsmätningar, Norrsken, Polära stratosfärsmoln, Radio-inducerade optiska emissioner, Rymdfysik, Spektroskopiskt avbildande mätningar, Tomografi.

The Auroral Large Imaging System
—Design, operation and scientific results

Abstract: The Auroral Large Imaging System (ALIS) was proposed in 1989 by Åke Steen as a joint Scandinavian ground-based network of automated auroral imaging stations. The primary scientific objective was in the field of auroral physics, but it was soon realised that ALIS could be used in other fields, for example studies of Polar Stratospheric Clouds (PSC), meteors and other atmospheric phenomena.

This report describes the design, operation and scientific results from a Swedish prototype of ALIS consisting of six unmanned remote-controlled stations located in a grid of about 50 km in northern Sweden. Each station is equipped with a sensitive high-resolution (1024×1024 pixels) unintensified monochromatic CCD-imager. A six-position filter-wheel for narrow-band interference filters facilitates absolute spectroscopic measurements of, for example, auroral and airglow emissions. Overlapping fields-of-view resulting from the station baseline of about 50 km combined with the station field-of-view of 50° to 60° enable triangulation as well as tomographic methods to be employed for obtaining altitude information of the observed phenomena.

ALIS was probably one of the first instruments to take advantage of unintensified (i.e. no image-intensifier) scientific-grade CCDs as detectors for spectroscopic imaging studies with multiple stations of faint phenomena such as aurora, airglow, etc. This makes absolute calibration a task that is as important as it is difficult.

Although ALIS was primarily designed for auroral studies, the majority of the scientific results so far have, quite unexpectedly, been obtained from observations of HF pump-enhanced airglow. ALIS made the first unambiguous observation of this phenomenon at high latitudes and the first tomography-like inversion of height profiles of the airglow regions. The scientific results so far include tomographic estimates of the auroral electron spectra, coordinated observations with satellite and radar, as well as studies of polar stratospheric clouds. An ALIS imager also participated in a joint project that produced the first ground-based daytime auroral images. Recently ALIS made spectroscopic observations of a Leonid meteor trail and preliminary analysis indicates the possible detection of water in the Leonid.

Keywords: Aurora, Artificial Airglow, HF pump-enhanced airglow, Multistation measurements, Polar Stratospheric clouds, Radio-Induced optical emissions, Space physics, Spectroscopic imaging observations, Tomography.

IRF Scientific Report 279
Language: English
ISSN: 0284-1703
ISBN: 91-7305-405-4 pp. 184 pages

Kiruna, April 2003

Urban Brändström

The Auroral Large Imaging System
—Design, operation and scientific results

Urban Brändström
Swedish Institute of Space Physics
Kiruna

April, 2003

Soli Deo Gloria

"Har jag i min tid något godt kunnat uträtta, gifwen derföre Gudi äran!
Hwad jag af mensklig swaghet felat, förlåten mig för Christi skull."
Ur konung Gustaf 1:s afskedstal till rikets ständer d. 16 juni 1560

Cover illustrations:
The large image is a portion of an all-sky colour image (see Section C.1) of an active auroral arc near zenith acquired on 12 December 2001 at 22:17:00 UTC with 4 s integration time. The five small pictures are all obtained with ALIS and show (from left to right):

1. White-light (i.e. no filter) image of a pulsating aurora from 11 April 1994 at 22:35:40 UTC obtained with 50 ms integration time by the ALIS station in Kiruna.
2. A polar stratospheric cloud (see also Figure 6.16 and Section 6.6.1) on 9 January 1997 at 14:19:30 UTC imaged in white-light and with 100 ms integration time by the ALIS station in Kiruna.
3. Top: The first unambiguous observations of HF pump-enhanced airglow that occurred on 16 February 1999 (see Section 6.4). The images are portions of ALIS images obtained at 17:32:25 UTC in the $O(^1D)$ 6300 Å emission-line with 5 s integration time at the ALIS station in Kiruna (left) and in Silkkimuotka (right). Bottom: A double-arc system imaged in the $O(^1S)$ 5577 Å emission-line on 25 March 1998 at 19:54:00 UTC by the ALIS imager in Silkkimuotka (integration time 100 ms). This image is part of a data-set used to estimate the auroral electron-spectra, see Section 6.5.1.
4. A Leonid meteor trail captured by the Kiruna ALIS station with a 4227 Å filter on 19 November 2002 at 03:48:00 UTC with 20 s integration time.
5. The same meteor trail, but imaged with an adjacent ALIS imager in Kiruna with a 5893 Å filter and 10 s integration time (refer to Section 6.6.2 for further information).

©Urban Brändström
Doktorsavhandling vid Institutet för rymdfysik
Doctoral thesis at the Swedish Institute of Space Physics
The Auroral Large Imaging System —Design, operation and scientific results.
Online version and errata at: `http://www.irf.se/~urban/avh/`
Typeset by the author in LaTeX.
Kiruna, April 2003
Rev. 2

IRF Scientific Report 279
ISSN 0284-1703
ISBN 91-7305-405-4 pp. 184 pages
Printed at the Swedish Institute of Space Physics
Box 812
SE-981 28, Kiruna, Sweden
April 2003

Sammanfattning

Ett gemensamt skandinaviskt markbaserat nät av automatiserade stationer för avbildande norrskensstudier föreslogs 1989 av Åke Steen. Systemet gavs namnet ALIS efter engelskans "Auroral Large Imaging System". De huvudsakliga vetenskapliga motiven för detta återfanns inom norrskensfysiken, men möjligheten att använda ALIS för andra ändamål som tex. studier av polära stratosfärsmoln, meteorer och liknande fenomen insågs tidigt.

Denna avhandling fokuserar på konstruktion och drift av en svensk prototyp till ALIS bestående av sex obemannade fjärrstyrda stationer i norra Sverige som är inplacerade i ett rutnät med ungefär fem mils sida. Vidare ges en sammanfattning av de vetenskapliga resultaten.

Varje station är utrustad med en känslig, högupplösande (1024×1024 bildelement) icke-bildförstärkt avbildande monokromatisk CCD detektor. Ett filterhjul med plats för sex smalbandiga interferensfilter möjliggör avbildande spektroskopiska absolutmätningar av tex. norrskensemissioner. Stationernas inbördes avstånd (ca. 50 km) och synfält (ca. 50°–60°) är anpassade så att synfälten överlappar varandra. Detta gör det möjligt att använda triangulering och tomografiska metoder för att ta fram höjdinformation för de observerade fenomenen.

ALIS var troligen ett av de första instrumenten som utnyttjade icke-bildförstärkta högkvalitativa CCD detektorer för spektroskopiska avbildande flerstationsstudier av ljussvaga fenomen som tex. norrskensemissioner. Därvid är absolutkalibrering av de avbildande instrumenten ett lika viktigt som svårt problem.

Även om ALIS huvudsakligen byggdes för norrskensstudier, så kom, helt oväntat, merparten av de vetenskapliga resultaten från ett annat näraliggande område, nämligen radio-inducerade optiska emissioner. ALIS gjorde de första otvetydiga observationerna av detta fenomen på hög latitud samt den första inversionen (med tomografiliknande metoder) av höjdprofiler från dessa data. Övriga vetenskapliga resultat inkluderar uppskattningar av norrskenets elektronspektra med tomografiska metoder, resultat från koordinerade mätningar med satelliter och radarsystem samt studier av polära stratosfärsmoln. En ALIS-detektor användes vidare i ett samarbetsprojekt som resulterade i de första markbaserade norrskensbilderna tagna under dagtid. Nyligen gjorde ALIS observationer av ett meteorspår från en Leonid där en preliminär studie ger vissa belägg för att vatten observerats i meteorspåret.

Nyckelord: Flerstationsmätningar, Norrsken, Polära stratosfärsmoln, Radioinducerade optiska emissioner, Rymdfysik, Spektroskopiskt avbildande mätningar, Tomografi.

Abstract

The Auroral Large Imaging System (ALIS) was proposed in 1989 by Åke Steen as a joint Scandinavian ground-based network of automated auroral imaging stations. The primary scientific objective was in the field of auroral physics, but it was soon realised that ALIS could be used in other fields, for example studies of Polar Stratospheric Clouds (PSC), meteors and other atmospheric phenomena.

This report describes the design, operation and scientific results from a Swedish prototype of ALIS consisting of six unmanned remote-controlled stations located in a grid of about 50 km in northern Sweden. Each station is equipped with a sensitive high-resolution (1024×1024 pixels) unintensified monochromatic CCD-imager. A six-position filter-wheel for narrow-band interference filters facilitates absolute spectroscopic measurements of, for example, auroral and airglow emissions. Overlapping fields-of-view resulting from the station baseline of about 50 km combined with the station field-of-view of 50° to 60° enable triangulation as well as tomographic methods to be employed for obtaining altitude information of the observed phenomena.

ALIS was probably one of the first instruments to take advantage of unintensified (i.e. no image-intensifier) scientific-grade CCDs as detectors for spectroscopic imaging studies with multiple stations of faint phenomena such as aurora, airglow, etc. This makes absolute calibration a task that is as important as it is difficult.

Although ALIS was primarily designed for auroral studies, the majority of the scientific results so far have, quite unexpectedly, been obtained from observations of HF pump-enhanced airglow. ALIS made the first unambiguous observation of this phenomenon at high latitudes and the first tomography-like inversion of height profiles of the airglow regions. The scientific results so far include tomographic estimates of the auroral electron spectra, coordinated observations with satellite and radar, as well as studies of polar stratospheric clouds. An ALIS imager also participated in a joint project that produced the first ground-based daytime auroral images. Recently ALIS made spectroscopic observations of a Leonid meteor trail and preliminary analysis indicates the possible detection of water in the Leonid.

Keywords: Aurora, Artificial Airglow, HF pump-enhanced airglow, Multistation measurements, Polar Stratospheric clouds, Radio-Induced optical emissions, Space physics, Spectroscopic imaging observations, Tomography.

Preface

> "Vi få ej välja ramen för vårt öde. Men vi ge den dess innehåll. Den som vill äventyret skall också uppleva det — efter måttet av sitt mod. Den som vill offret skall offras — efter måttet av sin renhet." *Dag Hammarskjöld*

It is a great privilege to have the opportunity to finish this work that is an attempt to provide a comprehensive compilation of material related to the Auroral Large Imaging System (ALIS). ALIS was conceived by Åke Steen, who had visions extending far beyond this work, and nothing of what is reported here would have been made possible without his vision, enthusiasm, stubbornness and ability to acquire the necessary funding. His efforts, however, would have been impossible without the altruism and excellent leadership of Bengt Hultqvist, who was director of the Swedish Institute of Space Physics (IRF) 1957–1994. Bengt Hultqvist also read a draft of this work and provided much valuable advice. I also want to thank the present director of IRF, Rickard Lundin, as well as Stanislav Barabash and Jan Pohjanen, for ensuring me the excellent undisturbed working conditions that enabled me to complete this thesis. Thanks to Ingrid Sandahl for taking care of ALIS since 2001.

To make a complete list of acknowledgements is virtually impossible, yet I feel obliged to attempt to list at least some names as representatives for a much larger group. I begin by specially thanking Lars Wittikko for many years of hard work in the ALIS project, and also as a representative of all those who deserved an acknowledgement, but have never received one. My apologies for those painful, but equally unavoidable omissions! I also apologise now if I have, despite my best efforts, failed to provide proper references and credits anywhere.

A very special acknowledgement to Takehiko Aso and Masaki Ejiri, for their friendship, humble attitude, enthusiastic support of ALIS, inspiration and excellent ideas that kept me from giving up many times. "Domo arrigato!"

I acknowledge Carl-Fredrik Enell, Björn Gustavsson, Peter Rydesäter, Tima Sergienko and Asta Pellinen-Wannberg for their efforts with ALIS and ALIS data as well as for countless hours of proofreading encouragement and much more. I am also very much indebted to Carol Norberg and Rick McGregor who had the tedious task of correcting my English and also provided many valuable comments. I thank Lars Nilsson as a personification of those with the special gift of mastering the Art of computer programming.

I would also like to thank the past and present staff of IRF, ANS, EISCAT, ESRANGE, NIPR, etc. represented by this far too short and incomplete list of names: Vesa Alatalo, Nils-Åke Andersson, Göran Axelsson, Peter Bergquist, Göte Johansson, Hugo Johansson, Jan Johansson, Magnus Johansson, Christer Jurén, Juha Liikamaa, Aarne Luiro, Torbjörn Lövgren, Mats Luspa, Arne Moström, Olle Norberg, Jonas Olsen, Walter Puccio, Markus Rantakeisu, Akira Urashima, Bengt Wanhatalo and Masatoshi Yamauchi. As representatives of the many co-authors and colleagues around the world I would like to acknowledge Viktor Alpatov, Laila Andersson, Anasuya Aruliah, Paul Bernhardt, Mikael Hedin, Ingemar Häggström, Jouni Jussila, Kari Kaila, Oleg Kornilov, Mike Kosch, Shu Lai, Hans Lauche, Thomas Leyser, William McNeil, Edmond Murad,

Michail Pudovkin, David Rees, Mike Rietveld, Tima Sergienko, Mikko Syrjäsuo, Trond Trondsen, Bo Thidé, Assar Westman, Ian McWhirter and Ola Widell.

Thanks to Trevor Preston, Maureen Ffitch and colleagues at AstroCam Ltd for valuable discussions and help regarding the CCD camera and its software. A special acknowledgement goes to all the thousands of voluntary programmers making up the free and open software communities. ALIS was funded through FRN (Forskningsrådsnämnden), NFR (Naturvetenskapliga forskningsrådet), Swedish National Space board (Rymdstyrelsen, fjärranalyskommitén), IRF and Vetenskapsrådet. Without the financial support of the tax-payers of Sweden, Japan and other nations, as well as other funding sources, none of this research would have been possible.

I would have been completely unable to finish this work without the music of Johan Sebastian Bach, Ludwig van Beethoven, Franz Berwald and many others. Dag Hammarskjöld's book Vägmärken [Transl. as Markings; *Hammarskjöld*, 1963, 1964] provided guidance and inspiration to carry on.

Ett alldeles speciellt tack till min mamma, Astrid Brändström, som ställt upp för mig mer än någon son kan begära. En stor kram till min fästmö Anette Snällfot, som tålmodigt har stått ut med många olägenheter på grund av mina envisa försök att färdigställa detta arbete. Tillråga på allt drabbades hon av korrekturläsning och tryckeribestyr. Tack för allt stöd och all uppmuntran, jag hade inte klarat mig utan er! Sist ett postumt tack till alla de som på många sätt bidragit till detta arbete men som aldrig fick uppleva dess färdigställande.

Björkliden i april 2003

Urban Brändström

Contents

Preface **I**

1 Introduction **1**
1.1 Auroral imaging . . . 2
1.1.1 Auroral height estimations . . . 3
1.1.2 Spectroscopic techniques . . . 3
1.2 Summary . . . 4

2 ALIS, the Auroral Large Imaging System. **5**
2.1 The ALIS stations . . . 8
2.1.1 Scientific considerations . . . 8
2.1.2 Selecting sites for the ALIS stations . . . 10
2.2 IT hardware and infrastructure . . . 11
2.2.1 Computers . . . 13
2.2.2 The NIPU . . . 13
2.2.3 Communication systems . . . 15
2.2.4 Station data storage . . . 16
2.2.5 Data archiving and availability . . . 16
2.2.6 Operating Systems . . . 16
2.3 The ALIS control centre . . . 17

3 The ALIS Imager **21**
3.1 Some basic concepts . . . 21
3.1.1 Spectral radiant sterance (radiance) . . . 21
3.1.2 The Rayleigh . . . 22
3.1.3 Spectral radiant incidence (irradiance) . . . 23
3.1.4 Number of incident photons . . . 25
3.1.5 The CCD as a scientific imaging detector . . . 25
3.1.6 Quantum efficiency . . . 25
3.1.7 Noise . . . 26
3.1.8 Signal-to-noise ratio . . . 27
3.1.9 The signal-to-noise ratio of an ICCD . . . 28
3.1.10 Threshold of detection and maximum signal . . . 29
3.1.11 Dynamic range . . . 30
3.2 Selecting an imager for ALIS . . . 30
3.2.1 Comparison of an ICCD with a CCD imager . . . 30
3.2.2 Frame rate . . . 34

3.3 The CCD imager for ALIS . . . 35
3.3.1 The camera head . . . 35
3.3.2 The camera control unit . . . 36
3.3.3 Configuring the imager . . . 36
3.3.4 The user port . . . 38
3.3.5 Operational remarks . . . 38
3.4 The optical system . . . 39
3.5 Interference filters . . . 40
3.5.1 The filter wheel . . . 41
3.6 The camera positioning system . . . 44
3.7 Summary . . . 47

4 Calibrating ALIS 49
4.1 Removing the instrument signature . . . 49
4.1.1 Bias removal . . . 51
4.1.2 Dark-current . . . 52
4.1.3 Flat-field correction . . . 52
4.1.4 Bad-pixel correction . . . 53
4.1.5 Summary . . . 54
4.2 Intercalibration . . . 54
4.2.1 Absolute calibration . . . 58
4.2.2 Removing the background . . . 61
4.2.3 Related issues . . . 62
4.3 Geometrical calibration . . . 62

5 Controlling ALIS 65
5.1 Making an observation with ALIS . . . 66
5.1.1 Modes of operation . . . 68
5.1.2 Alarms and other exceptions . . . 68
5.2 OPERA . . . 69
5.2.1 User interfaces . . . 69
5.2.2 AIDA . . . 69
5.2.3 Station software . . . 71
5.2.4 Experiences and future plans . . . 72

6 Scientific results from ALIS 75
6.1 Scientific objectives of ALIS . . . 76
6.2 ALIS data analysis . . . 78
6.2.1 Investigations of new data-analysis methods for ALIS . . . 78
6.3 Tomography and triangulation . . . 83
6.3.1 Methods, initial studies and simulations . . . 83
6.3.2 Summary of results from computer tomography of ALIS-data 83
6.4 HF pump-enhanced airglow . . . 85
6.4.1 The EISCAT Heating facility . . . 86
6.4.2 ALIS observations of enhanced airglow . . . 86
6.4.3 Observations on 16 February 1999 . . . 86
6.4.4 Discussion . . . 94
6.5 Auroral studies . . . 101

6.5.1 An estimate of the auroral electron spectra . . . 102
6.5.2 Coordinated observations with satellite and radar . . . 105
6.5.3 Auroral vorticity . . . 105
6.5.4 Studies of the ionospheric trough . . . 107
6.5.5 Daytime auroral imaging . . . 107
6.5.6 The relation between the thermospheric neutral wind and auroral events . . . 108
6.6 Other studies . . . 110
6.6.1 Polar stratospheric clouds . . . 110
6.6.2 Astronomical applications — water in a Leonid? . . . 113

7 Concluding remarks **119**

A The Instrumentation Platform **121**
A.1 Station housing . . . 122
A.2 Environmental subsystems . . . 127
A.3 Power subsystems . . . 127
A.4 Housekeeping Unit . . . 130
A.5 Timing . . . 131
A.6 Communication . . . 132
A.7 Station computer . . . 132
A.8 The mobile imaging platform . . . 132

B Data for the ALIS imagers **135**

C Related work **139**
C.1 A new digital all-sky camera . . . 139
C.2 Colour video recordings of aurora . . . 141

D Continued operations with ALIS **145**
D.1 Assessing the present status of ALIS . . . 145
D.1.1 The ALIS imagers . . . 147
D.2 Summary . . . 149
D.2.1 A longer perspective . . . 150

Bibliography **153**

Index of acronyms **171**

Index of notation **173**

Index **177**

List of Figures

2.1 First proposed layout of ALIS 6
2.2 Proposed layout of Swe-ALIS 7
2.3 Fields-of-view and station baseline 9
2.4 Map of the present ALIS 12
2.5 The NIPU 14
2.6 The ALIS Control Centre 17
2.7 Block-diagram of the ALIS Control Centre 18
2.8 The ALIS Operations Centre 19

3.1 Quantum efficiency vs. wavelength for the SI-003AB CCD 26
3.2 *SNR* vs. column emission 31
3.3 *SNR* vs. integration time 33
3.4 The effect of on-chip binning 33
3.5 Dividing a full-frame CCD into sub-arrays. 34
3.6 The six ALIS imagers 35
3.7 Schematic diagram of the optical system 39
3.8 The six-position filter wheel 41
3.9 Electronics for the filter wheel and CPS 43
3.10 The Camera Positioning System 45
3.11 ALIS preset camera positions projected to 110 km altitude 46
3.12 Block diagram of ALIS imager subsystems 48

4.1 Coordinates and notation for the CCD in the ALIS Imager 50
4.2 Calibration sources used for ALIS calibration 55
4.3 Column emission rates for the calibrators 57
4.4 Example filter transmittance curve 59
4.5 Typical ALIS background image 64

5.1 Block diagram of OPERA 70
5.2 Station software 72

6.1 An example of the difficulties of auroral image classification. 80
6.2 Geometry of the HF pump-enhanced airglow experiments 87
6.3 Maximum and average column emission time series as seen from four stations 89
6.4 Sequence of airglow images from the Silkkimuotka ALIS station . . 90
6.5 A series of images of enhanced 6300 Å airglow 91
6.6 Results of triangulation of the maximum volume emission. 92

6.7 Triangulation of the displacement of the two peaks in Figure 6.4 . 93
6.8 Fabry-Perot interferometer measurements of the neutral wind at 240 km altitude. 94
6.9 EISCAT UHF radar measurements of electron density 95
6.10 Volume rendering of the artificially-enhanced airglow region above Tromsø 98
6.11 Estimates of the $O(^1D)$ excitation rates 100
6.12 Estimated electron flux 103
6.13 Estimated electron flux 104
6.14 Auroral images from 16 February 1997 106
6.15 Daytime auroral image 109
6.16 PSC images and altitude profiles 112
6.17 ALIS images of a meteor trail 115
6.18 Projected meteor altitude profile 116
6.19 Meteoroid altitude profiles 117

A.1 Block diagram of the GLIP 122
A.2 Transmittance curves for plexi-glass 124
A.3 The GLIP in Tjautjas 125
A.4 Detail of the GLIP dome 126
A.5 Electrical installation of a GLIP 128
A.6 Rear view of the Power Distribution Unit 129
A.7 The Housekeeping Unit 130
A.8 GPS-receiver 131
A.9 The mobile imaging platform 132

C.1 A digital colour all-sky camera 140
C.2 Sample auroral image from the all-sky camera prototype 141
C.3 Colour video frame of aurora with a meteor trail 143

D.1 Block diagram of the upgraded GLIP 148
D.2 Block diagram of future GLIPs 150
D.3 A decentralised future ALIS 151

List of Tables

2.1 ALIS time-line 6
2.2 Example imager coverages 10
2.3 Geographical coordinates of the ALIS stations 11

3.1 ICCD parameters for the PAI 31
3.2 Some CCD parameters for `ccdcam5` 32
3.3 CCD-read noise at various pixel clocks 37
3.4 Filter placement standard for ALIS 42
3.5 Optional filters and their usage 42
3.6 ALIS preset camera positions 47

4.1 Preset DC-bias levels 51
4.2 Total number of pixels and bias-pixels for the six ALIS imagers. . . 51
4.3 Results from recent intercalibration workshops 56
4.4 Ratios of calibration results 57
4.5 Calibration results for ALIS 60
4.6 Measured fields-of-view for the ALIS imagers 63

6.1 Summary of image processing tools 78
6.2 Summary of data analysis tools 79
6.3 An auroral classification scheme 81
6.4 Overview of HF pump-enhanced airglow experiments with ALIS . 88
6.5 Filters for meteor studies 114

A.1 GLIP Acronyms 123

B.1 Some CCD parameters for `ccdcam1` 135
B.2 Some CCD parameters for `ccdcam2` 135
B.3 Some CCD parameters for `ccdcam3` 136
B.4 Some CCD parameters for `ccdcam4` 136
B.5 Some CCD parameters for `ccdcam5` 136
B.6 Some CCD parameters for `ccdcam6` 137

D.1 GLIP Acronyms 148

Chapter 1

Introduction

> Stig min klang mot sol mot norrskensbågar vida,
> Väck sovande fjäll, slumrande myr och mo!
> Vig åt arbete in fält, som fruktsamma bida,
> Vig dem till sist en gång åt den eviga tystnadens ro!
>
> *Albert Engström*

> "And I looked, and, behold, a whirlwind came out of the north, a great cloud, and a fire infolding itself, and a brightness was about it, and out of the midst thereof as the colour of amber, out of the midst of the fire."
> *Ezekiel 1:4*

> "Norr-skenets rätta hemvist, det högsta av vår atmospher, är för oss och alla våra undersökningar otilgängeligt. Ögat och synen äro de ende medel, hvilka til röns inhämtande därvid kunna användas. Men äfven dem är ej tillåtit, at skåda Norr-skenen sådane som de äro i sig sjelfve, utan endast så, som de, på långt håll, visa sig för våra bedrägliga omdömen." *Wilcke [1778]*

The colourful and highly dynamic northern lights are one of the most fascinating and beautiful phenomena seen in the night sky. For as long as there have been people present at suitable locations, they have probably postulated over the origin and purpose of the aurora, first in terms of myths, superstitious interpretations, or religious beliefs and later on in terms of scientific methods. Ancient works by *Aristotle* [ca. 340 B.C.]; *Pliny* [ca. 77] and *Seneca* [ca. 63] with vivid descriptions of low latitude aurora are reported by *Chamberlain* [1995]. It is sometimes speculated if some ancient biblical texts might contain early descriptions of auroral events, such as, for example the vision of Ezeikel around 593 B.C., as quoted above [*Siscoe et al.*, 2002; *Raspopov et al.*, 2003, and references therein].

Many sources report that the name: "Aurora Borealis" (northern lights) was assigned by *Gassendi* [1651], however, research by *Siscoe* [1978] indicates that these terms existed earlier, and that they might be traceable to Galileo Galilei or his disciple Guiducci [*Eather*, 1980, p. 51].

When modern science emerged, explanations of the aurora began to be formulated. Initially only visual observations were available [for example *Gassendi*, 1651; *Celsius*, 1733; *de Mairan*, 1733]. In a speech to the king (Gustav III) and

the newly established Royal Swedish Academy of Sciences, *Wilcke* [1778] summarises "the newest explanations of the northern lights". This speech includes a large set of early references.* *Wilcke* also remarks on the exceptional difficulties to make accurate recordings of auroral events. "The eye, the pen, and the brush of the fastest painter are too slow to record the changes"†. Yet, it would take more than one century until better tools became available. Meanwhile, artistic work, like drawings and paintings were the only available tools to record observations of northern lights [see references in *Eather*, 1980; *Pellinen and Kaila*, 1991]. Now, over 225 years later, and despite the giant leaps of technology, it is still a rather difficult task to make accurate auroral recordings.

1.1 Auroral imaging

Following the invention of photography the first successful picture of the aurora was taken by Brendel in 1892 [*Baschin*, 1900]. This paved the way for multi-station auroral imaging. One of the first large-scale auroral observation campaigns involving several stations was carried out by *Birkeland* [1908, 1913].

The most well-known imaging instrument is maybe the All-Sky Camera (ASC), which consists of a camera together with an optical arrangement of one or several mirrors providing near 180° field-of-view. This instrument exists in a variety of designs [for example *Stoffregen*, 1955, 1956; *Elvey and Stoffregen*, 1957; *Hyppönen et al.*, 1974, and others] and was pioneered by *Gartlein* [1947]. During the International Geophysical Year (IGY) of 1957–1958 a ground-based network of all-sky cameras was operating at 114 stations around the polar regions [*Stoffregen*, 1962]. Since then, improved versions of the all-sky camera have been the main observatory instruments for ground-based imaging of the aurora. Examples of present state-of-the-art digital all-sky cameras are the all-sky optical imager (ASI) in use at the Amudsen-Scott South Pole station [*Ejiri et al.*, 1998, 1999] as well as the cameras used in the Finnish MIRACLE network‡ [*Syrjäsuo*, 1996; *Syrjäsuo*, 1997; *Syrjäsuo*, 2001]. These all-sky cameras represent a considerable improvement over earlier instruments. Since a filter-wheel is present, spectroscopic measurements are possible. A somewhat different, and less advanced approach, is presented in Section C.1, where a commercial digital colour camera is used.

The intense development of television cameras starting in the late 1940's led to the emergence of better low-light imaging detectors based on television image-tubes, for example image orthicons and intensified vidicons. This enabled direct electronic recording of auroral image data. Absolute measurements with this class of detectors is very difficult, mainly due to calibration difficulties related to their non-linear response. Therefore these detectors have mainly been used for white-light imaging.

According to *Jones* [1974], the first use of image orthicon television camera systems for auroral observations were by *Davis and Hicks* [1964]. Image-intensified vidicon tubes were introduced by *Scourfield and Parsons* [1969]. Since

*See also [*Chamberlain*, 1995, Appendix VIII], regarding historical references.

†Free translation by the author, see the quote at the beginning of Chapter 3

‡`http://www.geo.fmi.fi/MIRACLE/`

then, technology has improved considerably and there exists a plethora of auroral imagers based on television type cameras, often in a combination with an image intensifier. An example of a modern television-type imager is the excellent Portable Auroral Imager (PAI) intended for high-resolution auroral imaging [*Trondsen*, 1998]. A few more examples of television-type imagers are mentioned in Section 3.2.1.

Space-borne optical imagers simplified the monitoring of large-scale auroral features. The Viking imager [*Anger et al.*, 1987] may serve as an excellent example of this [see *Pellinen and Kaila*, 1991, for a more complete listing of space-borne imagers]. Polar/VIS[§] is a more recent example of the versatile capabilities of space-borne auroral imaging techniques. For global auroral imaging, the capability to use UV-emissions to measure sunlit day-side aurora is a great advantage [*Steen*, 1989]. However, auroral imaging from space *does not* make ground-based and rocket-borne studies obsolete, they are both powerful and complementary methods that should not be underestimated. For example, small- and medium-scale phenomena are difficult to study from space due to the spatial smearing caused by the orbital motion, as well as imprecisely known value of the effective albedo [*Steen*, 1989]. Furthermore the orbital motion prohibits continuous studies in a certain local time sector, as well as along a certain magnetic field-line. The best results tend to emerge when different observing methods are combined.

1.1.1 Auroral height estimations

The number of reliable height estimations of the aurora before those obtained from photographic methods are very few [*Størmer*, 1955]. The first measurement of the height of an aurora was made between 1726 and 1730 by *de Mairan* [1733] resulting in an estimated height of about 400–1300 km. Further reading on early height determinations is found in the works of *Wilcke* [1778]; *Størmer* [1955], and references therein.

By obtaining auroral photographs simultaneously from two or more locations, it is possible to employ triangulation techniques to estimate the height of the aurora. The first results from this method were obtained by *Størmer* [1911]. Later on the methods were improved and simplified [for example *Vegard and Krogness*, 1920], as described in the cornerstone work by *Størmer* [1955].

For examples of more recent height-determinations of the aurora see *Brandy and Hill* [1964]; *Romick and Belon* [1967]; *Brown et al.* [1976]; *Stenbaek-Nielsen and Hallinan* [1979]; *Kaila* [1987]; *Steen* [1988a,b]; *Aso et al.* [1990]; *Jones et al.* [1991]; *Aso et al.* [1993, 1994]; *Frey et al.* [1996], and references therein. However, embarking onto a detailed discussion of the many recent measurements extend far beyond the scope of this introduction.

1.1.2 Spectroscopic techniques

The auroral signal contains a considerable amount of spectral information. The first measurements of the auroral spectra were carried out by *Ångström* [1868, 1869]. He also named the convenient unit Ångström (1 Å = 0.1 nm). Another

[§] `http://eiger.physics.uiowa.edu/~vis/`

important contributor to auroral spectroscopy was *Vegard* [1913]. Further information on auroral spectra, as well as more references are provided by *Jones* [1974] and *Chamberlain* [1995].

Sadly, spectrographs and spectrometers are rare instruments in present day auroral studies. As much more sensitive detectors exist today, a re-examination of the spectral features of the aurora might prove rewarding.

At the present time, the dominating instrument for spectroscopic studies of aurora is the interference filter photometer. This instrument is used either for fixed single-point measurements, or in a scanning or imaging configuration. Examples of contemporary instruments are found in *Kaila* [2003a].

1.2 Summary

This short introduction can in no way provide a complete overview of the field. Hopefully, it has at least provided a set of references for further studies and a rudimentary background to the desire to build ALIS as a multi-station imaging network capable of absolute spectroscopic measurements of column emission rates within the field-of-view of a traditional all-sky camera, as well as the capability to image a common volume, thus enabling triangulation and auroral tomography.

For further reading related to low-light optical instrumentation for auroral measurements see, for example, *Høymork* [2000], and references therein. *Galperin* [2001] presents an interesting discussion regarding the multiple scales of auroral phenomena. Such considerations are important for selecting a suitable baseline and field-of-view of a multi-station imaging system. An extensive review of instruments and networks for optical auroral studies was presented by *Pellinen and Kaila* [1991]. This was about the same time as work on ALIS commenced and therefore their work is recommended as an additional introduction, as well as an illustration of the power of coordinated studies with many instruments, regardless of whether they are ground-based or space-borne.

This work is organised in seven chapters and four appendices. A reader only interested in the scientific results from ALIS might wish to skip directly to Chapter 6, however, please consider quickly browsing through Chapters 2–4 for an introduction to the possibilities and limitations of the instrument. Technical details, related work and future plans are deferred to the appendices.

Chapter 2

ALIS, the Auroral Large Imaging System.

> "One of the symptoms of an approaching nervous breakdown is the belief that one's work is terribly important." *Bertrand Russell*

The first proposal for an Auroral Large Imaging System (ALIS), [*Steen*, 1989] suggested a net of 28 auroral imaging stations in northern Scandinavia spaced 100 km apart and with an average field-of-view (FoV) of 90° (Figure 2.1). It was anticipated that ALIS would be jointly funded and operated by the participating countries. In a later publication, [*Steen et al.*, 1990], the Swedish part of ALIS (Swe-ALIS) was considered in more detail. Here the station baseline was reduced to 50 km for 14 stations within Sweden with an average field-of-view of 60° (Figure 2.2). In 1990 funding for the costs for an initial subset of Swe-ALIS was received. This "mini-ALIS" would consist of four to eight stations (corresponding to stations numbered 1–8 in Figure 2.2). As design and construction work commenced, it became practice to use the acronym "ALIS" instead of "mini-ALIS" or "Swe-ALIS". As the title suggests, this practice will be adhered to also in this thesis. However, it is useful to remember that the present work represents only a first small step towards the auroral large imaging system that was originally envisioned [*Steen*, 1989; *Steen et al.*, 1990].

Design work on ALIS started in the fall of 1990. Construction work on the basic infrastructure started in 1991. The first camera became operational at the end of 1993 and the first auroral observations were carried out with it during early 1994. Later in 1995 ALIS consisted of 3 complete stations (and 3 stations without cameras), and participated for the first time in a scientific campaign [*Aso et al.*, 1998a,b]. During this campaign two additional intensified CCD-cameras were operated, giving a total of five observing sites. At this time most ALIS stations had no filter-wheels or camera positioning systems. In the following years, ALIS expanded to six fully-equipped stations. Table 2.1 shows the ALIS time-line.

This chapter focuses on the basic scientific and technical considerations affecting the design of the six-station ALIS, which was in full operation until April 2001.

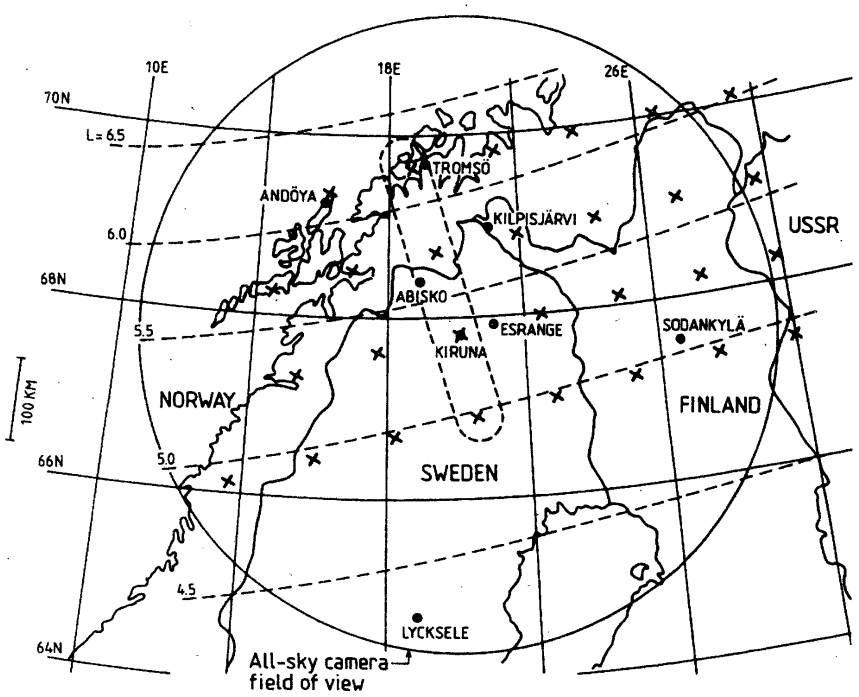

Figure 2.1: The first proposed layout of ALIS with 28 stations in northern Scandinavia separated by about 100 km, each with a field-of-view of about 90°. The suggested station sites are marked with crosses. The four stations enclosed in a dotted line represent a suggested mini version of ALIS. The large circle illustrates the field-of-view of an all-sky camera in Kiruna at ionospheric altitudes. [After *Steen*, 1989]

Year	1993	1994	1995	1996	1997	1998	1999	2000	2001
Stations	3	4	6	6	6	8	9	9	9
Cameras	1	1	4	5	5	6	6	6	6
Images	51	454	2374	3020	4034	15053	18905	19844	55878

Table 2.1: The ALIS time-line 1993–2001. 'Stations' represent the number of stations on site. 'Cameras' denotes the number of operational ALIS cameras, 'Images' lists the total number of images recorded each year.

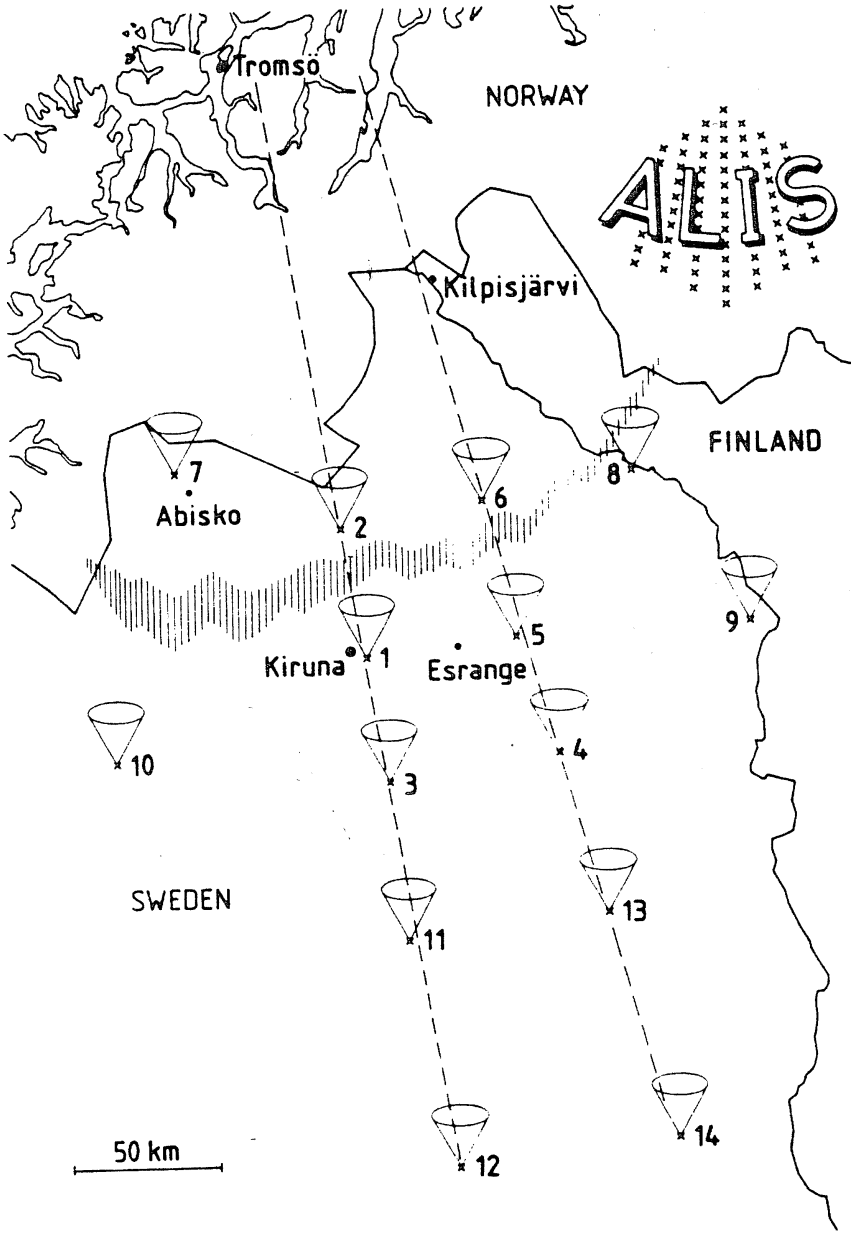

Figure 2.2: A proposed layout for the Swedish part of ALIS (Swe-ALIS). This layout was partly followed when deciding the final sites for the ALIS stations as given in Figure 2.4 and Table 2.3. [after *Steen et al.*, 1990]

2.1 The ALIS stations

The design and deployment of the ALIS stations involves a large number of considerations. Each station must be designed for unmanned remote-controlled operation during extended time-periods in low-population regions with a sub-arctic climate. The technical design of the ALIS-station, which constitutes a Ground-based Low-light Imaging Platform (GLIP), is considered in Appendix A.

The main scientific instrument at the ALIS-station is the ALIS-imager (covered in detail in Chapter 3). Although the stations are primarily designed for optical instrumentation, the design permits a variety of other instruments to share the common infrastructure. The general requirement on any additional scientific module is that it fits physically, does not interfere with existing equipment and is compatible with the resources available at the GLIP (for example power and communication). A number of scientific modules (for example auroral spectrometers, photometers, cloud cameras) were planned but are not yet realised. For a period, three stations, (1) Kiruna, (3) Silkkimuotka and (6) Nikkaluokta were equipped with pulsation magnetometers operated by the University of Newcastle, Australia. So far these have only used the mains power and not been remote-controlled. A radio-experiment involving a new type of antenna and a 3D-receiver is planned to be installed for testing at some of the ALIS stations [*Puccio*, 2002].

2.1.1 Scientific considerations

While large-scale auroral phenomena are most conveniently studied from space, medium to small-scale phenomena are usually studied using ground-based instruments. ALIS was designed to make absolute measurements of auroral phenomena within the field-of-view of a traditional all-sky camera (Figure 2.1).

In order to make accurate absolute measurements of auroral emissions, the optimal situation exists when the observation is carried out close to the magnetic zenith of the observation site. As the zenith angle increases, the need for photometric corrections due to spatial smearing as well as atmospheric effects also increases rapidly. On the other hand, if the field-of-view is too small, many more stations are required in order to obtain an acceptable spatial coverage and overlapping fields-of-view suitable for triangulation at auroral altitudes. Selecting a field-of-view in the range of 50° to 90° with a station baseline of 50–100 km appeared as a suitable compromise, and also economically feasible. Figure 2.3 illustrates the effects of station baselines and fields-of-view in these ranges. Note that the fields-of-view under consideration in this section are along the x/y directions on the CCD, *not* to be confused with the diagonal, or optical field-of-view, refer to Figure 4.1 and Table 4.6 for details. It is immediately seen that a 50° field-of-view combined with a 100 km baseline will not provide sufficient overlap for auroral triangulation and tomography (assuming the lower edge of the auroral curtain at about 105 km [*Størmer*, 1955]). Consequently, a baseline of about 50 km was selected together with a field-of-view of about 50° (see Table 4.6 for details). However, as four stations were put into operation, it was realised that increasing the field-of-view to about 60° would reduce the artifacts during auroral tomography (see references in Section 6.3), as well as providing better triangulation possibilities for studies of lower lying objects, for example polar-

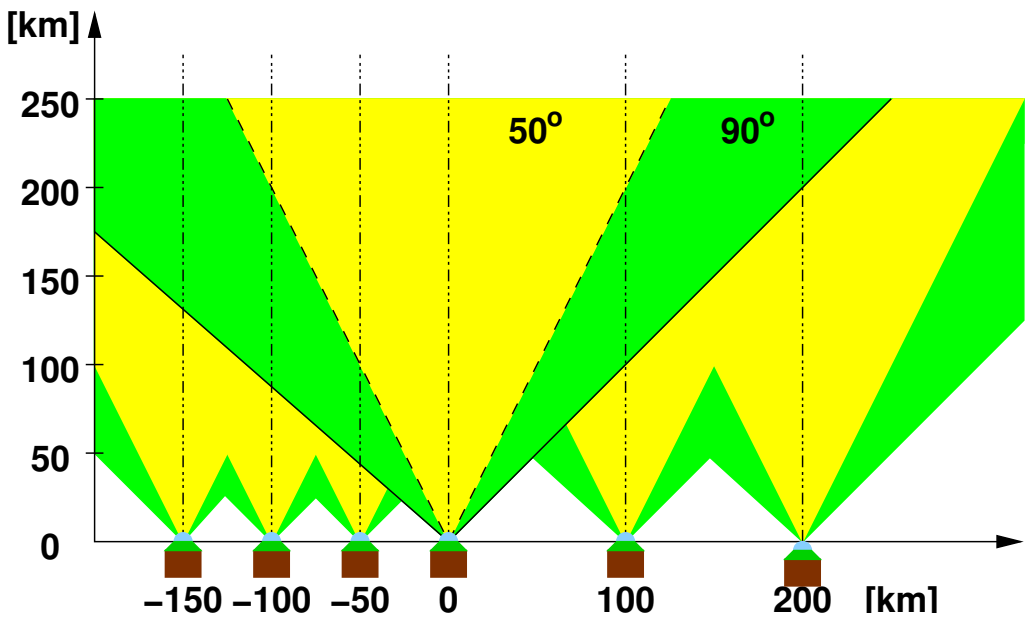

Figure 2.3: At a 50 km baseline (left) stations looking into zenith with a field-of-view of 90° (green) have overlapping fields-of-view from about 25 km. Limiting the field-of-view to about 50° (yellow) raises the height of overlap to 50 km. Increasing the station baseline to 100 km (right), the fields-of-view overlaps from about 50 km at 90°, and from about 100 km at about 50° field-of-view. It is furthermore seen that it is desirable to have steerable cameras in order to image a common volume with as many stations as possible (see also Figure 3.11).

			coverage in [km] at altitudes [km]:					
FoV	pixels	FoV_p	40	80	105	250	500	1000
50°			**37**	**75**	**98**	**233**	**466**	**933**
	64	0.78°	0.55	1.09	1.43	3.41	6.82	13.64
	128	0.39°	0.27	0.55	0.72	1.70	3.41	6.82
	256	0.20°	0.14	0.27	0.36	0.85	1.70	3.41
	512	0.10°	0.07	0.14	0.18	0.43	0.85	1.70
	1024	0.05°	0.03	0.07	0.09	0.21	0.43	0.85
60°			**46**	**92**	**121**	**289**	**577**	**1155**
	64	0.94°	0.65	1.31	1.72	4.09	8.18	16.36
	128	0.47°	0.33	0.65	0.86	2.05	4.09	8.18
	256	0.23°	0.16	0.33	0.43	1.02	2.05	4.09
	512	0.12°	0.08	0.16	0.21	0.51	1.02	2.05
	1024	0.06°	0.04	0.08	0.11	0.26	0.51	1.02

Table 2.2: Examples of approximative imager coverages in km (boldface), at some altitudes of interest given either a 50° or 60° imager field-of-view. For *each* field-of-view, the corresponding linear field-of-view per pixel (FoV_p) and pixel-coverage (in km) for a pixel looking in the zenith direction are given. (see also Section 4.3). The number of pixels also reflects some common binning factors in use with the present six ALIS imagers (see also Figure 3.4).

stratospheric clouds. Locating the two 60° imagers at appropriate stations thus provided a possibility for enhancing the results of tomography and triangulation.

The next parameter to consider is the spatial coverage and achievable field-of-view per pixel, FoV_p. Table 2.2 lists the linear coverage at some altitudes of interest for both the whole field-of-view, as well as for a pixel looking in the zenith direction. Note that these values are only to be interpreted as a first order approximation (see also Table 4.6 in Section 4.3). At 105 km altitude and 1024 pixels, the achievable pixel field-of-view is in the order of 100 m in zenith.

2.1.2 Selecting sites for the ALIS stations

Selecting the actual sites for the stations involved compromises. Although the first paper on ALIS [*Steen*, 1989] assumed that some stations would have to generate their own power and rely on microwave or satellite communications, budgetary considerations required the stations to be located in the vicinity of existing power and telecommunication lines. It was decided that the first station should be located close to the Swedish Institute of Space Physics (IRF) in Kiruna, in order to simplify development. The final decision on where to locate the remaining ALIS stations was based on a careful evaluation of a number of sites with regard to station separation (about 50 km) and geometry of ALIS with respect to tomographic as well as general auroral observation requirements, the proximity to commercial electrical power, telecommunication infrastructure and road access. Another important criteria was to find sites with low levels of man-made light pollution and a reasonably free horizon.

The highest priority was to populate the Tromsø–Kiruna meridian with sta-

				latitude			longitude			h
No.	Adr.	Site name	Acronym	°	′	″N	°	′	″E	m
1	S01	IRF	KRN	67	50	26.6	20	24	40.0	425
1	S01	Knutstorp	KRN	67	51	20.7	20	25	12.4	418
2	S02	Merasjärvi	MER	67	32	50.7	21	55	12.3	300
3	S03	Silkkimuotka	SIL	68	1	47.0	21	41	13.4	385
4	S04	Tjautjas	TJA	67	19	57.8	20	45	2.9	474
5	S05	Abisko	ABK	68	21	20.0	18	49	10.5	360
6	S06	Nikkaluokta	NIL	67	51	6.7	19	0	12.4	495
7	S07	Kilvo	KIL							
8	S08	Nytorp	NYT							
9	S09	Frihetsli	FRI							
10	S10	Mobile	BUS							

Table 2.3: Geographical coordinates of the ALIS stations. Notes: Station No. 1 moved in the summer of 1999, see text. Stations No. 7–8 were deployed on site but never used. Station No. 9 was never deployed. Station No. 10 is mobile.

tions, thereafter expansions towards east and west were desired. Practical considerations led to the stations being deployed in the following order (see Figure 2.4): (1) Kiruna, (2) Merasjärvi, (3) Silkkimuotka, (4) Tjautjas, (5) Abisko and (6) Nikkaluokta. After that, an expansion southward was planned with stations (7) Kilvo and (8) Nytorp. This was mainly in order to accommodate measurements of southward expansion of the auroral oval during the upcoming solar maxima. Later the plans were changed in favour of one station in Norway, (9) Frihetsli, to be possibly followed by a station at the EISCAT site at Ramfjordmoen, Norway. The motivation for this change of plans was to give a better support to combined measurements with EISCAT. Awaiting this expansion northward, a tenth mobile station provided zenith coverage along the Tromsø magnetic field-line during active experiments with HF pump-enhanced airglow and the EISCAT radar facility (Section 6.4). A summary of site numbers, names, acronyms and geographic coordinates is found in Table 2.3 and in Figure 2.4.

Station (1) Kiruna was initially located in the optical laboratory at IRF, Kiruna but had to be moved a couple of kilometres (to Knutstorp, close to the Kiruna EISCAT-site) in the fall of 1999 due to ongoing construction work and rising levels of man-made light pollution at the original site.

2.2 IT hardware and infrastructure

As might be expected, an unmanned large-scale remote-controlled facility like ALIS requires considerable amounts of Information Technology (IT), both in terms of computers and datacommunication infrastructure. As work on ALIS was initiated, much of what is taken for granted today simply did not exist, or was far too expensive. In other cases the technical evolution took unexpected turns, making some choices of technology appear awkward and obsolete today.

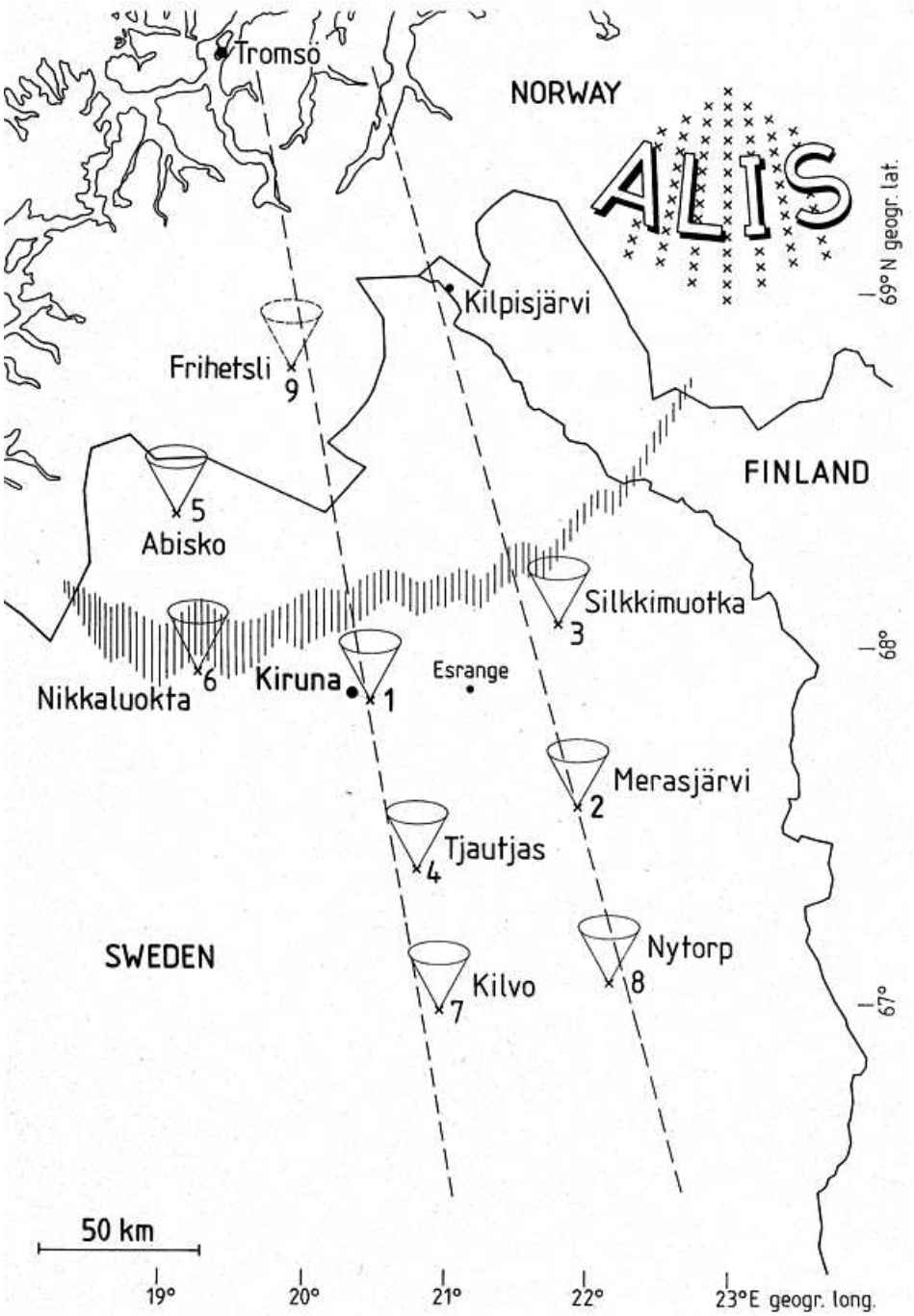

Figure 2.4: Map of northern Scandinavia displaying the final locations of the ALIS stations. See also table Table 2.3. The Control-Centre as well as a secondary Operations Centre is located in Kiruna.

2.2.1 Computers

A variety of computer architectures and operating systems were available when work on ALIS started. At an early stage command and control functions were separated from image processing, data storage and transmission. The first specification of the computer systems for ALIS [*Brändström and Steen*, 1992] included a main computer and a dedicated Image Processing Computer (IPC) in the control centre. At the stations, one computer would be responsible for controlling the station, while a special dedicated unit, called the Near-sensor Interface and Processing Unit (NIPU), would handle the large amounts of data ($\geq$ 2 Mbytes/s) created by the imagers.

A Hewlett Packard HP-755 PA-RISC workstation was selected as the control centre main computer. Budgetary constraints prohibited the use of similar computers at the stations. Therefore it was decided to use IBM-PC compatible machines (i486). Due to the fast development of computer hardware, the station computers have been replaced after typically 3 years of operation. The current system still uses various PCs (ranging from i486 to Pentium III). At the control centre the HP-755 computer lasted until 1999 when it was replaced by two PCs. The aim of having a dedicated image processing computer has not been realised as no real-time data is yet available due to the absence of high-speed lines to the stations. Dataanalysis is performed on various workstations.

2.2.2 The NIPU

The datahandling, image processing and data storage at the stations were supposed to be handled by a dedicated computer. Around 1990, a very promising device for this purpose was the Transputer, a parallel processing device communicating with other devices over four serial links. Another interesting device was the Intel I860 floating-point processor. A prototype system was built using the T222 and T800 Transputers. Apart from the imager itself it was also desirable to control the Camera Positioning System (CPS) as well as the filter-wheel from the NIPU. In this way the NIPU would control all subsystems related to the imager. The ALIS imager would produce over 2 Mbytes/s, which was too fast for the T222/T800 Transputer links (capable of 20 Mbits/s). However a new Transputer, the T9000, was expected to be released around 1992. This device would have enhanced links capable of 100 Mbits/s and increased processing power (25 MFLOPS), and would thus be well-suited for demanding image-processing applications [*Pountain*, 1991]. Designs were made for this device, but its release was postponed several times due to technical problems. Since the camera controller for the ALIS-Imager (Chapter 3) was also based on a Transputer, the T222, a T800 in the NIPU was chosen as an intermediate solution for handling the incoming image data. Due to the limitations of the link-speed of these Transputers, data was to be transferred to the NIPU over a 16-bit parallel interface. Six NIPUs of this design were built (Figure 2.5).

Meanwhile the fast development of the PCs eventually made the Transputers obsolete, and around 1997 it was decided that a second PC would take over the responsibilities of the NIPU. A prototype PCI-board with a DSP was designed and tested, but during this work technical problems with the parallel read-out from

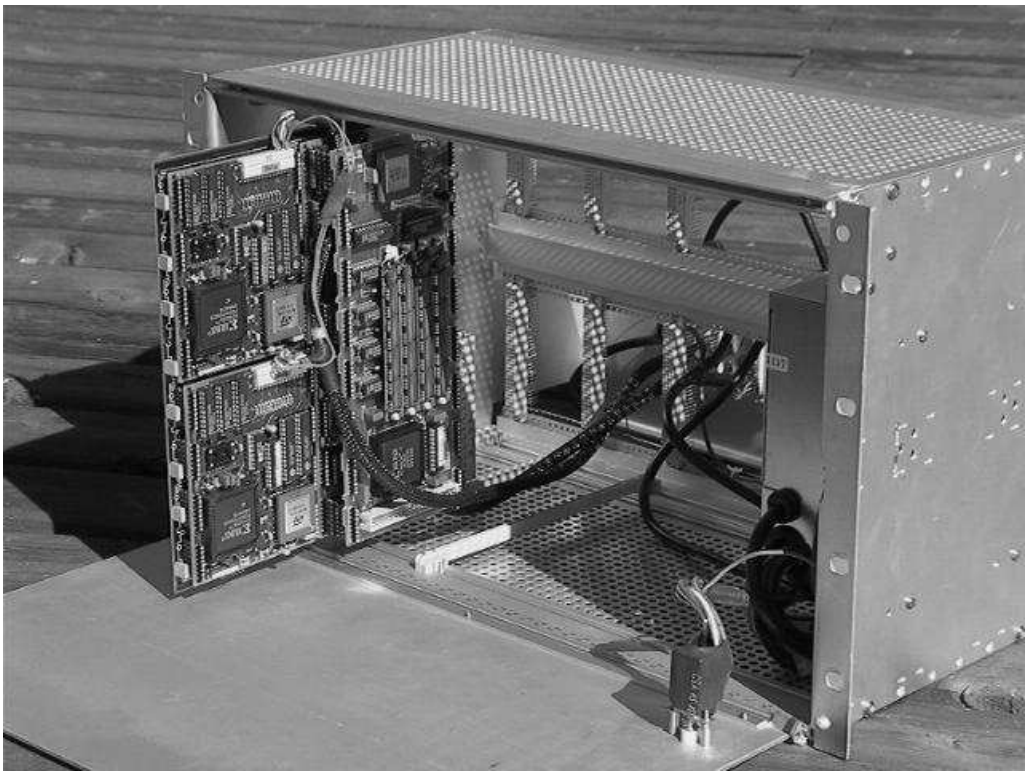

Figure 2.5: The NIPU. The board contains four T222 modules, each controlling the α and β axes of the camera-positioning system as well as the filter-wheel and an additional Transputer intended (but never used) for GPS-timing. The large module is the T800-board with memory and parallel interface for image capture from the 16-bit parallel interface of the camera controller. Ample space is provided for future expansions with T9000 boards.

the camera controller were discovered (Section 3.3.4). Since these problems could not be resolved, the resulting decrease of the maximum imager frame-rate made both the NIPU and the second PC for receiving image data superfluous. Therefore the six already existing NIPUs ended up as rather over-designed controllers for the camera-positioning system (Section 3.6) and the filter-wheels (Section 3.5.1).

2.2.3 Communication systems

When design work on ALIS began, the fastest off-the-shelf modem available was at 2400 bits/s, and with a special, rather expensive, leased-line one could attain 9600 bits/s. The first ALIS paper [*Steen*, 1989] specified a $\geq$ 10 Mbits/s communication link capable of near real-time image transfer to the control centre. A network of microwave links was considered but deemed far too expensive, as was the case with the fibre-optic lines passing near two of the stations (Merasjärvi, Silkkimuotka, see below).

Dial-up telephone lines were too slow, and faster means of communication too expensive. It was anticipated that the fast technological development in this field would make faster communication lines available at a reasonable cost. Thus it was decided that ALIS would use slow dial-up modem lines for command, status information and to transmit reduced quick-look images to the control centre. A future "to be defined" high-speed link to the control centre would provide the high-speed communication required for real-time transfer of raw image data. Meanwhile, local data storage, and on-site image processing of the data would be employed at the stations.

The dial-up lines were one of the major sources of trouble in ALIS during the early years. This was mainly due to bad telephone lines and old electro-mechanical telephone switching equipment. This led to extensive efforts to troubleshoot modem lines and to develop reliable communications software. Also the modem technology and quality of the telephone lines improved considerably over the years. Today the dial-up lines are capable of reliable 28800 bits/s communication, using the standard Point-to-Point Protocol (ppp) [*Simpson*, 1994].

The high-speed link remains to be defined. The optimal solution would be optical fibres ($>$ 100 Mbits/s), but other solutions are also possible, such as ADSL (500 kbits/s), ISDN ($<$ 128 kbits/s), radio-links ($>$ 1 Mbits/s), etc.

Stations (2) Merasjärvi and (3) Silkkimuotka are located in the proximity of nodes for high bandwidth fibre-optic communication lines. (5) Abisko is located close to the Abisko Scientific Station (ANS) which recently acquired high-speed fibre optic Internet connection.

Presently only the Kiruna station has a 2 Mbits/s Ethernet connection to Internet realised by a microwave-link to IRF, the rest of the stations are connected by means of 28 kbits/s dial-up modem lines. The rapidly increasing demand for high-speed Internet subscriptions among the general public might speed up the process of getting faster communication lines for all ALIS stations at a reasonable cost.

2.2.4 Station data storage

Various solutions for the local data storage at the stations have been considered over the years. Initially it was intended to store the image data onto Digital Data Storage (DDS) tapes which around 1992 had a storage capacity of up to 1 Gbyte. However, this solution proved slow and unreliable, mainly due to the hostile environment at the stations during tape-changes (moist, rapid temperature changes, etc.). Other solutions were also studied, but most of these were too complicated, too expensive or both. If faster communications would have been available, data could be stored on hard-disks, and downloaded to the control-centre in near real-time, or during non-measuring time. As the DDS drives tested at the first stations were not as reliable as expected, large (i.e. 2–9 Gbytes around 1992) external SCSI hard-disks were used instead. When a disk became full, it was exchanged manually, either by neighbours to the stations, or by staff from IRF. This solution proved simple and reliable. The only disadvantage was the usually rather long time (typically months) before raw-data from all stations became available for archiving and analysis.

2.2.5 Data archiving and availability

Reduced quick-look images (about 16 kBytes) are transmitted to the control centre and distributed to the operations centre (and web-site) in near real-time during measurement. However, these images are only intended for monitoring, and are of far too poor resolution for scientific analysis.

As the raw-data disks reach the control centre, recordable CDs (CD-R) of ALIS data are produced, and archived. All ALIS data produced so far are also made freely available on the world-wide web (see `http://www.alis.irf.se` for details) The main archive web-site is maintained by Peter Rydesäter who also provides a SQL database and search tools (see also Section 6.2).

The image data is stored in the Flexible Image Transfer System (FITS), [NASA, 1999]. This format is in wide use by the astronomical community, and found to be particularly suited to store scientific image data, as all supplementary information regarding an image (exposure time, filter, CCD temperatures, subsequent processing etc.) can be stored in the image header in a flexible way. FITS is recognised by many image processing packages, and free conversion programs to most other image formats exist on the Internet for most operating systems.

The size of the image-files is 16 bits/pixel (2 bytes) where the number of pixels is dependent on the configured spatial resolution (see Table 2.2 and Section 3.2). The total size of a set of images is also dependent on the number of stations involved and the temporal resolution selected.

2.2.6 Operating Systems

It was an early requirement to have a true multi-tasking operating system such as Unix for ALIS. HP-UX, which was delivered with the workstation selected for the control centre fulfilled this demand. The decision to use the IBM-PC architecture at the stations limited the choice of operating systems to SCO-Unix and MS-DOS. SCO-Unix was quite expensive compared to its reliability, so the

reluctantly chosen remaining option was to use MS-DOS at the stations. This lead to limitations in the flexibility of the system.

Some years later highly reliable and free operating systems such as Free-BSD and GNU/Linux emerged. It was immediately realised that a change to one of these operating systems at the stations would be necessary to meet the required data-handling specifications. In 1997 all stations had changed operating systems to Debian GNU/Linux, and in the fall of 1999 the HP-UX operating system in the control centre was also changed to GNU/Linux as the old HP workstation was replaced.

2.3 The ALIS control centre

The ALIS control centre (CC), is located in the optical laboratory of IRF in Kiruna (Figure 2.6). In the CC there are computers for controlling ALIS, commu-

Figure 2.6: The ALIS control centre at the optical laboratory as it looked around 1993. To the left are workstations and the station computer for the Kiruna station. The station overview map and console for the HP-755 workstation are seen in the center-right part of the photo. The two racks to the right contains monitors for the low-light TV-cameras, video recorders and timing systems.

nication equipment (e.g. modem pools for dial up connections) and workstations for running ALIS (Figure 2.7). In 1999, as ALIS station (1) Kiruna was moved (Section 2.1.2) a secondary point for controlling ALIS, an Operations Centre (OC) was established at the same place as station 1 (Figure 2.8). This was done in order to minimise disturbances from construction work at the CC. It is desirable to be able to run supporting low-light instruments and to make visual observations

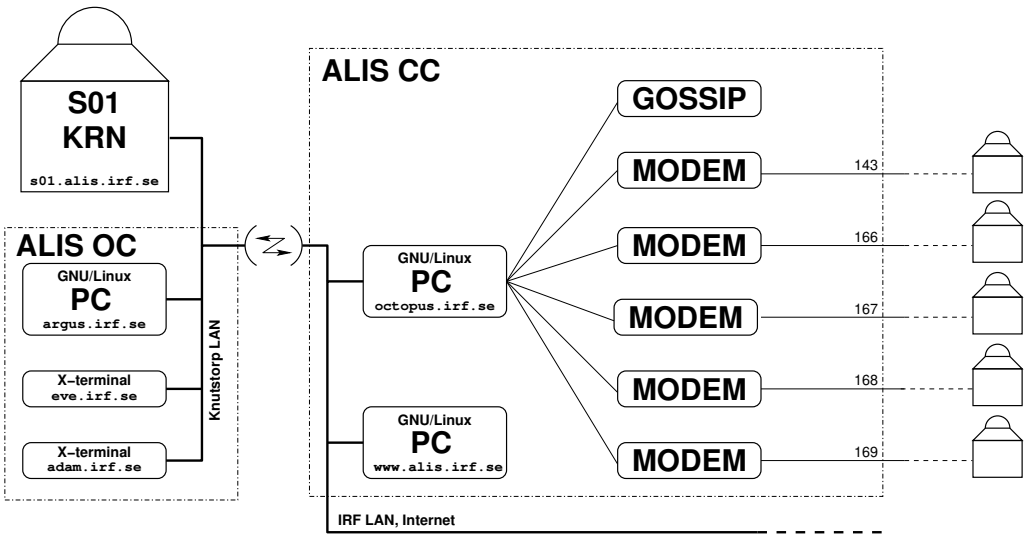

Figure 2.7: Block-diagram of the ALIS control centre (CC) at the optical laboratory, IRF Kiruna. The control centre consists of the gateway for dial-up access to the remote stations (`octopus.irf.se`) and its modem-pool. ALIS is controlled from the main computer (`www.alis.irf.se`) which also contains the web-server for ALIS. GOSSIP is a status display showing status and alarm information from the stations on a map [*Tornéus*, 1992]. The operations centre (OC) was initially located at the CC, but was later moved to Knutstorp (see text). It consists of a PC workstation and two X-terminals. Supporting optical instruments, for example low-light TV cameras, are also available at the OC. ALIS station 1 is located at the same site as the OC and they are both connected to the IRF LAN over a microwave link.

Figure 2.8: The ALIS operations centre that was established at Knutstorp (close to the EISCAT-site in Kiruna) in 1999. Two low-light TV-cameras (one with all-sky, and one with $\approx 40^\circ$ field-of-view) are used to give the operator a real-time display of the sky. These images are displayed on the monitors in the upper left part of the photograph. Below are two video tape recorders. The six ALIS stations are monitored and controlled from the computer terminals below, and some quick-look images from ALIS are seen on the screens.

when running ALIS. While most ALIS operations have been undertaken from the CC or OC, it is worth noting that ALIS can be controlled from almost any computer with a suitable Internet connection. During unattended operations, a pager call can be used to alert the operator on duty of abnormal conditions. The pager is also used for alarm messages (for example fire, trespass, power-failures, etc.) from the housekeeping units at the stations during non-measuring periods.

In the beginning, there were many technical requirements on the CC [for example *Steen*, 1989; *Steen et al.*, 1990]. As ALIS evolved the requirements on the CC were relaxed, and if, all stations obtain high-speed Internet connections, it will be completely superfluous, at least from a technical point of view. On the other hand, experience has shown that a dedicated centre for running ALIS campaigns, where scientists and staff can gather and run the observations, review results as well as solve problems, yields far better results as compared to if one single person runs ALIS from home or an office. Therefore it is probably important to have a dedicated operations centre for ALIS, despite the fact that ALIS can be run from almost anywhere.

Chapter 3

The ALIS Imager

> "For now we see through a glass, darkly; but then face to face: now I know in part; but then shall I know even as also I am known." *1 Cor. 13:12*

> "Orten, hvarifrån de [Norr-skenen] åskådas; tiden då de visa sig; deras ställning på himmelen; ombyteliga figur och vackra färgor; äro nästan de ende omständligheter, som därvid, äfven med svårighet, kunna i akt tagas. Ögat, pennan och den snällaste Målares pensel, äro för senfärdige, att teckna alla deras förändringar. Deras fladdrande ombyten förvilla imaginationen, och man bör vara god geometra, at skilja utseendet och figuren ifrån själva tingen, för at ej med allmänheten och forntiden däraf tillskapa tusende syner och vidunder, uti blotta luften." *Wilcke [1778]*

Spectroscopic measurements of auroral and airglow emissions have belonged to the realm of photometer measurements, while imaging techniques mainly have been tools for studies of morphology and dynamics. This chapter will discuss the required specifications for the ALIS imager in order to enable absolute spectroscopic measurements of column emission rates. Calibration issues will be discussed in Chapter 4.

3.1 Some basic concepts

There exist a number of textbooks [for example *Theuwissen*, 1995; *Holst*, 1998, and references therein], reports [for example *Eather*, 1982; *Lance and Eather*, 1993], and articles [for example *Janesick et al.*, 1987, and references therein] on solid-state imaging with CCD detectors. This section will provide a short summary of some fundamental concepts required to specify a CCD-imaging system suitable for the needs of auroral and airglow imaging.

Holst [1998] defines the term *radiometry,* as the *"energy or power transfer from a source to a detector"* while *photometry* is defined as *"the transfer from a source to a detector where the units of radiation have been normalised to the spectral sensitivity of the eye."*

3.1.1 Spectral radiant sterance (radiance)

The basic quantity from which all other radiometric quantities can be derived is spectral radiant sterance, L. Given a source area, A_s, radiating a radiant flux,

Φ, into a solid angle, Ω. The spectral radiant sterance in energy units, L_E, then becomes:

$$L_E(\lambda) = \frac{\partial^2 \Phi(\lambda)}{\partial A_s \partial \Omega} \left[\frac{\mathrm{W}}{\mathrm{m}^2\ \mathrm{sr}}\right] \tag{3.1}$$

where λ is the wavelength. Expressing the spectral radiant sterance in quantum units (L_γ) the following equation is obtained:

$$L_\gamma = \frac{L_E}{h\nu} = \frac{L_E \lambda}{hc} \left[\frac{\mathrm{photons}}{\mathrm{s\ m}^2\ \mathrm{sr}}\right] \tag{3.2}$$

Here ν is the frequency, h is Planck's constant and c is the speed of light. Please note spectral radiant sterance (radiance) is not to be confused with surface brightness which is a photometric unit involving the characteristics of the human eye [see *Holst*, 1998, pp. 20,26].

3.1.2 The Rayleigh

In terms of measurement techniques the aurora can be regarded as a five-dimensional signal with three spatial dimensions, one temporal and one spectral dimension. The desired physical quantity is usually the volume emission rate, $\epsilon(\mathbf{r}, t, \lambda)$, which cannot be found directly from measurements. However the rate of emission from a 1 m^2 column along the line of sight is normally just $4\pi L_\gamma$ for any isotropic source with no self-absorption [*Hunten et al.*, 1956].

Consider a cylindrical column of cross-sectional area 1 m^2 extending away from the detector into the source. The volume emission rate from a volume element of length dl at distance l is $\epsilon(l, t, \lambda)$ photons $\mathrm{m}^{-3}\,\mathrm{s}^{-1}$. The contribution to L_γ is given by:

$$dL_\gamma = \frac{\epsilon(l, t, \lambda)}{4\pi}\, dl \left[\frac{\mathrm{photons}}{\mathrm{s\ m}^2\ \mathrm{sr}}\right] \tag{3.3}$$

Integrating along the line of sight, l :

$$4\pi L_\gamma = \int_0^\infty \epsilon(l, t, \lambda) dl \tag{3.4}$$

This quantity is the column emission rate, which *Hunten et al.* [1956] proposed as a radiometric unit for the aurora and airglow. (See also *Chamberlain* [1995, App. II]) The unit is named after the fourth Lord Rayleigh, R. J. Strutt, 1875–1947, who made the first measurements of night airglow [*Rayleigh*, 1930]. (Not to be confused with his father, J. W. Strutt, 1842–1919 remembered for Rayleigh-scattering etc.) In SI-units the Rayleigh becomes [*Baker and Romick*, 1976]:

$$1\ [\mathrm{Rayleigh}] \equiv 1\ [\mathrm{R}] \triangleq 10^{10} \left[\frac{\mathrm{photons}}{\mathrm{s\ m}^2\ \mathrm{column}}\right] \tag{3.5}$$

The word *column* denotes the concept of an emission-rate from a column of unspecified length, as discussed above. It should be noted that the Rayleigh is an apparent emission rate, not taking absorption or scattering into account. However, *Hunten et al.* [1956] emphasise that *"the Rayleigh can be used as defined without any commitment as to its physical interpretation, even though it has been*

chosen to make interpretation convenient." The spectral radiant sterance (L_γ) in Equation 3.2 can be obtained from the column emission rate I (in Rayleighs) according to *Baker and Romick* [1976]:

$$L_\gamma = \frac{10^{10} I}{4\pi} \left[\frac{\text{photons}}{\text{s m}^2 \text{ sr}} \right] \tag{3.6}$$

Although not a proper SI-unit, the Rayleigh is often used in the field of auroral and airglow measurements. It is also frequently misunderstood and abused. It is important to remember that *the Rayleigh only is usable when the wavelength is specified.* Due to the plethora of Rayleigh definitions [*Baker and Romick*, 1976], it is always wise to state the definition of the unit before using it. In the following text, the Rayleigh will be used according to the original definition [*Hunten et al.*, 1956, but in SI-units] as defined above.

Using the recommended column emission rates in Rayleighs for the International Brightness Coefficients (IBC) as an example, the following spectral radiant sterances are obtained [*Chamberlain*, 1995, App. II]: IBC-I aurora, corresponding to 1 kR at 5577 Å is often described as the lowest column emission rate detectable by the unaided human eye. Usually this is compared to the luminous incidence of a moonless cloudy night which is about 10^{-4} Lux*. By the use of Equations 3.2 and 3.6, the spectral radiant sterance in energy units (L_E) can be calculated:

$$L_E(1 \text{ [kR]}) = \frac{10^{13} hc}{4\pi\lambda} = \frac{10^3 hc}{4\pi \times 5577} \approx 300 \left[\frac{nW}{\text{s m}^2 \text{ sr}} \right] \tag{3.7}$$

Similarly the brightest IBC-IV corresponding to 1 MR at 5577 Å, which is often compared to the luminous incidence of the full-moon of about 10^{-1} Lux* becomes:

$$L_E(1 \text{ [MR]}) \approx 300 \left[\frac{\mu W}{\text{s m}^2 \text{ sr}} \right] \tag{3.8}$$

3.1.3 Spectral radiant incidence (irradiance)

Spectral radiant incidence (irradiance), E, is defined as radiant power incident per unit area onto a target, in this case typically the effective aperture of the optics, A_{app}, image area, A_i, area of CCD-detector, A_{CCD}, or the area of a CCD pixel, A_{pix}.

The transmittance, $T(\lambda, ...)$, of an optical system is a function of many parameters, for example wavelength λ, viewing angle, temperature, etc., and must be experimentally determined (See Chapter 4). Here it is enough to state that the total transmittance is given by the product of the individual transmittances of the various components of the optical system:

$$T = \prod_{\forall X} T_X = T_a T_o T_f \ldots \tag{3.9}$$

Where T_X is exemplified by T_a, T_o and T_f which are the transmittance of the atmosphere, optics and filter, respectively. In the following text T will denote the product of appropriate transmittances according to Equation 3.9.

*According to *Holst* [1998, p. 28]

Consider an extended source of area, A_s, of given column emission rate, I, imaged by an optical system, here represented by a single lens with given focal length, f, and f-number, $f_\#$. The relation between the aperture-stop, d_{app}, f and $f_\#$ is given by:

$$f_\# = \frac{f}{d_{app}} \tag{3.10}$$

Setting the source at distance r_s from the lens, which is at the distance r_i from the detector and letting Ω_{ds} be the solid angle of the lens aperture as seen from the source, (assuming small angles), the photon flux, $\Phi_{\gamma_{app}}$, at the lens aperture then becomes:

$$\Phi_{\gamma_{app}} = L_\gamma A_s T_a \Omega_{ds} = L_\gamma A_s T_a \frac{A_{app}}{r_s^2} \quad \left[\frac{\text{photons}}{\text{s}}\right] \tag{3.11}$$

The spectral radiant incidence at the aperture, $E_{\gamma_{app}}$, then becomes:

$$E_{\gamma_{app}} = \frac{\Phi_{\gamma_{app}}}{A_{app}} = \frac{L_\gamma A_s T_a}{r_s^2} \quad \left[\frac{\text{photons}}{\text{s } m^2}\right] \tag{3.12}$$

The spectral radiant incidence at the image plane, E_{γ_i}, is given by (by substituting Equation 3.10 and assuming a circular aperture):

$$E_{\gamma_i} = \frac{\Phi_{\gamma_{app}}}{A_i} = L_\gamma \frac{A_s}{A_i} T \frac{\pi d_{app}^2}{4 r_s^2} = L_\gamma \frac{A_s}{A_i} T \frac{\pi f^2}{4 r_s^2 f_\#^2} = L_\gamma \frac{A_s}{A_i} T \frac{\pi f^2}{4 r_s^2 f_\#^2} \quad \left[\frac{\text{photons}}{\text{s } m^2}\right] \tag{3.13}$$

Noting that, for thin lenses and small angles:

$$\frac{1}{r_s} + \frac{1}{r_i} = \frac{1}{f} \tag{3.14}$$

In this case:

$$r_s \gg r_i \Rightarrow r_i \approx f \tag{3.15}$$

The lens-magnification formula is:

$$M^2 = \left(\frac{h_i}{h_s}\right)^2 = \frac{A_i}{A_s} = \left(\frac{r_i}{r_s}\right)^2 \tag{3.16}$$

where h_i and h_s denote the height of the image and source respectively. Inserting Equations 3.6 and 3.14-3.16 into Equation 3.13, the following equation for E_{γ_i} is obtained:

$$E_{\gamma_i} = \frac{T\Phi_\gamma}{A_i} = T L_\gamma \frac{\pi}{4 f_\#^2} = T \frac{10^{10} I}{16 f_\#^2} \quad \left[\frac{\text{photons}}{\text{s m}^2}\right] \tag{3.17}$$

Note that this equation is only accurate for small angles, an off-axis image will have reduced incidence compared to an on-axis image. This is called the "natural vignetting", $\cos^4\theta$, and is usually inserted as a multiplication factor in Equation 3.17, as required.

However, the actual vignetting is highly dependent on the characteristics of the optical system. Therefore the vignetting as well as other aberrations, and the transmittance (T) must be experimentally determined. This will be considered further in Chapter 4 and references therein.

3.1.4 Number of incident photons

Using Equation 3.17 the number of photons reaching the image plane, n_{γ_i}, can be calculated:

$$n_{\gamma_i} = E_{\gamma_i} t_{int} A_i = T t_{int} A_i \frac{10^{10} I}{16 f_{\#}^2} \text{ [photons]} \tag{3.18}$$

Here t_{int} is the integration time in seconds. The number of photons hitting the CCD, $n_{\gamma_{CCD}}$, are:

$$n_{\gamma_{CCD}} = n_{\gamma_i} T_w T_{CCD} \frac{A_{CCD}}{A_i} \text{ [photons]} \tag{3.19}$$

Here T_w is the transmittance of the optical window protecting the CCD, and T_{CCD} is the transmittance of the CCD substrate (in the case of a back-side illuminated CCD). Likewise, the number of photons hitting an individual pixel, $n_{\gamma_{pix}}$, is:

$$n_{\gamma_{pix}} = n_{\gamma_{CCD}} \frac{A_{pix}}{A_{CCD}} = T t_{int} A_{pix} \frac{10^{10} I}{16 f_{\#}^2} \text{ [photons]} \tag{3.20}$$

(using Equations 3.18–3.19 and Equation 3.20). Again, please remember the caution at the end of Section 3.1.3

3.1.5 The CCD as a scientific imaging detector

"During the past couple of decades the Charge Coupled Device (CCD) sensor has gradually replaced the tube type sensors, such as the vidicon, due to its advantages in size, weight, power consumption, noise characteristics, linearity, dynamic range, photometric accuracy, spectral responsitivity, geometric stability, reliability, and durability" [*Janesick et al.*, 1987]. As an auroral imager, the CCD is thus almost an ideal detector for ground-based as well as for space-borne instruments. The CCD can be used either as the primary photon detector, or in an Intensified CCD (ICCD) configuration. Whether to use a CCD or an ICCD is mainly a matter of requirements on temporal resolution and signal-to-noise ratio, *SNR*. This section will begin with a short review of a number of parameters describing the performance of a CCD detector.

3.1.6 Quantum efficiency

The quantum efficiency, Q_E, is a measure of the number of electrons generated per incident photon:

$$Q_E = \eta_E Q_{EI} \left[\frac{e^-}{\text{photons}} \right] \tag{3.21}$$

where η_E is the effective quantum yield (electrons generated, collected, and transferred per interacting photon per pixel) and Q_{EI} is the interacting quantum efficiency (interacting photons per incident photons per pixel) [*Janesick et al.*, 1987]. However, for the purpose of this text it is only needed to consider Q_E, which for the purpose of this text, is the same as the detective quantum efficiency (DQE).

Quantum efficiency for a CCD is wavelength dependent, and is of no value unless the wavelength is specified. High performance scientific thinned, back-side illuminated anti-reflection coated CCD devices might have as high quantum

efficiency as 80–90% in the visible region as demonstrated in Figure 3.1. As

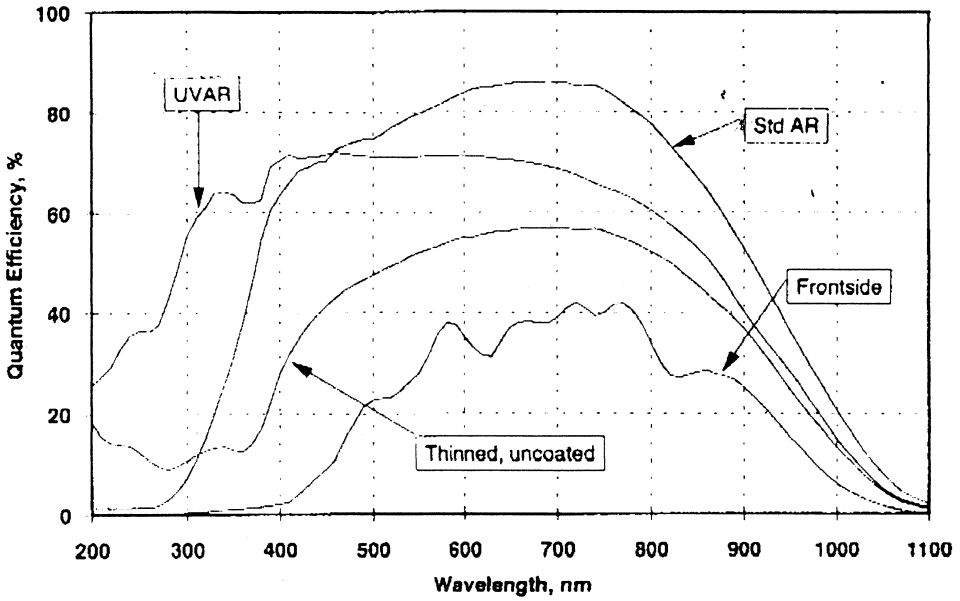

Figure 3.1: Quantum efficiency vs. wavelength for the SI-003AB CCD (ALIS `ccdcam5`) as published in the manufacturers data-sheet. Four curves are presented: with standard anti-reflection coating ("StdAR") UV anti-reflection coating ("UVAR"), uncoated, thinned, back-side illuminated ("Thinned uncoated") and front-side illuminated ("Frontside"). The ALIS imagers have a standard anti-reflection coating.

a comparison, Q_E for typical consumer CCDs lies in the range 30–70%. The average number of photoelectrons, $\overline{n}_{e_\gamma^-}$, obtained from $n_{\gamma_{pix}}$ (Equation 3.20) is:

$$\overline{n}_{e_\gamma^-} = Q_E n_{\gamma_{pix}} \left[e^-\right] \tag{3.22}$$

3.1.7 Noise

Aurora and airglow are so-called photon-limited signals, where the quantum nature of light limits the achievable signal-to-noise ratio. Photon arrival follows Poisson statistics, where the variance is equal to the mean. The sum of the standard deviation of the noise resulting from the photoelectrons, $\langle n_{e_\gamma^-} \rangle$, and dark-current noise, $\langle n_{e_d^-} \rangle$, is denoted shot noise, $\langle n_{e_s^-} \rangle$, and is obtained from the following equation:

$$\langle n_{e_s^-} \rangle = \sqrt{CTE^N \left(\langle n_{e_\gamma^-} \rangle^2 + \langle n_{e_d^-} \rangle^2 \right)} = \sqrt{CTE^N \left(\overline{n}_{e_\gamma^-} + \overline{n}_{e_d^-} \right)} \approx \sqrt{\overline{n}_{e_\gamma^-} + \overline{n}_{e_d^-}} \tag{3.23}$$

Here $\langle X \rangle^2$ stands for the variance of quantity X and $\langle X \rangle$ is the standard deviation. $\overline{X}$ denotes the mean value. CTE^N stands for the Charge Transfer Efficiency (CTE) where N is the number of transfers. Usually $CTE^N \approx 1$ for reasonably sized CCD devices. Note that $n_{e_\gamma^-}$ would be present even for an ideal detector.

Additional noise sources include: reset noise, on-chip and off-chip amplifier noise (1/f-noise and white noise). Of particular interest for low-light applications is that the 1/f-noise, which is the main source of the read noise ("noise-floor"), increases in proportion to the square root of the read-out frequency ("pixel-clock"), thus requiring a suitable compromise between noise performance and frame-rate. The analogue-to-digital converter has a quantisation noise, also switching transients coupled through the clock signals, electro-magnetic interference, etc., sums up to the total noise. There is pattern noise due to differences in dark-current and photo response non-uniformities [*Holst*, 1998]. At high signal levels the total noise is dominated by pattern noise (pixel to pixel sensitivity variations within the CCD) for most CCDs, at low signal levels the read noise ("noise floor") dominates [*Janesick et al.*, 1987]. Many of these noise sources can be reduced to negligible levels by good electronic design practices. In particular, the dark-current (and reset noise) is reduced by cooling the CCD. By the use of Double Correlated Sampling (DCS) the reset noise can be almost eliminated. The quantisation noise is eliminated by using a sufficiently high resolution ADC. It is, however, beyond the scope of this work to embark onto a detailed analysis of the noise-sources in CCD imagers, instead a simplified noise model from *Holst* [1998] is adopted:

$$\langle n_{e^-_{CCD}} \rangle = \sqrt{\langle n_{e^-_s} \rangle^2 + \langle n_{e^-_r} \rangle^2 + \langle n_{e^-_p} \rangle^2} \ \left[e^-_{RMS} \right] \tag{3.24}$$

The standard deviation of the noise floor (or read noise), $\langle n_{e^-_r} \rangle$, is usually stated in the imager specification as 'read noise', or easily obtained from a zero exposure. This noise source increases with the square-root of the pixel clock frequency, which imposes an *SNR* constraint onto the frame-rate.

The pattern noise, $\langle n_{e^-_p} \rangle$, is the sum of Fixed Pattern Noise (FPN), resulting from pixel-to-pixel variations in the dark-current, and Photo Response Non-Uniformities (PRNU). An approximate worst case value is provided by *Holst* [1998]:

$$\langle n_{e^-_p} \rangle = \sqrt{\langle n_{e^-_{FPN}} \rangle^2 + \langle n_{e^-_{PRNU}} \rangle^2} \approx \langle n_{e^-_{PRNU}} \rangle \approx U \overline{n}_{e^-_\gamma} \approx \frac{\overline{n}_{e^-_\gamma}}{\sqrt{n_{e^-_{max}}}} \ \left[e^-_{RMS} \right] \tag{3.25}$$

However, for the low signal levels considered here, pattern noise is neglected. Then the total noise approximation for a bare CCD becomes (by substituting Equation 3.23 into Equation 3.24):

$$\langle n_{e^-_{CCD}} \rangle \approx \sqrt{\overline{n}_{e^-_\gamma} + \overline{n}_{e^-_d} + \langle n_{e^-_r} \rangle^2} \ \left[e^-_{RMS} \right] \tag{3.26}$$

It should be remembered that this equation is an approximation.

3.1.8 Signal-to-noise ratio

The measured signal-to-noise ratio in terms of the digital output, DN, or in terms of root-mean-square electrons e^-_{RMS} is defined as follows:

$$SNR_{CCD} = \frac{DN_{signal}}{DN_{noise}} \approx \frac{\overline{n}_{e^-_\gamma}}{\langle n_{e^-_{CCD}} \rangle} \tag{3.27}$$

Substituting Equation 3.26 the *SNR* can now be calculated with the help of Equations 3.20 and 3.22 and the total noise is given by Equation 3.26:

$$SNR_{CCD} \approx \frac{\overline{n}_{e^-_\gamma}}{\sqrt{\overline{n}_{e^-_\gamma} + \overline{n}_{e^-_d} + \langle n_{e^-_r} \rangle^2}} \tag{3.28}$$

For an ideal photon detector Equation 3.28 becomes:

$$SNR_{\gamma\text{ideal}} = \sqrt{\overline{n}_{e^-_\gamma}} \tag{3.29}$$

3.1.9 The signal-to-noise ratio of an ICCD

In the image-intensifier, for each primary photoelectron emitted by the photo-cathode (pc), the image-intensifier produces a burst of approximately 10^3 secondary CCD electrons, typically by the use of a micro-channel plate (MCP) between the photo-cathode and phosphor screen. The phosphor screen is then optically coupled to the CCD by the use of lenses or a fibre-optic taper[†].

The number of photons reaching the image plane (n_{γ_i}) is given by Equation 3.18. The average number of signal electrons generated by the photo-cathode, $\overline{n}_{e^-_{\gamma,pc}}$, for a pixel area A_{pix} projected onto the photo-cathode, by the fibre-optic minification ratio, M_{FO} is given by [see *Holst*, 1998, p. 196]:

$$\overline{n}_{e^-_{\gamma,pc}} = Q_{E_{pc}} \overline{n}_{e^-_{\gamma i}} \frac{A_{pix}}{A_i} = Q_{E_{pc}} T t_{int} M_{FO}^2 A_{pix} \frac{10^{10} I}{16 f_\#^2} \quad \left[\mathrm{e}^-_{\mathrm{RMS}}\right] \tag{3.30}$$

After the MCP the number of electrons are amplified with the average MCP gain, $\overline{g}$, i.e. average number of secondary photoelectrons, $\overline{n}_{e^-_{\gamma MCP}}$, produced per photo-cathode electron $\overline{n}_{e^-_{\gamma,pc}}$

$$\overline{n}_{e^-_{\gamma MCP}} = \overline{g}\, \overline{n}_{e^-_{\gamma,pc}} \quad \left[\mathrm{e}^-_{\mathrm{RMS}}\right] \tag{3.31}$$

The photoelectrons are then converted back to photons by the phosphor screen with a phosphor efficiency, η_P, and then re-imaged onto the CCD via a fibre optic taper. The transmittance losses here are denoted T_{FO}. Finally the photons hit the CCD and are converted to photoelectrons:

$$\overline{n}_{e^-_{\gamma CCD}} = \eta_P Q_{E_{CCD}} T_{FO}\, \overline{n}_{e^-_{\gamma MCP}} \quad \left[\mathrm{e}^-_{\mathrm{RMS}}\right] \tag{3.32}$$

By applying the following approximation:

$$Q_{E_{ICCD}} = Q_{E_{pc}} \eta_P Q_{E_{CCD}} T_{FO} \approx Q_{E_{pc}}$$

the following equation is obtained (using Equations 3.30-3.32):

$$\overline{n}_{e^-_{\gamma CCD}} = \overline{g}\, \overline{n}_{e^-_{\gamma,pc}} = \overline{g}\, Q_{E_{pc}} T t_{int} M_{FO}^2 A_{pix} \frac{10^{10} I}{16 f_\#^2} \quad \left[\mathrm{e}^-_{\mathrm{RMS}}\right] \tag{3.33}$$

[†]In this text, the term "ICCD" is used for the combination of an image intensifier and a CCD, regardless of coupling type, or if they are manufactured as one unit or not.

As with the CCD (see Equation 3.23), the photo-cathode produces both photon-noise and dark-current noise :

$$\langle n_{e^-_{s,pc}} \rangle = \sqrt{\langle n_{e^-_{\gamma,pc}} \rangle^2 + \langle n_{e^-_{d,pc}} \rangle^2} \ \left[\mathrm{e^-_{RMS}}\right] \tag{3.34}$$

Another noise source, unique to the ICCD, is the electron multiplication noise, which is due to the statistical distribution of the number of secondary photoelectrons[‡]. Taking this uncertainty in $\overline{g}$ into account, the combined variance with the photon noise becomes:

$$\langle n_{e^-_{\gamma,pc}} \rangle^2 = k_{MCP}\, \overline{g}^2\, \overline{n}_{e^-_{\gamma,pc}} \approx 2\overline{g}^2\, \overline{n}_{e^-_{\gamma,pc}} \tag{3.35}$$

Here, k_{MCP} is the microchannel excess noise. The photo-cathode dark-current noise, is also dependent on $\overline{g}$ in the same way:

$$\langle n_{e^-_{d,pc}} \rangle^2 = 2\overline{g}^2\, \overline{n}_{e^-_{d,pc}} \tag{3.36}$$

Taking Equation 3.26 as an approximation for the total CCD noise, and inserting into it Equations 3.35 and 3.36, for the ICCD noise sources, leads to the following expression for the total noise for the ICCD, $\langle n_{e^-_{ICCD}} \rangle$:

$$\langle n_{e^-_{ICCD}} \rangle \approx \sqrt{2\overline{g}^2\, (\overline{n}_{e^-_{\gamma,pc}} + \overline{n}_{e^-_{d,pc}}) + \overline{n}_{e^-_d} + \overline{n}_{e^-_r}} \tag{3.37}$$

By applying Equations 3.33 and 3.37 into Equation 3.27 the following approximation for the *SNR* of an ICCD, SNR_{ICCD}, emerges:

$$SNR_{ICCD} \approx \frac{\overline{g}\, \overline{n}_{e^-_{\gamma,pc}}}{\sqrt{2\overline{g}^2\, (\overline{n}_{e^-_{\gamma,pc}} + \overline{n}_{e^-_{d,pc}}) + \overline{n}_{e^-_d} + \overline{n}_{e^-_r}}} \tag{3.38}$$

As seen, increasing the gain of the image intensifier makes the CCD noise-sources negligible, but *does not* increase the *SNR*. For very high gain, Equation 3.38 is reduced to:

$$SNR_{ICCD} \approx \frac{\overline{n}_{e^-_{\gamma,pc}}}{\sqrt{2(\overline{n}_{e^-_{\gamma,pc}} + \overline{n}_{e^-_{d,pc}})}} \tag{3.39}$$

3.1.10 Threshold of detection and maximum signal

The threshold of detection is usually defined as $SNR = 2$ while the Noise Equivalent Exposure, *NEE*, is obtained when $SNR = 1$. The maximum signal, or Saturation Equivalent Exposure (SEE) is obtained when the charge well capacity, $n_{e^-_{max}}$, is reached. This occurs when:

$$n_{e^-_\gamma} \geq n_{e^-_{max}} - n_{e^-_d} \tag{3.40}$$

In most cases the maximum charge-well capacity, DN_{SEE}, is matched to the maximum ADC output DN_{max}. For the ICCD case, apart from the condition above, there is also a saturation level for the image intensifier to be considered. On the other hand, the high-voltage for the intensifier can be gated, acting like an electronic shutter.

[‡]A more detailed discussion of this noise source is found in works by *Holst* [1998, pp. 195–200], *Trondsen* [1998, p. 48], *Csorba* [1985, pp. 120–124] and *Hertel* [1989].

3.1.11 Dynamic range

The Dynamic Range, DR, is defined as the peak signal divided by the RMS noise and the DC-bias-level, DN_{DC}, (if any). The minimum ADC output, DN_{min}, is subtracted in the case of a signed integer output. DR is usually expressed in decibels.

$$DR = 20 \log_{10} \left(\frac{DN_{SEE} - DN_{min}}{DN_{DC} + DN_{NEE} - DN_{min}} \right) [dB] \tag{3.41}$$

An approximate theoretical value for DR is obtained by dividing the maximum signal (Equation 3.40) by the total noise, $\langle n_{e^-_{tot}} \rangle$, which is found in Equations 3.26 and 3.37 for the CCD and ICCD case respectively.)

$$DR \approx 20 \log_{10} \frac{n_{e^-_{max}} - n_{e^-_d}}{\langle n_{e^-_{tot}} \rangle} \; [dB] \tag{3.42}$$

3.2 Selecting an imager for ALIS

The selection process for an ALIS imager includes many considerations of scientific, technical as well as of an economical nature. Naturally this leads to various compromises. A complete ALIS imager consists of optics, filters and a detector with its electronics and supporting systems. The choice of detector determines many parameters of the other imager subsystems, therefore this choice will be discussed first.

3.2.1 Comparison of an ICCD with a CCD imager

An ICCD imager was considered early on in the ALIS project [for example *Steen et al.*, 1990] and indeed many excellent CCD imagers for aurora and airglow, as, for example, the HAARP imager [*Lance and Eather*, 1993], the Portable Auroral Imager (PAI) [*Trondsen*, 1998] and the new Finnish all-sky camera [*Syrjäsuo*, 2001] as well as some of the imagers operated by *Kaila* [2003a] are based on an image-intensified CCD. Yet, it is important to realise that most CCDs have a higher Q_E than that of the photo-cathode in an image-intensifier. For example, the PAI, used for high spatial and temporal resolution auroral imaging, have a $Q_{E_{CCD}}$ of 67 %, while the quantum efficiency of the photo-cathode is only 28%, both at $\lambda = 5577$ Å [*Trondsen*, 1998, p. 51]. Scientific grade CCDs might have a $Q_{E_{CCD}}$ of up to about 90% as demonstrated in Figure 3.1. Despite this a CCD is not always preferable to an ICCD.

Figure 3.2 plots SNR as a function of column emission rate, with $f_\# = 3.9$ and a fixed integration time of 16.7 ms (NTSC video standard). The CCD data were taken from the technical specifications for the PAI (Table 3.1) as well as from the specifications for an ALIS imager (`ccdcam5`, Table 3.2). Ideal photon detectors with the same pixel area as of the ALIS Imager (a) and the PAI (c), have thresholds of detection at approximately 20 kR and 40 kR respectively. The ALIS Imager, curve (b), reaches $SNR = 2$ at about 100 kR which is also the case for the PAI ICCD (d). Curve (e) for the unintensified CCD of the PAI (without image intensifier) does not reach $SNR = 2$ until at approximately 2 MR. Clearly,

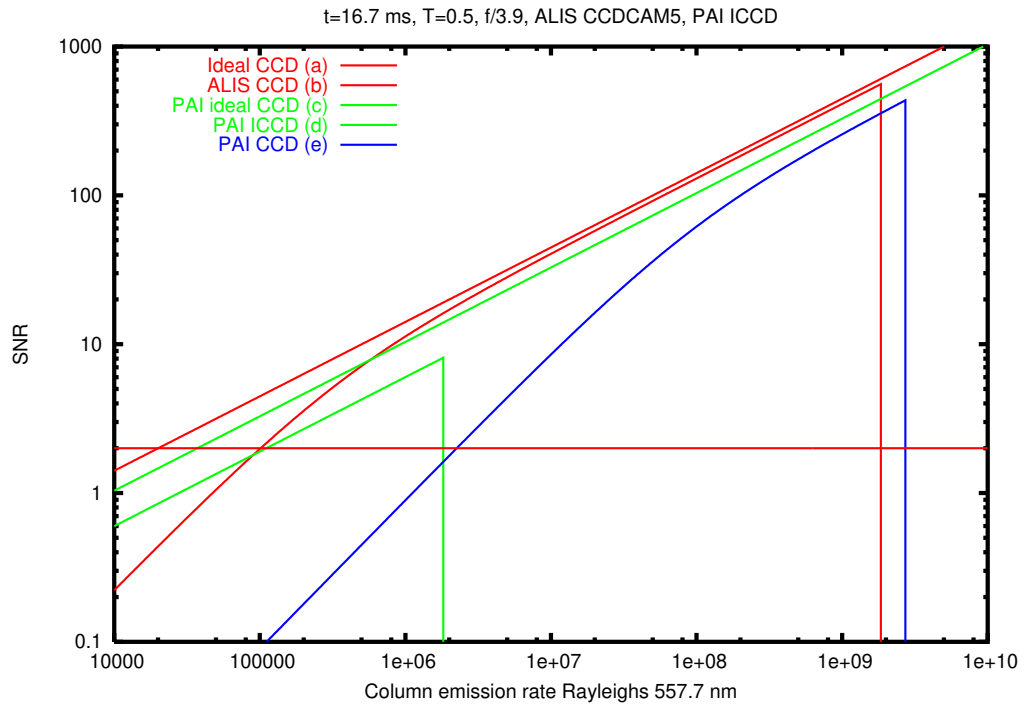

Figure 3.2: *SNR* vs. column emission, for f/3.9 optics with $T \approx 0.5$ and 16.7 ms on-chip integration time. (a) Ideal photon detector (Equation 3.29) with $A_{pix} = 576\,\mu m^2$ (ALIS). (b) Equation 3.28 for ALIS `ccdcam5` (Table 3.2). (c) Same as (a) but $A_{pix} = 310\,\mu m^2$ (PAI). (d) Equation 3.38 for the PAI ICCD (Table 3.1). (e) Same as (b) but for the PAI CCD without image intensifier. The horizontal line indicates the threshold of detection at $SNR = 2$.

Parameter	Symbol	`PAI`	Unit	Notes
MCP mean gain (medium)	$\overline{g}$	1500		
Photo-cathode dark-current	$\overline{n}_{e^-_{d,pc}}$	0.1	nAm^{-2}	
Photo-cathode quantum efficiency	$Q_{E_{pc}}$	28	%	at 5577 Å
CCD read noise	$\langle n_{e^-_r} \rangle$	80	e^-_{RMS}	
CCD dark current	$\overline{n}_{e^-_d}$	0.1	nAm^{-2}	b) at $21°C$
CCD full well (anti-blooming off)	$N_{e^-_{max}}$	80	ke^-	a)
CCD quantum efficiency	$Q_{E_{CCD}}$	67	%	at 5577 Å
CCD pixel area	A_{pix}	11.7×27.0	μm^2	
Fibre-optic minification ratio	M_{FO}	1.55		

Table 3.1: ICCD parameters for the portable auroral imager (PAI) obtained from *Trondsen* [1998, Table 4.1 p.51]. All values at room temperature. Notes: a) Value from data-sheet of the CCD. b) *Trondsen* has confirmed the value of $0.1\mathrm{mAm}^{-2}$ to be a typo.

Parameter	Symbol	ccdcam5	Unit	Notes
Read noise	$\langle n_{e_r^-} \rangle$	8.3	e^-_{RMS}	a) b)7.5@10.5μs/pixel
Dark current	$\overline{n}_{e_d^-}$	12.4	$e^-_{RMS}\ s^{-1}$	at $-15°C$.
Full well	$n_{e^-_{max}}$	316	ke^-	c)
Quantum efficiency	Q_E	89.8	%	4000 Å
Quantum efficiency	Q_E	98.9	%	5500 Å, at $-15°C$, d).
Quantum efficiency	Q_E	99.4	%	7000 Å, d).
Quantum efficiency	Q_E	55.3	%	9000 Å

Table 3.2: Some parameters for the CCD in ALIS-imager ccdcam5 (SI-003AB serial No. 6144GBR10-B2) as measured by the CCD-manufacturer. All values measured at $-45°C$ unless otherwise noted. Notes: a) quadrant with highest value. b) same parameter, as measured by camera manufacturer. c) quadrant A 3% linearity. d) questionable assuming a lower value of about 85% (Figure 3.1) [author's note]. (See also Tables B.1–B.6 in Appendix B)

this CCD is not suitable for low-light observations, without image intensifier. These results are in agreement with *Trondsen* [1998, Chapter 4].

At low column emission rates, the ALIS Imager and the PAI ICCD appear comparable in *SNR*. However, note that this is a misleading result, as the PAI ICCD, with its frame-transfer CCD, provides data at NTSC video rates (30 frames/s), while the read-out of the ALIS quad read-out full-frame CCD is limited to about 2.8 s at the stated read noise, resulting in a maximum frame rate of about 0.3 frames/s (see Table 3.3 in Section 3.2.2). Therefore, as already noted by *Trondsen* [1998] it might be concluded that the ICCD is the better choice for temporal resolutions $\leq 1s$ needed by the high temporal resolution requirements on the PAI.

While the CCD is a linear device, the image-intensifier is an electron-tube exhibiting non-linearities and aging effects making the already non-trivial task of absolute calibration even more complicated. Also image-tubes might bloom, causing the entire image to saturate, if part of the scene within the field-of-view saturates. Exposure to too bright point sources might lead to permanent image retention or intensifier damage [See for example *Holst*, 1998, and references therein]. For these reasons it was decided to further investigate the feasibility of using an unintensified CCD for the ALIS imagers. However, for such a system to be useful for studies of aurora and airglow, the unintensified CCD must provide acceptable *SNR* for column emission rates down to a couple of hundred Rayleigh, for integration times of about 1 s. Figure 3.3 displays the *SNR* plotted versus integration time for column emissions ranging from 100 R–1 MR. As seen IBC-I–IV have acceptable *SNR* for 1 s integration time. Examining Equation 3.28, it is seen that the *SNR* can be increased by increasing the number of photoelectrons, i.e. by increasing the pixel area, improving the transmittance, increasing the integration time, or by improving the quantum efficiency (see Equations 3.20 and 3.22). One possibility is to utilise on-chip binning factors ("super-pixels") to increase the pixel area as demonstrated in Figure 3.4. As seen, the threshold of detection improves by the product of the binning factor (i.e. the increase of pixel area). On the other hand, the spatial resolution is decreased by the same factor.

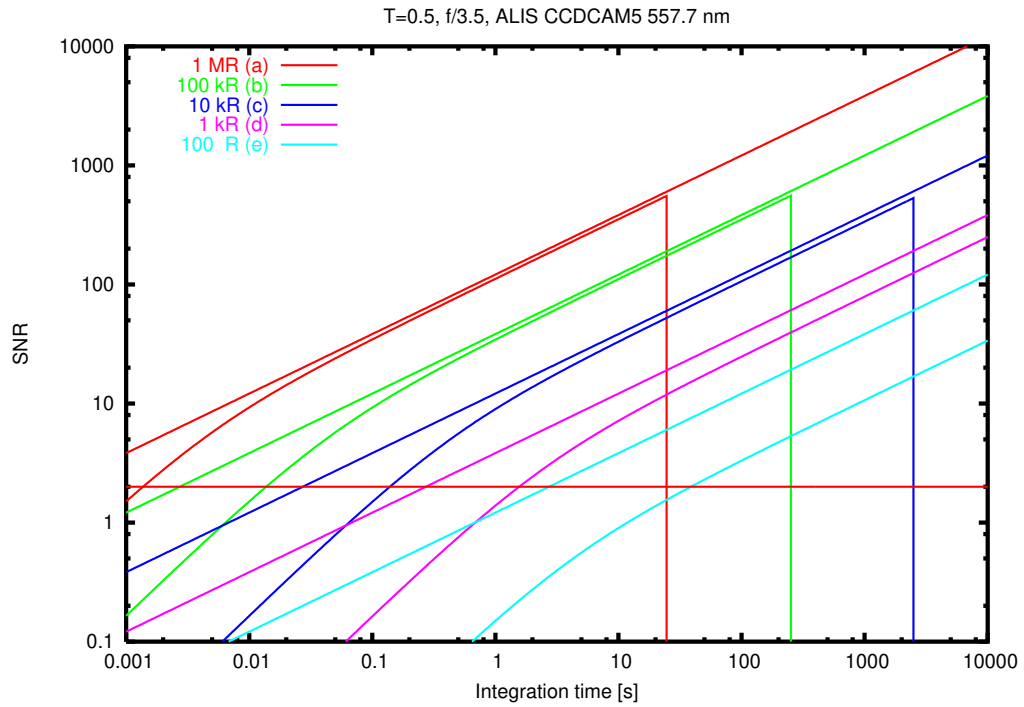

Figure 3.3: *SNR* versus integration time for (a) 1 MR IBC-IV (b) 100 kR IBC-III, (c) 10 kR IBC-II, (d) 1 kR, IBC-I and (e) 100 R. All at 5577 Å.

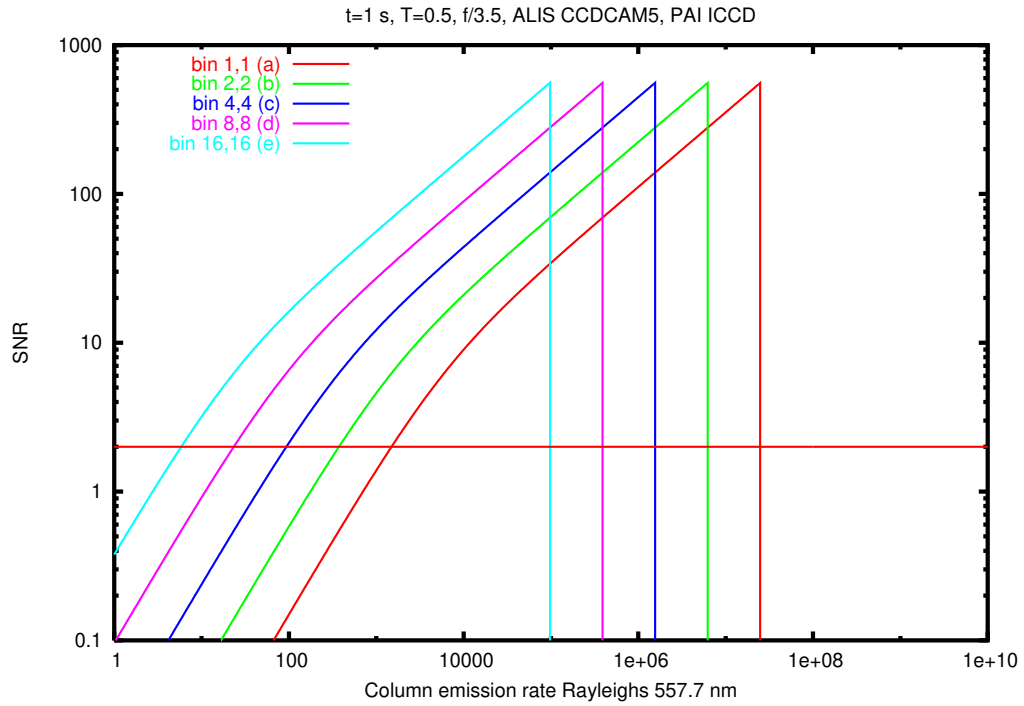

Figure 3.4: SNR vs. column exposure rates at 1 s integration time ($f_{\#} = 3.5, T = 0.5$) with binning factors: (a) 1×1, (b) 2×2, (c) 4×4, (d) 8×8 and (e) 16×16.

This also implies that the frame-rate increases, as there are less pixels to read-out. Thus, for any given measurement situation, application of on-chip binning factors provides a way to optimise a compromise between sensitivity, spatial and temporal resolution.

For high column emission rates the CCDs saturate after reaching their charge well-capacity. It should be noted that pattern noise is not taken into account in the plots. This noise would have decreased the *SNR* somewhat at high-signal levels, but is of little interest for photon-limited imaging situations.

3.2.2 Frame rate

The ALIS CCD is a full frame CCD. The read-noise (which increases as the square-root of the pixel-rate, mainly due to the 1/f-noise, see Section 3.1.7) in Table 3.2 was measured at a pixel read-out rate of $10.5\mu s$/pixel. At this rate it would take 11 s to read 1024^2 pixels. One way of getting around this problem is to divide the CCD into sub-arrays. The ALIS CCD is divided into four sub-arrays with identical read-out channels working in parallel (Figure 3.5). Table 3.3

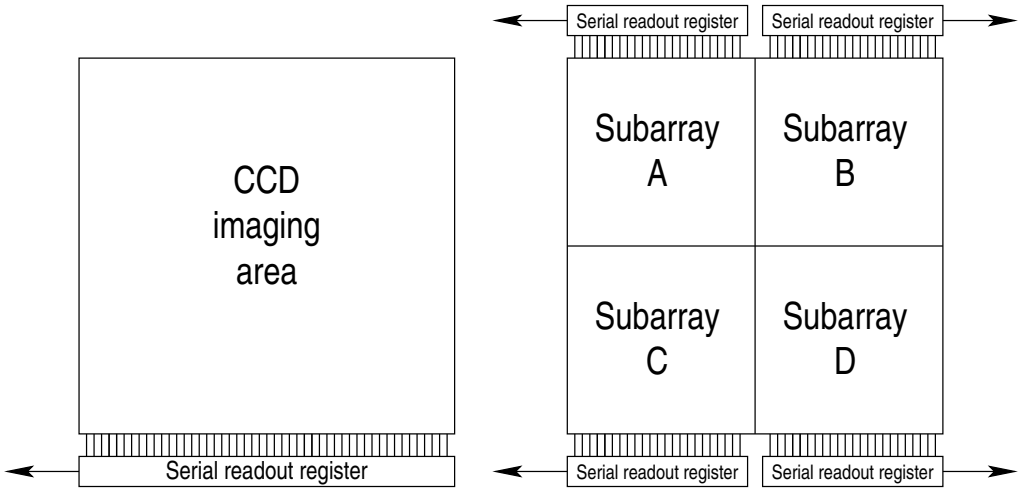

Figure 3.5: At a given pixel rate, a full frame CCD (left) takes four times as long to read-out as compared to an array divided into four sub-arrays (right), each with its own serial read-out register, sense node, amplifiers, S/H circuits and ADC:s.

illustrates the maximum achievable read-out rates for the ALIS CCDs.

The frame rate, FR, as a function of on-chip integration ("exposure") time, t_{int}, read-out time, t_{read}, and misc. time before the next image can be read, t_{misc}, (for example caused by the electronics, or the need to flush the CCD etc.) is given by:

$$FR = \frac{1}{t_{int} + t_{read} + t_{misc}} \tag{3.43}$$

3.3 The CCD imager for ALIS

Based on the discussion in the previous sections, it might be concluded that an ICCD imager is better for video-rate observations, mainly due to the long read-out time of a full-frame CCD. On the other hand, the large dynamic range, linearity and long time stability of a scientific-grade unintensified CCD make it an interesting choice for absolute spectroscopic imaging measurements of column emission rates down to about 1 s time resolution. Therefore it was decided to select a thinned back-side illuminated quad-read-out CCD for the ALIS imagers. At the time of specification no commercially available imager met the requirements of temporal resolution. One company was willing to modify their dual-read-out CCD camera head to a quad-read-out system, resulting in the imager system finally procured for ALIS. This section presents a short summary of some of the most important technical details of the six imagers. For further technical information about the imager hardware, etc., see *Preston* [1993, 1995]; *AstroMed Ltd.* [1993] and *AstroCam Ltd.* [1995]

3.3.1 The camera head

The CCD camera head (CCH) is of dimensions $125 \times 140 \times 144\ mm^3$ (Figure 3.6). A slightly larger front plate ($155 \times 170\ mm^2$) enables mounting the camera head

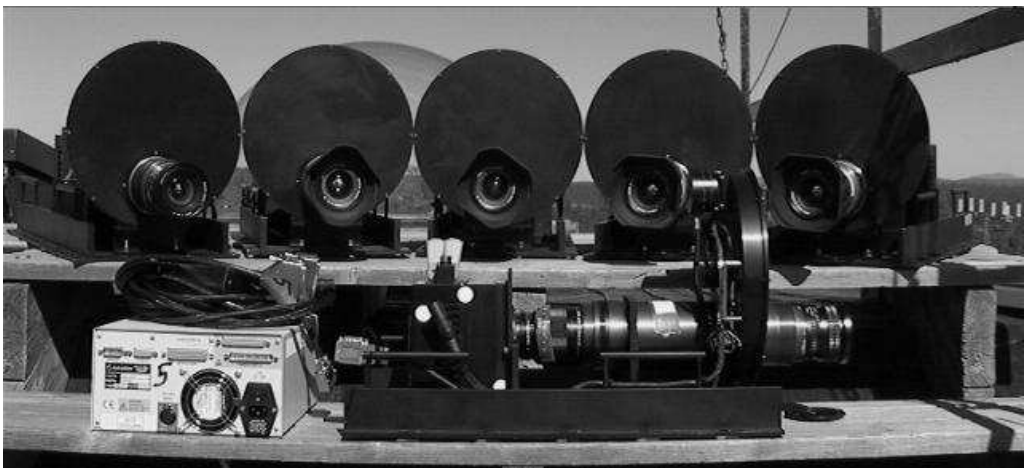

Figure 3.6: The six ALIS imagers. In the right forefront a sideview of an imager is shown. The front lens, telecentric part with filter wheel, and camera lens connected to the CCD camera head are seen. The white box on the left is a camera control unit.

to the structure supporting the camera head, optics and filter-wheel. Centred on the front plate is the optical interface, which consists of a removable ring with a Canon lens-mount. By replacing the ring, the lens-mount can be reconfigured to a Nikon lens-mount. Thus it is possible to attach a wide variety of standard objective lenses. The thinned back-side illuminated quad-read-out CCD is mounted onto a Peltier cooler inside a hermetically sealed compartment filled with an inert gas under low-pressure. Light enters through the front-plate hole, a mechanical shutter, and a high-quality optical window onto the CCD inside the

sealed compartment. Note that the CCD itself has no optical window exposing the chip and bonding threads to the environment of the compartment. Therefore, the sealed compartment may not be opened, unless in a clean room environment with adequate electrostatic discharge (ESD) protection measures as CCDs are extremely sensitive to ESD discharges. Also, proper equipment for venting and re-sealing the compartment needs to be present.

A vendor-provided CCD test report accompanied each CCD-chip, and excerpts from these reports, as well as some measurements provided by the camera manufacturer, are provided in Appendix B as Tables B.1–B.6 as well as in Table 3.2 above.

The camera head also contains a circuit board with low-noise preamplifiers and buffers for the four analogue read-out channels, etc. A heat-sink and a cooling fan on the back of the camera head cools the hot side of the Peltier cooler. Three temperature sensors measure CCD, ambient and heat-sink temperatures. Two round 2 m 37-way screened twisted flat-cables with "DSUB" connectors in each end connect the camera head to the camera control unit[§]. These cables are individually matched to each imager system and may not be interchanged. A third cable is powering the Peltier cooler.

3.3.2 The camera control unit

The camera head is powered and controlled by a Camera Control Unit (CCU). This unit includes analogue and digital signal processing chains for the four identical signal processing channels, as well as other control electronics and power supplies (Figure 3.6).

The CCU is controlled by a T222 Transputer, which communicates with its host systems over a Transputer-link (a kind of serial interface). CCD clocking and pixel read-out is controlled by an Erasable, Programmable Logic Device (EPLD) that is capable to read-out up to 4×4096 pixels without pausing. The analogue pixel values are digitised using four fast 16-bits Analogue to Digital Converters (ADCs). The data is then stored in four 4 kByte FIFO memories for subsequent transfer to the host computer, either on the Transputer link, or by way of a 16-bit parallel port. The maximum possible theoretical pixel rate is $1.5\mu s$/pixel. If desired, any CCD quadrant, or region of interest can be read-out separately.

3.3.3 Configuring the imager

All configuration settings of the CCD imager are under software control. A configuration file (`4400.cf`, see `http://alis.irf.se/alis/alis/ccdcam`) stored on the controlling computer is uploaded to the CCU during its boot procedure. This file contains configuration settings for CCD-size, clock timing, voltage and gain settings, etc. The configuration file is unique to each CCD and imager. By changing appropriate configuration settings, it is possible to reconfigure the imager for various situations. As each of the four signal processing channels have software selectable gain settings as well as DCS (Section 3.1.7) time constant and slope settings, this allows for a wide range of speed, gain and noise settings. Table 3.3 gives a brief overview of some of the possible trade-offs between noise performance and

[§]Note the cables are only about 1 m and flat on the prototype unit (`ccdcam1`)

ccdcam	pixels	$\frac{\mu s}{\text{pixel}}$	$\overline{n}_{e_r^-}$ $[e^-_{RMS}]$	$t_{read}[s]$	Notes
1	1124×1024	6	12–14	1.7	a)
1	1124×1024	8	9–12	2.3	a)
1	1124×1024	13	8–9	3.7	a) default
1	1124×1024	23	7	6.6	
2	1124×1024	1.6	28	0.5	
2	1124×1024	2.5	11	0.7	
2	1124×1024	4.1	10	1.2	
2	1124×1024	10.5	8	3.0	default
3	1124×1024	1.6	25	0.5	
3	1124×1024	2.5	13	0.7	
3	1124×1024	4.1	10	1.2	
3	1124×1024	7.0	9	2.0	default
4	1124×1024	1.6	25	0.5	b)
4	1124×1024	3.8	13	1.1	b)
4	1124×1024	6.7	10	1.9	b)
4	1124×1024	12.5	9	3.6	b) default
5	1056×1024	1.6	28	0.4	
5	1056×1024	2.5	11	0.7	
5	1056×1024	4.1	10	1.1	
5	1056×1024	10.5	8	2.8	default
6	1076×1024	1.6	25	0.4	
6	1076×1024	3.8	13	1.0	
6	1076×1024	6.7	10	1.8	
6	1076×1024	12.5	9	3.4	default

Table 3.3: CCD-read noise at various pixel clocks for the six ALIS imagers. The values are from the vendor-provided configuration files for the imagers.

read-out speed. For a more detailed understanding of these configuration possibilities, please refer to the imager documentation and configuration files. See also Table 3.2, Equations 4.7 and 4.8 in Section 4.2.1.

3.3.4 The user port

"Okay, Houston, we've had a problem here." *John Leonard Swigert, Jr.*

As the T222 Transputer links are capable of no more than 20 Mbits/s, image-data transfer at maximum pixel-clocking would be too slow. To remedy this the camera controllers are equipped with a 16-bit parallel interface. Originally it was intended that data from this interface would be read directly by the NIPU, however, due to the fast technical development, an extra computer responsible for receiving and storing the image data took over the role of the NIPU (see also Section 2.2.2). A prototype fast read-out interface card for a PC computer was built and tested. During these tests it was found that the user port omitted the 50 last pixels of each line on each of the four read-out channels (corresponding to a total of 102400 pixels in the centre 100 columns of the image) thus rendering the image data useless. Contacts were taken with the camera manufacturer to remedy this. This resulted in a new version of the camera controller software, fixing some of these problems, but now severe intermittent problems arose. Great effort was made to find the cause of these data-losses but without success. A solution to these problems still remains to be found, and meanwhile, the fast read-out mode had to be abandoned.

3.3.5 Operational remarks

At the time of writing, the ALIS imagers have been in operation for up to ten years. During this time they have produced a large number of images resulting in scientific findings as reported in Chapter 6, and references therein. The main technical obstacle has been poor frame-rate as discussed above.

The oldest, prototype imager, (`ccdcam1`) still works well, as does the newest imager (`ccdcam6`). The second camera (`ccdcam2`) developed a problem with ice on the CCD in 1999, probably due to a breach in the hermetic compartment. This problem should be fairly easy to resolve. The remaining cameras have had intermittent reliability problems related to the electronics. The occurrence of these problems has increased during the last couple of years. Another issue is that much of the camera electronics is becoming obsolete, severely affecting spare-parts availability. On a short time-scale (3–5 years), a limited maintenance operation will most likely bring 4–6 imagers back into operation. However, in a longer perspective, the now rather old imager electronics need to be completely replaced. During such a renovation it must be investigated if the most expensive part of the system (i.e. CCDs), and even the camera heads can be reused. All six CCD detectors are in good condition, and still among the best imaging detectors available for the scientific objectives of ALIS.

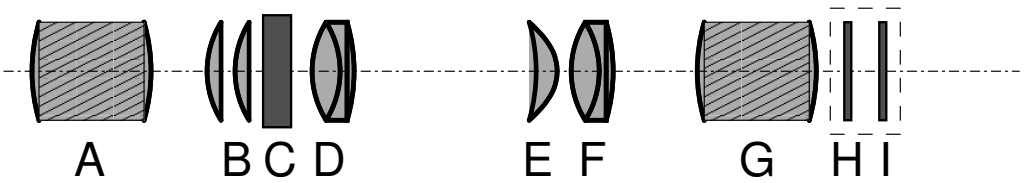

Item	ccdcam	Description
A	1,6	Front objective: Mamiya Sekor C 35 mm $f_{\#} = 3.5$
A	2–5	Front objective: Mamiya Sekor C 45 mm $f_{\#} = 2.8$
B	1–6	Two plano-convex telecentric lenses (plano side to rear)
C	1–6	$3''$ interference filter.
D	1–6	Field lens: Achromat, (lowest curvature side to rear)
E	1–6	Close-up lens 1: Meniscus, reverse configuration (convex side to rear)
F	1–6	Close-up lens 2: Achromat, reverse configuration (lowest curvature side to rear)
G	1–6	CCD camera lens: Canon FD 85 mm $f_{\#} = 1.2$
H	1–6	Window of the hermetically sealed CCD enclosure (inside CCD camera head)
I	1–6	CCD (inside CCD camera head)

Figure 3.7: Schematic diagram of the optical system for an ALIS imager. The two front objectives give a diagonal field-of-view of about 90° and 70° respectively. Information about the optical elements and their orientation after *Keo Consultants* [1994, 1997]

3.4 The optical system

To fully exploit the detector performance, a very fast custom designed optical system would need to be designed for ALIS. Ideally this would include a set of replaceable front-lenses, preferably mounted on a rotating disc in front of the filter-wheel, resulting in a remotely selectable field-of-view. As narrow-band interference filters are to be used, a telecentric lens system is required to have nearly parallel rays through the filters (see Section 3.5 for details). It was realised early that the requirement of changeable field-of-view had to be dropped due to reliability as well as budgetary constraints. Therefore, given the station separation, a field-of-view of approximately 50°–90° would be the best compromise (See also Figure 2.3 in Chapter 2). Following quotations from various optical manufacturers in the field, it was also quickly realised that the cost of *one* custom designed optical system would quickly exceed the entire project budget. Therefore a commercial telecentric optical system, frequently used in this field, was selected.

This system consists of a replaceable front-objective (A), two plano-convex telecentric lens-elements (B), a $3''$ filter holder (C, replaced by the IRF-designed filter-wheel Section 3.5.1), a field-lens (D), two close-up lenses (E,F) and a camera objective(G) (Figure 3.7). As discussed in Section 2.1.1, the station separation baseline was selected for a moderate field of view of about 50°–90°. For the first four imagers, the 45 mm front-objective resulted in a diagonal field-of-view of

about 50°. Experiences gained from tomographic reconstruction using images from these four systems resulted in a decision to slightly widen the field-of-view for the next two imagers. Consequently these were equipped with a 35 mm front-objective, giving a diagonal field-of-view of about 90°.

According to vendor specifications [*Keo Consultants*, 1994, 1997], the f-number setting on the front lens, $f_{\#fl}$, will determine image brightness on the CCD, as well as the maximum ray-angle through the filter, θ_{max}, given by the following approximate formula:

$$\theta_{max} = \arctan\left(\frac{1}{2f_{\#fl}}\right) \tag{3.44}$$

A photograph of the six ALIS imagers appears in Figure 3.6.

3.5 Interference filters

To make spectroscopic imaging, narrow-band interference filters are required. These filters are sometimes referred to as Fabry-Perot filters, as they are multiple cavity solid Fabry-Perot etalons [See for example *Macleod*, 1986; *Hernandez*, 1986, and references therein]. Rays passing through an interference filter must be nearly normal to the filter system. This dictates the use of a telecentric lens-system as discussed in Section 3.4.

The passband of an interference filter with effective index of refraction, N_e, ($N_e \approx 2$ for most interference filters) and filter centre wavelength at normal incidence, λ_{cw}, shifts to λ_θ at angle of incidence θ according to the following equation[¶]:

$$\lambda_\theta = \lambda_{cw}\sqrt{1 - \frac{sin^2\ \theta}{N_e^2}} \tag{3.45}$$

As seen, the passband shifts to shorter wavelengths at increasing angle of incidence. This fact is often utilised to fine-tune filters, or to measure background intensity by tilting the filter out of the passband for the emission line under study. In the case of the ALIS optics, let θ define a cone between normal incidence and θ_{max} given by Equation 3.44. Optimum filters for this situation should be designed as insensitive to angle as possible, and the bandwidth should be wide enough to pass the wavelength(s) of interest at all angles within the cone. Thus θ_{max} also defines the minimum possible bandwidth of the filter. Given a wavelength region of interest, specification of the optical system, filter centre wavelength (λ_{cw}) and desired filter-bandwidth, $\Delta\lambda$, an optimal filter is manufactured. As almost every batch of filters are tailored for a particular application, high-quality interference filters for imaging applications are rather expensive devices. Data on the filters used for ALIS appear in Tables 3.4-3.5. A discussion of the selected emission lines is found in the work by *Gustavsson* [2000, Chapter 2] and references therein.

[¶]from the filter manufacturer (`http://www.barrassociates.com/terms.php?type=angle`), see also [*Jones*, 1974]

3.5.1 The filter wheel

The filter wheel (Figure 3.8) has six positions for 76.2 mm (3″) interference filters

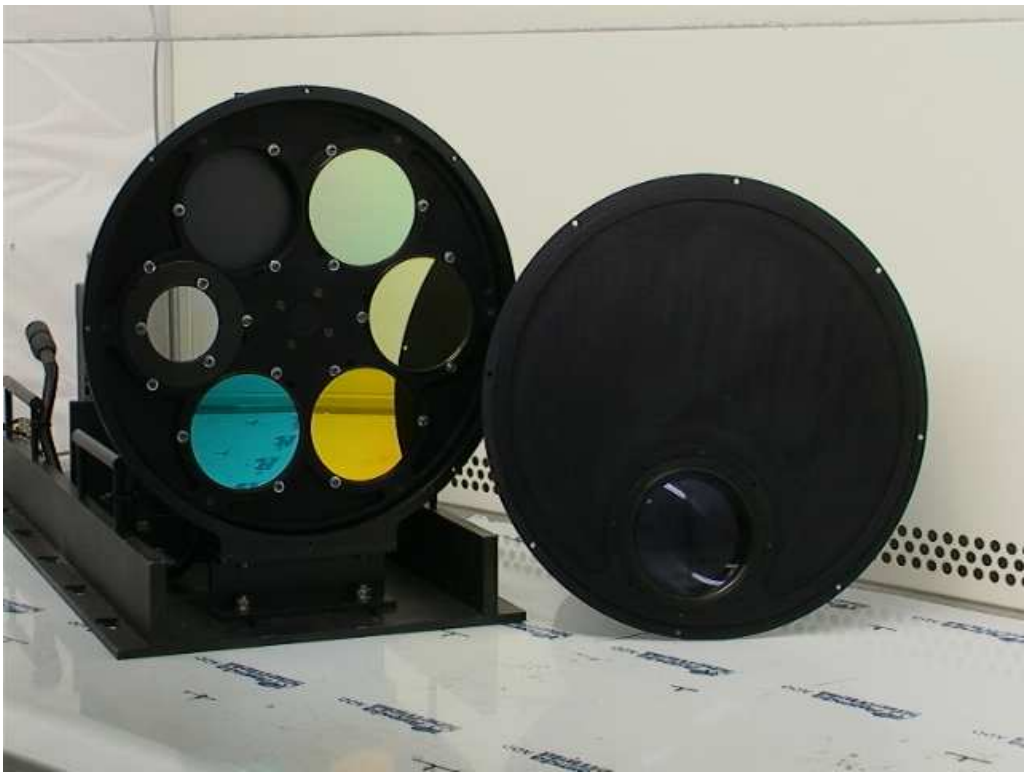

Figure 3.8: The six-position filter wheel with cover removed exposing the filter compartment. Starting at filter position zero (approximately five o'clock in the photo) filters for: $O(^1S)$ 5577 Å, $O(^1D)$ 6300 Å, 6230 Å (background), white light (empty), 5324 Å (a smaller filter in an adaptor ring intended for LIDAR studies), and finally in position five, the N_2^+ 1Neg. 4278 Å auroral filter. To the right the cover with the back end of the front lens is seen. A stepping motor attached to the rear top side of the filter wheel enclosure (not shown) actuates the filter wheel by a small cog-wheel driving cogs in the inner perimeter of the filter wheel. An angular encoder is attached to the filter wheel axis on the rear side of the enclosure (not shown).

numbered 0–5. Temperature stabilisation is achieved through a heating blanket and temperature sensors inside the filter compartment. Positions 0, 1, 3 and 5 have standardised filter assignments (Table 3.4), and the remaining two positions have been used for various other filters (Table 3.5). A stepping motor actuates cogs along the perimeter of the filter wheel. An angular encoder on the filter wheel axis senses the filter position. The filter change time is 1–2 s. The filter wheel cover, which also supports the front lens, is easily removable for filter changes etc. However, the cover should only be removed in a clean room, to avoid dust in the filter compartment. The power-supply and stepping motor drive electronics are mounted in a 19″ enclosure, the Filter Wheel Control unit (FWC) (Figure 3.9 and the block diagram in Figure 3.12).

Pos.	Emission	λ [Å]	Filter λ_{cw} [Å]	$\Delta\lambda$ [Å]	Notes
0	$O(^1S)$	5577	5590	40	
1	$O(^1D)$	6300	6310	40	
2					See Table 3.5
3					empty
4					See Table 3.5
5	N_2^+ 1Neg.	4278	4285	50	

Table 3.4: Filter placement standard for ALIS. The empty position is for white-light imaging (without filter). Two optional positions are available, see Table 3.5

λ [Å]	Filter CW λ_{cw} [Å]	$\Delta\lambda$ [Å]	usage	Positions at `ccdcam` 1	2	3	4	5	6
4227	4225	280	meteor studies						2
	6230	40	background filter.	2	2	2	2	2	
	5324	50	Lidar filter			4			
	5100	40	background filter.						2
5893	5898	200	meteor studies (Na)	2					
8446	8455	40	$O(3p^3P)$	4			4	4	4

Table 3.5: Optional filters and their usage. The last six columns display the filter position assignments for the six imagers. See Section 6.6.2 regarding the filters for meteor studies.

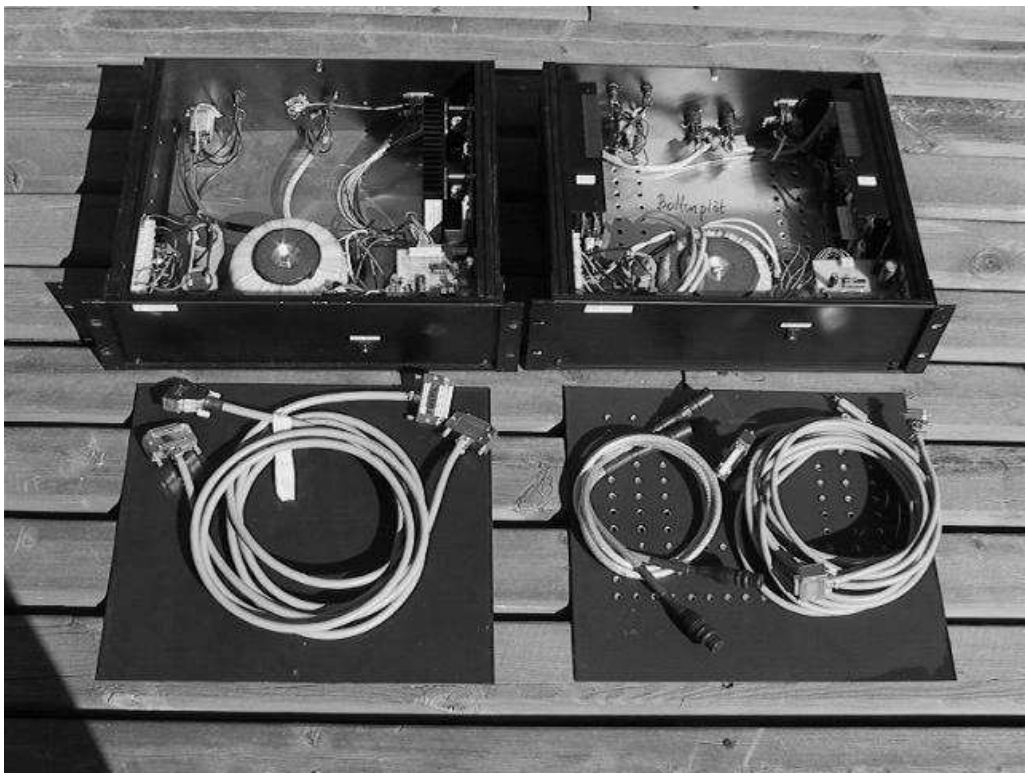

Figure 3.9: Left: Power supply, stepping motor drive circuits, cables etc. for the filter wheel. Right: The same equipment, but doubled for the camera positioning system (2 axes). See also Figure 3.12.

3.6 The camera positioning system

As the imagers are using moderate fields-of-view (Figure 2.3), a Camera Positioning System (CPS) is required in order to be able to configure ALIS for various imaging situations. For example, when running in a tomographic mode, observation of a common volume centred on an auroral arc is desired, while maximum sky coverage, or tracking of the foot-point of a spacecraft might be the objective of other observational modes. When observing for example HF-pump enhanced airglow (Section 6.4), the cameras need to point towards the anticipated region of enhanced airglow above the EISCAT-Heating facility in Tromsø

Initially a traditional azimuth/elevation drive with rotation in azimuth and elevation was considered, but it was found that such a drive would be difficult and expensive to build given the size and weight of the imager and the available space at the station. There is also a cable wrap problem associated with the azimuth drive, where the drive would have to rotate back 360° in certain imaging situations. Because of this, a solution consisting of three frames mounted inside one another was selected.

The two innermost frames are mounted on perpendicular axes. The ALIS imager is attached to the innermost frame (Figure 3.10). Stepping motors are connected to one end of each axis via a worm-gear assembly, and an angular encoder is attached to the other end. The worm-gear assembly gives an automatic brake when the stepping motors are disengaged, but also introduces a small lag. The innermost axis is denoted α and the outer axis β. In this way it is possible to reach any region on the sky, keeping the image rotations small and without wrapping the cables. Also the cable lengths can be kept short (about 0.5 m) and the imager is accessible for maintenance and fairly easy to remove. A worst-case repositioning typically takes less than 10 s, and the accuracy is 0.01° as long as the stepping motors are engaged.

The CPS Control unit (CPC) is a similar electronics unit to the FWC (Figure 3.9) and contains the power supply and electronics for the CPS. Both the FWC and the CPC are in turn controlled by the NIPU (Section 2.2.2). Conversion of set azimuth, a_ϕ, and zenith-angle, z_θ, of the optical axis, into α and β values is automatically done by the NIPU software according to these equations:

$$\alpha = \arctan(\sin a_\phi \ \tan z_\theta) \tag{3.46}$$

$$\beta = -\arcsin(\cos a_\phi \ \sin z_\theta) \tag{3.47}$$

Azimuth is defined as zero towards North and 90° towards east. Zenith angle is zero in zenith and increases towards the horizon, (i.e. $z_\theta = 90° - h_\theta$, where h_θ is the elevation). It is worth remembering that the azimuth value is undefined for small zenith angles. The maximum zenith angle is typically about 54°.

To simplify the use of ALIS, a set of standard pre-programmed positions for various typical observing requirements are available (Table 3.6 and Figure 3.11).

The present CPS has been in use since 1993. Since being put into operation the CPS appears to be reliable and it has worked for years without any major problems. Worm-gear adjustment due to mechanical wear, as well as some angular encoder failures, probably due to an aging laser-diode in the angular encoder,

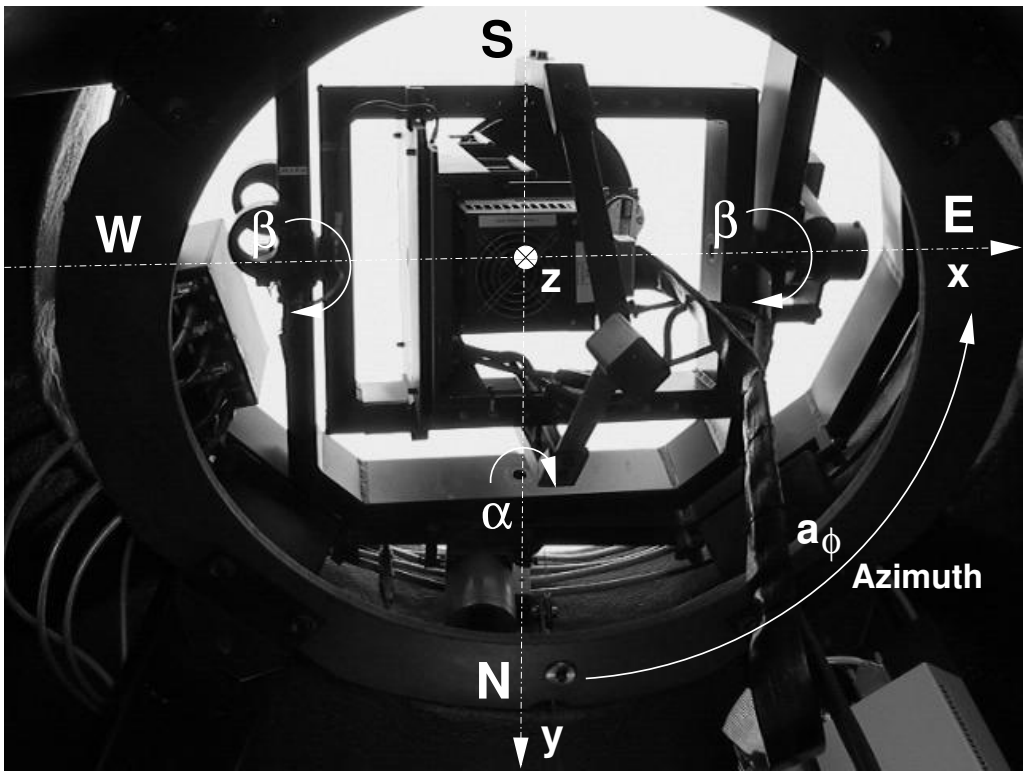

Figure 3.10: Bottom view of the camera positioning system at ALIS station 4 (Tjautjas). North is downward and east is to the left in the figure. Azimuth (a_ϕ) is 0° towards north and 90° towards east, as indicated by the arrow in the lower left part of the picture. Zenith angle (z_θ) is 0° in zenith and increases as the optical axis of the lens is lowered towards the horizon (decrease in elevation). α is zero in zenith and positive when tilting eastward. β is zero in zenith and positive southward (for $\alpha = 0$). The back end of the CCD camera head of an ALIS imager (`ccdcam1`) is mounted in the innermost frame, rotating about the β-axis. This frame is in turn mounted in the middle frame, rotating about the perpendicular α-axis, which, in turn, is attached to the outermost fixed frame. The stepping motors and gear boxes for the axes are seen in the lower middle, and right side of the photograph. Incremental angular encoders are at the opposite side of each axis. A part of the camera control unit is seen at the lower right-hand side. The unit is mounted on one of the four iron legs supporting the outermost frame. The plywood ring, together with the counter-weight at the bottom of the innermost frame serve as an emergency-stopping device for out-of-bounds CPS movements.

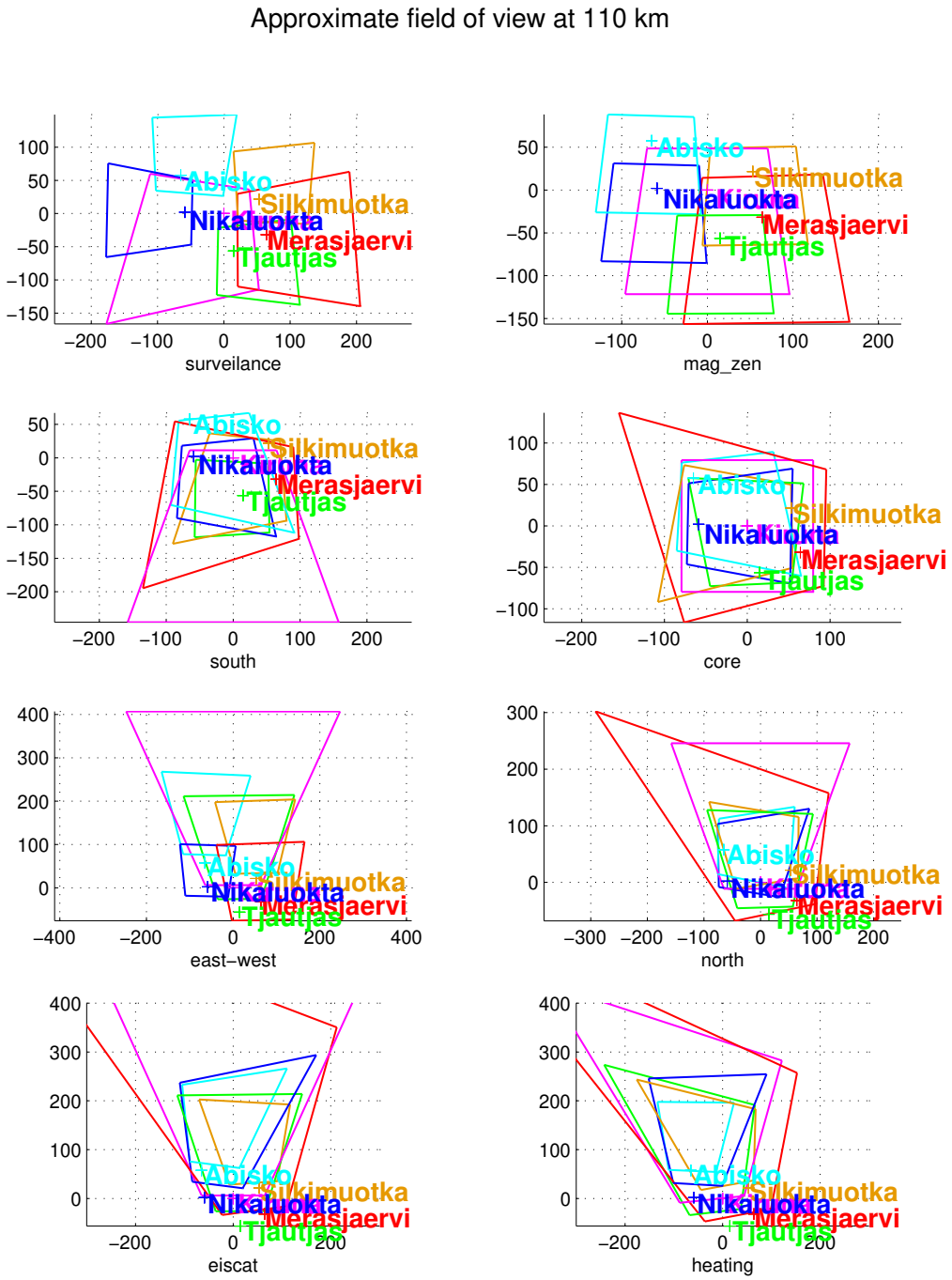

Figure 3.11: Projections to 110 km for the preset camera positions of Table 3.6. The axes are in km west-east (X) and north-south (Y) relative to Kiruna.

1 KRN		2 MER		3 SIL		4 TJA		5 ABK		6 NIL	
a_ϕ	z_θ	a_ϕ	z_θ	a_ϕ	z_θ	a_ϕ	z_θ	a_ϕ	z_θ	a_ϕ	z_θ
`core` — Centred on a volume above Kiruna											
0°	0°	298°	24°	249°	28°	346°	20°	130°	24°	90°	20°
`eiscat` — Optimised for field-aligned EISCAT studies											
0°	39°	348°	42°	350°	32°	0°	42°	20°	35°	15°	42°
`E-W` — Optimise east-west field-of-view											
0°	39°	0°	15°	0°	32°	0°	42°	0°	35°	0°	15°
`heating` — Optimised for HF-pump enhanced airglow											
346°	37°	340°	40°	330°	37°	345°	44°	5°	25°	5°	40°
`mag-Z` — Local magnetic zenith											
180°	12°	180°	12°	180°	12°	180°	12°	180°	12°	180°	12°
`north` — Centred on a volume north of Kiruna											
0°	30°	330°	33°	311°	25°	355°	33°	85°	22°	44°	26°
`south` — Centred on a volume south of Kiruna											
180°	30°	250°	23°	215°	28°	260°	7°	148°	31°	135°	23°
`surv` — Optimised for maximum field-of-view											
225°	20°	100°	14°	45°	12°	115°	15°	30°	14°	270°	20°

Table 3.6: ALIS preset camera positions. The columns give azimuth and zenith angles for the six stations. See also Figure 3.11.

have been encountered so far. Future CPS units will need a slight re-design of the hardware and a micro-controller replacing the obsolete NIPU. The existing devices will need upgraded electronics including new angular encoders as part of normal system maintenance.

3.7 Summary

This chapter has discussed the selection and design of the ALIS imager and its associated subsystems. In summary these systems consist of the following items:

ALIS imager: consisting of Optics (Section 3.4), filter-wheel (Section 3.5.1), with interference filters (Section 3.5) and the CCD Camera Head (CCH) mounted together as a removable unit. Six ALIS imagers exist to date, and they are denoted `ccdcam 1–6` (See Section 3.3.1 and Tables B.1–B.6 in Appendix B. *It is important not to confuse these numbers with the station numbers* (Table 2.3).

Camera Control Unit (CCU) : containing power-supply and electronics for the camera head. The CCUs are individually adapted for each camera head and must not be used with a different camera head.

Filter-Wheel Control unit (FWC) : containing power-supply and electronics for the filter-wheel (Figure 3.9).

Camera Positioning System (CPS) : Supports the ALIS Imager and provides the possibility to remotely point the camera to any desired region of the sky. The CPS is attached to the camera-stand (Section 3.6).

CPS Control Unit (CCU) : containing power-supply and electronics for the CPS (Figure 3.9).

Camera stand : consisting of four iron rods, directly attached to the corners of the iron frame supporting the house, thus the imager is not affected by vibrations in the house caused by for example strong winds (Section A.1).

A block diagram displaying the interrelationships of the various imager subsystems appears in Figure 3.12.

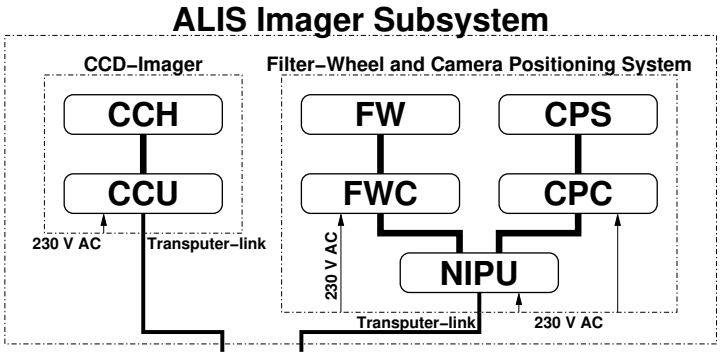

Figure 3.12: Block diagram of ALIS imager subsystems. Regarding the NIPU, see Section 2.2.2

Chapter 4

Calibrating ALIS

> "Gör vad du kan — och uppgiften skall vila lätt i din hand, så lätt att du med förväntan sträcker dig mot det svårare prov som kan följa.
>
> Det är när morgonglansen bytts i middagströtthet, när benmusklerna skälva vid anspänningen, vägen tycks oändlig och plötsligt ingenting vill gå riktigt som du önskar — det är då du *inte* får tveka." *Dag Hammarskjöld*

Calibration is the process of answering the following two basic questions:

1. What physical value does the pixel represent?

2. How is each pixel mapped to the observed object?

Answering these two rather simple questions is often no simple task.

In the case of a classical photometer, there is only one detector with a relatively narrow field-of-view. For an ALIS imager there are about 10^6 individual detectors (pixels) covering a moderate field-of-view (50°–60°). Calibrating image data is therefore a considerably more complex issue compared to calibrating a photometer.

An ALIS Imager produces two-dimensional images of size $m \times n$ pixels. Each pixel is represented by a signed 16-bit integer value (−32768–32767). This value is often referred to as digital output, DN_{ij}. The indices are pixel columns, i, and pixel rows, j, These go from the first to the last pixel in each direction (Figure 4.1). Note that the number of pixels in each direction should be divided by the on-chip binning factors (Section 3.2.1). Supplemental information is contained in the image header (for example azimuth, zenith-angle, integration time, filter, etc.).

4.1 Removing the instrument signature

First it is necessary to remove the instrument signature from the image data. This task is sometime called "data reduction". The procedure is to a large extent similar to that followed when reducing astronomical CCD image data [for example *Massey*, 1992]. In most cases the reduction is carried out first by removing additive effects, and then proceeding with multiplicative effects.

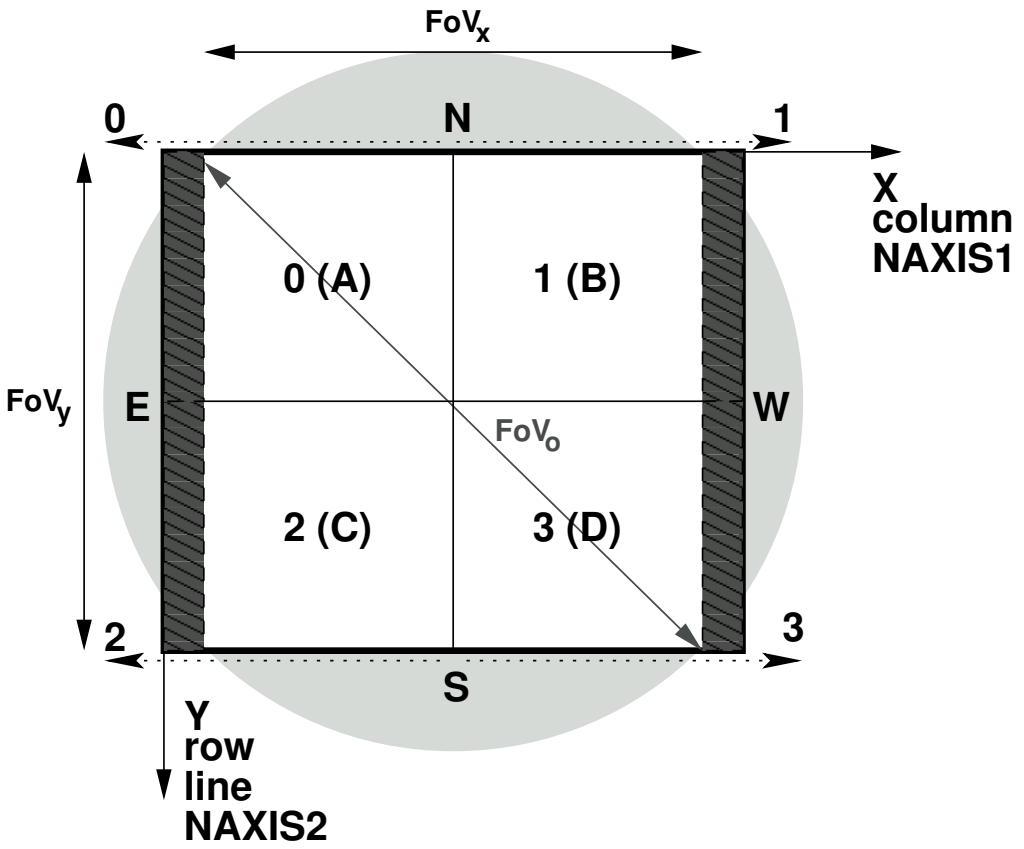

Figure 4.1: Coordinates and notation for the CCD in the ALIS images. The camera control unit reads out a line from each quadrant in parallel (along the dotted arrows 0–3). The pixels are then sent to the host computer, starting with quadrant 0. As this is finished, the next line is immediately read from the CCD. The host computer then sorts the pixels to form an image as indicated by the X and Y-axes in the figure. The approximate quarters (N, S, E, W) are only applicable to the fixed ALIS stations (i.e. not the bus). The quadrants are sometimes denoted 0–3 and sometimes A–D. The X-direction is also referred to as column or NAXIS1 and the Y-direction is sometimes referred to as row, line or NAXIS2. The shaded areas at the edges of the CCD indicate the bias-pixels, which are shaded from light. These are also called overscan-strip or reference-pixels. The optical field-of-view, FoV_o, is indicated with a grey circle and is measured diagonally across the CCD. The illuminated CCD (white) defines the field-of-view in x-direction, FoV_x, and the field-of-view in y-direction, FoV_y, (refer to Table 4.6).

4.1.1 Bias removal

The simplest way to remove the bias is to subtract an image obtained with zero integration time (usually called bias-frame or zero-exposure). However as the bias-frame is subject to the same read noise (Section 3.1.7) as the object-image, this will generally increase the noise by a factor of $\sqrt{2}$. Preparing a bias-correction image by averaging many bias-frames together reduces this problem. As the bias varies over time it would severely impair the temporal resolution if a large number of zero exposures needed to be taken at regular intervals. To remedy this most CCDs are equipped with some extra pixels at the edge of each line. These pixels are shaded from light and thus provide bias information for each line for each image read-out. In the case of the ALIS imager, there are bias-pixels (also called reference pixels, or overscan-strip) for each line of each quadrant on the CCD as indicated in Figure 4.1.

For each pixel, the bias (or DC-level), B_{ij}, can be expressed as follows:

$$B_{ij} = B_{Lj} + B_{\overline{Z}ij} + B_q + B_0 \ \text{[counts]} \tag{4.1}$$

Here B_0 is the black-level (or preset bias), as given in Table 4.1. This value is set in the CCD configuration file (Section 3.3.3).

`ccdcam`	Preset bias B_0
`1`	-25000
`2`	-30758
`3`–`4`	-30768
`5`–`6`	-31768

Table 4.1: Preset bias-levels (black-levels) for the ALIS imagers. The values are obtained from the configuration files for the imagers.

Bias variations between the four read-out channels can be equalised by subtracting the quadrant bias, B_q, for each quadrant $(0 \cdots 3)$. This value can be found by averaging pixels from either zero exposure or from the bias-pixels.

B_{Lj} is the overscan-strip correction, which is obtained by selecting good bias-pixels (not all are usable) and averaging them together on each line. The number of bias-pixels varies between the CCDs, as indicated in Table 4.2. The number of

`ccdcam`	Total pixels $(m \times n)$	Bias-pixels
`1`–`4`	1124×1024	$50 \times 512 \times 4$
`5`	1056×1024	$16 \times 512 \times 4$
`6`	1076×1024	$26 \times 512 \times 4$

Table 4.2: Total number of pixels and bias-pixels for the six ALIS imagers. The bias-pixels are given per quadrant. The number of imaging pixels is 1024×1024 for all six CCDs.

usable bias-pixels varies even more. A suitable smooth function can then be fitted to this averaged bias-column, although this is not done in the current version of the software.

As mentioned initially, to further enhance the bias removal, it is also possible to obtain k bias-frames (Typically at least 25 images), resulting in an averaged bias-correction image, $B_{\overline{Z}ij}$.

$$\forall(i,j):\ B_{\overline{Z}ij} = \frac{1}{k}\sum_{1}^{k}\left(DN_{Zij} - B_{Lj} - B_q - B_0\right)\ \text{[counts]} \tag{4.2}$$

This correction is normally only present when calibrating the imagers.

4.1.2 Dark-current

Correction for the dark-current is performed by taking several dark-exposures, i.e. long exposures ($t_{int} \geq 600$ s) with the shutter closed. The dark-current correction image, D_{ij}, is then produced by averaging these images together in much the same way as the averaged bias-correction image (Equation 4.2):

$$\forall(i,j):\ D_{ij} = \frac{1}{k}\sum_{1}^{k}\frac{1}{t_{int,k}}\left(DN_{Dij} - B_{\overline{Z}ij} - B_{Lj} - B_q - B_0\right)\ \text{[counts]} \tag{4.3}$$

Here $t_{int,k}$ is the integration time for image k.

However for the ALIS imagers, this correction has been found to be negligible for integration times less than 10–15 minutes. Therefore, no dark-current correction is made except for very special cases.

4.1.3 Flat-field correction

The purpose of the flat-field calibration is to remove multiplicative variations introduced by pixel-to-pixel sensitivity differences, vignetting in the optics, variation in transmittance on the filter surface, etc.. This is done by taking a large number of images of a uniform flat-field source:

$$\forall(i,j,\lambda):\ F_{ij\lambda} = \frac{1}{k}\sum_{1}^{k}\frac{1}{t_{int,k}}\left(DN_{Fij\lambda} - B_{\overline{Z}ij} - B_{Lj} - B_q - B_0 - D_{ij}\right) \tag{4.4}$$

In this equation $F_{ij\lambda}$ is the flat-field correction. The index, λ, indicates that the flat-field correction images should be obtained for each wavelength of interest. Normally this means one set of flat-field images per filter. However a calibration facility which can take measurements for several wavelengths within the filter passband would enable measurements of the combined effects of transmittances (Section 3.1.3) and quantum efficiency (Section 3.1.6) for the entire imaging system (and as a function of wavelength).

The moderate fields-of-view (50°–60°) for the ALIS imagers necessitate an integrating sphere of a sufficient diameter for flat-field calibration [i.e. about 1.5–2 m, see *Brändström*, 2000; Labsphere, 1997, and references therein.].

Numerous attempts were made to use simpler methods, such as cloudy skies, white screens, diffuse spherical lamp covers etc. to obtain reasonably good flat-field images. None of these attempts provided flat-field images of sufficient quality, as non-uniformities and gradients were hard to avoid with these simple approaches.

One ALIS imager (`ccdcam6`) has actually been calibrated in the integrating sphere facility at National Institute of Polar Research, Japan [*Okano et al.*, 1997]. The results from this calibration (using white light) are described by *Urashima et al.* [1999]. Due to the considerable distance to this facility it would be difficult to perform flat-field calibrations for all cameras, as would be required. Therefore it is hoped that a similar calibration facility will be established in the proximity of the optical instruments in northern Scandinavia. This was proposed by *Steen* [1998]. Such a facility would be beneficial to many imaging devices in Europe.

So far no proper flat-field calibration are done on the ALIS images on a regular basis. Instead, the flat-field correction is solely based on a mathematical model of the vignetting in the optical system [*Gustavsson*, 2000, Chapter 5]. (This model resembles the "natural vignetting" of $\cos^4\theta$ discussed in Section 3.1.3). Despite the fact that this model does not take variations in filter-transmission, pixel-to-pixel sensitivity variations, etc. into account, it has proved to work reasonably well.

4.1.4 Bad-pixel correction

Defects are unavoidable in the production of a CCD, so defect-free chips are extremely rare and expensive. The CCDs used for the ALIS imagers are of scientific grade, allowing for only a few pixel-defects. The pixel-defects, and how to detect them, can be summarised as follows [after *Holst*, 1998]:

Point defect: Pixel with deviation of more than 6 % compared to adjacent pixels when illuminated to 70 % saturation. (Expose a white area to about 70 % of the dynamic range.)

Hot point defect: Pixels with extremely high output voltage. Typically a pixel whose dark-current is 10 times higher than the average dark-current. (Take a zero or dark image.)

Dead pixels: Pixels with low output voltage and/or poor responsitivity. Typically a pixel whose output is one half of the others when the background nearly fills the wells. (Expose a white area.)

Pixel traps: A trap interferes with the charge transfer process and results in either a partial or whole bad line, either all white or all dark. (Take a zero, dark or object image, depending on type of trap)

Column defect: Many (typically 10 or more) point defects in a single column. May be caused by pixel traps (see above).

Cluster defect: A cluster (grouping) of pixels with point defects (see above).

Although the CCDs in the ALIS imager are of scientific grade, there are a few pixel-defects present on each CCD. These defects have been identified by manually inspecting the images. The bad pixels are then removed by substituting interpolated values from adjacent pixels.

4.1.5 Summary

The corrections discussed above (apart from the bad-pixel interpolation) are summarised in the following equation:

$$\forall(i,j):\ DN'_{ij} = \frac{F_{ij\lambda}}{t_{int}}\left(DN_{ij} - B_{\overline{Z}ij} - B_{Lj} - B_q - B_0 - D_{ij}t_{int}\right) \tag{4.5}$$

Here, DN'_{ij} is the corrected pixel value, which is normalised with respect to integration time t_{int}.

For most measurements, the following, simplified correction is applied

$$\forall(i,j):\ DN'_{ij} = \frac{F_{Mij\lambda}}{t_{int}}\left(DN_{ij} - B_{Lj} - B_q - B_0 - D_{ij}t_{int}\right) \tag{4.6}$$

The symbol, $F_{Mij\lambda}$ is the modelled flat-field correction, as discussed in Section 4.1.3.

Apart from the steps described above, occasionally some additional steps are carried out in order to prepare the data for subsequent analysis. These include various types of filtering to remove cosmic-ray events, stars, etc.

4.2 Intercalibration

Intercalibration is carried out in order to be able to compare measurements from different instruments. To facilitate this, three radioactive ^{14}C light-standards and a calibration lamp are used (Figure 4.2). These light-standards are intercalibrated against other light standards during European calibration workshops held at regular intervals [for example *Lauche and Widell*, 2000a,b; *Widell and Henricson*, 2001]. As several of the light-standards used at these intercalibration sessions are traceable to National Bureau of Standards (NBS) sources, it is thus also possible to perform absolute calibration [*Torr and Espy*, 1981]. Results from some of the most recent calibration workshops are summarised in Table 4.3. For the ^{14}C-sources in use for calibrating ALIS (phosphors: 920B, L1614 and Y275) the column emission rate is plotted against wavelength in Figure 4.3. Table 4.4 presents the ratios of column emission rates from the latest calibration workshop (Oulu, 2001) to earlier calibration sessions. Despite the 5730 years half-life of ^{14}C, deviations of 10–20% are present, even within a couple of years as also noted by *Kaila and Holma* [2000]. This is probably related to either errors in the intercalibration procedure, or to the light-emitting phosphor of the sources.

The original use of these light-standards has been to calibrate photometers. This has been done by placing the light-standard on top of the front-lens of the photometer, covering the entire field-of-view. The same procedure was followed when calibrating the ALIS imagers. As the light-emitting surface of the calibrator does not cover the entire field-of-view of the imager, this method has been questioned [*Gustavsson*, 1997]. Therefore, during the latest calibration workshop, the light sources were placed at a larger distance (within focus) of the imager. However due to various technical problems, the results were inconclusive. Therefore this question remains open.

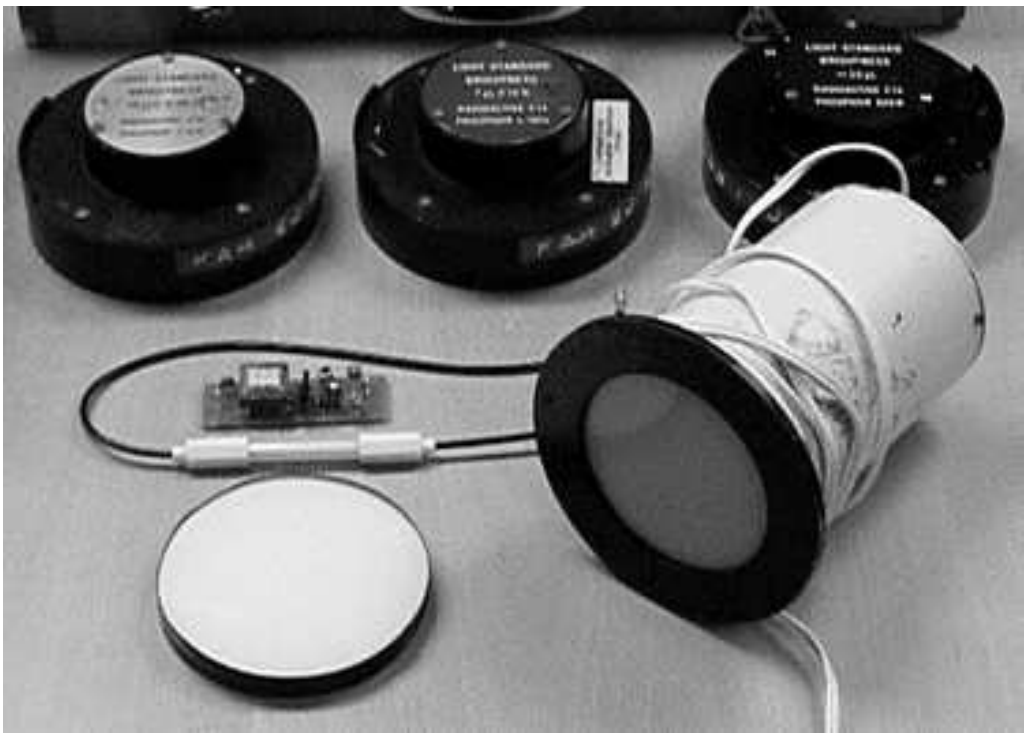

Figure 4.2: Top: The three ^{14}C phosphor light-standards with phosphor: Y-275, L-1614 and 920-B. Lower right: A calibration source with a tungsten lamp. (To the lower left are some parts from a calibration source based on a fluorescent light)

Sources		Column emission rate [R/Å] at Filter [Å]						
calibration	year	3914	4280	4866	5573	5882	6299	6562
Esrange, tungsten lamp								
Stockholm	2000	1.3	4.1	30	212	310	532	553
Oulu	2001	0.53	1.5	11.6	82	122	233	171
IRF, UJO 920B								
Lysebu	1985	5.1	126.0	61.5	18.6	10.5	6.7	8.1
Lindau	1999	4.4	102	60	22	12	7.6	2.4
Stockholm	2000	4.6	109	64	23	12.7	10	8.5
Oulu	2001	5.2	105	65	22	13	9.2	1.2
IRF, UJO L1614								
Lysebu	1985	0.07	0.73	32.5	27.7	8.7	2.5	4.3
Lindau	1999	0.6	1	37	33	9.3	1	2
Stockholm	2000	0.07	1.0	40	35	9.6	0.36	0.57
Oulu	2001	0.1	1.1	38	27	7	1.2	10.2
IRF, UJO Y275								
Lysebu	1985	0.03	0.3	3.8	251.0	378.0	217.0	113.0
Lindau	1999	0.01	0.2	3.8	263	383	282	165
Stockholm	2000	0.01	0.22	3.9	276	405	282	181
Oulu	2001	0.002	0.18	3.6	258	482	274	155
Mike Taylor, source								
Stockholm	2000	0.03	0.98	6.8	10	1.8	0.3	2.5
Sodankylä, blue lamp								
Lysebu	1985	2.0	6.0	10.1	9.9	15.3	4.0	0.66
Lindau	1999	2.3	7.2	12	9.3	10	7.5	7.2
Stockholm	2000	2.5	7.3	12.5	9.3	9.5	6.3	2.8
Oulu	2001	2.6	7.6	12	8.9	13	10	12
Sodankylä, tungsten lamp								
Lysebu	1985	0.12	0.71	5.4	31.8	62.8	125.8	137
Lindau	1999	0.1	0.75	5.6	33.5	65	137	192
Stockholm	2000	0.10	0.65	5.2	31	61	139	285
Oulu	2001	0.01	0.6	5	30	75	133	248
IRF, tungsten lamp								
Stockholm	2000	0.19	1.1	8.5	50	98	223	454
Oulu	2001	0.17	1.2	8	48	115	228	428
MPI-2 lamp								
Lysebu	1985	0.02	0.16	2.43	193.7	290.7	191.8	98.2
Lindau	1999	0.03	0.12	2.2	172	258	213	235
Stockholm	2000	0.01	0.13	2.3	175	266	153	105
Oulu	2001	0.01	0.01	2.3	169	251	193	105
S.Chernouss, Glow lamp								
Oulu	2001	13	143	66	84	374	392	59
S.Chernouss, Tungsten								
Oulu	2001	0.01	1.6	5.5	36	293	947	679

Table 4.3: Results from a selection of recent intercalibration workshops: The column emission rates are given in [R/Å] (Rayleighs/Ångström). (Some sources have been omitted in order to fit the table on one page.) [after *Lauche and Widell*, 2000a,b; *Widell and Henricson*, 2001, and earlier calibration workshop reports]

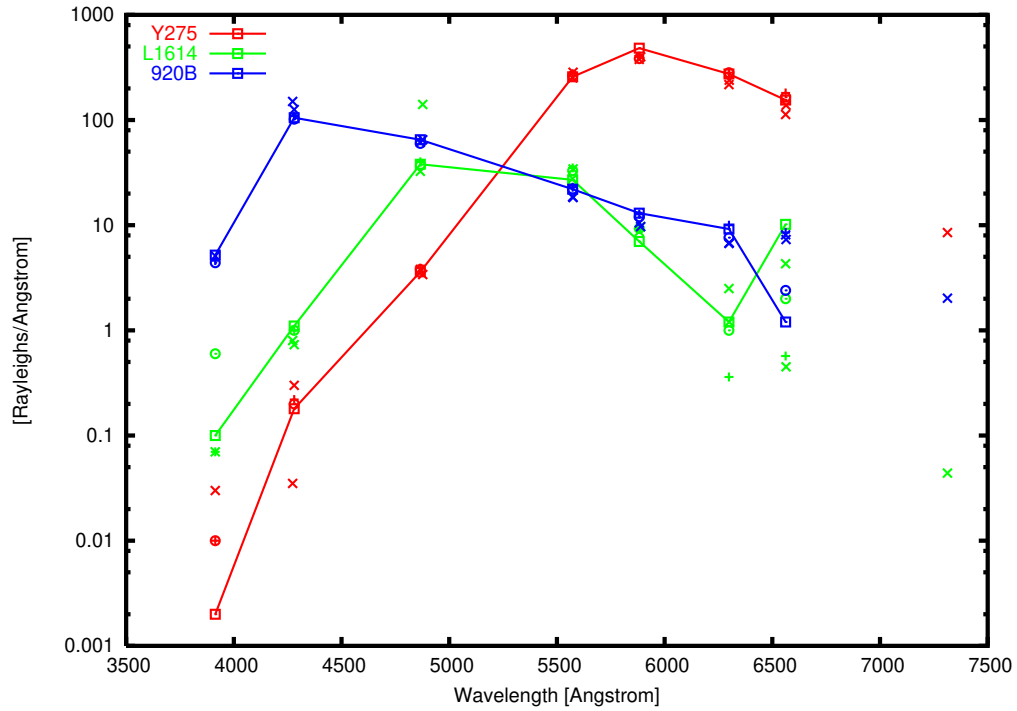

Figure 4.3: Column emission rates [R/Å] as a function of wavelength [Å] for the three radioactive ^{14}C light-standards with phosphor: 920-B (blue line), L-1614 (green line) and Y-275 (red line). These plots also include intercalibration results from the Aberdeen 1980 workshop [*Torr and Espy*, 1981]. These values are not shown in Table 4.3. Legend: Intercalibration sessions of 1981 'x' 1985 '+', 1999 '*', 2000 'o' , and 2001 '□'. The lines connect the results from the latest calibration workshop, held in Oulu 2001. (The last points on these lines for the L1614 and 920B calibrators are probably measurement errors)

Source	Year	column emission ratios (2001/year) at Filter [Å]						
		3914	4280	4866	5573	5882	6299	6562
y275	1985	0.07	0.60	0.95	**1.03**	1.28	**1.26**	1.37
y275	1999	0.20	0.90	0.95	**0.98**	1.26	**0.97**	0.94
y275	2000	0.20	0.82	0.92	**0.93**	1.19	**0.97**	0.86
l1614	1985	1.43	1.51	1.17	**0.97**	0.80	0.48	2.37
l1614	1999	0.17	1.10	1.03	**0.82**	0.75	1.20	5.10
l1614	2000	1.43	1.10	0.95	**0.77**	0.73	3.33	17.89
920b	1985	1.02	**0.83**	1.06	**1.18**	1.24	1.37	0.15
920b	1999	1.18	**1.03**	1.08	**1.00**	1.08	1.21	0.50
920b	2000	1.13	**0.96**	1.02	**0.96**	1.02	0.92	0.14

Table 4.4: Ratios of results from the latest calibration workshop [Oulu, 2002, see *Widell and Henricson*, 2001] to earlier calibration sessions. Bold face indicates results for wavelengths where the calibrators are most commonly used. See also Table 4.3 and Figure 4.3

4.2.1 Absolute calibration

The digital-output, DN_{ij}, and number of generated photo-electrons per pixel $\overline{n}_{e^-_{\gamma ij}}$ is related by:

$$DN_{ij} = G_S \; \overline{n}_{e^-_{\gamma ij}} \, [\text{counts}] \tag{4.7}$$

where G_S is the imager system gain, [*Preston*, 1993, 1995]:

$$G_S = \frac{G_{CCD} \; G_P \; t_{DCS}}{B_{ADC} \; \tau_{DCS}} \left[\frac{\text{counts}}{e^-_\gamma} \right] \tag{4.8}$$

Here, G_{CCD} is the CCD output sensitivity, G_P is the programmable gain setting (5 or 10), t_{DCS} is the DCS integration time, B_{ADC} is the ADC bit weight (90.6 μV/counts), and τ_{DCS} is the DCS integrator time constant. These parameters are configured during CCU start-up (Section 3.3.3).

Combining Equation 4.6 with Equations 3.20 and 3.22 yields for uniformly illuminated central pixels of the CCD, DN_{Cij} :

$$\frac{I_{cal}}{DN_{Cij}} = \frac{1}{t_{int}} \frac{16 f_\#^2}{10^{10} \, G_s \, Q_E \, T \, A_{pix}} \left[\frac{R}{\text{counts}} \right] \tag{4.9}$$

The "known" column emission rate, I_{cal}, which is obtained from a light-standard by integrating over the filter passband, $\lambda_1 \cdots \lambda_2$ is given by:

$$I_{cal} = \int_{\lambda_1}^{\lambda_2} I_{ls}(\lambda) \, d\lambda \approx I_{ls}(\lambda_2 - \lambda_1) = I_{ls} \, \Delta\lambda \, [R] \tag{4.10}$$

Here, the column emission rate of the light standard, $I_{ls}(\lambda)$, is a function of wavelength λ, that must be integrated over the filter passband, $\Delta\lambda$. However during the intercalibration workshops, $I_{ls}(\lambda)$ is measured only for one wavelength in the filter passband, hence the approximation in Equation 4.10 (see Table 4.3 and Figure 4.3).

Now, consider the right-hand part of Equation 4.9. The quantum-efficiency, transmittance and system gain is a function of wavelength and pixel-coordinates among other things, such as for example filter-temperature (i.e. $Q_E = Q_E(\lambda, i, j, \ldots)$, $T = T(\lambda, i, j, \ldots)$ and $G_S = G_S(i, j, \ldots)$). Due to the difficulties of determining these functions as well as the approximations and uncertainties related to the $f_\#$ Equation 4.9 is rewritten as follows:

$$\frac{I_{cal}}{DN_{Cij}} = \frac{1}{t_{int}} \, C_{abs\lambda c} \, F_{ij\lambda} \left[\frac{R}{\text{counts}} \right] \tag{4.11}$$

Here $F_{ij\lambda}$ (Equation 4.4) corrects for both the dependence on pixel-coordinates as well as on wavelength for a particular filter. (The index λc in the absolute calibration constant, $C_{abs\lambda c}$, indicates that the constant is unique for each filter of each imager c). Hence, *the importance of a proper flat-field calibration cannot be underestimated* (Section 4.1.3). Unfortunately, a proper flat-field calibration is not yet available for ALIS, and some approximations are required:

$$\frac{I_{cal}}{DN_{Cij}} \approx \frac{1}{t_{int}} \, C_{abs\lambda c} F_{Mij\lambda} \int_{\lambda 1}^{\lambda 2} T'(\lambda) d\lambda \approx C_{abs\lambda c} F_{Mij\lambda} \left[\frac{R}{\text{counts}} \right] \tag{4.12}$$

In this case the modelled flat-field correction $F_{Mij\lambda}$ of Equation 4.6 is used together with a normalised filter transmittance function, $T'(\lambda)$, by integrating over the vendor-provided filter transmittance curve and normalising (i.e. set $T'(\lambda) = 1$) at peak filter transmittance (Figure 4.4). However for most filters

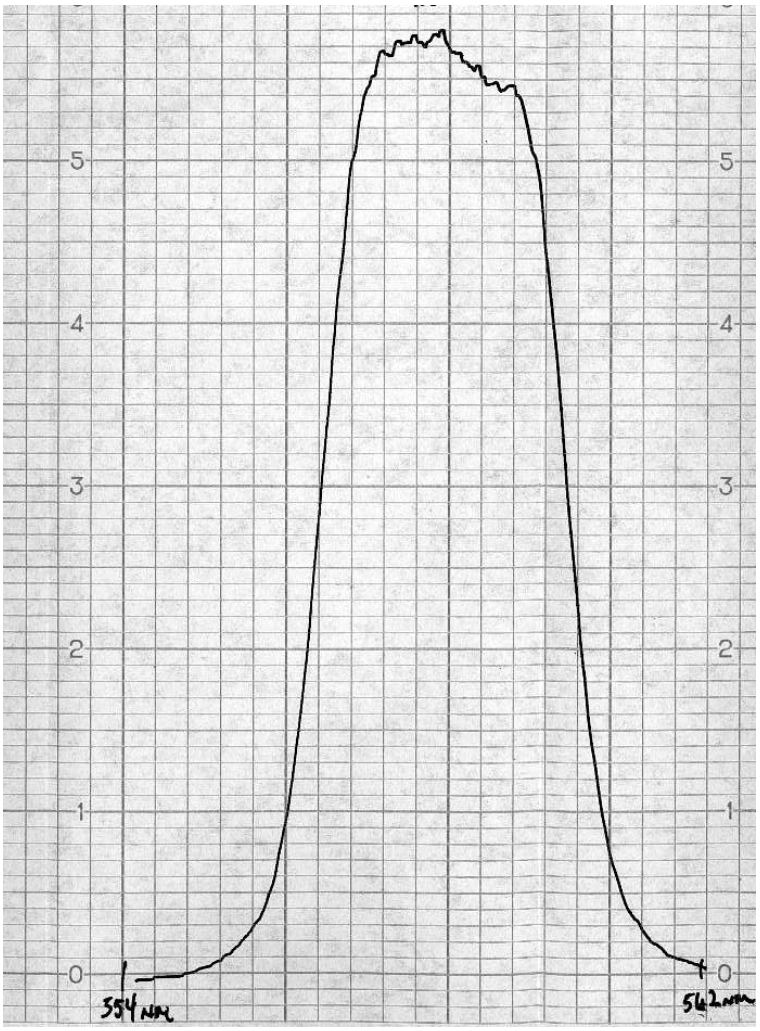

Figure 4.4: Example filter transmittance curve $T_f(\lambda)$ as measured by the filter manufacturer for a 40 Å wide 5590 Å filter (Lot. No. 3697). The measured peak transmittance of the filter is 0.6 and the centre wavelength at normal incidence (λ_{cw}) and filter bandwidth is measured to 5587.2 Å and 38.4 Å respectively. This filter is intended for the $O(^1S)$ 5577 Å auroral emission line. The deviation from normal incidence shifts the centre wavelength, which explains why a centre wavelength of 5590 Å was selected, (see Equation 3.45 in Section 3.5). As can be seen, this filter has a rather uniform transmittance in the passband.

it is acceptable to take $T'(\lambda) \approx 1$ over the entire filter-passband. Equations 4.5 and 4.11 yield the following equation (substituting Equation 4.10) to be used when a proper flat-field calibration is available:

$$C_{abs\lambda c} = \frac{1}{\overline{DN'}_C} \int_{\lambda_1}^{\lambda_2} I_{ls}(\lambda)\, d\lambda \quad \left[\frac{R}{\text{counts}}\right] \tag{4.13}$$

where $\overline{DN}'_C$ is obtained by averaging together a number of uniformly illuminated pixels in the central part of the image.

The present more approximative calibration is described by Equations 4.6 and 4.12:

$$C_{abs\lambda c} \approx \frac{1}{\overline{DN}'_C} \int_{\lambda_1}^{\lambda_2} I_{ls}(\lambda)\, d\lambda \int_{\lambda 1}^{\lambda 2} T'(\lambda) d\lambda \approx \frac{I_{ls}\Delta\lambda}{\overline{DN}'_C} \left[\frac{R}{\text{counts}}\right] \tag{4.14}$$

Hence, an absolute-calibration must be carried out for each filter of each imager.

The results from the two most recent absolute calibrations of the ALIS imagers are found in Table 4.5. As can be seen, the last absolute calibration of the ALIS

ccd cam	λ_{cw} [Å]	$\Delta\lambda$ [Å]	$\overline{DN}'_C$ [counts]	$\langle DN'_C \rangle$ [counts]	96-07-10 $C_{abs\lambda c}$ [R/counts]	97-05-21 $C_{abs\lambda c}$ [R/counts]	2001 adj. $C_{abs\lambda c}$ [R/counts]
1	5590	40	217.5	2.6	32.4	46.2	47.4
1	6310	40	173.4	2.6		50.1	63.2
1	6230	40	254.2	2.9		34.1	43.1
1	4285	50	116.8	3.4		53.9	44.9
2	5590	40	300.6	3.6	28.2	33.4	34.3
2	6310	40	339.3	3.5	25.6	25.6	32.3
3	5590	40	484.2	4.1	21.9	20.7	21.3
3	6310	40	427.3	2.8	22.2	20.3	25.6
4	5590	40	468.0	5.3	23.7	21.5	22.1
4	6310	40	402.2	4.1	23.7	21.6	27.3
5	5590	40	333.8	4.0		30.1	30.9
5	6310	40	390.5	4.2		22.2	28.1

Table 4.5: Calibration results from ALIS obtained in 1996 and 1997. The large difference for `ccdcam1` occurs because it was equipped with filter-wheel and new optics between these calibrations. Some filters (see Tables 3.4 and 3.5), as well as `ccdcam6` were not yet available during these calibrations. Both calibrations used the Lysebu, 1985 intercalibration. The last column gives values of the calibration of 21 May 1997, adjusted by the 2001 intercalibration result (Table 4.3). Finally it should be noted that no suitable light-standard for calibration of the 8455 Å filters is available.

imagers was carried out in 1997. At that time `ccdcam6` was not yet delivered; neither were all filters available. Also no suitable light-standard is available for the near-infrared 8446 Å emission line. An attempt was made to perform a recalibration of all imagers and filters in 2001. However this effort failed due to technical problems and limited time. Hence a new calibration must be performed as soon as possible.

A comparison of auroral measurements from `ccdcam6` and a Russian photometer (calibrated in Russia) both co-located in Kiruna indicates a disagreement in absolute intensities of $\approx 20\%$ between the two instruments [*Sergienko*, 2003]. This comparison as well as extrapolated values have been in use for the filter/imager combinations not appearing in Table 4.5 (i.e. `ccdcam6`. See also Tables 3.4 and 3.5).

There is furthermore an interesting possibility of performing absolute calibration by using known spectra of stars, which has been done for the 8446 Å

emission-line [*Gustavsson*, 2003]. This method would simplify the calibration procedures considerably. However this is a new method and these results have yet to be intercalibrated with the present calibration method. Regardless of whether the new method will be a verification procedure, or replace the present calibration procedure, it will no doubt represent a major improvement of the absolute calibration for ALIS.

Due to the inherent difficulties of absolute intensity calibration, an error of the order of 50 % is often regarded as acceptable. The largest errors appear to be related to the intercalibration of the light-standards (about 10–20 %, refer to Table 4.4). Furthermore, the calibration results appear to be fairly stable over one year (Table 4.5). On the other hand there are still many uncertain factors in the calibration procedure, most notably the absence of a uniform source needed for the flat-field calibration (Section 4.1.3). Therefore, to be on the safe side, it might be stated that the absolute calibration error lies in the range of 25–50 %. The intercalibration error of the ALIS imagers is probably much lower, at least for pixels in the central region of the image. For an imaging instrument, these errors are probably to be considered as acceptable. However improvements are still required.

Finally, the absolute calibration is applied to the object-images (DN'_{ij}, see Equations 4.5 and 4.6):

$$I_{ij} = C_{abs\lambda c} DN'_{ij} - I_{bg,ij} \ \ [R] \tag{4.15}$$

In this equation, I_{ij} is the calibrated pixel-value, and $I_{bg,ij}$ is the sky background correction.

4.2.2 Removing the background

Different schemes are employed to remove the sky background in Equation 4.15, depending on available data and the measurement situation. Therefore background removal is only outlined here.

In the case of HF pump-enhanced aurora, linear interpolation with time is sometimes used. Also a polynomial could be fitted line by line on each side of the emission region. In the most recent papers (Section 6.4) weighted sums of keograms through the emission region and on the side of it are used. This is done under the assumption that there is no aurora.

Regarding PSC studies (Section 6.6.1), brute-force median/min. filtering was applied [*Enell*, 2002].

For general auroral studies, background determinations are extremely difficult, as there is always some diffuse aurora present. In this case background images must be obtained by using a filter for a wavelength region with no auroral emissions. For the ALIS imagers, background filters are available: 5100 Å and 6230 Å. However these filters have seldom been used as they are only present at some stations (Section 3.5). For the future, permanent background photometers might be a solution of the problem.

4.2.3 Related issues

On-chip binning

The absolute calibration has been found to scale accurately with the binning factors, thus:

$$C_{abs\lambda c,binxy} = \frac{C_{abs\lambda c}}{x_{bin} \times y_{bin}} \tag{4.16}$$

Where $C_{abs\lambda c,binxy}$ is the absolute calibration constant with binned pixels, x_{bin} is the binning-factor in the x-direction, y_{bin} is the binning factor in the y-direction.

Linearity

As no variable light-standard is available, the linearity has been checked by varying the integration time (t_{int}). As expected, the CCD detector appears to be completely linear until it reaches the saturation-equivalent exposure (Section 3.1.10).

Interference filters

Both the transmission characteristics and passband of a narrow-band interference filter are subject to aging effects. The filter-wheels of the ALIS imagers are also sometimes subject to high temperatures due to day-time sunlight. This is known to have a permanent degenerative effect on the filters. Questions have therefore been raised regarding the long-term stability of the filters. To clarify these issues, it would be desirable to re-measure filter characteristics for the filters. This was planned for the autumn of 2001, but had to be postponed for a number of reasons.

Another concern is to measure the transmittance of the filter, $T_f(i, j, \lambda)$, as a function of pixel indices, (i, j), (columns, lines). A monochromator system for filter transmission measurements was developed for ALIS [*Vaattovaara and Enback*, 1993]. Provided that an ALIS imager has a valid flat-field calibration, it should in principle be possible to check the transmittance of the optical system (including the filter) as a function of wavelength and pixel coordinates. Such a study would be beneficial for all optical instruments, using interference filters, and could provide answers to questions posed by *Kaila and Holma* [2000] regarding absolute calibration of wide field-of-view photometers and camera systems.

4.3 Geometrical calibration

The task of mapping the field-of-view of each pixel to the observed object is called geometrical calibration. As this topic is extensively covered in *Gustavsson* [2000, Chapter 4–5] it will only be briefly touched upon here. First a set of star-images are obtained for the viewing direction under consideration. Then the positions of the stars are calculated from a star-catalogue (Bright Star Catalogue (BSC))* and mapped down to the image coordinates. Then preferably more than 100 stars, evenly distributed across the image, are identified. Finally a transfer function is adjusted so that the calculated and actual positions of the stars overlap. This

*ftp://adc.gsfc.nasa.gov/pub/adc/archives/catalogs/5/5050

transfer function is then used for calculating the field-of-view of each pixel of the CCD. Table 4.6 displays the fields-of-view of the ALIS imagers as calculated from the transfer-function.

	field-of-view			
ccdcam	FoV_o	FoV_x		FoV_y
1	90.4°	59.3°	×	60.5°
$\langle FoV \rangle$	1.2°	1.1°		0.9°
2	71.8°	48.5°	×	48.7°
$\langle FoV \rangle$	0.2°	0.1°		0.1°
3	71.7°	48.8°	×	48.8°
$\langle FoV \rangle$	0.1°	0.6°		0.3°
4	72.2°	49.9°	×	49.6°
$\langle FoV \rangle$	0.1°	0.1°		0.1°
5	71.8°	49.6°	×	49.1°
$\langle FoV \rangle$	0.2°	0.2°		0.1°
6	102.1°	66.1°	×	68.6°
$\langle FoV \rangle$	1.1°	0.4°		0.2°

Table 4.6: Measured fields-of-view for the ALIS imagers. These values are obtained from the geometrical calibration procedure using star images. Note that the CCD is a square inscribed in a circular field-of-view. Also note that the fields-of-view are calculated in a spherical geometry.

The optics used for the ALIS imagers is aberration limited, rather than diffraction limited. The effect of this aberration limited focus is shown in Figure 4.5. As can be seen the point spread function varies over the image plane, from 1–2 pixels in the centre to a few pixels at the edges. This will smoothen and widen images of sharp and narrow structures, in particular in the corners of the images. At the present no attempts are made to deblur/sharpen the effect of the PSF [*Gustavsson*, 2000, pp. 46–47].

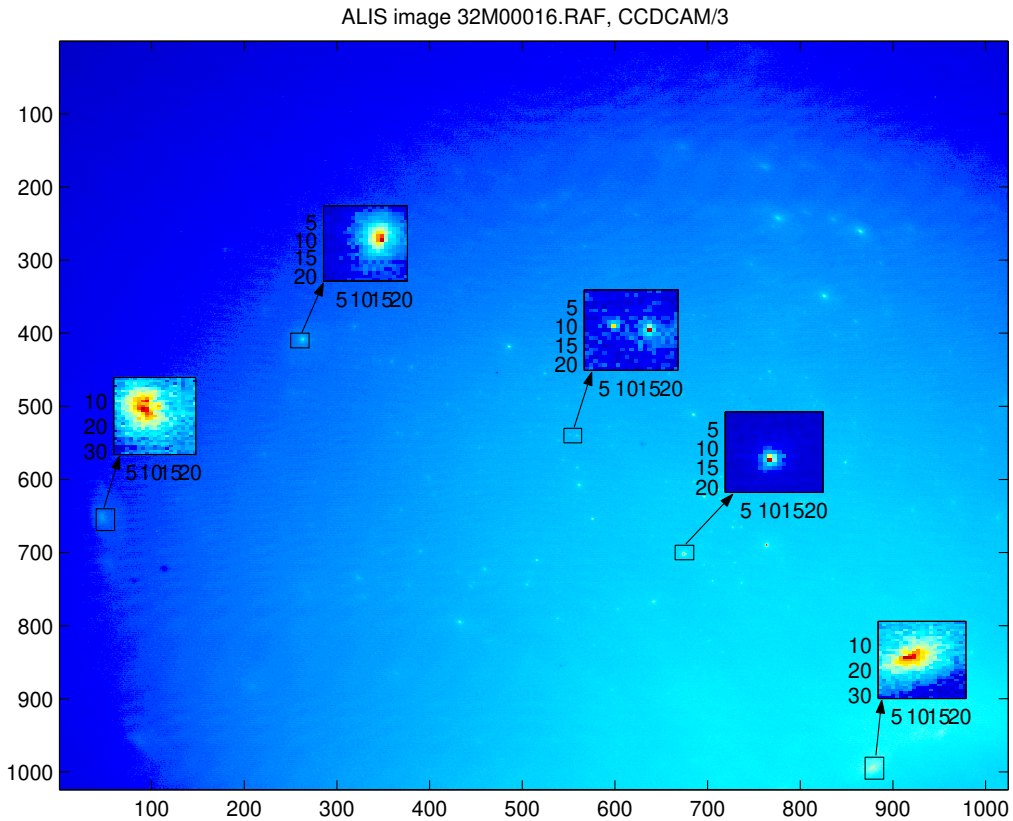

Figure 4.5: A typical ALIS background image with a selection of magnified stars displaying the variation of the point spread function (PSF) over the image. [after *Gustavsson*, 2000, Figure 5.6].

Chapter 5

Controlling ALIS

> "For the highest payoff per dollar risked it should be remembered that communication system development is normally a ten year leadtime cycle process. Much better work in this field appears to result from a small number of people working for a long period of time than from a large massive crash effort attempting to generate a complete system within short time"
>
> *F. R. Collbohm*

Software for ALIS falls into two main categories: data analysis software (Section 6.2) and software for controlling ALIS. In the early phase of work on ALIS, initial ideas for how to develop the software for controlling ALIS were discussed by *Steen et al.* [1990]; *Johansson* [1991]; *Nilsson and Nyström* [1992] and *Nilsson* [1994]. While the main ideas for the control centre software have been in use until now, this is not the case for the station software.

ALIS is a complex and highly configurable instrument compared to traditional ground-based auroral imaging equipment. Someone once remarked that "comparing ALIS with a traditional all-sky camera is like comparing EISCAT with an ionosonde". ALIS is a campaign-orientated instrument and therefore needs more attention prior to measuring compared to traditional imagers. This gives large amount of flexibility for performing new types of scientific studies, but also introduces new problems. First of all, ALIS is a new instrument, with new and partly unexplored possibilities, and to learn those possibilities takes long time. While absolute measurements from photometers have been analysed for almost half a century, there is no common established practice to deal with such data expanded to two dimensions (not to mention three dimensions). Traditionally images have belonged to the realm of morphological measurements (some exceptions exist). Another concern is the tremendous increase in the amount of data produced, and how to process and analyse the data in a way that enables and improves the possibilities for physical interpretation. The point of this discussion is simply that it is difficult to develop a control system for something that is to a large extent new and unknown. Other difficulties arise from technical limitations, as well as from the rapid technical development, causing some components to become obsolete before they are finished and making it difficult to put priorities in the right order. (In the beginning of the project various proprietary programming environments had to be procured and learned, often at a high cost. Some years later, more standardised, reliable and free software emerged, partly making the earlier efforts

superfluos. If that had been known in advance, those resources could have been spent on other tasks.) The development of a control system for ALIS was therefore carried out by successive approximation and "survival of the fittest" ideas. The following sections will provide a brief overview of a vast subject that is best described by running ALIS and studying the source code.

5.1 Making an observation with ALIS

Experience has suggested the following steps for configuring ALIS for an observation:

1. **Defining a scientific rationale:** This is of course the first and most important task. Naturally it is almost impossible to predict the outcome of any observations. Nevertheless, well planned measurements with a clear view of what needs to be done tend to yield better results than "ad hoc" operations.

2. **Selecting stations:** Normally it is best to use as many stations as possible, but there might be observation schemes that require only a subset of the stations. It is also important to plan what changes to the rationale are necessary in case some stations cannot take part in the observation (for example due to clouds or technical problems).

3. **Selecting imager viewing directions:** This can be either the standard preset viewing-directions (Figure 3.11 and Table 3.6) or specially calculated viewing directions for a particular measurement. It is advisable to prepare a strategy for possible changes if the observed phenomena moves outside of the field-of-view. In most cases it is best to avoid changes of the viewing directions during a measurement. "Chasing the aurora" usually results in poor data. Another concern is to make sure that the selected positions are geometrically calibrated against the star background (Section 4.3).

4. **Selecting filters:** Filter selection usually follows directly from the scientific rationale. However all filters are not available at all stations (see Tables 3.4 and 3.5). Filter change time increases with the distance between the filters on the filter-wheel (nominally 1–2 s). It might also be necessary to obtain background intensities by exposing images with background filters.

5. **Selecting integration times:** The minimum integration time is defined by the shortest exposure resulting in an acceptable *SNR*. As the spectral sensitivity varies for the imager, there is normally a need for longer exposures for shorter wavelengths. Maximum exposure is defined by the longest exposure without saturating the CCD, or, more frequently, by requirements set by the desired temporal resolution. The risk of saturating the CCD must be considered at high binning factors as the sensitivity increases with the binning factors (Figure 3.4). Occasional saturated images pose no threat to the CCD, but yield unusable data. Finding an optimal integration time has proven to require large amounts of experience from earlier measurements. (see also Chapter 3)

6. **Selecting temporal resolution:** The temporal resolution is currently limited to one image per 30–60 s at maximum resolution, and is generally never better than 30 images per minute at higher binning factors. These figures vary somewhat between the imagers. Also times for filter changes must be considered.

7. **Selecting spatial resolution and sensitivity:** This is generally a compromise between temporal resolution, sensitivity, framerate and disk-space. Note that increasing the temporal resolution by binning might lead to saturation problems due to the increase in sensitivity.

8. **Deciding on data storage strategies:** As the disk space at the stations is limited, it is advisable to estimate the amount of data produced and decide what data should be kept, when to retrieve the data and if deleting presumed unusable images should be allowed, etc.

9. **Coordination with other instruments:** Such as EISCAT measurements, satellite passes, rocket launches etc. This involves many considerations (for example when does a satellite pass occur? Should ALIS image along the foot-point of the satellite pass?). It is also essential to establish communication with the control centres of participating facilities.

10. **Selection of a suitable operational mode for the observation:** Available modes are: automatic, semiautomatic or manual, see Section 5.1.1. In order to increase the number of observations of a particular phenomenon it would be desirable to have more automatic runs, however, experiences indicate that at the present, the best results emerge from manned semiautomatic runs.

11. **Defining and testing the required configuration of ALIS:** No usable bug-free program exists. Therefore everything should be tested as thoroughly as possible before running the actual observation. It is also important to start up all systems in ALIS well in advance. The imagers need to be thermally stable and defrosting of the domes as well as booting subsystems at the stations might also take some time. (Estimate at least 1–2 days for testing a new measurement scheme, and 2–4 hours to start up ALIS.) It is also advisable to perform some rudimentary last checkout procedures about one hour prior to starting the measurements.

12. **Waiting for the right conditions:** This might be a long wait. In this phase, it is advisable to take images at all stations at regular intervals to check weather conditions and system performance. It is also a good practice to be prepared for many different kinds of observations. For example, if conditions for observing HF-pump enhanced airglow are not right, there might be an excellent auroral event instead.

13. **Run the observation:** During measurements many unexpected things can happen, so it is good to be well-prepared with alternatives. Two to three people in the control centre are the ideal for most measurements: one who takes care of technical problems and runs the system, one who concentrates

on taking scientific decisions and possibly one who coordinates with other instruments. Taking good notes is essential, as analysis might not occur until months later.

14. **Retrieve the raw-data from the stations:** It is time-consuming to retrieve raw-data from the stations. All six stations can be visited in less than a week, but this requires a lot of driving. Usually the disks are brought back only during scheduled maintenance trips to the stations, or as the disks become full. If exceptionally interesting data have been recorded, it might still be desirable to retrieve it as quickly as possible.

15. **Analysing and publishing the results:** First one needs to select data, then this data-set must be preprocessed and calibrated before the actual analysis and publication phase starts. These final steps rely on good record-keeping in the previous steps.

5.1.1 Modes of operation

The modes for controlling ALIS are summarised below:

Manual control: By sending commands directly to ALIS, a user is able to control observations interactively. This mode of operation is most frequently used for checking observing conditions (cloudiness, etc.), for troubleshooting and for maintenance.

Semiautomatic operation: In this mode a user controls ALIS by running observation control programs (usually these are shell-scripts at the stations) that are uploaded, prepared and tested in advance. This is the normal operating mode.

Automatic operation: In this mode, an observation control program is loaded and run automatically at a predefined time. This mode can easily be switched to semi-automatic mode if the user wishes to change anything. Exceptions can be reported using a paging system if the control centre is unmanned. Due to the vast amounts of data produced, automatic measurements are uncommon.

5.1.2 Alarms and other exceptions

Many exceptions can be properly acted upon automatically, while others require manual interaction. These exceptions trigger alarms, which are displayed at ALIS-CC and at all user interfaces. If user interface is active, an automatic paging system will also alert the operator on duty. Typically, a pager call occurs for A-Alarms or fatal alarms, (see below) but the paging system can be configured to alert a user when an interesting measurement situation is emerging, etc. ALIS exceptions are classified in three alarm categories:

Fatal alarms: Fire, trespass or other severe conditions threatening the hardware.

A-Alarms: Conditions causing the imaging to stop at one or several stations (power failures, filter-wheel problems, unrecoverable run-time errors, etc.).

B-Alarms: Other conditions affecting the quality of observations (timing problems, communication problems, over- or under-exposed images, etc.).

5.2 OPERA

The complete collection of software for controlling ALIS is called an OPERations system for ALIS (OPERA). The three main components of OPERA are briefly described below.

5.2.1 User interfaces

The main graphical user interface for ALIS is an X-windows application (`parsifal`) that has been supported on various computing platforms (HP-UX, Sun-OS (Solaris), GNU/Linux, Windows-95 and Java). It provides a user-friendly way to configure and run ALIS as well as to display quick-looks and status information. Commands can be sent to the system, either by user-defined menus or directly by typing them on a command line. From `parsifal` it is possible to monitor and control ALIS in many ways, to receive and view quick-look images, to communicate with other ALIS users, to upload experiment configurations, etc.. A text-only user interface, (`tosca`), is available for controlling ALIS over slow communication lines (implemented in Lisp as a major mode for the Emacs editor). From around 1999, as the stations become networked over ppp (Section 2.2.3) it also became possible to configure and control the stations over direct TCP/IP connections (for example by making a direct `telnet` login to the desired station computer). It is foreseen that the need for a dedicated control centre and special user-interfaces will vanish as it will be possible to control ALIS from an ordinary web-browser in the future.

5.2.2 AIDA

A central set of server processes, Alis Internal Data Administration (AIDA) runs at the control centre, accepting connections from user interfaces and directing user-commands to the desired set of stations. Furthermore, requests from the stations affecting users, or other stations, are routed to their proper destinations. AIDA also handles alarms and other exceptions and activates the paging system if no user-interface is online. The concept of AIDA as a central node (or crossbar-switch) has survived since the first implementation (around 1992), but is subject to change in the future as all stations become networked. When this happens, a central node is no longer required, as this functionality can be undertaken by any station. Therefore the need for a dedicated control centre will also diminish with time. All of the AIDA software was written in a Unix/C environment from the beginning, first under HP-UX and later ported to GNU/Linux. A block-diagram of the AIDA software and user interfaces appears in Figure 5.1. See [*Nilsson*, 1994] for a more detailed description of AIDA.

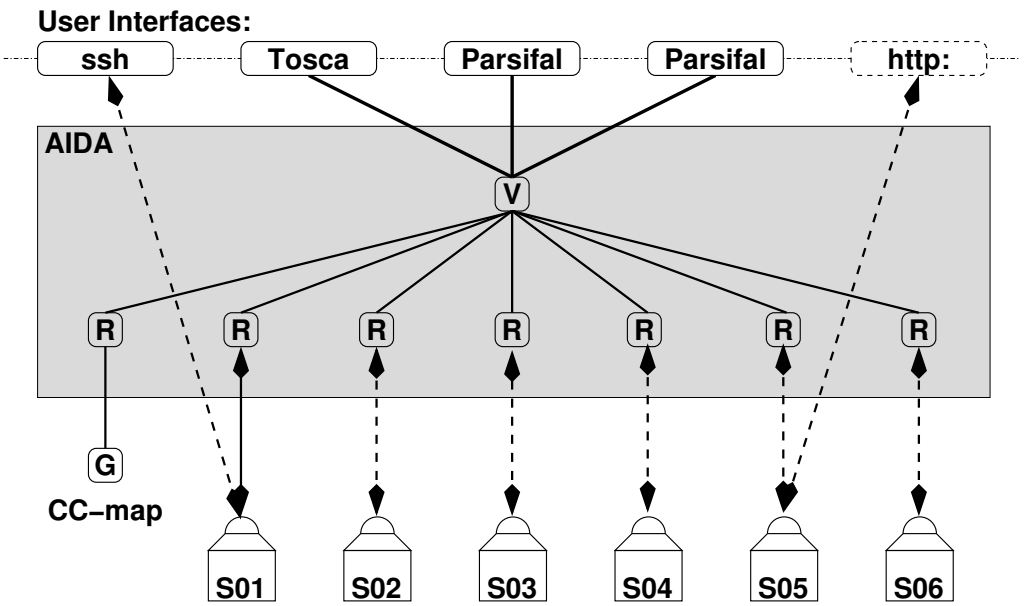

Figure 5.1: Block diagram of OPERA. Any number of user-interfaces (`parsifal`, `tosca`) can connect to AIDA in order to control ALIS. In AIDA a central supervising process V (`verdi`) routes all information between the different user-interfaces and the stations. The stations are connected to `verdi` via an interface process, R (`radames` controls a RS-232 serial line and a modem, or `rigoletto` that provides a TCP/IP connection to a station over an existing network connection). The control centre status display map (Figure 2.7) is connected in the same way as an ALIS station. The user-interfaces labeled `ssh` and `http` indicate the possibility to control the stations over a shell-login, or from a standard web-browser. This will eventually make the control centre software superfluous, as the functionality of AIDA will be available at each station.

5.2.3 Station software

The present ALIS stations are to a large extent controlled by station-control programs running in the station computer (SC). As long as MS-DOS was used as the operation system for the station computer (Section 2.2.6) a huge application program (`HENRIK`) controlled the station. Due to the many and absurd technical limitations of MS-DOS, this program had problems meeting the required specifications, especially with respect to speed, reliability and the data-handling capacity. As GNU/Linux emerged as a reliable and free multi-tasking operating system, it was quickly realised that a change of operating-system at the stations was top priority. Around 1997, `HENRIK` was quickly ported to GNU/Linux; the resulting program was called `arnljot`. Although this was a major improvement, it was still a ported huge MS-DOS program including large amounts of code written exclusively to bypass MS-DOS limitations. To remedy this, a major rewrite of the code was initiated, removing all "MS-DOS-artifacts", as well as splitting the program in three parts: `aniara` handling the overall station control and communication with the control centre; `mima`, controlling the imager; and `nipu` handling the NIPU, (Section 2.2.2). These programs have been in routine operation since 1999.

`aniara` supervises most functions at the station and provides an interface to AIDA. Among many other things, `aniara` handles alarm conditions, stores configurations, and acknowledges "sanity-checks" sent from the Housekeeping Unit (Section A.4) after verifying that the station computer is operating properly. A simple text-oriented user interface to ALIS, mainly intended for system maintenance is also provided by `aniara`. As AIDA is slowly phased out, `aniara` will most likely take over some of its functionality.

`mima` is the imager control program. It boots up the camera-control unit (Section 3.3.2), configures the imager (Section 3.3.3), retrieves the image-data as well as creates and saves FITS images onto the local disks (Section 2.2.5). This program is thus responsible for putting all the supplementary information into the FITS header (integration-time, filter, UTC, viewing direction, CCD-temperatures, etc.).

`nipu` is a program for controlling and booting the NIPU. This program is used to calibrate the FPS and CPS, select filters (Section 3.5) and viewing-directions (Section 3.6).

Apart from the software discussed above, it is also worth mentioning the following software packages at the station:

CCU-software: Vendor-provided Transputer binaries for the camera-control unit (Section 3.3.2). This code is uploaded by `mima` during the imager boot-up phase.

HU-firmware: The Housekeeping Unit (Section A.4) firmware is written in assembler and stored in an Erasable Programmable Read-Only Memory (EPROM). It provides low-level interfaces to various GLIP systems (Appendix A), watchdog functions for the station computer, as well as alarm

and error-recovery functions. If the station computer is shut-down or malfunctioning, the housekeeping unit will take over the communication line and alert the control centre about the error condition at the station. It is then possible for the operator at the control centre to communicate directly with the housekeeping unit to diagnose the situation and often resume normal operation in less than ten minutes.

`ntpd` This freely-available daemon controls station timing (Section A.5).

NIPU software: Software for the Transputers in the NIPU are uploaded at NIPU start-up by the `nipu` program at the station computer. The NIPU software was written in Occam and Transputer-C.

Figure 5.2 presents the interrelationships of the various software at the stations superimposed onto a block-diagram of an ALIS station (Appendix A).

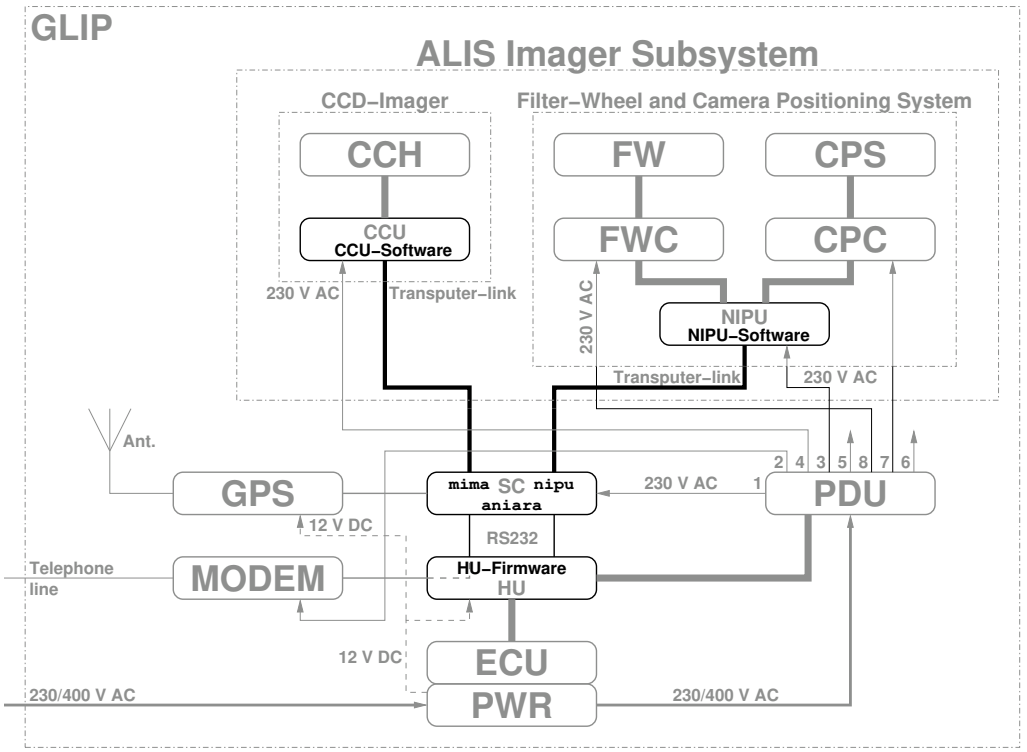

Figure 5.2: ALIS station software superimposed onto the block-diagram of an ALIS station (refer to Figure A.1 in Appendix A); `mima` uploads the vendor-provided CCU-software and controls the imager; `nipu` uploads the NIPU software and controls the CPS and FPS; `aniara` is the main station-control program. The housekeeping unit is controlled by firmware in an EPROM.

5.2.4 Experiences and future plans

ALIS software has now existed for over a decade. During the early years, technical obstacles, and in particular problems related to the many limitations of the

operating system at the stations, dominated. Following the major OS upgrade to GNU/Linux, most of these software problems have now been eliminated. The importance of reliable and free operating systems cannot be over-estimated. Many man-years of programming efforts could have been saved if proprietary software could have been avoided in the first place.

Regarding the user-interfaces, it seems inevitable that an effort will be required to create a web-oriented standard user interface for ALIS. AIDA will probably be depreciated in favour of moving this functionality to the stations. This will also increase redundancy of the ALIS control system. At the stations a simple and flexible approach seems to be to let each major functionality to be represented by an application program. An interesting development is the networked "parameter-server" that can be used to configure ALIS as well as to retrieve status information in a consistent way over the entire network of stations and user-interfaces.

The lag between the desired and present control system for ALIS is in the order of 1–2 man-years. Finally it should never be forgotten that software development is an evolutionary process that requires continuous upgrades and maintenance.

Chapter 6

Scientific results from ALIS

> "Vetenskapsmannen är en byggmästare. Att samla vetenskapliga uppgifter kan jämföras med att samla stenar till ett hus; en hög med uppgifter är inte mer "vetenskap" än en hög stenar är ett hus. Obearbetade vetenskapliga resultat är bara en död stenhög" *Kristian Birkeland*

> "Wovon man nicht sprechen kann, darüber muß man schweigen"
> *Ludwig Wittgenstein*

This chapter attempts to provide a summary of the scientific results obtained from the analysis of data from ALIS. It is important to stress that this can only be a brief review of published scientific results in order to demonstrate the scientific applicability of ALIS in particular, and of multi-station imaging in general. The reader is urged to read the original papers for more complete and detailed information about the scientific results summarised.

Interesting results often emerge from unexpected directions. HF pump-enhanced airglow was not mentioned among the scientific objectives in the early ALIS papers. However, this topic existed as an auxiliary scientific objective until 16 February 1999, when the first unambiguous observations of this phenomenon at high-latitudes were made. Since then it has been the main scientific objective of the ALIS measurements. Hence, a large portion of this chapter (Section 6.4) is therefore devoted to these observations.

It is essential for a proper interpretation of the data-sets to do coordinated observations involving as many independent measurement systems as possible. ALIS has participated in a number of coordinated campaigns involving instrumentation such as the tri-static European Incoherent SCATter radar (EISCAT), the EISCAT Heating facility in Tromsø, the American FAST, POLAR and MSX satellites, and the German lee-wave campaign studying polar stratospheric clouds etc.

The author's main role has been to supervise and make the observations with ALIS and supporting instruments, retrieve, calibrate and validate the datasets, as well as to assist with data-analysis and interpretation of the data-sets. Most ALIS data-analysis software, and in particular the software for triangulation and tomography-like analysis has been designed and written by Björn Gustavsson. He also performed most of the data-analysis. Many other coauthors (see the bibliography) contributed to the physical interpretations of the data-sets obtained

from ALIS. This division of responsibilities appeared naturally in a small group with a large and technically complex project.

6.1 Scientific objectives of ALIS

The list below tries to summarise the scientific objectives of ALIS, from the first proposal [*Steen*, 1989] until the present time.

Non-stable auroral forms: Auroral events such as: substorm onsets, Westward Travelling Surges (WTS), surges, folds, spirals (or auroral vortices), rays and omega bands, and the not well-understood pulsating and flickering aurora belong to this category. These phenomena require observations with high temporal and spatial resolution. So far, ALIS has been used infrequently to make this type of observations, due to a combination of technical limitations (Section 3.3.4), as well as difficulties related to the scientific understanding of these phenomena. However, a theoretical paper on auroral vortices was published (Section 6.5.3).

Stable auroral forms: The stable auroral arc has been the topic for many studies during the last five decades. Despite this, the ionospheric environment in and around it is not yet fully understood. Detailed field-aligned measurements of ionospheric parameters combined with tri-static plasma-drift measurements by EISCAT, produce profiles on electron density, electron and ion temperatures ranging from some 90 km to 1000 km, as well as, horizontal electric-field estimates in the ionospheric F-region. To relate such measurements to the optical data from ALIS, as well as to satellite and other ground-based instruments would increase the scientific yield of studies of stable auroral forms. Some results of such coordinated observations with ALIS, EISCAT and the FAST satellite are discussed in Section 6.5.2. Another stable auroral form is the *diffuse aurora*, (added to the scientific objectives in *Steen et al.* [1990]) where the equatorward edge of the diffuse aurora has been used to estimate the size of the auroral oval. The main ionospheric trough is often associated with the equatorward edge of the auroral oval. Examples of "accidental" measurements of the trough are discussed in Section 6.5.4. Other studies (however, not always of stable aurora) that could be included here are : enhanced aurora [*Hallinan et al.*, 1985], black aurora, statistical studies of arc-thickness etc.

Characteristic energy of particles: By the use of spectroscopic ratios, the characteristic energy of the precipitating particles can be obtained [*Hecht et al.*, 1989; *Meier et al.*, 1989; *Strickland et al.*, 1994; *Rees and Luckey*, 1974]. To do this properly would require simultaneous measurements at two wavelengths at each station, thus doubling the data-flow and requiring at least two imagers at each station. Results obtained so far involve a single camera at each station and rapid filter changes (Section 6.5.1).

A 3-D image: Since the fields-of-view of the ALIS stations overlap, it is possible to estimate the altitude distribution of auroral emissions by utilising triangulation and tomographic inversion techniques. *Steen* [1989] expected

that ALIS would be able to produce 2-D maps of the altitude-distribution of the different auroral emissions. This would represent a pseudo 3-D image of the aurora. To develop techniques for visualising the variations in time and space of 3-D aurora was characterised as "an interesting but non-trivial exercise*". While the latter still lies in the realm of the future, ALIS-images have frequently been used for obtaining heights and volume distributions through triangulation and tomography-like inversion techniques. The progress in this field is reported in Section 6.3 and references therein.

Relation between electron and proton aurora: The main auroral particle species are electrons and protons. The intensity of the more diffuse proton aurora is much lower than the electron aurora. In order to study the relation between these two types of aurora, it was suggested to use the N_2^+ 1Neg. (4278 Å) and H_β (4861 Å) emission lines [see for example *Galand*, 2001, and references therein]. Although ALIS would be well-suited for studies of proton aurora, no measurements have been carried out to date.

The relation between the neutral wind and the aurora: Auroral intensifications appear to be related to rapid variations in the thermospheric neutral wind on a time scale which excludes contribution from the ion-drag force. This objective was added in *Steen et al.* [1990] and some initial studies were carried out (Section 6.5.6).

Non-auroral studies: It was envisioned that ALIS would make mainly auroral observations during dark periods. The system would also be available for other types of measurements. One such type of measurement is to study the formation of Polar Stratospheric Clouds (PSC) which is important for the understanding of ozone depletion. The results of some of these studies are summarised in Section 6.6.1. It was later proposed [*Steen et al.*, 1990] to study gravity wave modulation of airglow emissions. However, no such studies have been carried out to date. It was also speculated that ALIS could be used for other studies, for example high-altitude flashes, clouds and comets, etc. ALIS acquired some images of the Hale-Bopp and the Hyakutake comets; however these data have not yet been analysed. In summary, observations of HF pump-enhanced airglow quite unexpectedly ended up as the main topic for ALIS.

The majority of published ALIS results to date concerns studies of HF pump-enhanced airglow and therefore constitutes the main part of this chapter. When ALIS measurements stopped for the season each year due to the midnight sun period, one detector participated in a joint study to attempt daytime auroral imaging using an imaging spectrometer. This generated some interesting first results, as outlined in Section 6.5.5. Another sidetrack that might become productive in the future is the study of meteor trails. Some rather promising observations have already been carried out (Section 6.6.2).

*The problem is not so much the visualisation itself, but rather that human perception has evolved to interpret 2-D surfaces of 3-D objects. Evolution has never required an understanding of a true 3-D distribution.

Package name	*Description*
`Camera`	The cornerstone package, providing a set of functions for a black-box-model of the imaging process, mapping functions, as well as functions for manual and automatic stereoscopic triangulation.
`Starcal`	A tool to determine the characteristics of the camera-models and rotations by combining the information that can be obtained from images with the positions of the stars in the sky.
`Skymap`	A medium accuracy star-chart, used by `Starcal` to calculate the positions of the stars.
`EARTH`	A set of earth model functions based on WGS-84.
`Fits_tools`	A small toolbox for reading and pre-processing FITS image data.

Table 6.1: Summary of image processing tools provided by Björn Gustavsson at `http://www.irf.se/~bjorn/Starcal/`. They provide a small and self-contained set of functions for camera calibration as well as single and multi-viewpoint image data analysis. These tools are primarily intended for middle and upper atmospheric physics as well as for auroral research. (Quoted from: `http://www.irf.se/~bjorn/Starcal/Documentation/` see also *Gustavsson* [2000].)

6.2 ALIS data analysis

The primary raw-data output from ALIS is multi-station image data in FITS format (Section 2.2.5). Currently, the main part of the data-analysis software for ALIS includes programs for correcting the images, calibrations against the star background, auroral tomography and triangulation, spectroscopic and absolute measurements, etc. Most of the programs are written in Matlab and C, but some work was also carried out in IDL, NOAO/IRAF as well as other common image-processing environments. The main authors of the current data-analysis software for ALIS are Björn Gustavsson (see Table 6.1) and Peter Rydesäter (see Table 6.2). Carl-Fredrik Enell has developed additional tools for the analysis of PSC data [PSCWorks, see *Enell*, 2002, Appendix B]. A combination of the data-analysis tools mentioned was utilised to analyse nearly all of the observations summarised in this chapter.

6.2.1 Investigations of new data-analysis methods for ALIS

As ALIS produces large amounts of data, studies have been carried out to investigate various new and partly automated approaches to the problems of image processing, pattern recognition and image classification. Some references to published works on ALIS are presented below, however, this field is to a large extent highly experimental in nature and therefore these results are not included in the standard analysis of ALIS data.

To classify auroral images is not a straight-forward task. As noted by *Brändström et al.* [1998] it is sometimes difficult, even for an experienced observer, to discriminate between for example diffuse aurora and aurora behind thin clouds (Figure 6.1).

Package name	*Description*
`ALISFIX`	Loads images into Matlab, converts the FITS headers to a common format.
`ALISMOVIE`	Generates mpeg movies containing a single-frame overview of all stations.
`TOMO`	Iterative 3D-Tomography toolkit. Stand-alone version.
`TOMOMEX`	The same as `TOMO`, but compiled as a Matlab "mex" file.
`TOMOWS`	A Matlab API for the `TOMOMEX` package. Includes some graphical user interfaces for plotting
`ALISDB`	A set of scripts used to create arrays of structures describing ALIS images. These can be used to create static web-pages with quicklook overviews. The package can also be used as a pre-processor for the `TOMO` package.
`alisim`	A universal tool to preprocess, correct and display ALIS FITS images.
`ITERATOR`	Creates fast files for Matlab from a Matlab expression. Typically 6–16 times faster for the ALIS optical camera model.
`ALIS-SQL`	A searchable database for all ALIS images with download, viewing of quick-look images, etc. in use at `http://petrydpc.itm.mh.se/alis/`. Uses `alisim` to read the database and create quick-looks.
`fits_toolbox`	Tools to read, modify and write FITS headers.

Table 6.2: Summary of data analysis tools written by Peter Rydesäter, available at `http://petrydpc.itm.mh.se/tools/`. See also *Rydesäter* [2001] for more information.

Figure 6.1: An example of the difficulties of auroral image classification. In this image, clouds, stars, diffuse and black aurora are seen. [After Figure 8 in *Brändström et al.*, 1998]

Auroral classification scheme

Main morphological feature	Secondary morphological feature	Temporal feature	Vortex feature
Auroral arc one dimension is significantly larger than the other	Non-diffuse Diffuse Multiple (2,3,...) Rayed Striated Corona Dark aurora Enhanced Partly clouds Intensity	Active Quiet Pulsating	Spiral (E.g. WTS, omega, torch) Fold Curl
Fragmental auroral structure	Non-diffuse Diffuse Multiple (2,3,...) Rayed Striated Corona Dark aurora Enhanced Partly clouds Intensity	Active Quiet Pulsating	Fold Curl
Diffuse aurora covering a larger region	Dark aurora Partly cloudy Intensity	Pulsating	
Unidentified aurora			

Table 6.3: An auroral classification scheme (after a proposal by Å. Steen) used by the manual classification program for ALIS data. ("Dark aurora" stands for a class of phenomena commonly known as "black aurora")

Early on in the ALIS project, an auroral classification scheme was suggested (by Åke Steen, see Table 6.3). A classification program (developed by Petrus Hyvönen and later Mats Luspa) was written. The program was used to manually, but relatively quickly, classify the images according to the classification scheme in Table 6.3. This classification was very useful but time-consuming due to the large number of images from many stations. The quality of the image-classification was also dependent on the operator. This classification method was therefore abandoned, and investigations started to find automated methods of image classification.

In an exploratory study carried out by *Waldemark et al.* [1997]; *Eide et al.* [1997] Pulse Coupled Neural Networks (PCNN) were evaluated as a preprocessor for classifying image-data from ALIS. The PCNN is a biologically inspired neural network based on findings in the visual cortex of small mammals. The algorithm has been successfully applied in the field of mammography [*Kinser and Lindblad*,

1997] which, to some extent, possesses similar image processing and classification problems as encountered in auroral imaging. A three-step procedure for automatically classifying auroral images is outlined: (1) use a PCNN for image segmentation, (2) post-process the resulting data, either by using Singular Value Decomposition (SVD) or by applying a second PCNN for feature extraction, (3) carry out the actual classification using a traditional neural network. This work was followed up by *Rydesäter et al.* [1998] who concentrated on the problem of how to find auroral arcs, and on their location within the images. For this purpose an arc detection algorithm was constructed and tested. Initial attempts were made to enhance the algorithm with a Radial Basis Neural Network (RBNN). It was concluded that the arc detection algorithm gave a robust detection of auroral arcs and their direction. Preliminary results from the application of a RBNN was promising.

Alpatov et al. [2000] applied self-organising neural networks to ALIS data, for the detection of polar stratospheric clouds.

A different approach to the problem of automatic recognition of auroral forms is studied by *Pudovkin et al.* [1998]. Here a more traditional method, based on the analysis of isolines of auroral luminosity shapes is utilised. Classical forms such as ellipses, spirals and folds appear to be confidently retrieved. However, *Pudovkin et al.* [1998] notes that the entire field of auroral classification seems to be at an early stage: "There are needs for extensive and purposeful studies of the forms peculiar to certain geophysical conditions, with the nature of the physical process within the auroral plasma and their characteristic time and space scales being taken into account."

Rydesäter [2001] presents a survey of possible methods of implementing a Selective Imaging Technique (SIT) functionality in ALIS, as proposed by *Steen et al.* [1997a]. (This would be an algorithm or a device that automatically controls ALIS, or advises the operator to acquire data of specific interest when favourable conditions occur.)

A study on the effects of lossy compression of auroral image data is presented in *Rydesäter et al.* [2001]. At least for the images studied, it appears to be possible to compress images to approximately 5–12% of their original size without increasing errors.

Another topic is the study of the fractal dimension of auroral features. An initial study was carried out by *Alpatov et al.* [1996a,b]. It was concluded that fractal analysis methods can be used to segment auroral images into aurora, stars, clouds and background. However it remains to be seen if segmentation of the auroral features themselves can be related to physical processes responsible for the aurora.

Despite the fact that these studies provided promising preliminary results, much work remain before these methods can be applied to auroral imaging on a regular basis.

Apart from the work related to ALIS, many other groups are working in this field. An example of this is the very promising work by *Syrjäsuo* [2001, and references therein] on auroral detection/classification by automated image analysis.

6.3 Tomography and triangulation

Many earlier experiments have used multi-station measurements combined with triangulation techniques to estimate the height of the aurora (Section 1.1.1). Computer Tomography (CT) has its most well-known applications in the field of radiology[†] [*Cormac*, 1963a,b]. A similar method was applied by *Solomon et al.* [1984] to estimate the airglow distribution as measured by space-borne photometers. An emission distribution was characterised by *Jones et al.* [1991] by using data from a rocket and three ground-based scanning photometers. *Na and Lee* [1991] estimated ionospheric electron densities from radar measurements by the use of tomographic methods. *McDade and Llewellyn* [1994] presented methods to estimate airglow distributions from limb-scanning satellite measurements. By the use of image data from two monochromatic TV-cameras in Antarctica with a separation of 20 km *Aso et al.* [1990] studied the auroral emission distribution in slices.

6.3.1 Methods, initial studies and simulations

One primary scientific objective of ALIS was to provide the possibility to reconstruct the 3D auroral volume emission by applying tomographic inversion techniques on spectroscopic high-resolution images of aurora, airglow and related phenomena [*Steen*, 1989]. An initial study based on simulated ALIS-data was performed by *Gustavsson* [1992]. Later, the problems of auroral tomography were discussed during an auroral tomography workshop in Kiruna [*Steen*, 1993]. A more detailed model simulation study [*Gustavsson*, 1998] concluded that the capability to achieve results with acceptable horizontal and vertical resolution, exists. This paper also suggests a useful way to define a stopping criteria for iterative tomographic methods by combining adaptive low-pass filtering and feasibility tests, and concludes that "it is possible to achieve feasible reconstructions with the modified Multiplicative Algebraic Reconstruction Technique (MART)." An introductory overview of ground-based tomography, including a further investigation of resolution and error sensitivity is presented in *Gustavsson* [2000, Chap. 3] concluding that "the result of the tomographic inversion cannot retrieve fine scale internal structures. However, estimates of the spatial distribution of ionospheric emissions which, in general, have a comparatively simple shape, can be accurately obtained". The chapter also presents a strengthening of the statistical stopping criteria of *Veklerov and Llacer* [1989].

6.3.2 Summary of results from computer tomography of ALIS-data

At an early stage a close scientific and technical collaboration was established with colleagues at Kyoto University, and later at the National Institute for Polar

[†]Incidentally, the term "tomography" existed in radiological applications decades before computerised tomography became a real possibility. See, for example, *Lodin* [1935]; *Weinbren* [1946], and other references discussed in *Backlund* [1956]. Typically a series of X-ray exposures were obtained while the X-ray tube and film-cassette rotated around the patient. Back then, the tomographic inversion had to be performed by the brain of the radiologist observing these series of X-ray images.

Research (NIPR), Tokyo. During a joint campaign (ALIS-Japan 1) held in March 1996, the first results of auroral tomography were obtained as reported in *Aso et al.* [1998a]. At this time ALIS had only three imagers, and two additional intensified CCD-cameras were provided by our Japanese colleagues [*Aso et al.*, 1993, 1994], resulting in a total of five imaging stations. A modified MART was used for tomographic analysis, presenting initial results of tomography for a folded arc, and a double-arc system [*Aso et al.*, 1998a]. An auroral model with a folded arc is also discussed in this paper.

In *Aso et al.* [1998b] initial results and model comparisons using a modified version of a Simultaneous Iterative Reconstruction Technique (SIRT) [*Gilbert*, 1972] were applied to data from the March 1995 ALIS-Japan 1 campaign. The method was also verified by numerical simulations. An auroral fold occurring at 23:40:30 UTC on 26 March 1995 was selected for testing the tomographic analysis with the modified SIRT method assuming magnetic field-aligned auroral structures. Projecting back the reconstructed volume onto the original images reveals a disparity of about 10% or less. The modified SIRT method was found to be a promising CT application in the field of auroral studies. In total, four joint ALIS-Japan campaigns have been undertaken so far, and some of these data are still in the analysis phase.

Aso et al. [2000] reports on tomographic analysis of auroral images by the modified SIRT method. Auroral images were obtained on 9 February 1997 at 19:46:00 UTC in the $O(^1S)$ 5577 Å emission line as well as at 18:31:30 UTC in the N_2^+ 1Neg. 4278 Å emission line. The latter case showed a bright folded arc south of Kiruna and a faint thin arc north of Kiruna. The peak height of the intense aurora appears lower than the faint arc. Given favourable conditions for auroral tomography, it is possible to study the basic auroral formation process. To demonstrate this *Aso et al.* [2000] also performed a numerical simulation for the reconstruction of a slightly folded auroral structure using data from seven stations. Furthermore, the authors report on initial triangulation results applied to the studies of nacreous clouds. Some more reports of ALIS observations of nacreous clouds are summarised in Section 6.6.1.

Triangulation and tomography-like methods were applied to the studies of HF pump-enhanced airglow (Section 6.4). A solution to the inverse problem for a particularly ill-posed problem, with data from only three stations south of the emission region, is discussed in *Gustavsson et al.* [2001a].

In *Gustavsson et al.* [2001b] a constrained tomographic inversion was used to estimate the N_2^+ 1Neg. 4278 Å altitude distribution, which allowed an estimate of the energy distribution of the electron flux (Section 6.5.1).

This section has provided a rather brief summary of a very large subject. For further, more detailed studies, the reader is encouraged to read the cited papers, and, in particular, the main reference for three-dimensional imaging with ALIS by *Gustavsson* [2000].

Future developments to be expected in this field include the investigation of smooth basis functions and approximated projection algorithms for faster tomography [*Rydesäter and Gustavsson*, 2001].

6.4 HF pump-enhanced airglow

By transmitting a powerful high-frequency (HF) ("short-wave") radio signal into the ionosphere it is possible to modify the ionosphere given that the ionospheric conditions are favourable (i.e. high enough electron concentration, and little or no auroral activity). Such experiments may excite plasma processes on a wide range of temporal and spatial scales [*Leyser et al.*, 2000]. It is possible to produce enhanced optical emissions, which are far to weak to be detected by the unaided human eye, but that can be detected with sensitive imagers and photometers. These optical emissions can be used as a diagnostic tool to study electron energisation during driven plasma turbulence. For example, it is possible to study what the roles of heating and electron acceleration are for dissipating the turbulence [*Leyser et al.*, 2000]. The naturally occurring airglow emissions at 6300 Å and 5577 Å (from the two lowest excited states of oxygen, $O(^1D)$ and $O(^1S)$) can be enhanced by transmitting a high-powered short-wave radio signal into the ionospheric F-region plasma. The low noise and high quantum-efficiency of the ALIS imager (Chapter 3) makes ALIS an ideal instrument for studying optical effects from active ionospheric experiments.

HF pump-enhanced airglow [‡] has been studied at low latitudes (Arecibo, Puerto Rico) since the early 1970s by *Carlsson et al.* [1982] and *Bernhardt et al.* [1989]. At mid-latitudes, experiments have been carried out in: Platteville, U.S.A., [*Sipler and Biondi*, 1972; *Haslett and Megill*, 1974], Moscow, Russia, [*Adeishvili et al.*, 1978], and in Sura, Russia [*Bernhardt et al.*, 1991]. However, at high (auroral) latitudes, there was only one previous report of HF pump-enhanced airglow before 1999 made by *Stubbe et al.* [1982].

The airglow enhancement has been attributed to excitation of metastable states of atomic oxygen by energetic electrons accelerated in plasma instabilities, [*Perkins and Kaw*, 1971; *Weinstock and Bezzerides*, 1974; *Weinstock*, 1975; *Gurevich et al.*, 1985] and by energetic electrons from the tail of the heated thermal electron plasma [*Mantas*, 1994; *Mantas and Carlson*, 1996; *Gurevich and Milikh*, 1997]. Electron collisions with energies above 3.5 eV yield the excited $O(^1D)$ metastable state, which radiates at 6300 Å [*Bernhardt et al.*, 1991]. The second excited metastable state $O(^1S)$, which radiates at 5577 Å, is obtained for electron energies from about 4.5 eV and upwards. For comparison, the ionospheric background electron temperature is typically 0.1–0.2 eV. Further, it has been proposed that the $O(^1D)$ state may be thermally excited and that the scarcity of observations of simultaneous 6300 Å and 5577 Å enhancements imply that acceleration of electrons may require special experimental and ionospheric conditions that are not often fulfilled [*Mantas and Carlson*, 1996].

[‡]As long as the enhancements were only observed in the $O(^1D)$ (6300 Å) and occasionally in the $O(^1S)$ (5577 Å) emission lines, the natural term was "HF pump-enhanced airglow". With the recent observations in the N_2^+ 1Pos. (6600 Å) emission [*Djuth et al.*, 1999], and N_2^+ 1Neg. (4278 Å) and $O(3p^3P)$ (8446 Å), a more correct term would be something like "HF pump-enhanced optical emissions" or maybe "Radio-induced optical emissions". However, the old term "HF pump-enhanced airglow" will be retained in this text for compatibility with earlier papers.

6.4.1 The EISCAT Heating facility

The EISCAT Heating facility is located at Ramfjordmoen near Tromsø, Norway (69.6°N, 19.2°E, 86.3 m above sea level, L=6.2, magnetic dip angle I=78°) [*Rietveld et al.*, 1993]. The facility is located about 200 km north of Kiruna (See Figure 6.2). Up to 1.2 MW of CW power in the frequency range from 3.85 to 8 MHz can be generated by twelve transmitters of 100 kW each. There are three antenna arrays, covering the frequency ranges of 5.4-8 MHz, 3.85–5.65 MHz and 5.4–8 MHz. Array 1 has a beam width of 7° with a gain of 30 dB corresponding to 1200 MW Effective Radiated Power (ERP). Arrays 2–3 have beam widths of 14.5°, a gain of 24 dB and a maximum ERP of 300 MW. The main HF wave parameters such as frequency, polarisation, beam direction, and maximum power are chosen and set up at the time of tuning-up the transmitters. It is furthermore possible to modulate, power-step, change polarisation modes and to change the direction of the beam during an experiment [*Rietveld et al.*, 1993].

The EISCAT Heating facility enables strong excitation of plasma turbulence in a wide range of angles to the geomagnetic field. This is due to the fact that the pump electric field is directed parallel to the geomagnetic field at the reflection height, and essentially perpendicular to the magnetic field at only a few kilometres lower altitude [*Leyser*, 1991].

6.4.2 ALIS observations of enhanced airglow

Starting in 1995, a series of experiments were carried out, attempting to produce enhanced airglow with the EISCAT Heating facility, and to detect it with ALIS. *Stubbe et al.* [1982] noted that such experiments require: a sufficiently high ionospheric critical frequency, dark and clear skies, no auroral activity and a low or at least stable natural airglow background. As seen from Table 6.4 many events are yet to be analysed. In the following text emphasis will be on the 16 February 1999 event.

6.4.3 Observations on 16 February 1999

The first unambiguous observation of HF pump-enhanced airglow at auroral latitudes was made on 16 February 1999 [*Brändström et al.*, 1999]. This evening the skies were clear at most ALIS stations and there was no auroral activity ($K_p \approx 0$). ALIS operated between 16:15 and 18:30 UTC taking a new image every 10 s with 5 s integration time for the $O(^1D)$ 6300 Å emission line. The sensitivity of the CCD-cameras was enhanced 64 times by on-chip binning 8×8 pixels, thus reducing the spatial resolution from 1024×1024 pixels to 128×128 pixels. All ALIS-cameras were pointing towards the anticipated region of enhanced airglow. This is the so called "heating-position" (see Table 3.6 and Figure 3.11), centred at an altitude of approximately 250 km above the EISCAT Heating facility (Figure 6.2). Ten transmitters were operating with an output power of 85 kW each. Thus a total transmitted power of 850 kW, yielded an ERP of around 125 MW. The transmitted frequency was 4.04 MHz, reflecting in the ionospheric F-region, and the ordinary mode (O-mode) beam was tilted 6° south from the vertical (which is about half the angle between the vertical and the geomagnetic field

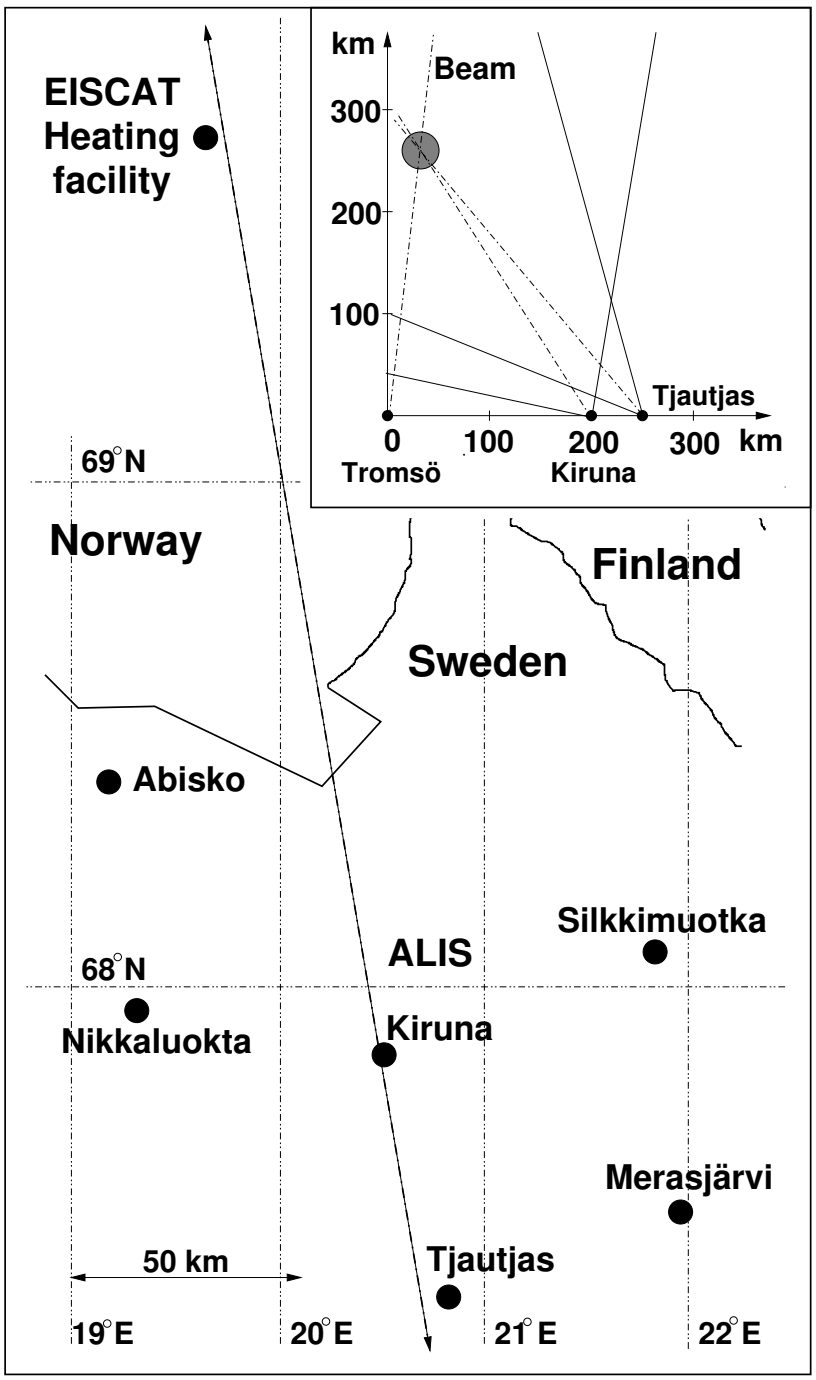

Figure 6.2: Geometry of the HF pump-enhanced airglow. Some of the ALIS stations (see text) observed pump-enhanced airglow over the EISCAT Heating facility. *Inset:* A vertical cut along the Tromsø–Kiruna meridian. The dot indicates the anticipated region of enhanced airglow and the solid lines indicate the field-of-view of the cameras. [After Figure 1 in *Brändström et al.*, 1999]

Dates	**HEA**	**Remarks**
1995 11-25	no	
1995 11-28	no	10 min on 5 min off
1995 11-30	no	
1998 11-18	no	
1999 02-16	yes	*Brändström et al.* [1999]; *Gustavsson et al.* [2001a]; *Leyser et al.* [2000]; *Sergienko et al.* [2000]
1999 02-18	?	
1999 02-19	?	
1999 02-21	yes	5577 Å, 6300 Å *Gustavsson et al.* [2003]
1999 02-22	no	
1999 03-15	yes	
1999 03-16	yes	
1999 03-17	yes	
2000 11-19	?	
2001 02-24	yes	
2001 03-19	no	
2001 03-21		Cloudy over ALIS but HEA reported by *Kosch et al.* [2002b]
2002 03-07	yes	Freq. stepping. 4278 Å, 5577 Å, 6300 Å
2002 03-10	yes	4 min on 2 min off 4278 Å, 5577 Å, 6300 Å, 8446 Å
2002 11-02–11-07	no	
2002 11-08	yes	Freq. stepping
2003 02-24–03-07	no	Too much auroral activity

Table 6.4: An overview of most HF pump-enhanced airglow experiments carried out with ALIS. The column HEA indicates if HF pump-enhanced airglow was observed. Question marks indicate uncertainty at the time of observation. As seen, the events which have proved most interesting so far are 16 February 1999 and 21 February 1999. Analysis and new measurements are still in progress as this is written.

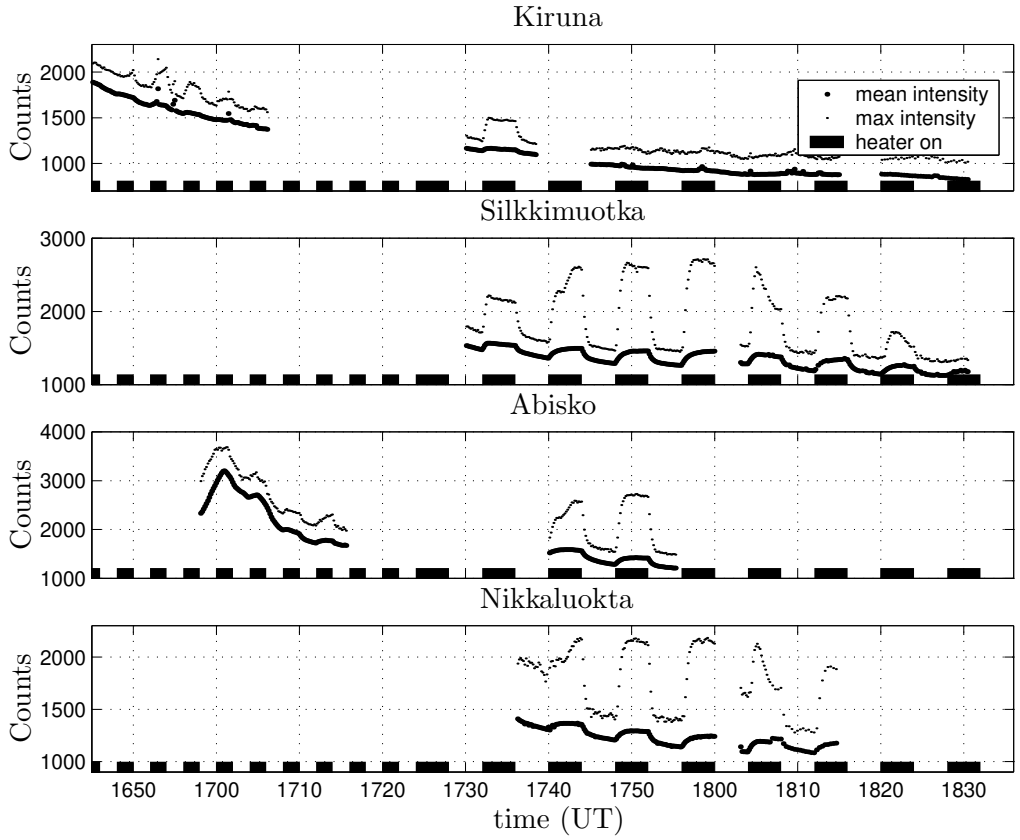

Figure 6.3: Maximum and average column emission of the 6300 Å airglow as seen from four stations. The intensity modulations correlate well with the transmitter-on/off cycles. After 17:40 UTC the Kiruna camera was directed to local zenith, imaging the natural background airglow. [After Figure 1 in *Gustavsson et al.*, 2001a]

in the ionospheric F-region above the transmitters). The transmitters (or "HF-pump") were cycled on/off with a duty cycle of 50%. Between 16:32 and 17:22 UTC the transmitters were cycled 2 min on/2 min off. Between 17:24 and 18:32 UTC this was changed to 4 min on/4 min off.

When the transmitters were cycled 2 min on/2 min off, weak airglow enhancements were observed [*Brändström et al.*, 1999; *Leyser et al.*, 2000; *Gustavsson et al.*, 2001a]. Starting at 17:32 UTC and continuing until 18:30 UTC (transmitters 4 min on/4 min off) pump-enhanced airglow was observed by all ALIS stations in operation. Due to occasional thin clouds and technical problems, some data-losses occurred. In Figure 6.3 the maximum intensity of the 6300 Å emission is plotted against time for each image from the four stations observing between 16:40 and 18:40 UTC.

The airglow intensity has an e-folding growth time of about 60 s after transmitter-on, and decays with an e-folding decay time of about 35 s after transmitter-off. After the growth time following transmitter-on, the maximum intensity of the emission appears to have a different temporal evolution at different transmitter-on/off periods. This feature may be due to irregularities in the

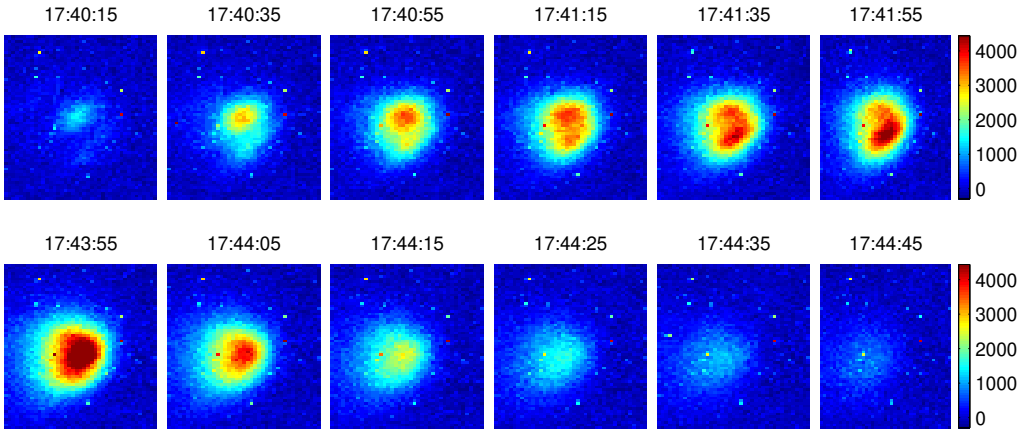

Figure 6.4: Sequence of airglow images from the Silkkimuotka ALIS station for 20 s intervals following transmitter-on at 17:40:00 UTC (top), and at 10 s intervals following transmitter-off at 17:44:00 UTC (bottom). The intensity scale is in raw counts. Two peaks of airglow intensification are clearly visible in the transmitter-on sequence. [After Figure 3 in *Brändström et al.*, 1999]

background ionosphere, which drift through the transmitted beam.

A series of images of the airglow intensity is shown in Figure 6.4. Transmitter-on occurs at 17:40 UTC, beyond which the airglow region and intensity is seen to slowly grow, forming two peaks. The upper one appears to saturate, after which the lower peak underneath intensifies, and eventually merges with the first peak. Transmitter-off occurs at 17:44 UTC, beyond which the airglow slowly decays. The peak intensity was estimated to be approximately 300 ± 100 R. (See Section 4.2.1, regarding the estimated error of the absolute calibration).

Figure 6.5 shows data from the Silkkimuotka station obtained near transmitter-on at 17:48:00 UTC and -off at 17:52:00 UTC. Both the intensity and size of the patch are seen to slowly increase after transmitter-on, and to decay slowly after transmitter-off.

From Figure 6.3 it is seen that simultaneous data from up to three stations exist for some time periods. This enables triangulation of the height of the airglow region. As shown in the top panel in Figure 6.6, the typical height of the maximum emission was found to be 230–240 km from 17:32 UTC to 18:08 UTC. For the transmitter-on at 18:12 UTC, the enhanced airglow altitude is 250-260 km. In the bottom panel it is shown that the airglow region was positioned approximately 160–170 km to the north of Kiruna and 50 km to the west.

In Figure 6.7, it is seen that the initial location of the two interaction regions are approximately 20–30 km apart. The initially more intensive northernmost region of excitation is fairly immobile, while the southernmost moves 30 km northward in 4 minutes corresponding to a velocity of 100 ± 20 m/s [*Gustavsson et al.*, 2001a].

Also, the ionospheric F-region neutral wind was measured by Fabry-Perot interferometers (FPI) [*Aruliah et al.*, 1996; *Gustavsson et al.*, 2001a]. Figure 6.8

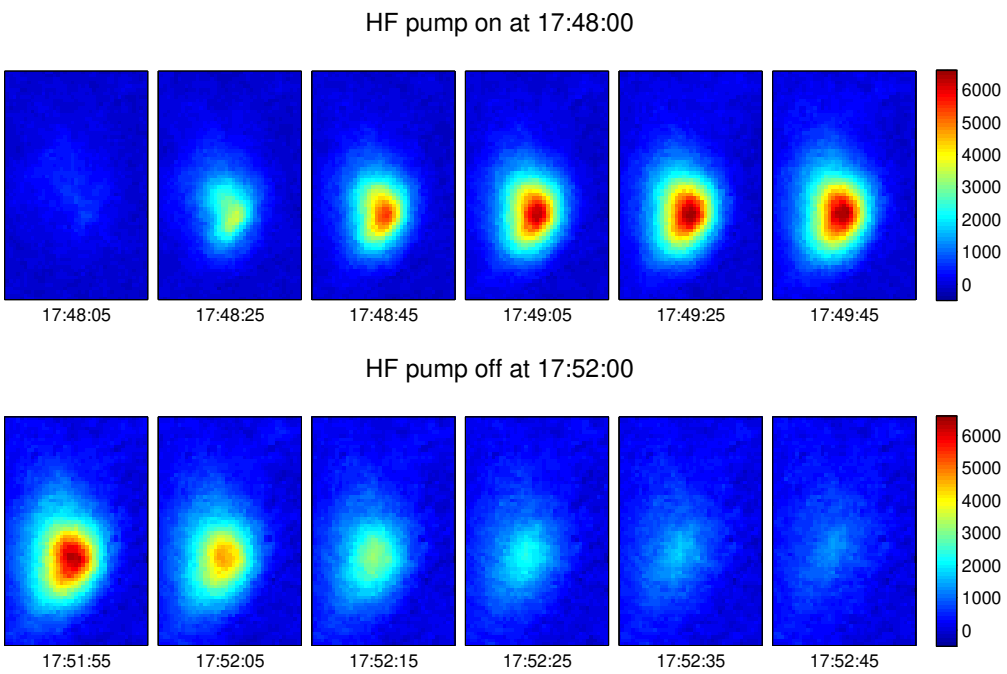

Figure 6.5: A series of images of enhanced 6300 Å airglow recorded at the Silkkimuotka station for the period 1748–1752 UTC. The upper panel displays an image sequence just after transmitter-on, and the lower panel shows images near transmitter-off. [After Figure 3 in *Leyser et al.*, 2000]

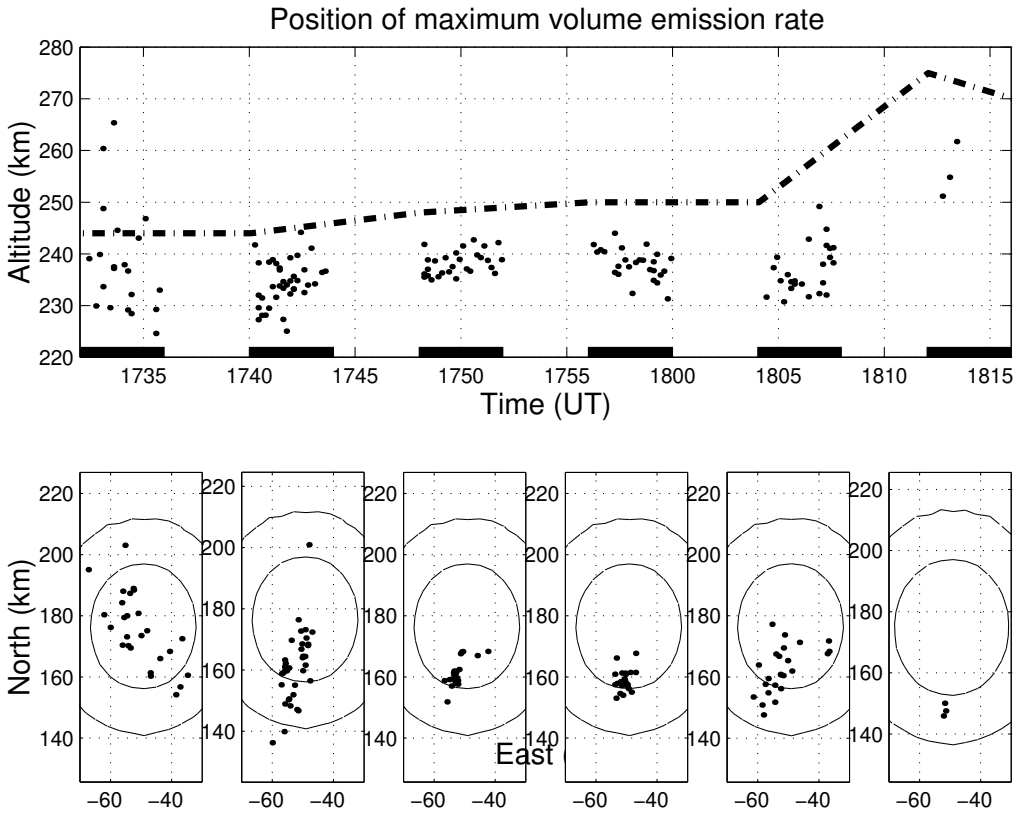

Figure 6.6: The upper panel shows the triangulated altitude of maximum enhanced airglow. The thick dashed line represents the altitude of the enhanced ion line as observed by EISCAT. The lower panels shows the horizontal location relative to Kiruna of the enhanced airglow region for the corresponding pulse. The dashed contours are the projections of the -1 and -3 dB free space antenna pattern projected to the reflection height. [After Figure 6 in *Gustavsson et al.*, 2001a]

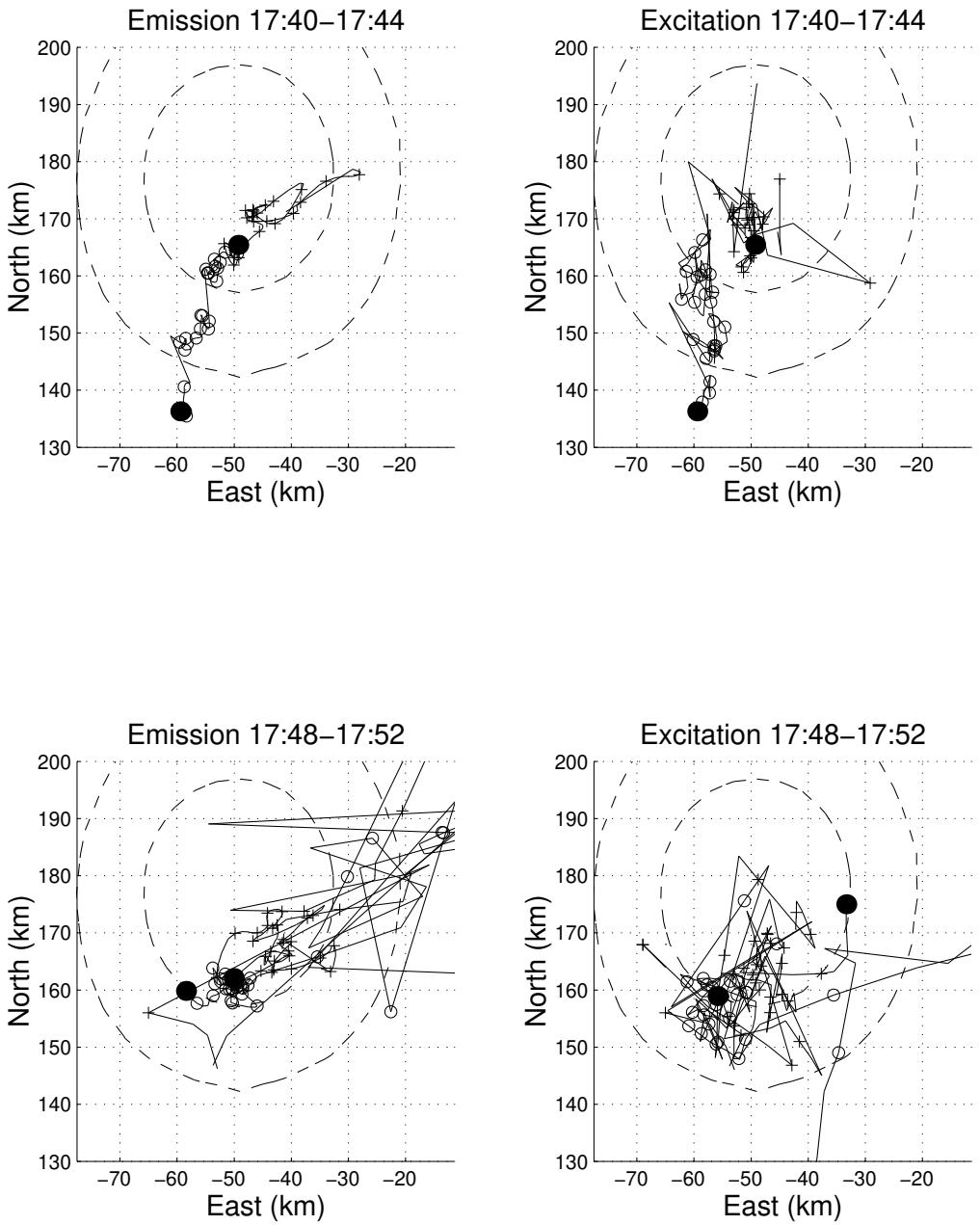

Figure 6.7: Upper left: trajectories of the centres of 6300 Å airglow emission, starting at the black points. Upper right: centres of $O(^1D)$ excitation. Lower left: centres of 6300 Å airglow emission. Lower right: centres of $O(^1D)$ excitation. There are 10 s between the markers in all panels, and all distances are relative to Kiruna. The dashed contours are the -1 and -3 dB projections of the HF-pump beam. [After Figure 4 in *Gustavsson et al.*, 2001a]

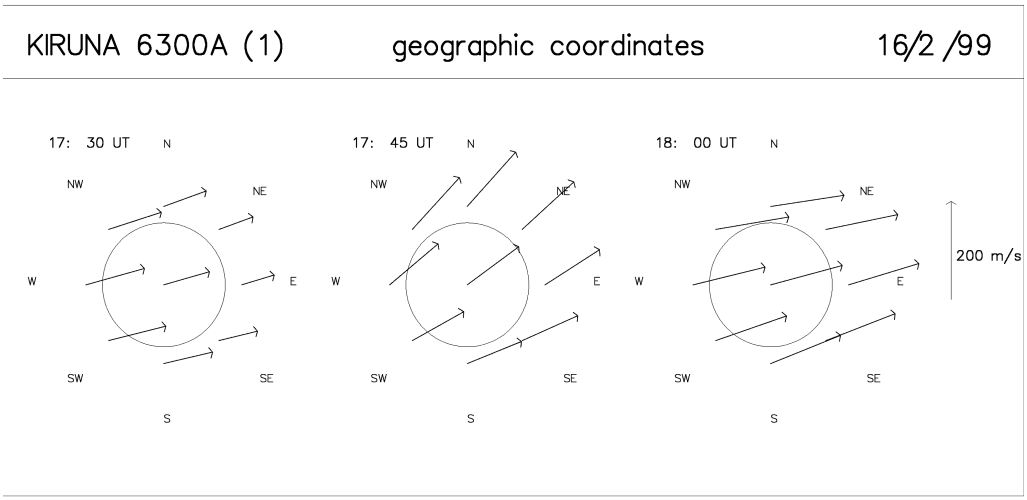

Figure 6.8: Fabry-Perot interferometer measurements of the neutral wind at 240 km altitude. The circle represents the field of view of the FPI looking at 45° elevation. This represents a circle above Kiruna with a radius of approximately 240 km. [After Figure 3 in *Gustavsson et al.*, 2001a]

displays winds varying between eastward and north-eastward, with velocities of 130-180 m/s. At 17:45 UTC the wind direction was $42° \pm 5°$ (north-eastward) with a velocity of 150 ± 5 m/s. Fabry-Perot neutral wind measurements (Figure 6.8) agree well with the north-eastward drift of the "centre of emission".

The EISCAT-UHF radar, operated at about 930 MHz, measured background plasma parameter values. The radar was operating in the common-program-1 mode with a GEN-type long pulse and alternating code [*Wannberg*, 1993], and was directed parallel to the geomagnetic field [see *Leyser et al.*, 2000, for additional information about the radar measurements].

Figure 6.9 displays these measurements of electron density, electron temperature and ion temperature versus time and altitude, with a range resolution of 22.5 km. Enhanced electron temperature is clearly seen for the transmitter cycle period of eight minutes (17:24–18:32 UTC). The electron temperature rises from an unperturbed background temperature of approximately 1000 K to about 3500 K, which corresponds to an increase of 250%. The exceptionally high temperature measurement at 18:20–18:24 UTC might be contaminated by pump-enhanced ion lines. The temperature enhancement extends several tens of km below the pump reflection height and several hundred kilometres above the reflection height [*Leyser et al.*, 2000]. A decay of the ionospheric electron density is seen in the top panel of Figure 6.9, as expected after sunset.

6.4.4 Discussion

The first report of HF pump-enhanced airglow at high latitudes was made by *Stubbe et al.* [1982] at the EISCAT Heating facility, Ramfjordmoen, Norway on October 5, 1981 at 17:40-18:20 UTC. In this experiment, photometers recorded a 50% increase (about 20 R) of the red-line (6300 Å) and a 15% decrease of the

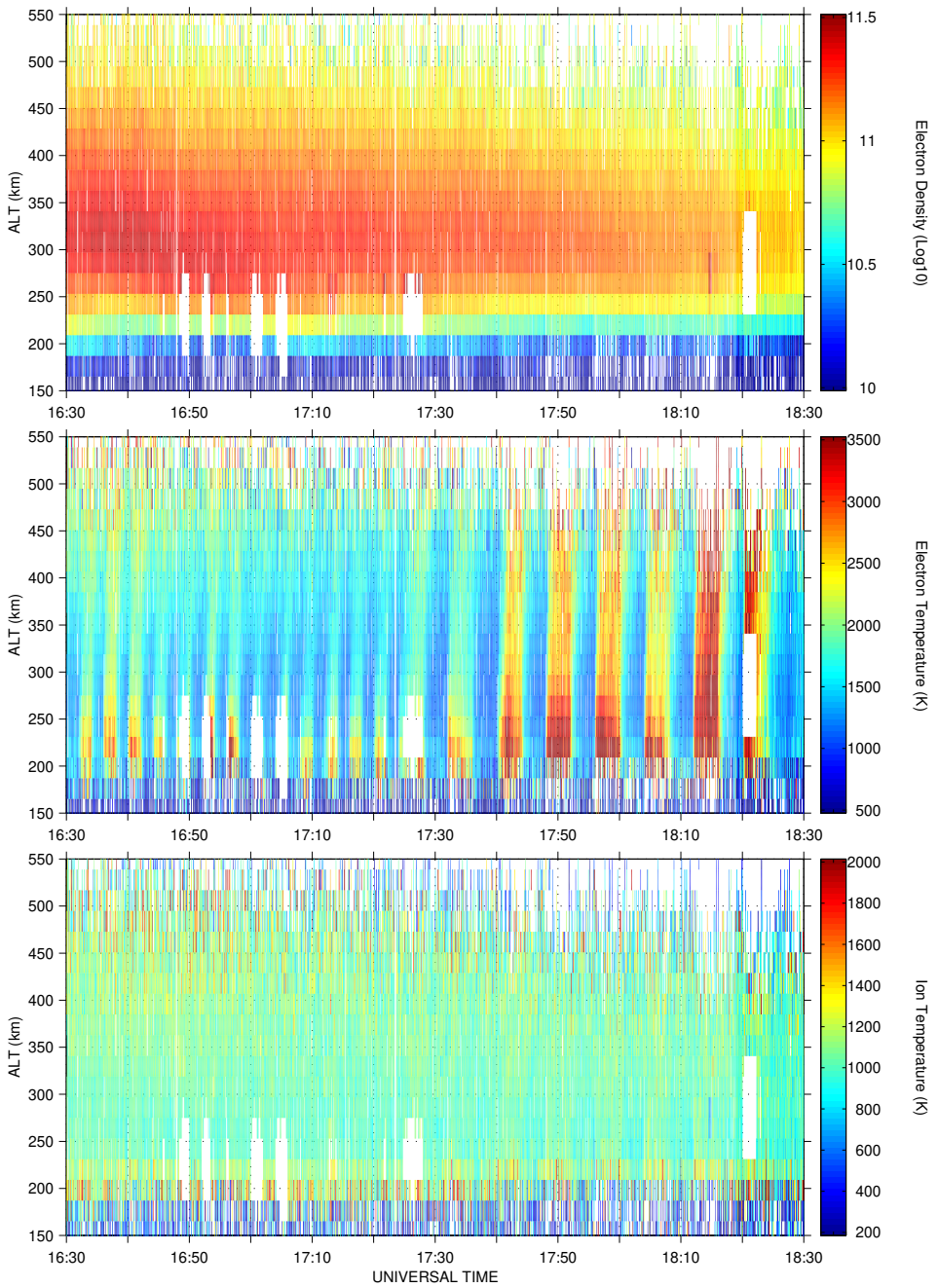

Figure 6.9: EISCAT UHF radar measurements of electron density (top panel), electron temperature (middle panel) and ion temperature (lower panel) on 16 February 1999. The data are for altitude gates spaced 22.5 km apart, which were analysed with 5 s time resolution. The blank areas below 350 km altitude are regions where the ion-line was enhanced by the HF-pump wave, causing the standard analysis to be invalid. [After Plate 3 in *Gustavsson et al.*, 2001a]

green line (5577 Å) during transmitter-on periods. The frequency was 5.423 MHz, and an O-mode beam with an ERP of 260 MW was switched 5 min on/5 min off. However, simultaneous observations made by *Henriksen et al.* [1984] did not find any evidence of pump enhanced airglow, which casted some doubts on the results by *Stubbe et al.* [1982]. In both of these observations, the optical instrumentation was scanning photometers with field-of-view of about 5°. This could have introduced aiming problems, causing the photometers to measure in the wrong region of the sky. On the other hand, it must be noted that Radio Frequency Interference (RFI) is more likely to produce false positive results from a photometer, as compared with an imager as a shift of bias of a single readout channel is more likely to be affected than all pixels in an image. These remarks illustrate why multi-station imaging measurements are superior to photometers given enough sensitivity. Such cameras were not available at the time of the experiments cited above.

The first clearly unambiguous observations of high-latitude HF pump-enhanced airglow were made on 16 February 1999, as described in the previous section. The positive result of this and subsequent observations might be attributed to some of the following reasons: improved optical instrumentation, more favourable ionospheric conditions, the approaching solar maximum. While the previous positive observation by *Stubbe et al.* [1982], relied on photometer measurements made from the same site as the EISCAT Heating facility, the results from 16 February 1999 were obtained by several stations located about 150–200 km away from the heating facility. Therefore, direct RFI from the transmitters can be clearly ruled out for these observations. The observations have also been confirmed by simultaneous measurements from an independent imager [*Kosch et al.*, 2000b,a, 2002b] on several occasions. It could therefore be stated that the validity of these observations are beyond all reasonable doubt. In addition, HF pump-enhanced airglow was observed at auroral latitudes at the High Frequency Active Auroral Research Program facility (HAARP) facility in Alaska [*Pedersen and Carlson*, 2001].

In *Brändström et al.* [1999] the observations of 16 February 1999 are found to be similar to the observations by *Bernhardt et al.* [1991] where an 165 MW, 5.828 MHz O-mode beam produced $\geq$ 200 R of airglow near zenith above the SURA-facility (latitude 56°N) in Russia.

The two intensity peaks in Figure 6.4, resemble seed irregularities as discussed by *Bernhardt et al.* [1991]. The drift-pattern of the two intensity peaks (Figure 6.7) is probably associated with electric fields and neutral-wind convection. During the next transmitter-on period 17:48–17:52 UTC, (Figure 6.5) a single patch of enhanced airglow appeared. *Leyser et al.* [2000] attributes this variability to possible large-scale plasma density irregularities in the pump-plasma interaction region.

The altitude of maximum volume emission is slightly lower than the pump reflection height of approximately 250 km as measured with the Dynasonde and EISCAT-UHF radar. These measurements are consistent with model calculations of the airglow emission altitude for different source altitudes of monoenergetic electrons [*Bernhardt et al.*, 1989].

The observed decay time of the airglow of approximately 30–35 s is signi-

ficantly shorter than the 110 s lifetime of the $O(^1D)$ metastable state [*Solomon et al.*, 1988]. However, at 240 km altitude, the effective life time of the $O(^1D)$ emission is reduced due to collisional quenching by excitation of vibrational states in N_2 and O_2 to as low values as 30 s [*Sipler and Biondi*, 1972; *Bernhardt et al.*, 1991]. Thus, the observed decay time is consistent with the effective life time of the $O(^1D)$ state being reduced by quenching [*Leyser et al.*, 2000].

Sergienko et al. [2000] used EISCAT measurements of the electron temperature to estimate the position and magnitude of the heating source. The magnitude of a modelled electron heating source was adjusted to give the best fit to the observed time-behaviour of the electron temperatures at all altitudes. This procedure led to a determination of the position and magnitude of the electron-heating source at 220 km altitude and 6×10^4 eVs^{-1} cm^{-3} respectively. A good agreement with the measured and calculated electron temperatures were obtained. The next step was to compare modelled and measured column emission rates of the $O(^1D)$ (6300 Å) line. Assuming a thermal excitation mechanism led to large overestimates of the modelled column emission rates as compared to an accelerated electron excitation mechanism. The paper shows that the assumption of abnormal electron heating generated by the transmitted wave leads to a possible explanation of the observed electron-temperature variations, but cannot account for the observed airglow variations. A process resembling acceleration by Langmuir turbulence (where the electrons above 2 eV are non-Maxwellian with a uniform energy distribution from 3–10 eV) might be an alternative explanation for airglow enhancements. This modelling was done according to the analysis by *Bernhardt et al.* [1989] and by calculating the production rate of the $O(^1D)$ state by electron impact according to the Monte Carlo model for electron transport into the atmosphere by *Ivanov and Sergienko* [1992].

It was, however, later found out that the electrons are more likely accelerated by upper hybrid turbulence [see *Leyser et al.*, 2000] instead of Langmuir turbulence. For example, if the pump-frequency is close to a multiple of the electron gyro-frequency, the optical emissions in 6300 Å and 5577 Å becomes very faint [*Kosch et al.*, 2002a] while the Langmuir turbulence is very strong. This is also consistent with results from tomographic inversion, which resulted in a too low altitude for Langmuir-turbulence. [*Leyser and Gustavsson*, 2003]

The most complete treatment of the observations from 16 February 1999 (so far) is presented in *Gustavsson et al.* [2001a]. This paper presents the first estimate of the volume distribution the HF pump-enhanced airglow emission obtained from a tomography-like analysis of the image data. Where data from three stations exists (17:40–17:56 UTC), the tomography-like inversion procedure gives reliable results [see *Gustavsson et al.*, 2001a, for details]. For periods with data from only two stations a stereoscopic triangulation method was employed to determine the position of the enhanced airglow region. In Figure 6.10 the result of the tomography-like inversion is presented. The shape of the excitation varies from prolate along the magnetic field to slightly oblate. Also, the existence of two separable regions is clearly seen in the figure. These results were validated by back-projecting images from the reconstructed volume and comparing them to the original images. Comparing the images [see *Gustavsson et al.*, 2001a] gives a typical maximum error of ±10%. Thin drifting clouds in Abisko as well as

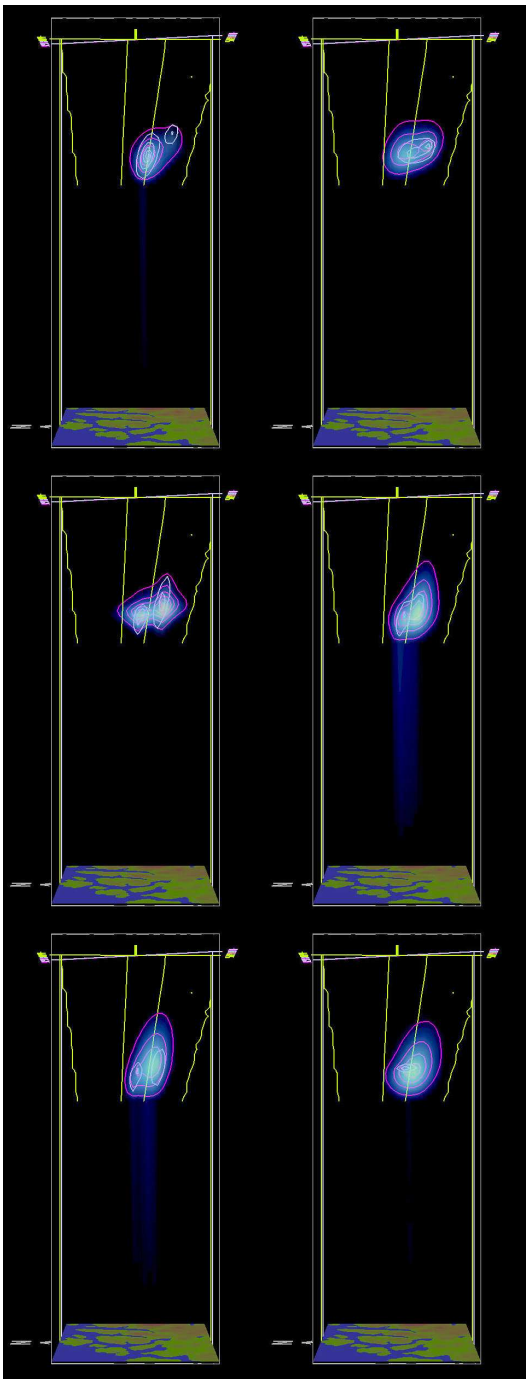

Figure 6.10: Volume rendering of the artificially enhanced airglow region above Tromsø, as seen from the west. The bottom plane shows the map of the Tromsø/Kiruna region. The yellow lines are the HF-pump 70% and 10% beam widths in the meriodonal plane, the purple and orange contours are the 6300 Å emission and the $O(^1D)$ excitation. UTC is (left→right top→ bottom) 17:32:50, 17:33:20, 17:33:50, 17:34:30, 17:34:50, 17:35:20. [After Plate 5 in *Gustavsson et al.*, 2001a]

uncertainties in the relative sensitivities (Chapter 4) of the cameras contribute to the errors.

There are significant differences between the two pulses, as shown by calculating the "centres of emission and excitation" (Figure 6.7). The north-eastward drift of the "centre of emission" agrees well with the FPI measurements of the neutral wind. These intensity variations and drift patterns indicate that the energy dissipation of the HF-pump wave depends on the background ionosphere.

Calculating the altitude-averaged lifetime according to *Bernhardt et al.* [1989] an effective lifetime of 25 ± 2 s is obtained during the pulses and 30 ± 2s for the first minute after the pumping. Applying these results, *Gustavsson et al.* [2001a] made a model-independent estimate of the altitude average excitation distribution according to *Bernhardt et al.* [1989] displaying a systematic pattern: initially a patchy structure appears, after 15–25 s the excitation grows in a smaller region, where the surrounding region either saturates or decreases, as shown in Figure 6.11. These results show how nicely multi-station spectroscopic imaging of HF pump-enhanced airglow can visualise the complexity and temporal evolution of the pump-ionosphere interaction. Clearly, many more experiments are needed to fully understand the underlying physics.

For periods with image data from only two stations, triangulation with manual identification of corresponding points was employed. This gave an estimate of the maximum emission altitude varying from 230–240 km at 17:32–18:08 UTC, but from the transmitter-on period starting at 18:12 UTC, the height was 250–260 km (Figure 6.6). A reasonable estimate of the error is ± 3 km. Periods with the largest spread in altitude (17:32, 18:04 UTC) occurred when a rise in altitude of the enhanced ion line was observed. The paper also contains a discussion of temporal and intensity variations and a section on theoretical airglow modelling.

From the analysis of the data-set from 16 February, in part summarised above, *Gustavsson et al.* [2001a] make a plausible claim that *the enhanced airglow is not excited by the high-energy tail of a purely Maxwellian electron distribution* and raise a number of questions:

- What physical processes control the complex drift pattern?
- What physical process controls the transition from the initial complex excitation structure?
- During what physical conditions can more than one region of strong $O(^1D)$ excitation coexist?

A brief summary of all results obtained hitherto, including some so far unpublished results, is provided in *Leyser et al.* [2002].

A recent publication [*Gustavsson et al.*, 2003] reports on the first nearly simultaneous observations of HF pump-enhanced airglow at $O(^1D)$ 6300 Å and $O(^1S)$ 5577 Å. These results were obtained during 21 February 1999 at 4.04 MHz, transmitting vertically with an ERP of 73 MW and an 8 minutes transmitter-on/off cycling period. ALIS station 5 in Abisko alternated between 5577 Å and 6300 Å during the same heater pulse. The regions of enhanced airglow are nearly identical, suggesting that the sources of the emissions are co-located in the ionospheric F-region. During the same transmitted pulse an estimated maximum

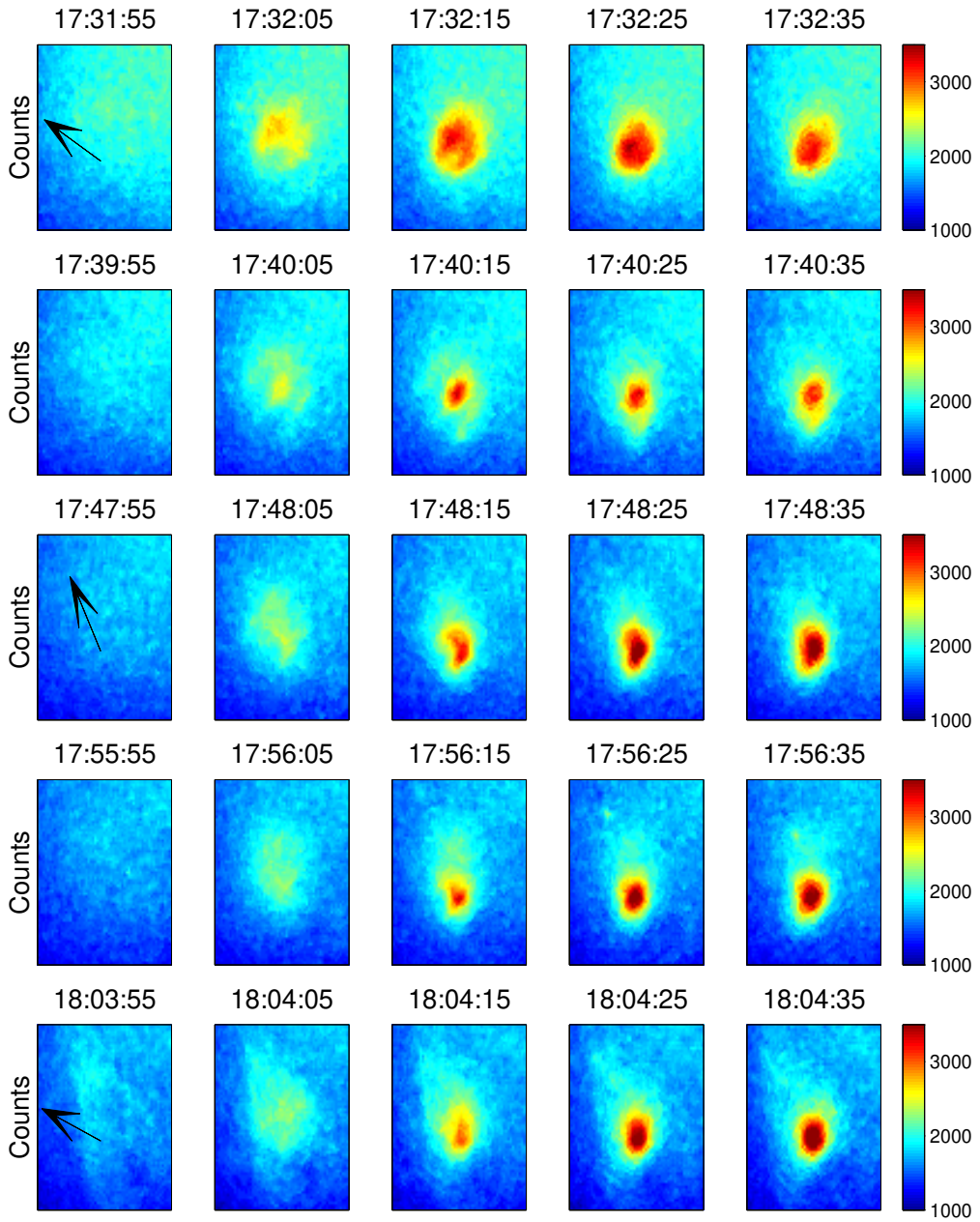

Figure 6.11: Estimates of the $O(^1D)$ excitation rates for the period just before transmitter-on and the four 10 s periods just after transmitter-on for five pulses. The arrows are the neutral wind direction projected to the images. All images are from the ALIS station in Silkkimuotka. [After Plate 7 in *Gustavsson et al.*, 2001a]

column emission rate of about 40–60 Rayleighs in 6300 Å and with a maximum column emission rate of about 10–20 Rayleighs in 5577 Å were observed. These preliminary results indicate that an intensity-ratio of 5577 Å and 6300 Å of about 0.3–0.4 implies that the excitation is caused by a non-thermal electron population. Previously obtained intensity ratios were 0.05–0.3 [*Haslett and Megill*, 1974], and 0.08 [*Bernhardt et al.*, 1989].

HF pump-enhanced airglow in the N_2^+ 1Neg. 4278 Å emission was observed in photometer data from 2001 by *Kaila* [2003b]. In March 2002 ALIS observed HF pump-enhanced airglow in N_2^+ 1Neg. 4278 Å. In this experiment the transmitted wave was stepped up and down in frequency through the third harmonic of the ionospheric electron gyro frequency. The airglow was simultaneously imaged with one CCD camera operated at 6300 Å by M. Kosch in Skibotn, and the mobile ALIS station (Section A.8) located at the same place. The ALIS camera recorded emissions in 5577 Å as the frequency was stepped downward through the gyro harmonic, and weaker 4278 Å emissions as the transmitted frequency was stepped up again. This is the first time that pump-enhanced ionisation of the thermosphere has been directly observed. Furthermore, the frequency dependence of the 4278 Å emission gives input to theoretical modelling of electron acceleration for HF-frequencies near the harmonics. It is important in future experiments to be able to reconstruct the volume distribution of the N_2^+ 1Neg. emission and compare with the volume distribution of for example $O(^1D)$ to study the role of the underlying plasma dynamics perpendicular and parallel to the geomagnetic field [*Leyser et al.*, 2002]. Therefore it is essential to obtain more multi-station measurements with ALIS in the future.

6.5 Auroral studies

Although ALIS was built for auroral observations, and consequently most of its observing time was spent on auroral observations, the amount of published scientific results in this field have been sparse. One explanation is that once the HF pump-enhanced airglow experiments proved successful, it was deemed far more productive for a small group to spend time publishing these results. Other contributing factors are the technical problems affecting the maximum framerate (Section 3.3.4). Furthermore, as ALIS is a new type of instrument, much remains to be learned about how to exploit it in the optimal way. The amount of data is also somewhat limited as auroral studies often are dependent on a variety of coordinated observations with other instruments.

When planning coordinated studies with satellites as well as ground-based radars and optical instruments, many criteria need to be fulfilled; near new-moon, clear skies, the satellite magnetic footprint needs to be reasonably close to the ground-based instruments, radar observing-time needs to be applied for and scheduled [*Hedin et al.*, 1999]. Furthermore, the probability of observing the desired auroral phenomena must be maximised for the ground-based sites taking part in the study. For campaigns involving satellite passes, slow magnetic midnight passes are optimal. Yet, fulfilling all of these criteria for a successful observation might take a very long time. Therefore patience, long-term stability and flexibility in changing the scientific objectives are key-issues. An auroral

event cannot be made to occur at the desired time or place to fit a particular measurement. However, well-planned observations will increase the probability of making useful observations. In this section some of the results related to auroral studies are summarised.

6.5.1 An estimate of the auroral electron spectra

One of the traditional emission lines of choice for monochromatic auroral imaging is the $O(^1D)$ 6300 Å emission line [*Solomon et al.*, 1988; *Meier et al.*, 1989]. However, the excitation mechanism of that line is still under some debate [*Meier et al.*, 1989]. As the excited $O(^1D)$ state is quenched at lower altitudes, the ratios of the column emission rates for the $O(^1D)$ 6300 Å and N_2^+ 1Neg. 4278 Å emission-lines have been taken as an indicator of the characteristic energies of the precipitating electrons. The long radiative lifetime of the $O(^1D)$ 6300 Å emission line makes comparisons with the rapid N_2^+ 1Neg. 4278 Å and $O(^1S)$ 5577 Å emission-lines difficult, particularly for active auroral events.

In 1996 the first ALIS station was equipped with filters for the $O(3p^3P)$ 8446 Å emission line. Initial observations confirmed a sufficient signal strength for the ALIS-Imagers, and subsequently all stations were equipped with filters for this emission-line.

A preliminary study [*Steen et al.*, 1999a] presents data from 25 March 1998. Two ALIS stations (Kiruna and Merasjärvi) provided data from an auroral event occurring at the end of a geomagnetically disturbed period. An eastward travelling fold similar to that described by *Steen et al.* [1988] first appeared in the west and traversed the Kiruna zenith at about 1000 m/s as estimated from all-sky images. After that, the arc broke up and was replaced by a diffuse auroral band. The fold was observed in $O(^1D)$ 6300 Å, $O(^1S)$ 5577 Å, N_2^+ 1Neg. 4278 Å, and $O(3p^3P)$ 8446 Å. The observed fold appeared almost identical in all emission-lines, except, as expected in the slow $O(^1D)$ emission. This initial study concluded that the $O(3p^3P)$ 8446 Å auroral morphology appears similar to that of N_2^+ 1Neg. 4278 Å.

In a more extensive study [*Gustavsson et al.*, 2001b], two methods for estimating characteristics of primary electron spectra are compared and used to describe the auroral event of 25 March 1998. One method uses the spectral information in the images (Figure 6.12), while the other method is based on an inversion of the N_2^+ 1Neg. 4278 Å altitude distribution. Using the second method, ALIS can currently give estimates of the primary electron distribution with a time resolution of about 10 s (Figure 6.13). The paper concludes that only two dimensional measurements are able to follow the dynamics of this type of event, as single-point measurements cannot distinguish between temporal and spatial variations. Estimating the characteristic energy of precipitating electrons by combining measurements in 4278 Å, 6300 Å and 8446 Å provides useful results for temporal variations slower than 100 s. The primary electron spectra retrieved from the altitude distribution of the N_2^+ 1Neg. 4278 Å emission can give estimates of the electron characteristics with 10 s time resolution, but only for discrete auroral structures. To fully exploit the information obtainable from these kind of observations requires a combination of spectral and spatial analysis and to compare the results with two-dimensional electron transport and ionospheric models.

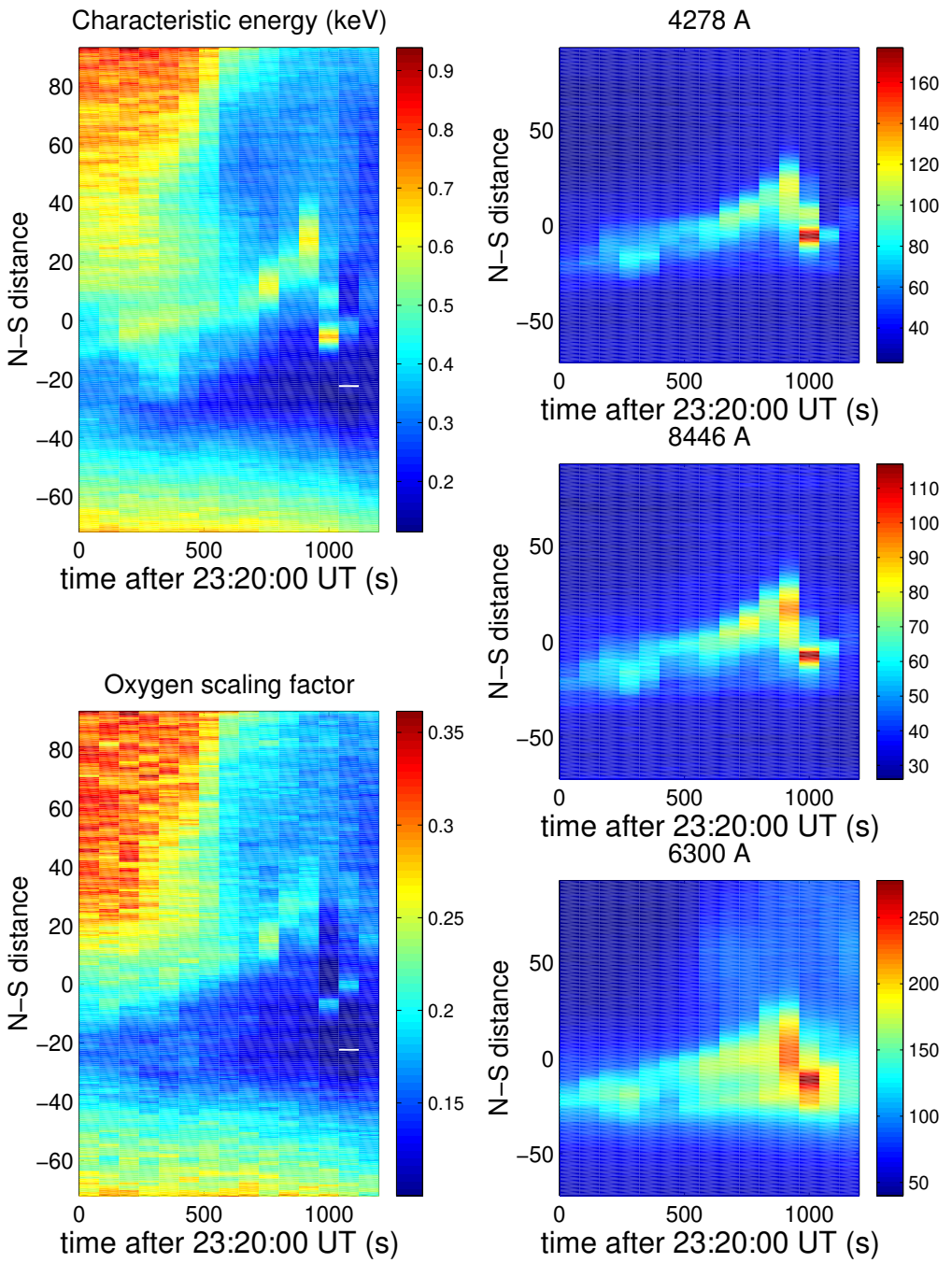

Figure 6.12: The right column displays meridional cuts through images from the Kiruna ALIS station. These "keograms" are projected to an altitude of 120 km and the axes are in km relative to Kiruna. As can be seen the arcs drift slowly northward while brightening. After 900 ± 10 s a fold sweeps eastward and the arc rapidly moves south and fades. The left columns shows characteristic energy (top) and oxygen scaling factor (bottom) as calculated from the spectroscopic ratios of I_{8446}/I_{4278} and I_{6300}/I_{4278}. [After Figure 6 in *Gustavsson et al.*, 2001b]

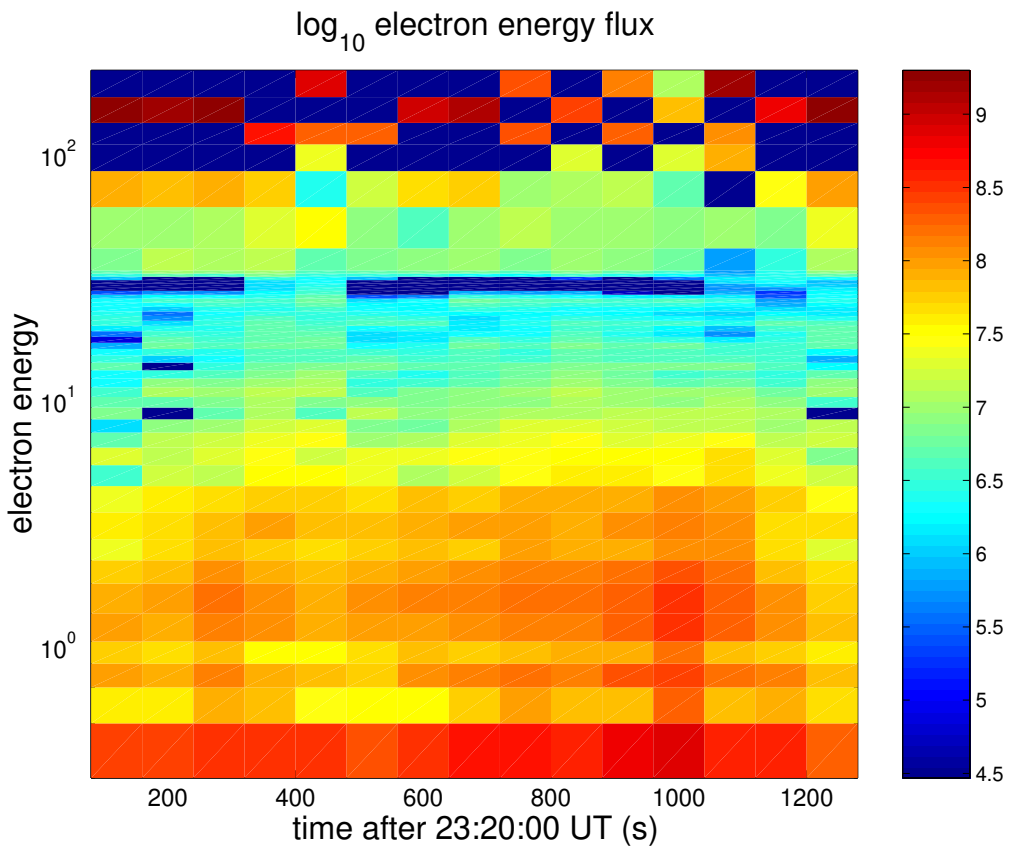

Figure 6.13: An estimation of the energy flux by inversion of N_2^+ 1Neg. 4278 Å altitude distribution. About 400 s after 23:20:00 UTC there appears to be a slight increase in both total flux and typical energy. [After Figure 6 in *Gustavsson et al.*, 2001b]

6.5.2 Coordinated observations with satellite and radar

During 7, 8 and 16 February 1997, ALIS, a five-channel, meridian scanning photometer [*Kaila*, 2003c], and EISCAT performed simultaneous observations during several auroral events when the FAST satellite [*Carlson*, 1992] passed in orbits with close magnetic projections to the ground-based instruments.

A preliminary collection of data from these observations was presented by *Brändström et al.* [1997a]. Later these events were also discussed by *Andersson* [2000, Chapter 4] A recent, more comprehensive study is in the preparation-phase, as briefly outlined below from an abstract by *Sergienko* [2003].

On 16 February 1997 the FAST satellite passed through the auroral oval over Northern Scandinavia one hour before a local substorm onset. The magnetic projection of the satellite orbit was within the field-of-view of ALIS. Given the high temporal resolution of FAST particle detectors combined with the sensitivity and spatial resolution of ALIS, studies of fine auroral structures became an interesting possibility. The FAST electron spectrogram displays three well-defined regions with clear borders between them. The most polarward region is a multiple inverted-V structure with an electron characteristic energy of 3–5 keV, while the middle region is characterised by homogeneous Maxwellian electron spectra with a characteristic energy of about 3.5 keV. Chaotic, weak fluctuations in the precipitating electron energy flux are also observed. The third, most equatorward region, involves two different populations of electrons. The first of them is an extension of the particles from the second region while the other population consists of energetic electrons (about 10 keV) with a perceptible periodic structure in the precipitating part of the particle flux.

The auroral data from ALIS correlate nicely with the electron spectrum peculiarities, as observed by FAST. The most poleward region of the electron spectra corresponds to the bright auroral arcs moving towards the equator, while the second part of the electron spectra conjugates with a region where the short-lived auroral rays and small patches appear chaotic against the weak diffuse background. In the equatorward parts of the auroral images, a very regular spatial luminosity structure, consisting of thin and weak auroral stripes is seen. A sample image of the auroral situation during the FAST pass at 20:10:00 UTC appears in Figure 6.14.

Calculations of the emission intensities with an auroral 5577 Å emission model using the measured electron spectra have given a good quantitative agreement between the structured high energy electrons and the auroral stripes. The stripes stretch along the geomagnetic latitudes, have a width less than 2 km, and are separated by the background luminosity by approximately the same distance. The intensities of the stripes vary in longitude and with time, but their positions do not change in latitude, at least not during the 15 minute observation by ALIS. Possible formation mechanisms for the regular striped auroral structures will be discussed in another publication in preparation [*Sergienko*, 2003]

6.5.3 Auroral vorticity

The east-west elongated auroral arc is frequently destroyed by an instability process involving the development of a series of vortex structures of various scales.

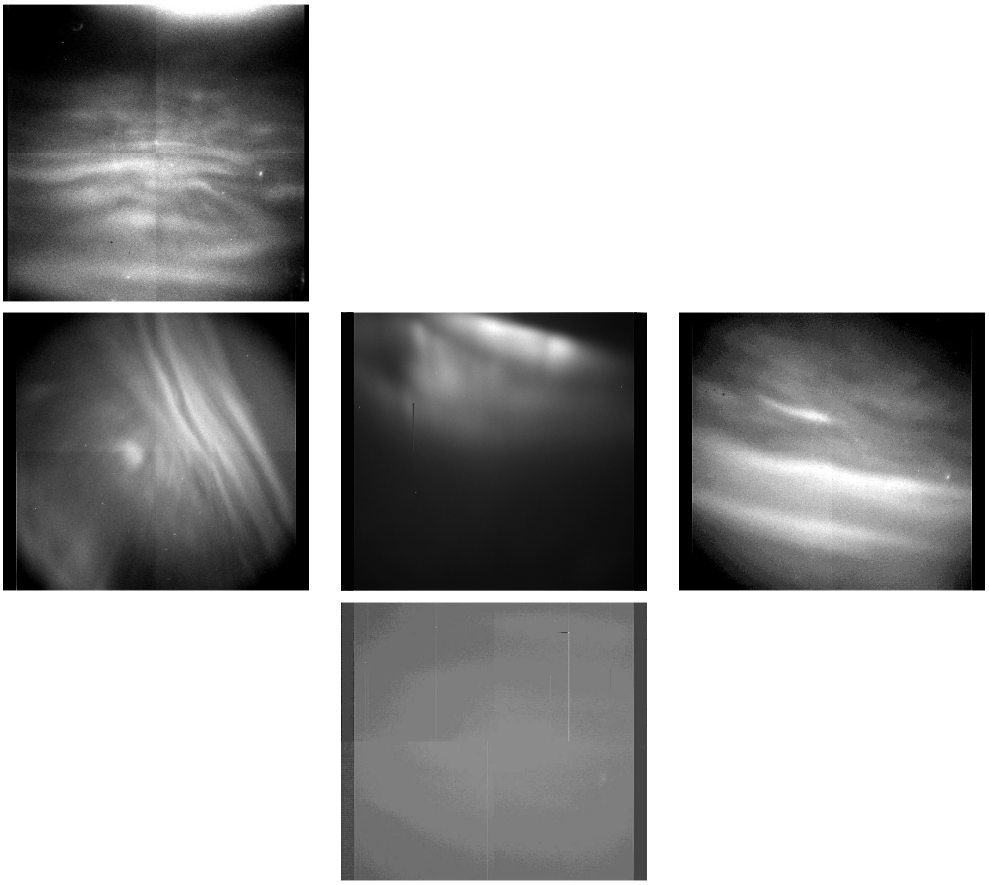

Figure 6.14: Example auroral images from 16 February 1997 during the FAST pass at 20:10:00 UTC; Abisko (top left), Nikkaluokta (middle-left), Kiruna (middle), Silkkimuotka (middle-right and Tjautjas (bottom). All images are in 5577 Å and with $t_{int} = 2$ s. The orientation of the Kiruna imager is $a_\phi = 0°$ and $z_\theta = 40°$. Nikkaluokta had no CPS at this time (hence the rotation) and was imaging zenith. The remaining stations are in the magnetic zenith position ($a_\phi = 180°$ $z_\theta = 12°$).

Vorticity, ζ, is the measure of rotation in a fluid, $\zeta = \nabla \times \mathbf{u}$ (where $\mathbf{u}$ is the fluid velocity). *Pudovkin et al.* [1997] published a theoretical and experimental review of data connected with vorticity in the magnetospheric plasma and on its signatures in the auroral dynamics. Early ALIS images were used in this paper to exemplify what can be learned from studying vortex structures in the aurora. Such studies can yield an abundant information on the physical state of the magnetospheric plasma as well as the processes developing in it. For example, by observing auroral forms with high temporal and spatial resolution, it is possible to determine the distribution of the electric field and field-aligned currents in the magnetosphere. The shape of auroral vortices, carry information on the nature of the Magnetohydrodynamical (MHD) instabilities responsible for the excitation of the observed turbulence. Subsequent experimental work by for example *Trondsen* [1998, and references therein] is an excellent example of research in this field. Due to technical problems affecting the maximum achievable temporal resolution (Section 3.3.4), ALIS has not been perfectly suited to continue studies in this field.

6.5.4 Studies of the ionospheric trough

An example showing that ALIS sometimes can provide usable supporting measurements, even when not operated in a scientific mode is presented by *Hedin et al.* [1999, 2000]. In this study of the main ionospheric trough, all the EISCAT radars were for the first time operated in a four-beam configuration close to the meridian plane in order to obtain a wide area of observation without the loss of temporal resolution [*Hedin et al.*, 2000]. This combined "meta-radar" has a huge fan-like observation area, of about 70°N–80°N in geographic latitude [*Hedin et al.*, 2000]. Supporting measurements were provided by the FAST satellite and ALIS. During the night of 14 March 1997, ALIS was only operated occasionally since there were no significant aurora, and the conditions at some stations were partly cloudy. The images were obtained randomly in order to check cloud conditions etc. However, some images happened to be acquired at relevant times for the trough study, displaying faint, diffuse auroral structures around the time when the trough poleward boundary passed over the field-of-view of ALIS. The position of the diffuse aurora obtained from ALIS was consistent with extrapolated data from the more direct measurements by EISCAT [*Hedin et al.*, 2000]. This observation of the trough was found to be typical as it had all the common features as compared to earlier studies. Calculations of the apparent southward motion of the trough were consistent with it having an oval shape. The trough was seen to be wider towards magnetic midnight. The paper concludes by stating that "the earlier proposed linear equations for trough motions are shown not to be valid over the latitude range in question".

6.5.5 Daytime auroral imaging

The problem of isolating atmospheric airglow and auroral emissions from scattered sunlight has been solved in a number of ground-based experiments, such as: *Noxon and Goody* [1962]; *Bens et al.* [1965]; *Barmore* [1977]; *Cocks et al.* [1980]; *Conde and Jacka* [1989]; *Conde et al.* [1992].

Normally measurements with ALIS stop for the season around 15 April, and operations resume in late August or early September. This is because the bright summer nights at arctic latitudes prevent ALIS from performing low-light measurements. However, some experiments have been made to try to image the aurora from ground even during this off-season. In this case the normal ALIS imagers (Chapter 3) are not usable, instead the camera head was dismantled and used together with a prototype imaging spectrometer for daylight auroral imaging. The main part of this new imaging instrument was an imaging optical spectrometer based on two 50 mm diameter capacitance-stabilised Fabry-Perot etalons [*Rees et al.*, 1981; *McWhirter*, 1993; *Rees et al.*, 1996, 1999] placed directly in series with each other and with a narrow-band (2 Å) interference filter. In front of this a wide-angle (35 mm) lens with telecentric optics was mounted. The output image consisting of interference fringes was imaged by a 300 mm lens onto a CCD camera-head from an ALIS-Imager (Chapter 3) operated with 2×2 on-chip binning. The spectrometer had a wavelength bandwidth of 3.7 pm [*Rees et al.*, 2000]. Since two capacitance-stabilised etalons were used, it was possible to tune the spectrometer by varying the optical path-differences of both etalons, placing the narrow annulus corresponding to 6300 Å emission line at any radius within the image. By scanning the position of the 6300 Å annulus and taking ten successive images at each scan position, it was possible to construct a two-dimensional sky-image at 6300 Å (Figure 6.15). This image was the main accomplishment over earlier studies. In this initial work a suitably-normalised previously published [*Delbouille et al.*, 1973] solar spectrum was subtracted since no suitable arrangement for measuring the solar spectrum across the entire image was present for the prototype instrument. Due to this, the intensities of the 6300 Å emission line were only roughly estimated, so neither useful Doppler-shifts (corresponding to wind) nor line-widths (corresponding to temperature) could be extracted.

With modest modifications, this instrument could be used to make optical auroral observations under all day-time solar illumination conditions, albeit with low temporal resolution.

6.5.6 The relation between the thermospheric neutral wind and auroral events

The thermosphere and ionosphere are coupled to the magnetosphere via electric fields and field-aligned currents [*Aruliah et al.*, 1996]. Intensification of the aurora is found to be related to rapid variations in the thermospheric neutral wind on a time scale that excludes contribution from the ion-drag force [*Steen and Collis*, 1988]. Instead the neutral wind variations must be understood in the context of large-scale coupling between the ionosphere and magnetosphere. ALIS can provide high resolution auroral images, that combined with neutral wind vector fields obtained by Fabry-Perot interferometer measurements can yield a better understanding of the relation between the thermospheric neutral-wind and the aurora.

Measurements of the F-region neutral wind using Fabry-Perot interferometers have been carried out in Kiruna since the early 1980's in collaboration with groups in the U.K. [*Aruliah et al.*, 1996]. In 1997, two scanning mirror Fabry-Perot interferometers were operated in collaboration with the Atmospheric Physics Laborat-

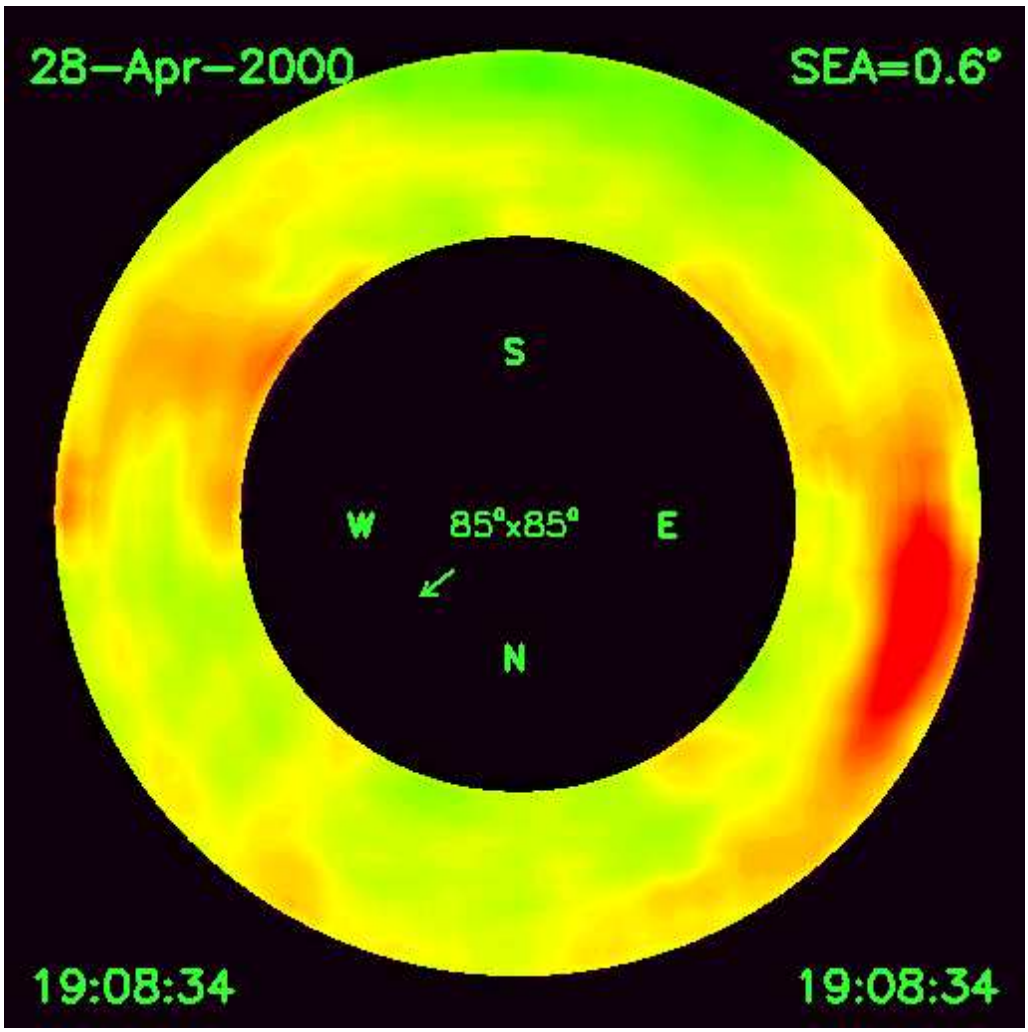

Figure 6.15: Daytime auroral image in 6300 Å acquired on April 28, 2000 at 19:08:34 UTC. The solar elevation angle was 0.6°. Bright features of the $O(^1D)$ 6300 Å emission-line are seen in north-east as well as in south-west. (Courtesy of David Rees)

ory at University College London [*McWhirter*, 1993; *Aruliah et al.*, 1996], as well as one Doppler Imaging System (DIS) [*Rees et al.*, 1997] in collaboration with Utah State University and Hovemere Ltd. In a preliminary study [*Brändström et al.*, 1997b] data from the latter instrument was compared to auroral images obtained from ALIS. The Doppler Imaging System (DIS) used in Kiruna consists of an all-sky lens, an interference filter for the 6300Å airglow/auroral emission and a Fabry-Perot etalon. The resulting interference fringes are imaged by an intensified Peltier-cooled CCD camera. In the subsequent analysis, each of the six interference fringes are divided into 24 sectors for which the Doppler shift of the input signal is calculated. Each sector thus corresponds to the Doppler-shift in a certain region of the sky, making it possible to 'image' the neutral wind velocity.

During the winter of 1996/1997 events with conjugate all-sky, ALIS and DIS observations were collected. Events when there was clear sky, auroral activity and preferably discrete auroral forms with a strong signal in the $O(^1D)$ 6300 Å emission line were selected. A collection of data from 10 January 1997 was described by *Brändström et al.* [1997b]. (Other promising events also exist for example 7–9 February 1997). When a stable arc was seen, the neutral wind was mainly northward. Preliminary analysis of the dataset suggests that the wind is directed perpendicular to the arc, with very low wind speeds parallel to the arc. This observation is supported by observations from 10 January. Another interesting feature in the data is the apparent westward drift of diffuse auroral structures at the same time as the wind turns eastward around 19:30 UTC. However these results are to be considered only as a demonstration of measurement possibilities. These studies have not been followed up so far.

6.6 Other studies

6.6.1 Polar stratospheric clouds

ALIS was optimised for studies of auroral phenomena at altitudes ranging from 90–300 km (Chapter 2). Despite this, it was realised early [*Steen*, 1989; *Steen et al.*, 1990] that ALIS might also be useful for the study of PSCs. Such clouds occur when regions of liquid or solid aerosols form in the altitude range of 15–30 km due to the low stratospheric temperatures that can be reached during the polar night in Arctic and Antarctic polar vortex combined with the additional rapid cooling caused by lee-waves [for example *Hesstvedt*, 1960; *Toon et al.*, 1986; *Crutzen and Arnold*, 1986; *Tolbert*, 1996, and references therein]. PSCs have been observed for more than a hundred years and *Mohn* [1893] attempted to make an altitude estimation by visual observations but arrived at uncertain results (23–100 km). One of the first accurate measurements of PSC altitude was performed by *Størmer* [1930], using photographic triangulation techniques. The presence of stratospheric clouds causes increased stratospheric ozone depletion [*Solomon et al.*, 1986] and because of this, the interest in PSC studies increased at the end of the last century.

ALIS is used to detect the appearance of PSCs and also to obtain temporal variation in the 3D distribution of the cloud surfaces. In 1997 ALIS made PSC observations, presenting a temporal development of the two-dimensional altitude

distribution during three events, 9, 11 and 16 January 1997 [*Steen et al.*, 1997b]. Measurement techniques and the derivation of a composite colour image (derived from three images obtained with narrow-band interference filters for the three main auroral lines 6300 Å, 5577 Å and 4278 Å) are presented in *Steen et al.* [1999b] and *Enell et al.* [1999c]. According to *Steen et al.* [1999b] "it would, at least in principle be possible to invert the particle size distribution in the PSC by measuring the absolute colour variation, 3-D surface location, wind parameters and temperature, using an optical transport model". *Enell et al.* [1999b] states that, in certain cases, it might be possible to retrieve the particle size distribution in a section across the PSC from narrow-band images in several wavelengths. An example of time development of an altitude contour of PSC cloud-bases calculated by triangulation was also presented in this paper.

A feasibility study regarding the use of multi-station imaging systems for studies of PSC physics was presented by *Enell et al.* [2000], proposing a method to solve for particle sizes using bistatic multi-wavelength observations. As it has not yet been possible to apply this method to real measurements, numerical simulations for an ideal case (single scattering, spherical particles) work with reasonable results, even if random noise is added. Despite these positive results, a major complication is that light is scattered not only from the cloud particles, but also from the entire atmospheric column observed. A background correction, assuming a smoothly varying atmospheric background must therefore be applied. An example of a background correction by quad-tree decomposition is discussed by *Enell et al.* [1999a]. Should this method prove to be practically applicable, an important issue might be to determine the probability that actual PSC incidence gives rise to visually observable mother-of-pearl clouds, for example for interpretation of historical reports of PSC sightings. Such studies would be of interest for modellers of atmospheric chemistry and radiative transfer.

Enell et al. [2003] presented a case study of the development of visible PSCs observed by ALIS. The paper concerns automatic and manual altitude determination of PSC observations made on 9 January 1997 from two ALIS stations (Figure 6.16). It is shown that semi-automatic detection of stratospheric clouds is possible, and that short-term dynamics such as altitude variations can be tracked. The PSCs, observed during twilight, were found to be moving within a stationary sloping surface, and some evidence was provided that they were lee-wave induced. *Enell et al.* [2003] suggests that in future studies "it would be desirable to image PSC with polarisation-sensitive devices in order to characterise the scattered light with a full set of Stokes parameters at different wavelengths. This might be a way to yield information about the particle shapes as well as the nature of the multiple scattered light illuminating the PSCs." Furthermore, imaging of PSCs under different conditions, i.e. direct or scattered sunlight, moon-light, and even extinction of starlight, deserves further experimental investigations. The PSC events summarised here were published by *Enell* [2002]. This work constitutes the main reference for PSC observations with ALIS.

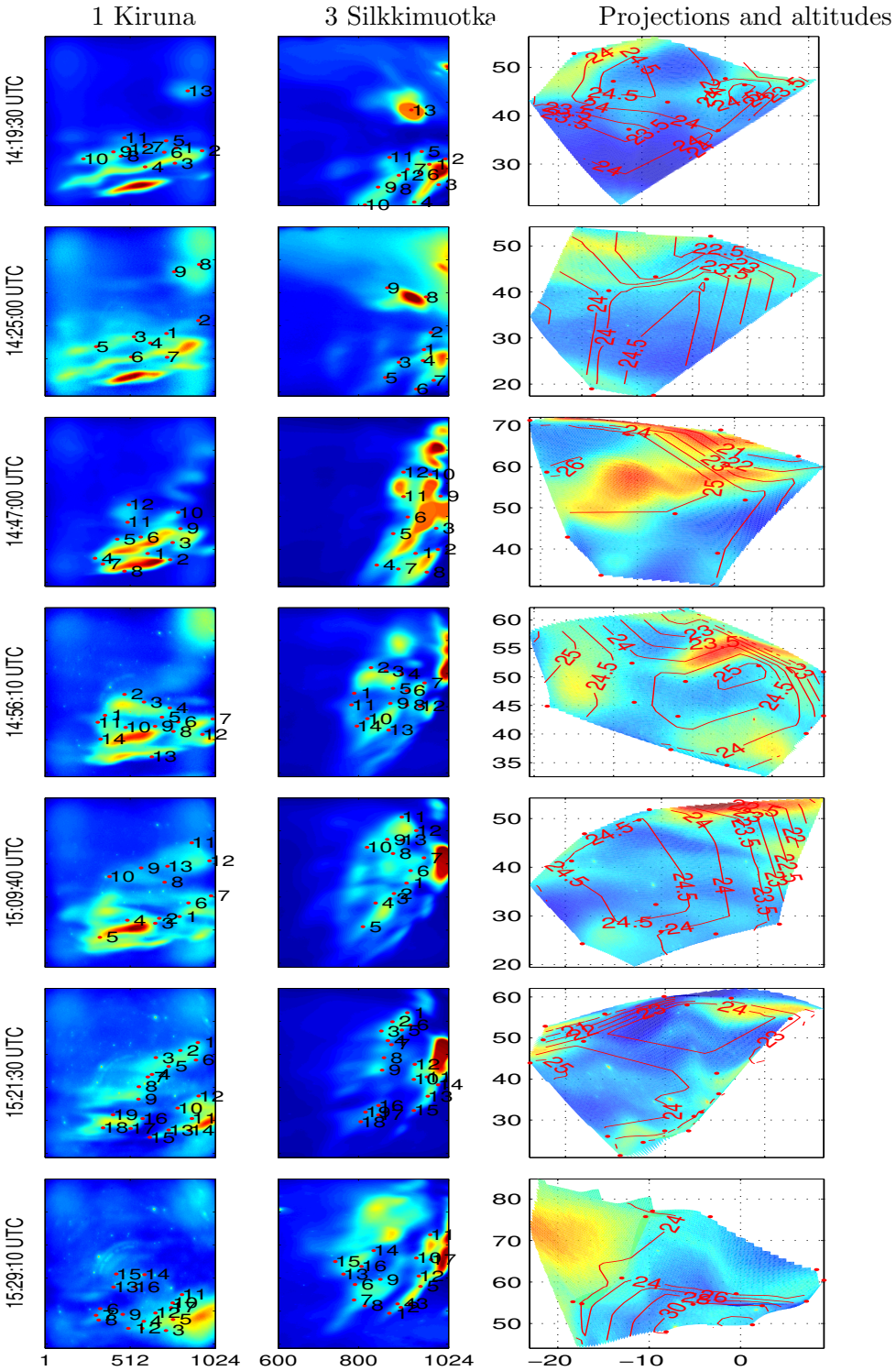

Figure 6.16: Columns 1 and 2: Time series of images (from Kiruna and Silkkimuotka, respectively) with identified PSC points (the colour-scales show the pixel values in 10^4 A/D counts after background subtraction). Rows 1-1024 and columns according to the abscissae are shown. Column 3: Contour surfaces of altitudes [km] spanned by these points, superimposed on projections of the images from station 1. The axes show W-E and N-S distances in kilometres from Kiruna. [After *Enell et al.*, 2003])

6.6.2 Astronomical applications — water in a Leonid?

Vi missade på Mars, kom ur dess bana
och för att undgå fältet Jupiter
vi lade oss på kurvan ICE-tolv
i Magdalenafältets yttre ring,
men mötte stora mängder leonider
och väjde vidare mot Yko-nio.
Vid fältet Sari-sexton uppgav vi försöken
att vända om.

Harry Martinsson, Aniara

Early on it was realised that ALIS might be usable for spectroscopic studies of certain astronomical objects, such as comets and meteoroids ejected from comets. Images were acquired of both the Hyakutake and Hale-Bopp comets, however none of these data-sets have yet been analysed.

Meteor showers are one of few processes taking place above the troposphere that are observable by the naked eye. This influx of extraterrestrial matter to Earth, on the order of 100 tons per day [*Love and Brownlee*, 1993] gives rise to the permanent layer of metal atoms in the 80–110 km altitude region [*Höffner and von Zahn*, 1999]. The study of these phenomena has important implications with respect to irregularities in long range radio communications, sporadic E-layers, as well as the survivability of artificial satellites, etc.

Modelling studies [*McNeil et al.*, 1995, 2001] combined with LIDAR observations [*Höffner and von Zahn*, 1999; *von Zahn et al.*, 1999] as well as observations by the GLO-1 instrument on the space-shuttle [*Gardner et al.*, 1999] have yielded significant new information on the mechanisms involved in the formation of meteor-trails and their properties.

When cosmic dust particles enters the Earth's atmosphere, heating and ablation of the material causes deposition of metals at altitudes between 80 and 110 km. As the atmospheric density increases exponentially along the particle trajectory, the ablation increases with decreasing altitude. On the other hand, due to atmospheric friction, the particle eventually reaches its terminal velocity, corresponding to a temperature lower than that needed for ablation to take place. Particle mass and particle velocity determine the altitude at which ablation takes place. Given high enough velocity (about 30 km/s) a particle ablates completely, otherwise parts of the material fall to ground unablated [*McNeil et al.*, 1998]. In essence this means that different elements are released from the meteor at different times, as demonstrated by *von Zahn et al.* [1999] using ground-based LIDARs.

ALIS could be used to study such differential ablation phenomena in meteor trails. The easiest meteoroid constituents to observe are the quite common sodium (Na) and calcium (Ca). These elements have strong emission lines at 5893 Å and 4227 Å [*Ceplecha and Rajchl*, 1963]. The evaporation is a temperature-dependent process for the different constituents. According to the differential ablation model there is a distinct altitude difference of several kilometres for the sodium and calcium deposition distributions. This should be quite easily seen with two or more ALIS stations equipped with the proper filters, especially for slow meteors. However, there are other practical problems concerning observa-

tions of this type. A meteor is most often seen during a short interval of just one second or less, and this must occur while the shutter is open. To maximise the possibility of acquiring an image of a meteor-trail, the stations should be operated with overlapping exposures, so that there are always at least two imagers with open shutters. In this way simultaneous imaging from up to six stations might occur, so that the altitude distribution of the meteor trails could be triangulated, while some stations simultaneously image the trails in the rather strong sodium (5893 Å) and calcium (4227 Å) emission lines [*Ceplecha and Rajchl*, 1963].

In a simulated study [*Brändström et al.*, 2001a] it was suggested that ALIS would operate with all six stations. The imagers would be oriented to observe a common volume, in order to enable triangulation of altitudes. The CCD-detectors are operated in maximum resolution mode (1024×1024 pixels) and with the longest possible integration times without saturating the CCD (on the order of several minutes). The dynamics is recorded by quickly opening and closing the shutter, with a period of 50 ms. (In principle this should be possible, but there are still some technical problems to be solved. Another option is to install a separate "meteor-shutter".) Performing the observations in this way increases the probability of observing a meteor and gives the possibility to study the velocities of a particular meteor at different altitudes.

In order to attempt experiments involving meteor observations, two filters with suitable passbands were procured (Table 6.5).

λ_{cw} [Å]	$\Delta\lambda$ [Å]	corr. passband [Å]	usage
4227	280	4087–4356	Covering Ca I and Fe I emission-lines [*Ceplecha and Rajchl*, 1963] as well as a water band around 4230 Å [*Dressler et al.*, 1992]
5893	200	5793–5978	Covering Na emission-lines at 5893 Å [*Ceplecha and Rajchl*, 1963]

Table 6.5: Filters for meteor studies. The table gives centre wavelengths, filter bandwidth, corrected passband and emission lines of interest.

Some preliminary studies were carried out during the Leonid showers of 1996 (without the meteor filters), 1999, 2000 and 2001. These observations yielded no usable results mainly due to bad weather conditions, although, important knowledge about how to perform an observation of this type was gained. The main objective with these experimental observations was to try to observe a predicted differential ablation process.

Successful observations of a meteor trail using two adjacent ALIS stations (Kiruna, and the mobile station) were obtained on 19 November 2002, at 03:48 UTC. The observed Leonid probably originated from the population ejected from the comet 55P/Tempel-Tuttle in 1767 according to the dust-trail simulations and observations by *McNaught and Asher* [1999]. Consequently this meteoroid was on its 7th period around the sun and still quite young in the sense that it had not lost much of its volatile constituents. Four images of this meteor trail appear

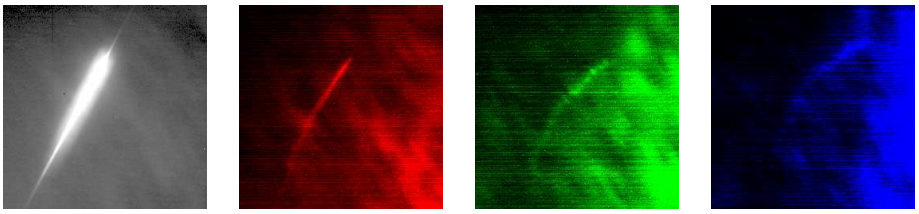

Figure 6.17: Portions of ALIS raw-data images of a meteor trail acquired on November 19, 2002. From left to right: (1) A 20 s exposure starting at 03:48:00 UTC in 4227 Å. (2) 10 s exposure at 03:48:00 UTC in 5893 Å (3) Same filter and integration time, but exposed at 03:48:30 UTC and (3) at 03:49:00 UTC. The false colours correspond to the colours in Figure 6.18

in Figure 6.17.

In Figure 6.18 projected altitude profiles for the images in Figure 6.17 appear.

Figure 6.19 shows the meteor-trail projected in altitude versus horizontal distance scale as observed through the two filters and with intensity profiles for both wavelengths. The relatively high intensity, the length of the trail as well as the short life time of the 4227 Å component were unexplained from the beginning. The 5893 Å component was seen in three consecutive images ranging over 1.5 minutes while the strong 4227 Å emission line was seen only within one 20 seconds exposure. The 4227 Å echo became visible already from 160 km altitude while the other one appeared at about 130 km altitude.

Similar optical observations of high-altitude Leonids have been reported from 1998 Leonids by *Spurny et al.* [2000] and there is still no good explanation for them. While their observations were made in white light, the rather wide passband of the filter used for the ALIS-observations might provide a hint as to a possible origin of these unusual high and bright Leonids. The 280 Å bandwidth of the 4227 Å filter corresponds to a corrected passband of about 4077 Å to 4356 Å (Equation 3.45). *Dressler et al.* [1992] report luminescence measurements of $N_2^+ + H_2O$ supra-thermal charge transfer collisions and have measured hydrogen atom Balmer series and N_2^+ emissions at high energies overlapping the passband of the ALIS observations. This observation can thus restrict the origin of these high-altitude meteors to one possible explanation. The water is still bound to some minerals in these young meteors. By reaching temperatures of above 1500 K which occurs already at about 130 km altitude in the meteor impact process, the water is suddenly released in a fast and bright process.

This explanation was found in March 2003. Therefore the value of observing water from meteoroides, cannot yet be evaluated, especially in the perspective of the present observing instrument ALIS. The analysis of this case continues and a manuscript is in preparation [*Pellinen-Wannberg et al.*, 2003].

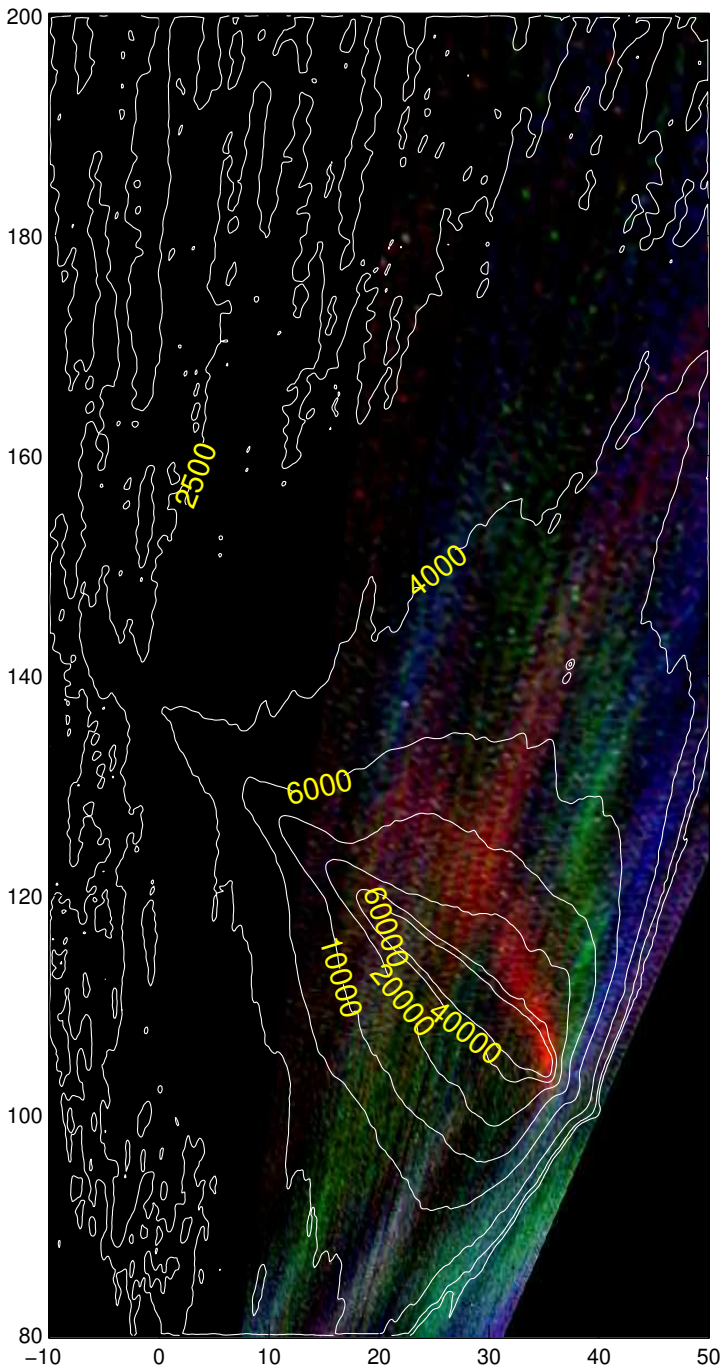

Figure 6.18: Projected altitude-profile of the raw-data in Figure 6.17. The iso-intensity lines corresponds to the 4227 Å image. The red, green and blue colours correspond to the three images in 5893 Å. It is possible to see how the Na emission in the meteor trail drifts with time from 03:48:00 UTC until 03:49:00 UTC.

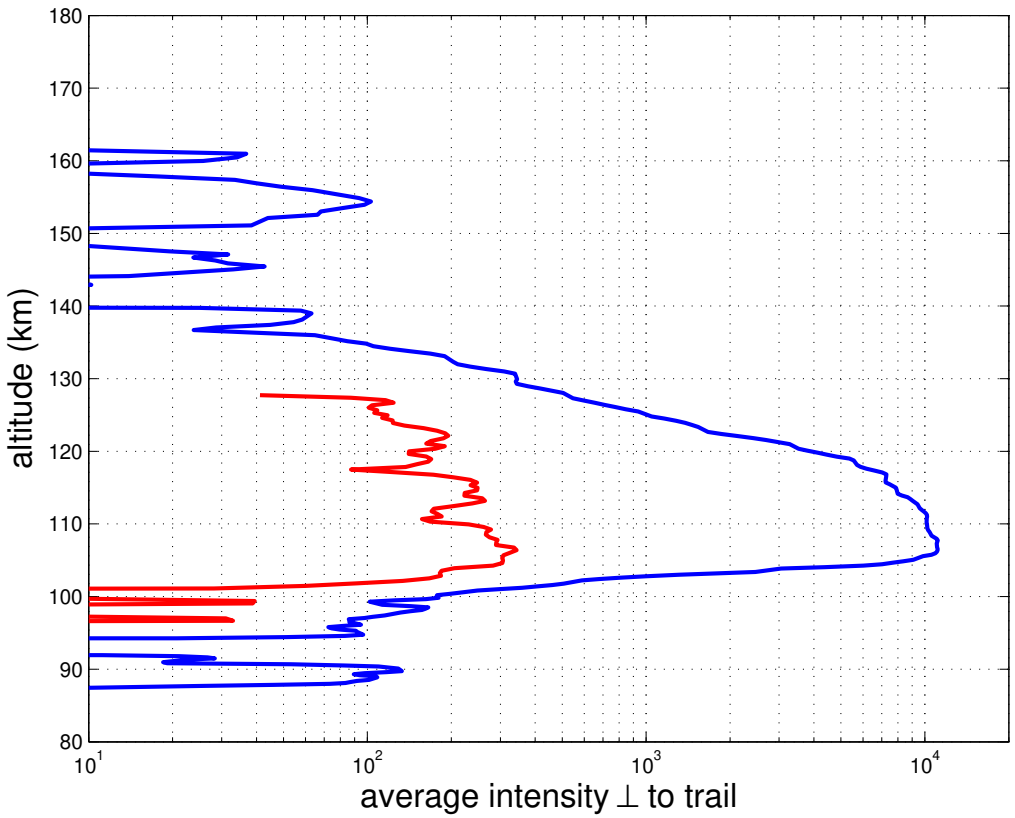

Figure 6.19: Altitude vs. average intensity perpendicular to the meteor trail in 5893 Å (red) and 4227 Å (blue). Note that the image in 4227 Å was saturated causing a cropping of the peak intensity, despite this, the altitude of the maximum intensity should be correctly estimated.

Chapter 7

Concluding remarks

> "Cur invideamus posteritati nostris laboribus frui?
> Majori laudi ducteur Seculo nostro observationes veras ad posteritatis memoriam transmisisse, quam falsas & facile refellendas hypotheses.
> Utinam priora Secula rerum naturalium experientias potius, quam varias opiniones nobis reliquissent!" *Celsius [1733]*

This report has attempted to provide a thorough documentation of the ALIS-project. Naturally, the focus of this work has been on the design, operation and calibration of the instrument, as this has been the main occupation of this author for more than one decade. Apart from ALIS, which provides imaging spectroscopic absolute-measurements of column emission rates, there has been some work carried out related to colour imaging of aurora, as is briefly described in Appendix C.

Since April 2001, only occasional campaigns related to the study of HF pump-enhanced airglow have been carried out with 1–2 stations that were operated manually. As there has recently emerged increased interest in a more extensive operation of ALIS, an outline of the required actions, as well as some ideas for the future appear in Appendix D.

Chapter 6 provided a survey of the versatile scientific applications of a multi-station low-light imaging system such as ALIS. Although many results already have been obtained, scientific questions that have arisen from this work require further analysis of existing data-sets as well as new measurements.

At present, the scientific highlights from ALIS include the first unambiguous observations of HF-pump enhanced aurora [*Brändström et al.*, 1999] and the first tomographic estimate of volume distribution of HF-pump enhanced airglow emissions [*Gustavsson et al.*, 2001a]. The task of following up some of the new scientific questions raised by these observations would alone motivate the continued operation of ALIS for many years. The recent promising observations of Leonid meteor-trails (Section 6.6.2) might also prove to be a fruitful field of future studies with ALIS.

As a spin-off effect, the combined use of the ALIS detector together with an imaging spectrometer resulted in the first daytime ground-based optical image of the aurora which was acquired on 2 May 1999 [*Rees et al.*, 2000].

It can therefore undoubtably be said that there exist strong multi-disciplinary scientific arguments for the continued operation of ALIS.

A reader interested in further information related to three-dimensional imaging of the aurora and airglow, geometrical calibration, etc., is recommended to study *Gustavsson* [2000], as these topics were only briefly touched upon in the present work. Further reading related to the processing of multi-station auroral image data is found in the work by *Rydesäter* [2001].

Simultaneous auroral imaging from space-borne optical instruments would be an effective complement to the ground-based images. Ideally a sounding rocket launched through an auroral structure, resulting in simultaneous measurements from both ground and space, would certainly provide new insights into the auroral altitude distribution and the possibility to further validate and enhance the 3D-reconstruction techniques.

Observations of the rich and interesting night-sky phenomena related to auroral and ionospheric space plasma physics as well as the environmentally important atmospheric physics is a long-term commitment involving many disciplines as well as ground-based and space-borne instruments of various types. The diversity of the scientific results summarised in this chapter provides an example of what can be achieved on a moderate budget.

In this field of science, long-term stability, not only in terms of continuous observations, but also in terms of budget and staffing, combined with long-term plans for technical maintenance and development is important.

Appendix A

The Instrumentation Platform

> "It might be the warriors who get the glory, but it's the engineers who build societies" *B'Lanna Torres*

Any scientific instrumentation, regardless of whether it is manual or automatic, ground-based or space-borne, needs some basic supporting infrastructure in the form of:

- Structural support of the instrument, for example the satellite platform or a measurement structure with instrument stand.
- Environmental subsystems, keeping environmental parameters (for example temperature) within acceptable limits.
- Power supply and conditioning devices.
- Control subsystems. Anything from a simple switch to a sophisticated telecommand system.
- Monitoring subsystems. Anything from eyeball observations of an instrument reading to a complex telemetry system.
- Communication] subsystems.
- Data processing and storage subsystems.

For space-borne instruments, many of these functions are provided by the spacecraft platform. In the ground-based case many of these requirements are often more relaxed due to a less-hostile environment and the proximity to the general infrastructure of human civilisation. However if unmanned measurement stations are deployed in a sparsely-populated area with a sub-arctic climate, some requirements on the instrument platform becomes as demanding as in the space-borne case. Thus the ALIS-project required a closer examination of the basic infrastructure than most ground-based facilities in the field. The required basic infrastructure for low-light imaging stations could to a large extent also be used by other instruments (not necessarily optical), or even in entirely different contexts. Thus, these efforts to provide a housing for the ALIS stations resulted in the concept of a Ground-based Low-light Imaging Platform (GLIP) which constitutes the major part of an ALIS station.

The GLIP was designed in such a way that it should be able to operate in the harsh climate of the Kiruna region without any manual attendance for a period of up to 8 months. It was a requirement to be able to monitor and control all necessary functions of the GLIP remotely, even if the normal means for controlling the station should fail. In the case of a total communication- and control failure, critical subsystems, such as heaters and sensitive detectors, should enter a safe survival mode. The station should furthermore be able to continue operation even if the control centre failed. Finally, the GLIP would be designed in a modular fashion, so that the various subsystems and instruments should be easy to replace for maintenance, etc. The major subsystems of the GLIP are described in the following sections; refer to the block diagram in Figure A.1.

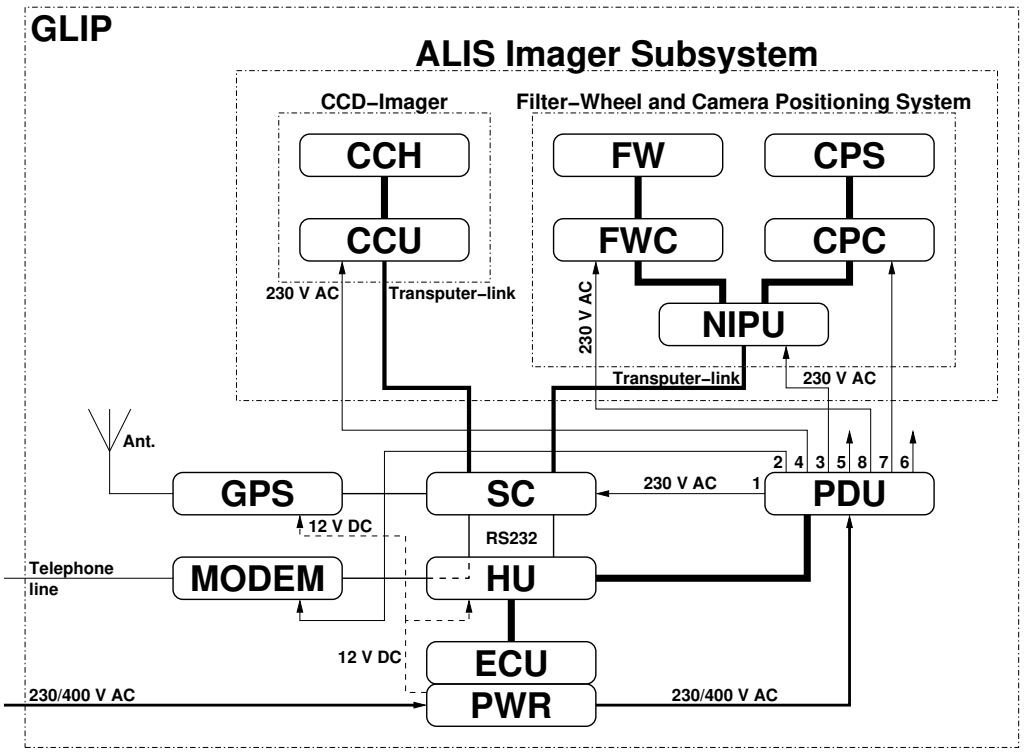

Figure A.1: Block diagram of the Ground-based Low-light Imaging Platform. The acronyms are explained in Table A.1

A.1 Station housing

The largest part of the GLIP consists of the station housing with the observing dome and instrument mount points. A Housing for ALIS (HALIS) must provide protection against the harsh climate: temperatures ranging from $-45°C$ to $+30°C$ (worst case), strong winds and intense solar radiation. The housing should also be easy to transport and assemble at distant locations. A special problem for an imaging station is the roof, where a large opening is required. On the prototype structure the roof was built in a traditional way, but the demand for

Acronym	Explanation	See also
AIS	ALIS Imager Subsystem	Chapter 3
CCD	Charge Coupled Device	
CCH	CCD Camera Head	Section 3.3.1
CCU	Camera Control Unit	Section 3.3.2
CPC	Camera Positioning system Control unit	Section 3.6
CPS	Camera Positioning System	Section 3.6
ECU	Environmental Control Unit	Section A.2
FW	Filter Wheel	Section 3.5.1
FWC	Filter-Wheel Control Unit	Section 3.5.1
GPS	Global Positioning System	Section A.5
HU	Housekeeping Unit	Section A.4
NIPU	Near-Sensor Interface and Processing Unit	Section 2.2.2
PDU	Power Distribution Unit	Section A.3
PWR	Power subsystem, the electrical installation of the GLIP	Section A.3
SC	Station Computer, the main computer at the GLIP	Section 2.2.1

Table A.1: Explanation of acronyms in Figure A.1.

a circular hole for the dome made this design complicated and ended up heavy and difficult to keep water-proof. Based on this experience, an improved roof was designed as described below.

The optical system could be said to start with the observing window. From the optical point of view, no window at all apart from the front lens itself would be the best solution. However in this case the imager must either be fixed, or the entire instrument housing must be mounted in a positioning system. The latter solution would be difficult to realise at a reasonable cost in the harsh climate. This fact, combined with the requirement of a pointable camera, led to the compromise of a half-spherical plexi-glass dome. Such domes have long been in wide use for auroral observations. The transmittance curve of the plexi-glass is shown in Figure A.2.

The bottom part of the HALIS is an iron frame (2 m $\times$ 2 m $\times$ 0.75 m) firmly anchored in such a way that the frame rests $\approx$ 0.5 m above the ground. In this way the wind can blow under the floor, preventing snow from piling up around it, while also stopping some animals from reaching the station house (Figure A.3). This design requires a well-insulated floor.

A quadratic structure of dimensions 2 m $\times$ 2 m $\times$ 1.5 m is attached onto the iron frame by means of four bolts. The structure is made of two layers of construction plywood, separated by a 5 cm layer of thermal insulation. The door is 1 m $\times$ 1.2 m.

Inside the structure the imager-stand, consisting of four iron rods, is directly attached to the corners of the iron frame. The imager is thus not affected by vibrations in the structure caused by strong winds, etc.

The removable roof is made of plastic reinforced with glass-fibres and thermal

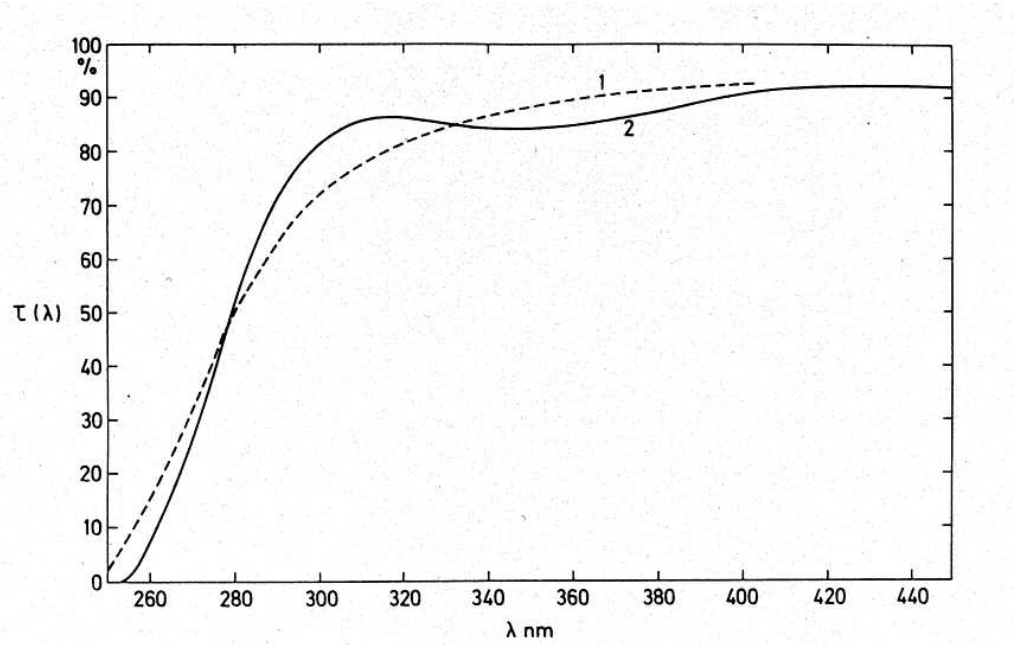

Figure A.2: Transmittance curves $T_{dome}(\lambda)$ for Plexi-glass Röhm GS2458 where λ is the wavelength in nm. Curve 1 corresponds to the transmission of a 3 mm thick Plexiglas sample obtained by Röhm, Darmstadt. Curve 2 has been measured by J. Stegman, MISU, Stockholm for a sample of 4 mm thickness. [After *Steen*, 1987]

insulation. The roof makes a smooth and water-proof transition from the square 2 m × 2 m cross-section of the structure to the circular 1 m diameter observing hole where the dome is mounted.

The semi-half-spherical observing dome is designed with a sleeve in such a way that the interface to the roof is water-tight (Figure A.4).

The HALIS can be transported and mounted at a distant location in less than one working day by 2–4 persons, using a simple trailer for road transportation, and assistance from a tractor or helicopter for the final move. The removable roof simplifies transportation and enables easy installation of large equipment modules into the station.

In total ten* HALIS of the design described above have been built for ALIS; eight are deployed on site and two of the structures are temporarily loaned out to ESRANGE. Some of the GLIPs have been on site for about ten years, without any major problems. A repainting of the plywood surfaces each decade seems appropriate to prolong the lifetime of the station.

Another experience gained from the early campaigns, (when two manned intensified CCD-cameras were operated at the Abisko and Nikkaluokta stations on a temporary basis), is that the GLIPs are not well-suited for manned operation. This is mainly due to condensation on the inner side of the dome, resulting from the humans in the station, and from frequent use of the door. After leaving the station, defrosting the dome might take up to 15 min depending on weather con-

*Two additional structures have been built for other users

Figure A.3: The GLIP in Tjautjas (4) showing how snow is prevented from building up around the station.

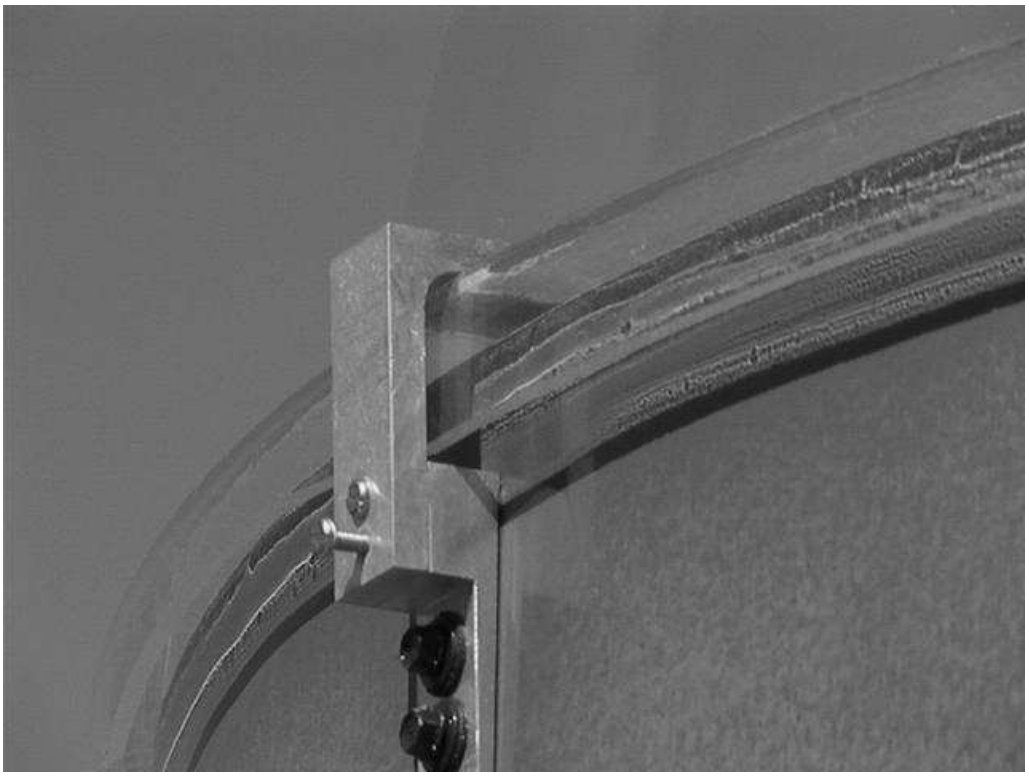

Figure A.4: Detail of the GLIP dome, showing the water-tight interface between the dome and the roof.

ditions. Therefore visits to the stations should be avoided close to measurement periods.

A.2 Environmental subsystems

Two electrical heaters (2×1 kW) heat the station. Defrosting of the dome can be enhanced by enabling heating spirals in the base of the dome (200 W) and an additional heated air-stream (2 kW). The power required for heating and defrosting might seem high, but is explained by the quite high thermal losses through the thin plexi-glass dome and, also by the unpredictable weather in the region, where a heavy snowfall might be followed by clear skies and good observing conditions in less than one hour. The station is protected from overheating by triple safety systems on the heating devices as well as by a cooling fan.

All environment control devices (heaters, dome-heater, auxiliary heater, cooling-fan), as well as the illumination and electrical outlets used during service visits to the GLIP, can be remote-controlled via the housekeeping unit (Section A.4). If the housekeeping unit fails, the environment control settings fall back to safe hardware-defined values.

During the midnight sun period, the black surfaces visible through the dome are exposed to intense sunlight and might reach high temperatures (up to about 100°C has been measured.) As ALIS is not imaging during this season, the domes are replaced with opaque covers during summertime. This also keeps the need for cleaning the domes (and thus the risk of scratches) to a bare minimum, by not exposing the dome to bird-droppings and insects. For summertime operations an air-conditioning device (cooler) is required so as not to exceed the temperature specifications of the equipment inside the dome.

A.3 Power subsystems

Although the original ALIS paper [*Steen*, 1989] stated that some stations would have to generate their own power, all GLIPs deployed so far have been located close to commercial power lines.

In Sweden, a typical electricity account gives access to 3×16 A at 230/400 V AC which provides much more than sufficient electrical power (about 11 kW) for heating and powering the GLIP. Thus only the energy cost has been of concern.

The electrical installation in the GLIP has more fuses than a typical household installation in order to minimise the loss of function caused by blown fuses.

The incoming power lines pass through the mains switch, energy meter and surge protection circuits before entering the main fuse box. There is a relay box for remote-controlling the heaters, defrosters, etc. (see Section A.2) from the housekeeping unit (Section A.4). Three thermostats are used for fail-safe temperature control if the housekeeping unit should fail to control the temperature properly. There are a number of outlets (230 V/10 A) for equipment and a three-phase outlet (3×10 A 230/400 V). Figure A.5 shows some of this equipment.

The Power Distribution Unit (PDU) (Figure A.6) distributes mains power to most subsystems at the station. The PDU contains eight independent outlets

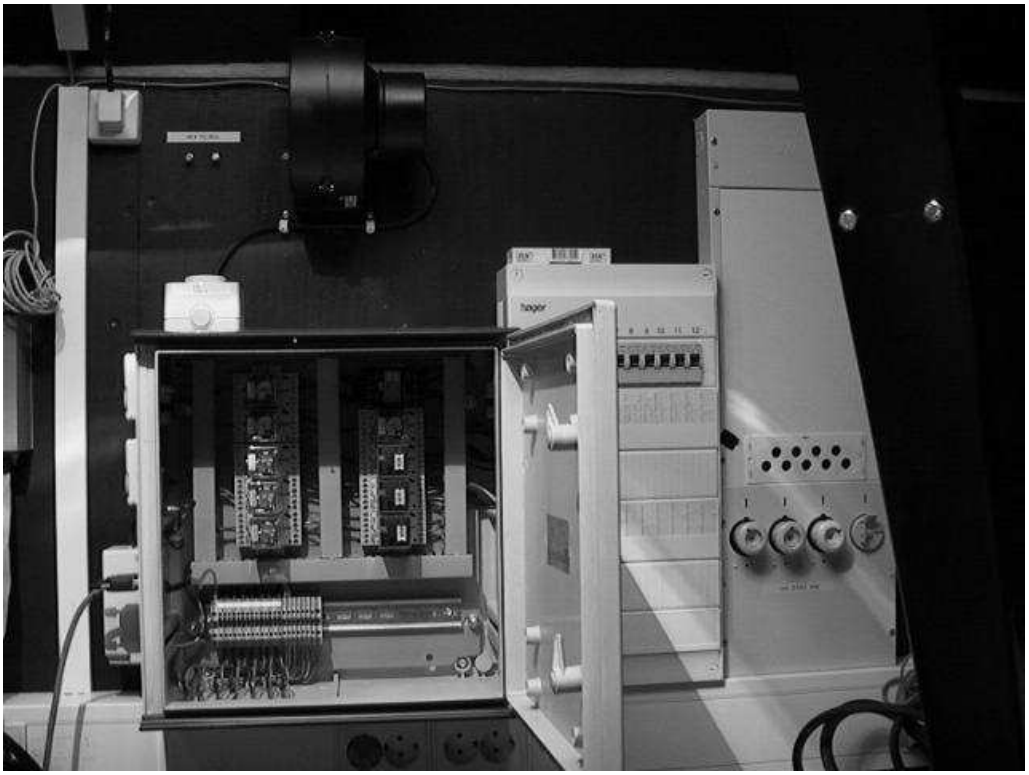

Figure A.5: The electrical installation of a GLIP. The cooling fan is seen in the upper-middle part of the image, below it is the environmental control unit (ECU) with thermostats and relays. To the right is the main fuse box and far right the main fuses and mains switch.

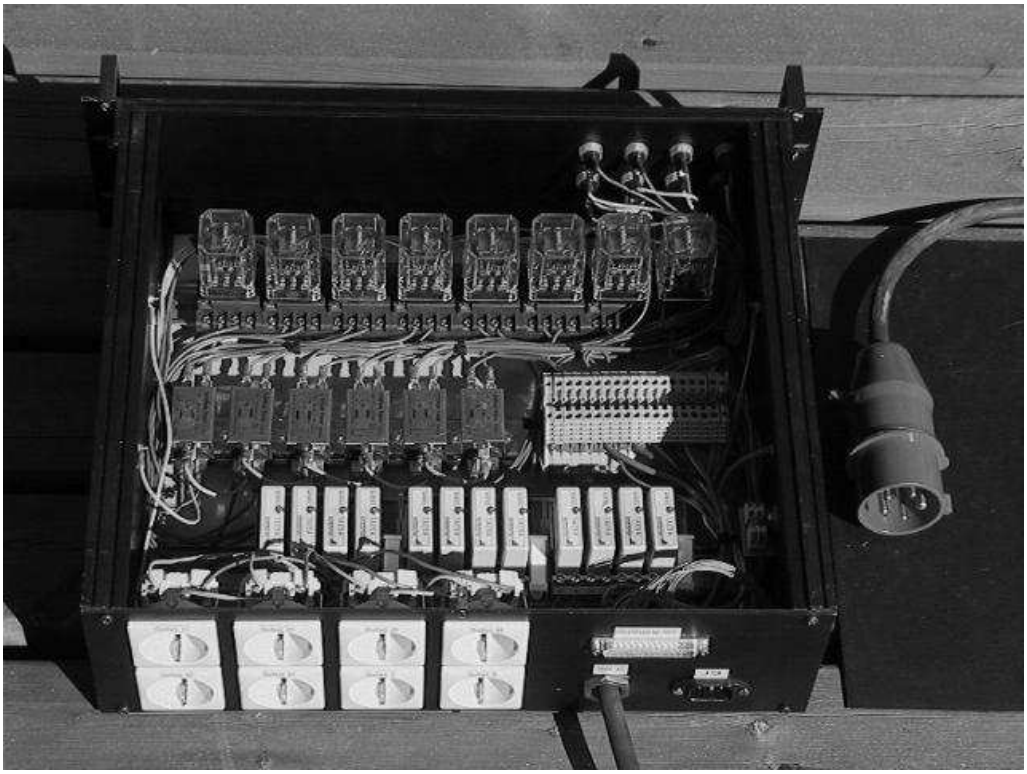

Figure A.6: Rear view of the Power Distribution Unit. The fuses are seen on the front panel (top), the relays for remote control are on the upper row, below them are surge filters and a terminal board. The bottom row contains the power sensors. The outlets are mounted on the back panel.

(230 V/10 A) with a power sensor and additional surge protection on each outlet as well as on the three incoming lines, thus enabling the housekeeping unit to monitor power failures on any of the incoming three phases as well as power distribution problems related to the PDU itself.

There is also a 12 V 75 Ah lead-acid battery with an automatic charger powering the housekeeping unit and other devices requiring an uninterrupted 12 V DC supply, such as the GPS receiver, etc.

A GLIP consumes up to 10000 kWh annually. Most of this energy is used by the heating and defrosting equipment. Some sites have had a rather large number of power failures, and it has been suggested that an Uninterrupted Power Supply (UPS) should be installed at each station to prevent the loss of measurements due to transients and short-term power outages.

If GLIPs are to be mounted in remote areas with no commercial power, they might have to generate their electrical power on site and therefore might require other solutions for heating and defrosting the dome.

A.4 Housekeeping Unit

The present Housekeeping Unit (HU) (Figure A.7) was designed in 1990, and is based on a similar, older system that proved reliable for many years. It is based on the 6502 microprocessor and the firmware is written in assembler and stored in EPROM. It also has non-volatile RAM with a real-time clock, a serial interface, A/D converter, a number of digital-I/O interfaces, various sensors and controls. The housekeeping unit is powered by uninterrupted 12 V DC (max 1 A) from the lead-acid battery.

Figure A.7: The ALIS Housekeeping Unit.

The housekeeping unit monitors battery and mains voltages, outdoor- dome- filter- and ambient temperatures, illumination level, fire- and trespass alarm sensors, precipitation (snow/rain) and the proper functioning of the station computer. It controls the power distribution unit, the environment control unit (Section A.2) and the access to the dial-up communication line.

If the station computer ceases to function properly, the housekeeping unit will take actions to bring the station into a safe state and alert the control centre of the situation. By sending commands directly to the housekeeping unit it is then possible to diagnose the situation and restart the station. Due to this solution, almost no trips to the stations have been required for system malfunctions.

The present housekeeping unit has been in use since 1991 and proven very reliable but must unfortunately soon be replaced as many of its components are obsolete. The next generation of housekeeping units will be based on a number

of networked micro-controllers, possibly with a GSM telephone as a redundant communication link.

A.5 Timing

Timing and synchronisation of measurements at the different stations are critical for essentially all scientific measurements. The timing-system must be decentralised since the GLIPs are not necessarily online all the time during a measurement. Several possibilities were considered, such as frequency references at each station, the Omega navigation system, the Global Positioning System (GPS) etc. Since GPS provided superior accuracy and reliability at an affordable cost, this system was selected for the GLIPs (Figure A.8). The first GPS receiver used in ALIS

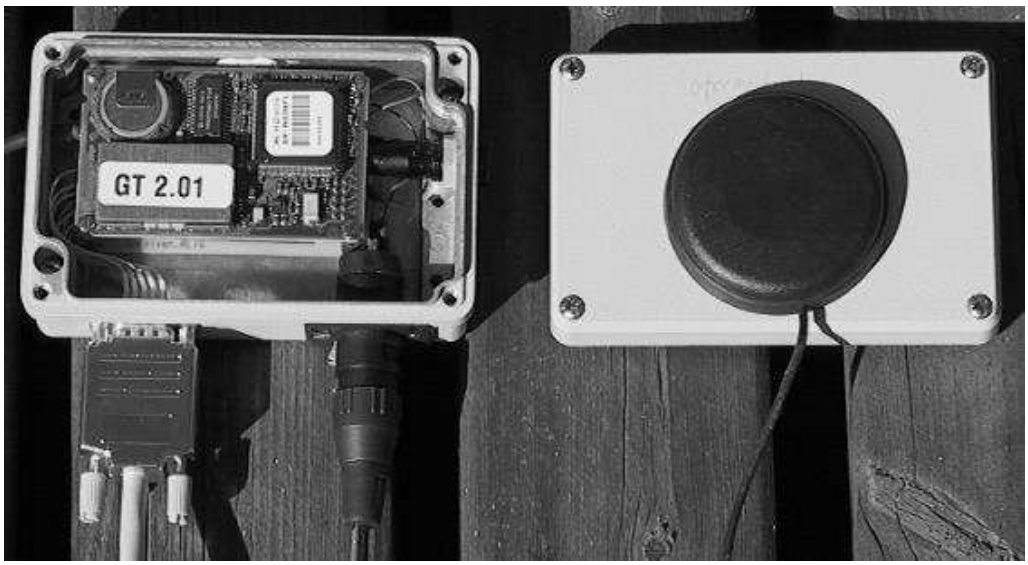

Figure A.8: The GPS receiver currently used in ALIS. Left: Receiver board with connectors for RS-232 and power (12 V DC). Right: GPS antenna.

was contained on an ISA-board that was plugged into the station computer. Later GPS units were external, communicating over RS-232. Both versions had a 1 Pulse Per Second (PPS) TTL-level output for precision timing. Early on the GPS devices had their own software, but they are now controlled by the Internet standard network time protocol (ntp) [*Mills*, 1992]. The ntp daemon (ntpd) running at each station interfaces directly to the output of the GPS receiver, as well as to other time-servers on the Internet, synchronising the PC clock to better than 1 ms precision against UTC. A software Phase-Locked Loop (PLL) implemented in the ntpd software allows timing to be preserved with good accuracy during periods when the timing sources are lost. While presently not needed, it is possible to further enhance timing accuracy to better than $1\mu s$ by using the 1 PPS signal from the GPS-receiver, giving almost atomic-clock precision to the stations. The GPS-receiver also provides information about the geographical position of the station.

Figure A.9: Left: Exterior view of the mobile imaging platform. Right: Interior view of the mobile GLIP. The Imager assembly is mounted under the dome, on top of the rack. Below, a computer monitor, the FWC, keyboard, NIPU, computer and external disks can be seen.

A.6 Communication

Any communication equipment capable of connecting the station to a remote control centre or network can be used at the GLIP. Except for the Kiruna station, which has a Ethernet connection, all GLIPs have been using 28 kbits/s dial-up modem lines (Section 2.2.3). At the station a Local Area Network (LAN) interconnects all networked devices.

A.7 Station computer

The main computer controlling most of the GLIP is called the Station Computer (SC). The SC is typically a PC (i486 or newer) with the Debian GNU/Linux operating system (Section 2.2.1). In case of station computer malfunction, the housekeeping unit (Section A.4) will take over control, bring down all equipment in the GLIP to a safe state, and alert the control centre about the situation.

A.8 The mobile imaging platform

In order to improve the coverage close to the Tromsø magnetic field line, a van was equipped with a small dome as seen in Figure A.9.

The ALIS imager, camera-controller, filter-wheel controller, NIPU and station computer were installed inside the van (Figure A.9). In this case the imager was fixed in zenith so no camera positioning system was required. Since the van was

manned during the observations, no housekeeping unit, power distribution unit, communications, etc. were required. However if an unmanned, remote-controlled configuration had been desired, this equipment could easily have been installed. A mobile generator was also included, so the station was independent of mains power. This station operated with good results in the years 1999–2003.

Appendix B

Data for the ALIS imagers

The following tables list a selection of items from the vendor-provided CCD test reports, as well as some measurements provided by the camera manufacturer. (Table B.5 is identical to Table 3.2). See Chapter 3 for more information.

Parameter	Symbol	`ccdcam1`	Unit	Notes
Read noise	$\langle n_{e_r^-} \rangle$	9.74	e^-_{RMS}	a) b) 8@13$\mu s/pixel$
Dark current	$\overline{n}_{e_d^-}$	853	$e^-_{RMS}\ s^{-1}$	at 20°C.
Full well	$N_{e^-_{max}}$	272	ke^-	
Quantum efficiency	Q_E	≥ 35	%	4000 Å
Quantum efficiency	Q_E	84.96	%	5500 Å, at $-10°C$.
Quantum efficiency	Q_E	≥ 60	%	7000 Å

Table B.1: Some parameters for the CCD in ALIS-imager `ccdcam1` (Tk1024AB, serial No. 1541BR0104) as measured by the CCD-manufacturer. All values at $-90°C$ unless otherwise noted. Notes: a) quadrant with highest value. b) same parameter, as measured by camera manufacturer.

Parameter	Symbol	`ccdcam2`	Unit	Notes
Read noise	$\langle n_{e_r^-} \rangle$	7.65	e^-_{RMS}	a) b) 7.9@10.5$\mu s/pixel$
Dark current	$\overline{n}_{e_d^-}$	12.28	$e^-_{RMS}\ s^{-1}$	at $-15°C$
Full well	$n_{e^-_{max}}$	281	ke^-	b) 230ke^- c)
Quantum efficiency	Q_E	82.3	%	4000 Å
Quantum efficiency	Q_E	88.4	%	5500 Å, at $-15°C$
Quantum efficiency	Q_E	89.4	%	7000 Å
Quantum efficiency	Q_E	48.7	%	9000 Å

Table B.2: Some parameters for the CCD in ALIS-imager `ccdcam2` (Tk1024A, serial No. 1743BR10-03R) as measured by the CCD-manufacturer. All values at $-45°C$ unless otherwise noted. Notes: a) quadrant with highest value. b) same parameter, as measured by camera manufacturer. c) quadrant A -3% linearity.

Parameter	Symbol	ccdcam3	Unit	Notes
Read noise	$\langle n_{e_r^-} \rangle$	7.62	e^-_{RMS}	a) b) $9@7\mu s/pixel$
Dark current	$\overline{n}_{e_d^-}$	17.75	$e^-_{RMS}\ s^{-1}$	at $-15°C$ b)5–6@ $-29°C$
Full well	$n_{e^-_{max}}$	313	ke^-	c)
Quantum efficiency	Q_E	83.0	%	4000 Å
Quantum efficiency	Q_E	99.3	%	5500 Å, at $-15°C$ d)
Quantum efficiency	Q_E	88.0	%	7000 Å
Quantum efficiency	Q_E	52.0	%	9000 Å

Table B.3: Some parameters for the CCD in ALIS-imager ccdcam3 (Tk1024A, serial No. 1668BR08-02) as measured by the CCD-manufacturer. All values at $-45°C$ unless otherwise noted. Notes: a) quadrant with highest value. b) same parameter, as measured by camera manufacturer. c) quadrant A 3% linearity. d) questionable assuming a lower value (Figure 3.1) [author's note]

Parameter	Symbol	ccdcam4	Unit	Notes
Read noise	$\langle n_{e_r^-} \rangle$	7.24	e^-_{RMS}	a) b) $9@12.5\mu s/pixel$
Dark current	$\overline{n}_{e_d^-}$	8.43	$e^-_{RMS}\ s^{-1}$	at $-15°C$
Full well	$n_{e^-_{max}}$	269	ke^-	c) b) 240
Quantum efficiency	Q_E	69.5	%	4000 Å
Quantum efficiency	Q_E	83.4	%	5500 Å, at $-15°C$
Quantum efficiency	Q_E	88.1	%	7000 Å
Quantum efficiency	Q_E	53.1	%	9000 Å

Table B.4: Some parameters for the CCD in ALIS-imager ccdcam4 (Tk1024AB, serial No. 4362BBR02-04) as measured by the CCD-manufacturer. All values at $-45°C$ unless otherwise noted. Notes: a) quadrant with highest value. b) same parameter, as measured by camera manufacturer. c) quadrant A 3% linearity.

Parameter	Symbol	ccdcam5	Unit	Notes
Read noise	$\langle n_{e_r^-} \rangle$	8.3	e^-_{RMS}	a) b)$7.5@10.5\mu s/pixel$
Dark current	$\overline{n}_{e_d^-}$	12.4	$e^-_{RMS}\ s^{-1}$	at $-15°C$.
Full well	$n_{e^-_{max}}$	316	ke^-	c)
Quantum efficiency	Q_E	89.8	%	4000 Å
Quantum efficiency	Q_E	98.9	%	5500 Å, at $-15°C$, d).
Quantum efficiency	Q_E	99.4	%	7000 Å, d).
Quantum efficiency	Q_E	55.3	%	9000 Å

Table B.5: Some parameters for the CCD in ALIS-imager ccdcam5 (SI-003AB serial No. 6144GBR10-B2) as measured by the CCD-manufacturer. All values at $-45°C$ unless otherwise noted. Notes: a) quadrant with highest value. b) same parameter, as measured by camera manufacturer. c) quadrant A 3% linearity. d) questionable assuming a lower value (Figure 3.1) [author's note].

Parameter	Symbol	`ccdcam6`	Unit	Notes
Read noise	$\langle n_{e_r^-} \rangle$	< 6	e^-_{RMS}	a)
Dark current	$\overline{n}_{e_d^-}$	< 3.3	$e^-_{RMS}\ s^{-1}$	a) at $-31.0°$
Full well	$n_{e^-_{max}}$	370	ke^-	a)
Quantum efficiency	Q_E	90	%	5500 Å a) b)

Table B.6: Some parameters for the CCD in ALIS-imager `ccdcam6` (SI003A/T-4 serial No. 6403GCR14-B2) as measured by the *camera* manufacturer. a) No CCD test report, measured by camera manufacturer. b) No Q_E measured, assuming a lower value (Figure 3.1) [author's note]

Appendix C

Related work

"Hier stehe ich und kann nicht anders." *Martin Luther*

When ALIS began operating, an "aiming-system" appeared as desirable. This was planned to consist of a simpler white-light video-rate camera intended mainly to assist the ALIS operator. Two old low-light TV-cameras were used for this purpose at the ALIS operations centre. However it was always desired to have real-time digital colour images available, even if ALIS was operated from a remote place. For many years this appeared as impossible or too expensive. Around 1999 commercially-available digital still- and video colour cameras began to reach the required sensitivity. This initiated a study, mainly intended to replace the present all-sky imager in Kiruna, but also with interesting implications for ALIS. This appendix briefly describes these efforts.

It is, however, of great importance to note that the imagers discussed here are in no way comparable to the ALIS imagers. A colour CCD camera can never be used for absolute measurements of column emission rates as it contains its own colour filters. On the other hand, the colour cameras can be of great value for providing overview information of the morphology and dynamics. Also, colour images and movies of auroral phenomena tend to be much more appealing for public outreach purposes, compared to the more scientifically useful, but "unexciting" monochromatic images.

C.1 A new digital all-sky camera

An all-sky camera has been operating in Kiruna since the International Geophysical Year in 1957 [*Stoffregen*, 1962]. In 1977 the camera was replaced with a new more automated camera [*Hyppönen et al.*, 1974]. This camera is still in operation, but a replacement was strongly desired as the data storage medium is 16 mm colour film, a medium soon to become obsolete, as well as expensive to develop and copy and difficult to digitise, and thus complicated to make available and distribute to the scientific community and general public. In Finland all 16 mm all-sky cameras have already been replaced by advanced new cameras with filter-wheels and narrow-band interference filters similar to ALIS, but with all-sky optics and intensified CCDs [*Syrjäsuo*, 2001]. Furthermore, a non-intensified spectroscopic all-sky imager is described by *Ejiri et al.* [1999] (see also Section 1.1). Here an

approach is investigated based on a commercial digital colour camera with replaceable standard optics. Such a camera can produce digital data of better, or at least similar quality, to the 16 mm colour films produced by the old camera. After testing a number of cameras, most were found to have too poor sensitivity or other problems. Eventually one camera with acceptable signal-levels for auroral imaging was found.

This camera (Fuji FinePix S1Pro, cost $\approx$ 30000 SEK) was equipped with a Nikon Nikkor 8 mm 1:2.8 objective-lens giving almost all-sky field-of-view (about $180^\circ \times 112^\circ$). Figure C.1 (Left) shows the prototype camera mounted in a dome of the optics lab in Kiruna. The final version will be mounted in an insulated

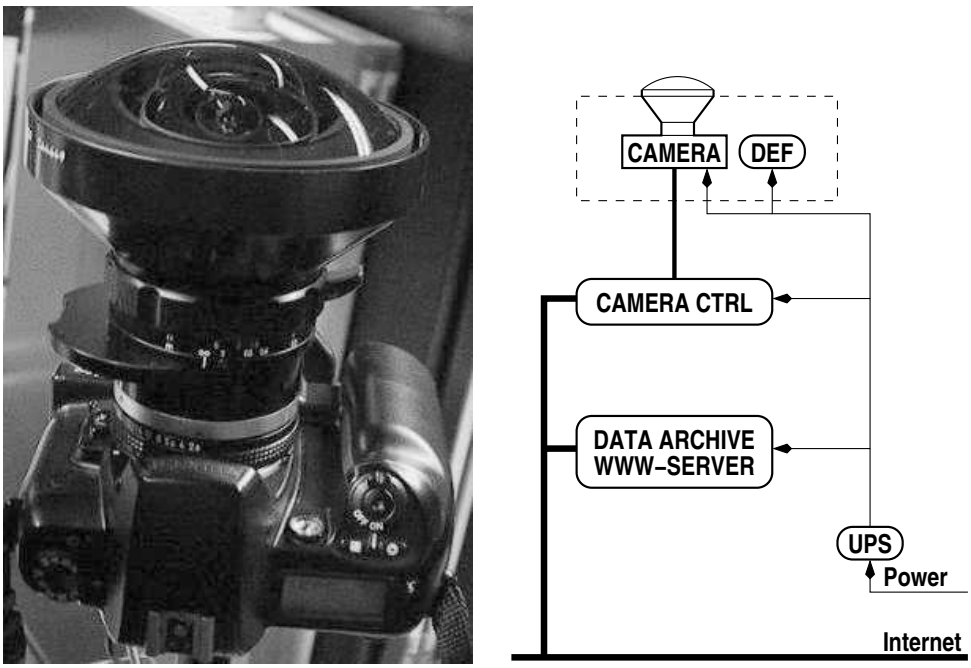

Figure C.1: Left: The prototype new digital all-sky camera (Fuji FinePix S1Pro) mounted on a tripod. The lens is a Nikon Nikkor 8 mm 1:2.8 giving almost all-sky field-of-view. Right: Block diagram of the new all-sky camera. The camera is controlled from a PC (CAMERA CTRL). The images (quick-looks and full-resolution images) are then downloaded to a data archive with a web-server. An UPS provides backup power. The camera is mounted in a heated insulated box with a defrosting device for the front-lens. Using two computers increases reliability and accessibility of the data-archive.

box together with all necessary equipment such as heaters, defrosters, etc.

The camera is controlled by a camera control computer (Figure C.1), and the image data is transferred to an archiving computer, where it is made available to the world-wide web. Monitoring and control of the camera can be done remotely using an ordinary web browser. A data storage medium suitable for long-term storage will be selected later, for example writable CDs or DVDs, etc. A sample images appears on the in Figure C.2. The large auroral image on the cover is also from this camera. This prototype camera eventually developed severe reliability problems related to its internal firmware, the USB interface (used for communication with the PC) and possibly also the shutter. Therefore the manufacturer

Figure C.2: Example image from the new all-sky camera prototype 2001-03-19 19:10 UTC. A digital version of this image can be downloaded from: `http://www.irf.se/~urban/28am`

suggested that it should be replaced by a newer model (Fuji FinePix S2Pro). This model has an IEEE-1394 interface (aka. "Firewire") instead of USB. As the new all-sky cameras are intended to operate continuously at least during the hours of darkness, exposing on average one image per minute, a major concern for both cameras tested is the long-term mechanical reliability of the shutter. So far no major problems have been encountered after a couple of months of operation. However it is highly desirable to have a spare camera in order to avoid data-gaps during maintenance operations. This work is to a large extent carried out by Arne Moström (programming) and Torbjörn Lövgren (photographer). For further information see `http://www.irf.se/data.html`

C.2 Colour video recordings of aurora

A new generation of semi-professional digital video (DV) camcorders have proved sensitive enough for almost real-time recordings (3–4 frames/s) of auroral phenomena [*Yamauchi*, 1999; *Brändström et al.*, 2001b]. One such camera (Sony DCR VX-2000E PAL) was procured by the author. The sensitivity for auroral scenes at 3 exposures/s was found to be of the same order as the unaided human eye (i.e. roughly 1 kR at 5577 Å). Several hours of auroral footage were recorded and the image quality is acceptable for TV-broadcasting and auroral visualisation for the general public (for example Swedish Television has broadcasted such material on two occasions). It has proved possible to record weak diffuse, pulsating

and black aurora with an acceptable signal-to-noise ratio. These cameras could therefore be a good tool for studies of auroral morphology and dynamics, as well as for providing supporting images for other instruments (ALIS, EISCAT, etc.). Another interesting future possibility is to use this type of camera together with methods for automated image analysis as described by [for example *Rydesäter*, 2001; *Syrjäsuo*, 2001] for automated control over spectroscopic imaging systems like ALIS. The following table summarises some of the features of the camcorder tested:

- 3 CCD $\approx$ 450 kpixels.
- Optics: $f = 6 - 72$ mm 1:1.6-2.4
- 12$\times$ optical zoom, 48$\times$ digital zoom.
- miniDV tapes (memorystick for still-images)
- IEEE-1394 "Firewire" capture directly to a computer.
- Colour auroral imaging possible from about 3 images per second up to video rate, depending on auroral intensity. Good sensitivity for Red and Green auroras, acceptable for blue.

A sample frame of an auroral scene with a meteor trail is displayed in Figure C.3. Video footage can be made available by the author on request.

Figure C.3: Sample frame from a auroral video obtained with a commercial mini-DV camcorder displaying green, red and blue aurora. A meteor-trail is seen in the lower middle part of the image. A digital version of this image can be downloaded from: `http://www.irf.se/~urban/28am`

Appendix D

Continued operations with ALIS

> "Determinismens huvudskäl är kausalitetslagen.
> Indeterminismens huvudskäl är ansvarskänslan." *Dag Hammarskjöld*

The design work on ALIS started in 1990. Thus most of the technology of the system is about ten years old and consequently the need for upgrades and technical maintenance has increased. Unfortunately, this has not been possible, mainly because of budgetary constraints. As the measurement season of 2000/2001 ended, ALIS was put into hibernation, mainly to give the author a chance to finish this report, but also due to a shortage of staff and funding. Since then, 1–2 ALIS imagers have occasionally been operated manually, primarily for studies of HF pump-enhanced airglow. In the fall of 2001 funding covering operation and some technical maintenance was received for the period 2002–2004.

From a scientific point of view, a continued and enhanced operation of ALIS can be motivated solely on the new questions raised by the observations of HF pump-enhanced airglow (Section 6.4). The recent promising observations of meteor trails (Section 6.6.2), as well as continued auroral studies (Section 6.5) also constitute strong arguments for a prolonged operation of ALIS.

This short appendix outlines how to assess the present status of ALIS in order to make a plan for bringing ALIS back into full operation. It is assumed that the present funding situation is stable for 2003/2004, and that performing new measurements, as well as analysing existing data, will enable a sustained funding at the present level, or higher. The most limited resource for ALIS has always been the staff. Here it is assumed that a stable group of at least 3–4 physicists, with a thorough scientific and technical knowledge of ALIS, is available to at least 50% for engineering and programming tasks, as well as general maintenance. (Ideally ALIS should have access to an electronics engineer and one programmer. However given the present situation this is not considered economically feasible.)

D.1 Assessing the present status of ALIS

Finding out the present status of ALIS is the inevitable first step in making a plan. As ALIS was closed, the status of the system was reported in [*Brändström*,

2001a,b]. Based on this information, an estimate of the efforts required to restart ALIS will be presented. It is important to note that in order to make a final plan, a thorough technical examination of vital systems is required. Such an investigation is estimated to take about two man-months (preferably two people for one month). However despite this, it should be possible to start immediate measurements with two imagers in parallel as the rest of ALIS is evaluated, the only constraint being staff availability.

The following list summarises anticipated status of the main technical systems (see also Figure A.1 in Appendix A).

The ALIS stations: In order to save money all stations have been left with electrical power switched off. To avoid equipment damage, heating should be turned on at least two weeks before attempting to turn on any equipment. The GLIPs (Appendix A) are expected to be found in good condition. However the domes will require cleaning, and some stations might require repainting.

Computers: With few exceptions, all computers should be usable. However, all computers are old, and failures cannot be excluded. As each station computer needs at least two ISA-slots for interface boards (NIPU, CCU), it is important to keep the old computers usable as long as possible as new computers with ISA slots are becoming rare. Although the NIPU must be replaced soon, it is not feasible to replace the CCU within a couple of years at the present funding level. Computer replacements must likely be scheduled within 1–2 years.

The NIPU: All NIPUs (Section 2.2.2) were working in 2001, and are expected to be used at least initially. It must be stressed, however, that the NIPUs are totally obsolete, they cannot be repaired, nor can any changes to the CPS and FPS be accommodated (for example replacements of angular encoders). As the NIPUs are essential for filter changes, it is important to replace these units as soon as possible. They can be replaced by micro-controllers at a reasonable cost.

Communication systems: All dial-up telephone lines must be checked. Some modems might require replacement. It should furthermore be investigated if station 5 in Abisko can be connected to Internet via the LAN at the Abisko Research Station. Continued efforts should be made to find cheaper and faster communication to the stations. (see also Section 2.2.3)

Station data storage: Most external disks used for local data storage (Section 2.2.4) at the stations are well past their safe technical lifetime, due to many hours of operation. They are also small by present standards. As disk-crashes at the stations may lead to large data losses, all disks should be replaced. The cost for procuring 10–12 external disks is relatively low.

Data archiving: Documentation and backup copying at alternate sites of the ALIS data-base is underway as this is written. It is recommended that the archive media be transferred from CD-R (Recordable CD-ROMs) to

DVD-R (Recordable DVD) to keep down the number of discs. (see also Section 2.2.5)

Operating systems: The operating systems for the control-centre computers must be upgraded to newer versions due to security and compatibility issues. At the stations it is preferable to keep the present operating systems as long as the old station computers are in use.

The control centre: At least two computers need to be replaced at the ALIS control centre since they are past their technical lifetime. At the operations centre no immediate replacements are required. Some computer screens should be replaced to improve working conditions.

Environmental subsystems: These systems should be usable for many more years (Section A.2).

Power subsystems: All stations should be equipped with UPS units for powering the instrumentation. Some stations lack good surge protection devices. A safety check should be carried out for all power subsystems, especially the PDUs.

Housekeeping units: Although obsolete, all housekeeping units (Section A.4) should be usable for many more years. Replacement will be required eventually as the current housekeeping units are only capable of handling dial-up lines. New housekeeping units can easily be built in the same way as the NIPU replacement micro-controllers.

GPS units: No changes anticipated, all timing units (Section A.5) should be working.

The mobile station: The van (mobile station, see Section A.8) is critical for some scientific objectives.

Software: Most ALIS software (Chapter 5) should be working. At the stations, some bug-fixes and upgrades of `mima` and `aniara` would be appropriate. Somewhat larger programming efforts are required in order to get a web-based and user-friendly new user-interface for ALIS. This could be carried out as a student project, but is not crucial to the operation of ALIS in the near future (one year). The NIPU replacement, as well as some other hardware upgrades, will require new control software as well as modifications to existing programs.

After performing these upgrades the block-diagram of a GLIP will change slightly, as indicated in the upgraded block-diagram of Figure D.1.

D.1.1 The ALIS imagers

Since ALIS closed down in 2001, two imagers with supporting systems have participated in observations with good results. All ALIS imagers were taken to Oulu in 2002 for the calibration workshop (see Section 4.2). Although the CCUs are becoming obsolete, the CCDs and camera heads are still state-of-the-art in

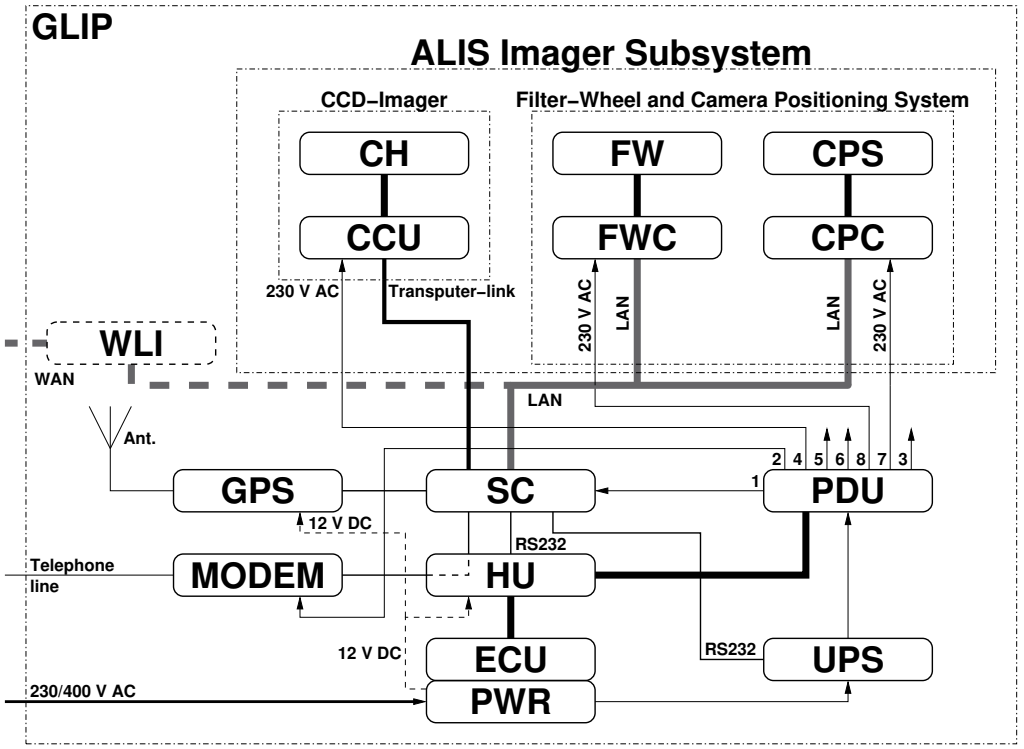

Figure D.1: In the first stage of the upgrade, the NIPU would be replaced by microcontrollers in the FWC and CPC. Also an UPS and possibly a faster network connection would be added at the stations. The acronyms are explained in Table A.1 and D.1

Acronym	Explanation
ICC	Imager Control Computer
LAN	Local Area Network
UPS	Uninterruptable Power Supply
WAN	Wide Area Network (connected to the Internet)
WLI	WAN/LAN Interface consisting of the WAN-Interface, a router, a switch and possibly also a firewall

Table D.1: Explanation of acronyms in Figures D.1–D.2 (See also Figure A.1 and Tables A.1 in Appendix A)

the field. Therefore prolonging their operational lifetime as long as possible is strongly to be desired. Procuring new imagers is not possible within the current budgetary limits. Two imagers (`ccdcam1,6`) are immediately usable for observations. Three imagers (`ccdcam3,4,5`) developed reliability problems during the Oulu visit in 2002. These problems are most likely solvable with moderate efforts. One imager (`ccdcam2`) had problems with ice-formation on the CCD, probably due to a breach in the hermetically-sealed CCD compartment. Instructions has been received from the manufacturer how to resolve this. However this is a delicate procedure involving a risk of damaging the CCD. Preferably this procedure should be carried out by the camera manufacturer.

A thorough testing of all imagers is required before being able to assess their status. Yet it appears feasible to have 4–6 imagers operational within about six months. On a longer time-scale (about five years) the CCUs at least must somehow be replaced, but this requires additional funding. The remaining subsystems related to the imager are discussed below:

Calibration: A cleaning of the optical systems, as well as focusing and calibration of each imager, is important to maintain and improve the data quality. This is estimated to take 2–3 nights per imager.

Interference filters: The change of filter transmittance with time due to aging is at present unknown, as is the filter transmittance as a function of pixel coordinates (Section 4.2.3). Measuring the transmittance could be made locally, but the monochromator system [*Vaattovaara and Enback*, 1993] must be modernised. For example, this can be done as a student final-year project.

Filter-wheels: One filter wheel (on `ccdcam5`) is experiencing mechanical problems. The remaining filter-wheels are operational, but all angular encoders are likely to fail in the near future (due to an aging laser-diode) Therefore these must be replaced, preferably as the NIPUs are replaced. As the filter-wheels are essential for successful measurements, this is a high-priority task.

Camera positioning system: All CPS units are subject to the same angular encoder problems described above. However replacing these angular encoders is not nearly as high priority as the filter-wheels. It is possible to lock some CPS units in a fixed observing position until new angular encoders can be installed. Furthermore as the filter-wheels are upgraded, spare angular encoders for the CPS are released. A mechanical maintenance and adjustment of all units are also strongly recommended.

D.2 Summary

In the near future (1–2 years) it is of highest priority to enable measurements with as many stations as possible, given the present budget and staff. This implies no major upgrades, and only performing a selection of the most critical maintenance tasks as discussed above. To increase the time for analysis and publication of data,

as well as for performing the necessary upgrades and maintenance, it might be an option to increase the student involvement in the observations, as well as in some software development and data-analysis.

The fate (i.e. funding) of ALIS in a longer perspective is directly dependent on what actions are taken in the upcoming 1–3 years. A stable core-group with thorough scientific and technical experience from ALIS operations is without doubt the most critical component.

D.2.1 A longer perspective

Given a sustained and increased funding in the future, upgrading (or replacing) the imagers is required in a longer perspective. Also all obsolete systems at the stations need to be replaced. The next step would probably be to expand ALIS towards Tromsø with station (9) Frihetsli (Figure 2.4 and Table 2.3) and possibly near the EISCAT site at Ramfjordmoen, as well as equipping the existing stations (7) Kilvo and (8) Nytorp with instruments. For such new stations a tentative block-diagram appears in Figure D.2. It must also not be forgotten

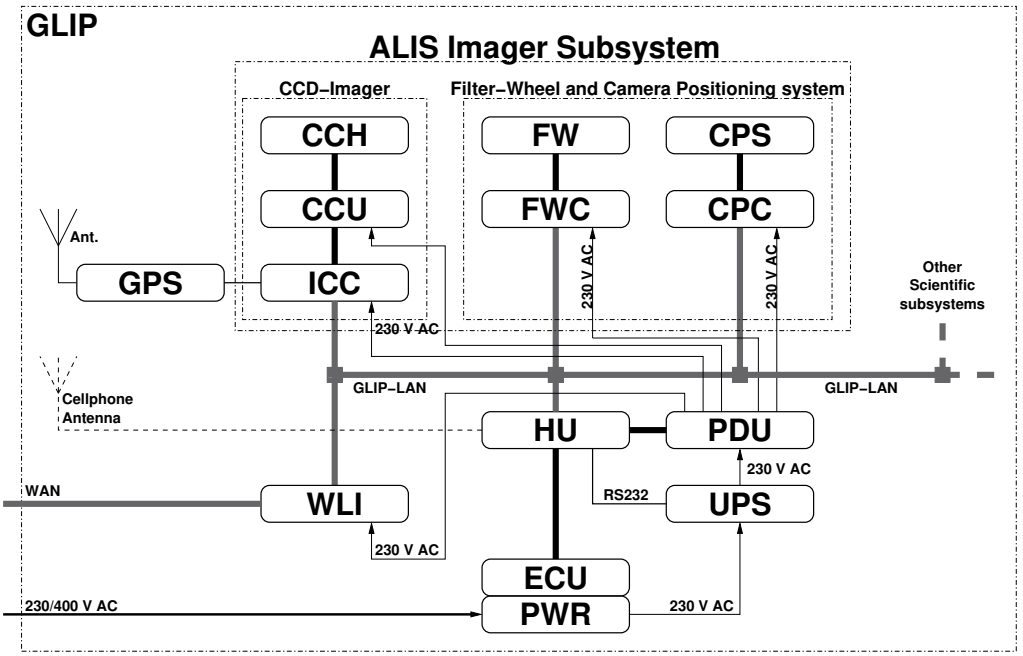

Figure D.2: For future new stations, the SC is replaced by an new HU, which might have a cell-phone interface for emergency operation. The imager is controlled by a dedicated computer, and the dial-up line is replaced by a high-speed Internet connection.

that the GLIPs are capable of housing several other instruments of various types (Section 2.1). Such instruments could include imaging spectrometers, dedicated cloud cameras, colour imagers for auroral imaging (Appendix C), magnetometers, riometers, ionosondes, etc.

Another issue is that as the stations become networked over permanent Internet connections, there will be no need for a dedicated control centre as illustrated in Figure D.3. Given an internationally-standardised set of interfaces, any collec-

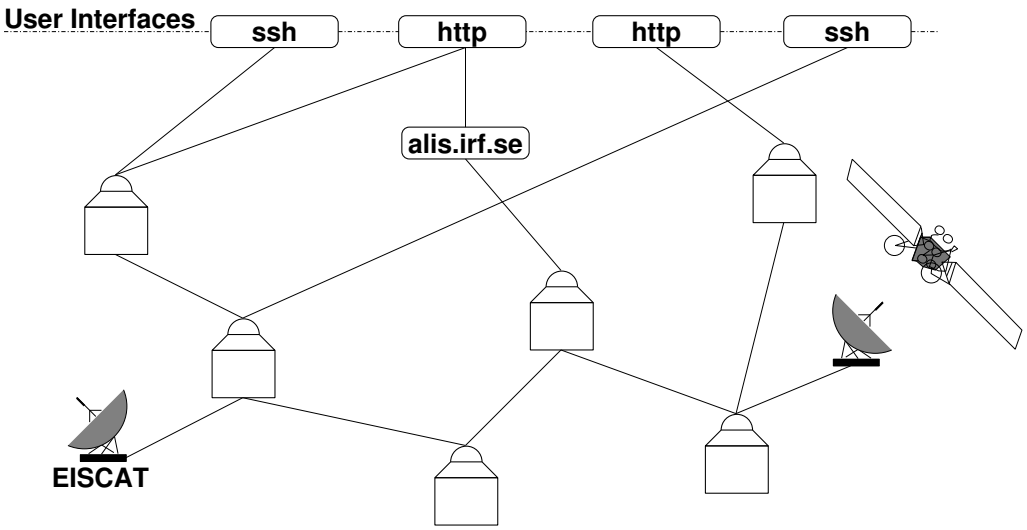

Figure D.3: A decentralised future ALIS: As the ALIS stations will most likely gain permanent Internet access in the future, the functions of the control centre will be decentralised to the stations. Connections to other stations, as well as other instruments (exemplified by EISCAT and a satellite) can then also be initiated as required.

tion of instruments could be quickly enrolled into simultaneous observations of a particular phenomena.

In the future perhaps scientific instruments will be placed on a standardised General Instrument Platform (GIP), which can be either ground-based, airborne, or placed on a spacecraft. Networks of such GIPs could then be spontaneously created, configured and controlled for specific scientific studies. Developing such ideas might enhance the availability and usage of the existing plethora of scientific instrumentation, in the same way as the world-wide-web enhanced simplified Internet usage.

Bibliography

Adeishvili, T. G., A. V. Gurevich, S. B. Lyakhov, G. G. Managadze, G. M. Milikh, and I. S. Shlyuger, Ionospheric emisson caused by an intense radio wave, *Sov. J. Plasma Phys.*, *4*, 721–726, 1978.

Alpatov, V., Å. Steen, and U. Brändström, Fractal analysis of the ALIS auroral images, 1996a, (draft manuscript).

Alpatov, V. A., A. A. Matveev, C.-F. Enell, B. Gustavsson, and U. Brändström, Investigations of the polar atmosphere with the use of dynamical characteristics of the processes and self-organizing neural networks on ground-based multi-position optical observations, in *Proceedings of the EGS General Assembly*, 2000.

Alpatov, V. V., U. Brändström, Å. Steen, and B. Gustavsson, Fractal analysis of auroral images from ALIS, (poster presentation), 1996b, The third international substorm conference (ICS3), Paris, France.

Andersson, L., Acceleration processes in auroral region, Ph.D. thesis, Swedish Institute of Space Physics, 2000, (IRF Scientific Report 270 ISBN: 91-7191-914-7).

Anger, C. D., S. K. Babey, A. L. Broadfoot, R. G. Brown, L. L. Cogger, R. Gattinger, J. W. Haslett, R. A. King, D. J. McEwen, J. S. Murphree, E. H. Richardson, B. R. Sandel, K. Smith, and A. Vallance Jones, An ultraviolet auroral imager for the Viking spacecraft, *Geophys. Res. Lett.*, *14*, 387–390, 1987.

Ångström, A. J., *Recherches sur le Spectre Solaire*, W. Schultz, Uppsala, 1868.

Ångström, A. J., Spectrum des Nordlichts, *Pogg. Ann.*, *137*, 161–163, 1869.

Aristotle, *Meteorologica*, vol. I, chap. 5, (ancient text), ca. 340 B.C.

Aruliah, A. L., A. D. Farmer, D. Rees, and U. Brändström, The seasonal behaviour of high-latitude thermospheric winds and ion velocities observed over one solar cycle, *J. Geophys. Res.*, *101*, 15,701–15,711, 1996.

Aso, T., M. A. Hashimoto, T. Ono, and M. Ejiri, On the analysis of aurora stereo observations, *J. Geomag. Geoelectr.*, *42*, 579–595, 1990.

Aso, T., M. Ejiri, H. Miyaoka, T. Ono, T. Hashimoto, T. Yabu, and M. Abe, Aurora stereo observations in Iceland, in *Proc. NIPR Symposium on Upper Atmos. Phys.*, vol. 6, pp. 1–14, National Institute of Polar Research, 1993.

Aso, T., M. Ejiri, H. Miyaoka, T. Ono, Y. Tetsuro, K. Muguruma, T. Hashimoto, and M. Abe, Aurora stereo observation in Iceland and its tomography analysis, *Trans. Inst. Electronics Communication Engineers*, *J77-DII*, 69–78, 1994, (in Japanese).

Aso, T., M. Ejiri, A. Urashima, H. Miayoka, Å. Steen, U. Brändström, and B. Gustavsson, First results from auroral tomography from ALIS-Japan multi-station observations in March 1995, *Earth Planets Space*, *50*, 81–86, 1998a.

Aso, T., M. Ejiri, A. Urashima, H. Miyaoka, Å. Steen, U. Brändström, and B. Gustavsson, Auroral tomography analysis of a folded arc observed at the ALIS-JAPAN multi-station campaign on March 26, 1995, in *Proceedings of the NIPR Symposium on upper atmosphere Physics*, vol. 11, pp. 1–10, National Institute of Polar Research, Tokyo, 1998b.

Aso, T., Å. Steen, U. Brändström, B. Gustavsson, A. Urashima, and M. Ejiri, ALIS — a state of the art optical observation network for the exploration of polar atmospheric processes, *Adv. Space Res.*, *26*, 917–924, 2000.

AstroCam Ltd., *4400 Programmer's reference manual*, AstroCam Ltd., 1995.

AstroMed Ltd., *4400 Programmer's reference manual*, AstroMed Ltd., 1993.

Backlund, V., Über die Technik der simultanen Telefilmsplanigraphie, *Acta Radiol. Suppl.*, *137*, 1956, (PhD Thesis).

Baker, D. J., and G. J. Romick, The Rayleigh interpretation of the unit in terms of column emission rate or apparent radiance expressed in SI units, *Applied Optics*, *15*, 1966–1968, 1976.

Barmore, F. E., High resolution observations of the 6300 Å oxygen line in the day airglow, *Planet Space Sci.*, *25*, 185–191, 1977.

Baschin, O., Die ersten Nordlichtphotographien etc., *Met. Z.*, *17*, 1900.

Bens, A. R., L. L. Cogger, and G. G. Shepherd, Upper atmospheric temperatures from Doppler line-widths — Observation of the OI dayglow emission at 6300 Å, *Planet Space Sci.*, *13*, 551–563, 1965.

Bernhardt, P. A., C. A. Tepley, and L. M. Duncan, Airglow enhancements associated with plasma cavities formed during ionospheric heating experiments, *J. Geophys. Res.*, *94*, 9071–9092, 1989.

Bernhardt, P. A., W. A. Scales, S. M. Grach, A. N. Keroshtin, D. S. Kotik, and S. V. Polyakov, Excitation of artificial airglow by high power radio waves from the SURA ionospheric heating facility, *Geophys. Res. Lett.*, *18*, 1477–1480, 1991.

Birkeland, K., *The Norwegian aurora polaris expedition 1902–1903. Volume I On the cause of magnetic storms and the origin of terrestrial magnetism. First section*, vol. 1, A. W. Brøggers bogtryckeri, Christiania (Oslo), Norway, 1908.

Birkeland, K., *The Norwegian aurora polaris expedition 1902–1903. Volume I On the cause of magnetic storms and the origin of terrestrial magnetism. Second section*, vol. 1, A. W. Brøggers bogtryckeri, Christiania (Oslo), Norway, 1913.

Brandy, J. H., and J. E. Hill, Rapid determination of auroral heights, *Canad. J. Phys.*, *42*, 1813–1819, 1964.

Brown, N. B., T. N. Davis, T. J. Hallinan, and H. C. Stenbaek-Nielsen, Altitude of pulsating aurora determined by a new instrumental technique, *Geophys. Res. Lett.*, *3*, 403–404, 1976.

Brändström, B. U. E., T. B. Leyser, Å. Steen, M. T. Rietveld, B. Gustavsson, T. Aso, and M. Ejiri, Unambigous evidence of HF pump-enhanced airglow, *Geophys. Res. Lett.*, *26*, 3561–3564, 1999.

Brändström, U., Reduction of CCD images from ALIS, ALIS internal note, 2000, (Intended for CCD-course).

Brändström, U., ALIS, a brief technical summary of the current situation, ALIS internal note, 2001a.

Brändström, U., ALIS stängt för säsongen, email to alis_folk@irf.se 2001-04-11, 2001b, (in Swedish).

Brändström, U., and Å. Steen, Report on the ALIS project, in *Proc. 19th Annual European meeting on atmospheric studies by optical methods, Kiruna, Sweden*, edited by Å. Steen, pp. 310–321, Swedish Institute of Space Physics, Kiruna, Sweden, 1992, IRF Scientific Report 209.

Brändström, U., Å. Steen, B. Gustavsson, L. Andersson, I. Häggström, A. Westman, A. Pellinen-Wannberg, T. Aso, K. Kaila, C. W. Carlson, D. Klumpar, and C. Catell, Preliminary results from coordinated measurements by FAST and groundbased optical and radar facilities, in Northern Scandinavia, during active auroral conditions, in *Proceedings of the 24th annual European Meeting on Atmospheric Studies by Optical Methods*, pp. 41–46, Sentraltrykkeriet A/S Bodø, 1997a, ISBN 82-994583-0-7.

Brändström, U., Å. Steen, B. Gustavsson, D. Rees, and M. J. Harris, Preliminary results from a comparision of observations of thermospheric neutral wind patterns and auroral emissions, in *Proceedings of the 24th annual European Meeting on Atmospheric Studies by Optical Methods*, pp. 37–40, Sentraltrykkeriet A/S Bodø, 1997b, ISBN 82-994583-0-7.

Brändström, U., Å. Steen, P. Rydesäter, B. Gustavsson, and T. Aso, ALIS, a multi station imaging facility with possibilities of future VI applications, in *Ninth workshop on Virtual Intelligence / Dynamic neural networks*, edited by

M. L. P. Thomas Lindbladh and J. Kinser, vol. 3728, pp. 108–114, Royal Institute of Technology, Stockholm, Sweden, The International Society for Optical Engineering, 1998, ISBN 0-8194-3202-4.

Brändström, U., B. Gustavsson, Å. Steen, and A. Pellinen-Wannberg, ALIS (Auroral Large Imaging System) used for optical observations of the meteor impact process, in *Proceedings of the Meteoroids 2001 Conference*, edited by B. Warmbein, vol. SP-495, pp. 331–336, European Space Agency, 2001a, ISBN 92-9092-805-0.

Brändström, U., T. Lövgren, A. Moström, C.-F. Enell, B. Gustavsson, T. Aso, M. Ejiri, Å. Steen, and P. Rydesäter, Brief report on ALIS (Auroral Large Imaging System), a new all-sky camera in Kiruna and auroral imaging using a mini-DV camcorder, in *Proc. of 28th Annual European Meeting on Atmospheric Studies by Optical Methods*, Sodankylä Geophysical Observatory, 2001b, (in press).

Carlson, C. W., The Fast Auroral SnapshoT explorer, *EOS, Transactions, American Geophysical Union*, *73*, 1992.

Carlsson, H. C., V. B. Wickwar, and G. P. Mantas, Observations of suprathermal electrons accelerated by HF-excited instabilities, *J. Atmos. Terr. Phys.*, *44*, 1089–1100, 1982.

Celsius, A., *Observationes de lumine boreali*, Norimbergae, 1733.

Ceplecha, Z., and J. Rajchl, The meteor spectrum with dispersion from 11 to 38 Å/mm, *Publishing House of the Czechoslovak Academy of Sciences*, *14*, 29–47, 1963, (Available from the NASA Astrophysics Data System).

Chamberlain, J. W., *Physics of the aurora and airglow*, Classics in geophysics, AGU (American Geophysical Union), 1995, (A reprint of the original work from 1961).

Cocks, T. D., D. F. Creighton, and F. Jacka, Application of a dual Fabry-Perot spectrometer for daytime airglow studies, *J. Atmos. Terr. Phys.*, *42*, 499–511, 1980.

Conde, M., and F. Jacka, Analysis of day-time observations of the 630 nm thermospheric emission over Mawson, Antarctica, *ANARE Res. notes*, *69*, 125–138, 1989.

Conde, M. P., P. Greet, and F. Jacka, The Ring effect in the sodium D2 Fraunhofer line of day skylight over Mawson, Antarctica, *J. Geophys. Res.*, *97*, 11,561–11,565, 1992.

Cormac, A. M., Representation of a function by its line integrals, with some radiological applications, I, *J. Appl. Phys.*, *34*, 2722–2727, 1963a.

Cormac, A. M., Representation of a function by its line integrals, with some radiological applications, II, *J. Appl. Phys.*, *35*, 2908–2913, 1963b.

Crutzen, P. J., and F. Arnold, Nitric acid cloud formation in the cold Antarctic stratosphere: a major cause for the springtime "ozone hole", *Nature*, *324*, 651–655, 1986.

Csorba, I., *Image Tubes*, Howard Sams, Indianapolis, Indiana, 1985.

Davis, T. N., and G. T. Hicks, Television cinemaphotography of Auroras and preliminary measurements of auroral velocities, *J. Geophys. Res.*, *69*, 1931, 1964.

de Mairan, J. J. D., *Traité Physique et Historique de l'Aurore Boréale*, Imprimerie Royale, Paris, 1733, (2ns ed., 1754).

Delbouille, L. G., L. G. Roland, and L. Neven, *Photometric atlas of the solar spectrum from 3000 to 10000 Å*, Institute d'Astrophysique de l'Universite de Liege, Cointe-Ougre, Belgium, 1973.

Djuth, F. T., P. A. Bernhardt, C. A. Tepley, J. A. Gardner, M. C. Keley, A. L. Broadfoot, L. M. Kagan, M. P. Sulzer, J. H. Elder, C. Selcher, B. Isham, C. Brown, and H. C. Carlson, Large airglow enhancements produced via wave-plasma interactions in sporadic E, *Geophys. Res. Lett.*, *26*, 1557–1560, 1999.

Dressler, R. A., J. A. Gardener, R. H. Salter, and E. Murad, Luminescence measurements of $Ar^+ + H_2O$ and $N_2^+ + H_2O$ suprathermal charge transfer collisions: Product state distribution from $H_2O^+\tilde{A}^2A_1 - \tilde{X}^2B_1$ analysis, *J. Chem. Phys.*, *96*, 1062–1076, 1992.

Eather, R. H., *Majestic lights the aurora in science, history and the arts*, AGU (American Geophysical Union), Washington D.C., 1980, ISBN: 0-87590-215-4.

Eather, R. H., Low light level imaging design, *Tech. rep.*, Air Force Geophysics laboratory, USAF, Hanscom AFB, Massachusetts USA, 1982, AFGL-TR-82-0308.

Eide, Å. J., V. Becanovic, U. Brändström, C. Holmström, M. Larsson, I. M. Lillesand, T. Lindblad, C. S. Lindsey, Å. Steen, and J. Waldemark, Pulse coupled neural network pre-processing of aurora images, in *AI Applications in Solar Terrestial Physics*, vol. WPP-148, pp. 201–205, European Space Agency, 1997.

Ejiri, M., M. Okada, M. Tsutsumi, M. Taguchi, and S. Okano, All sky imager observation of aurora and airglow at south pole station : Initial results, in *Proceedings of the 25th annual European Meeting on Atmospheric Studies by Optical Methods, Granada, Spain*, pp. 54–57, 1998.

Ejiri, M., T. Aso, M. Okada, M. Tsutsumi, M. Taguchi, N. Sato, and S. Okano, Japanese research project on Arctic and Antarctic observations of the middle atmosphere, *Adv. Space Res.*, *24*, 1689–1692, 1999.

Elvey, C. T., and W. Stoffregen, Auroral photography by all-sky camera, *Ann. IGY.*, *5*, 117–151, 1957.

Enell, C.-F., Optical studies of polar stratospheric clouds and related phenomena, Ph.D. thesis, Swedish Institute of Space Physics, Kiruna, Sweden, 2002, (IRF Scientific Report 278), ISBN: 91-7305-307-4.

Enell, C.-F., B. Gustavsson, Å. Steen, U. Brändström, P. Rydesäter, P. Johansson, T. Wagner, U. Friess, K. Pfeilsticker, and U. Platt, Optical studies of polar stratospheric clouds, in *Proceedings of SPIE, Satellite remote sensing of clouds and the atmosphere IV*, edited by J. E. Russell, vol. 3867, pp. 290–297, The International Society for Optical Engineering, 1999a.

Enell, C.-F., Å. Steen, B. Gustavsson, U. Brändström, P. Johansson, T. Wagner, U. Frieß, K. Pfeilsticker, and U. Platt, Studies of polar stratospheric clouds occurence at Kiruna, in *XXV annual European Meeting on Atmospheric Studies by Optical Methods*, pp. 122–126, Instituto de Astrofísica de Andalucia, Granada, Spain, 1999b.

Enell, C.-F., Å. Steen, B. Gustavsson, U. Brändström, P. Johansson, T. Wagner, U. Frieß, K. Pfeilsticker, U. Platt, and K.-H. Fricke, Detection of polar stratospheric clouds at Kiruna, in *Air pollution report 69, Mesoscale processes in the stratosphere*, edited by K. S. Carslaw and G. T. Amanatidis, vol. 18912, pp. 65–68, Office for Official Publications of the European Communities, European Commission, Luxembourg, 1999c, ISBN 92-828-4629-6.

Enell, C.-F., B. Gustavsson, Å. Steen, U. Brändström, and P. Rydesäter, Multistatic imaging and optical modelling of nacreous clouds, *Phys. Chem. Earth*, *25*, 451–457, 2000.

Enell, C.-F., U. Brändström, B. Gustavsson, S. Kirkwood, K. Stebel, and Å. Steen, Case studies of the development of polar stratospheric clouds using bistatic imaging, *Ann. Geophys.*, 2003, (in press).

Frey, S., H. U. Frey, D. J. Carr, O. H. Bauer, and G. Haerendel, Auroral emission profiles extracted from three-dimensionally reconstructed arcs., *J. Geophys. Res.*, *101*, 21,731–21,741, 1996.

Galand, M., Special section: Proton precipitation into the atmosphere, *J. Geophys. Res.*, *106*, 1–178, 2001.

Galperin, Y. I., Multiple scales in auroral plasmas, *J. Atmos. Solar and Terr. Phys.*, *64*, 211–229, 2001.

Gardner, J. A., A. L. Broadfoot, W. J. McNeil, S. T. Lai, and E. Murad, Analysis of the GLO-1 observations of meteoric metals in the thermosphere, *J. Atmos. Terr. Phys.*, *61*, 545–562, 1999.

Gartlein, C. W., Unlocking secrets of the northern lights, *Nat. Geograph. Mag.*, p. 673, 1947.

Gassendi, P., *De vita Pereskii, Anno 1621*, Edit. Hag. Com., 1651.

Gilbert, P., Iterative methods for the three-dimensional reconstruction of an object from projections, *J. Theor. Boil.*, *36*, 105–117, 1972.

Gurevich, A. V., and G. M. Milikh, Artificial airglow due to modifications of the ionosphere by powerful radio waves, *J. Geophys. Res.*, *102*, 389–394, 1997.

Gurevich, A. V., Y. S. Dimant, G. M. Milikh, and V. V. Va'skov, Multiple acceleration of electrons in the regions of high power radio-wave reflection in the ionosphere, *J. Atmos. Terr. Phys.*, *47*, 1057–1070, 1985.

Gustavsson, B., A study of feasible tomographic inversion techniques for ALIS, *Tech. Rep. 039*, Swedish Institute of Space Physics, Kiruna, Sweden, 1992, ISSN 0284-1738.

Gustavsson, B., Private communication, 1997.

Gustavsson, B., Tomographic inversion for ALIS noise and resolution, *J. Geophys. Res.*, *103*, 26,621–26,632, 1998.

Gustavsson, B., Three Dimensional Imaging of Aurora and Airglow,, Ph.D. thesis, Swedish Institute of Space Physics, Kiruna, Sweden, 2000, (IRF Scientific Report 267), ISBN: 91-7191-878-7.

Gustavsson, B., Private communication, 2003.

Gustavsson, B., T. Sergienko, M. T. Rietveld, F. Honary, Å. Steen, B. U. E. Brändström, T. B. Leyser, A. L. Aruliah, T. Aso, and M. Ejiri, First tomographic estimate of volume distribution of enhanced airglow emission caused by HF pumping, *J. Geophys. Res.*, *106*, 29,105–29,123, 2001a.

Gustavsson, B., Å. Steen, T. Sergienko, and B. U. E. Brändström, Estimate of auroral electron spectra, the power of ground-based multi-station optical measurements, *Phys. Chem. Earth*, *26*, 189–194, 2001b.

Gustavsson, B., B. U. E. Brändström, Å. Steen, T. Sergienko, T. B. Leyser, M. T. Rietveld, T. Aso, and M. Ejiri, Nearly simultaneous images of HF-pump enhanced airglow at 6300 Å and 5577 Å, *Geophys. Res. Lett.*, *29*, 2003, paper No. 10.1029/2002GL015350.

Hallinan, T. J., H. C. Stenbaek-Nielsen, and C. S. Deehr, Enhanced aurora, *J. Geophys. Res.*, *90*, 8461–8475, 1985.

Hammarskjöld, D., *Vägmärken*, Albert Bonniers Förlag AB, 1963, (In Swedish, reprinted 1999 ISBN:9100571121).

Hammarskjöld, D., *Markings*, Knopf, New York, 1964, (transl. by Leif Sjöberg and W. H. Auden, ISBN: 039443532X).

Haslett, J. C., and L. R. Megill, A model of the enhanced airglow excited by RF-radiation, *Radio Sci.*, *9*, 1005–1019, 1974.

Hecht, J. H., A. B. Christensen, D. J. Strickland, and R. R. Meier, Deducing composition and incident electron spectra from ground-based auroral optical measurements: Variation in oxygen density, *J. Geophys. Res.*, *94*, 13,553–13,563, 1989.

Hedin, M., I. Häggström, A. Pellinen-Wannberg, I. Häggström, L. Andersson, U. Brändström, B. Gustavsson, Å. Steen, A. Westman, G. Wannberg, T. van Eyken, T. Aso, C. Cattell, C. W. Carlson, and D. Klumpar, Trough observations with the EISCAT radars, ALIS auroral imaging system and FAST satellite, in *Proceedings of RadioVetenskap och Kommunikation 99*, edited by J.-O. Gustavsson, vol. 1, pp. 113–117, Högskolan i Karlskrona/Ronneby, Karlskrona, Sweden, 1999, ISBN 91-630-8156-3.

Hedin, M., I. Häggström, A. Pellinen-Wannberg, I. Häggström, L. Andersson, U. Brändström, B. Gustavsson, Å. Steen, A. Westman, G. Wannberg, T. van Eyken, T. Aso, C. Cattell, C. W. Carlson, and D. Klumpar, 3-D extent of the main ionospheric trough —a case study, *Adv. Polar Upper Atmos. Res.*, *14*, 157–162, 2000.

Henriksen, K., W. Stoffregen, B. Lybekk, and Å. Steen, Photometer and spectrometer search of the oxygen green and red lines during artificial ionospheric heating in the auroral zones, *Ann. Geophys.*, *2*, 73–76, 1984.

Hernandez, G., *Fabry-Perot Interferometers*, Cambridge University Press, 1986, ISBN: 0-521-32238-3.

Hertel, R. J., Signal and noise properties of proximity focused image tubes, in *Ultrahigh Speed and High Speed Photography, Photonics and Videography*, edited by G. L. Stradling, vol. 1155, pp. 332–343, The International Society for Optical Engineering, 1989.

Hesstvedt, E., On the physics of mother of pearl clouds, *Geofysiske Publikasjoner*, *XXI*, 1–32, 1960.

Holst, G. C., *CCD arrays, cameras and displays*, 2nd ed., The International Society for Optical Engineering, 1998, ISBN: 0-8194-2853-1.

Høymork, S. H., ed., *Sensors and Instruments for Space Exploration*, chap. 6. Measurements by optical methods, pp. 71–119, 2nd ed., Swedish Institute of Space Physics, Kiruna, 2000.

Hunten, D. M., F. E. Roach, and J. W. Chamberlain, A photometric unit for the aurora and airglow, *J. Atmos. Terr. Phys.*, *8*, 345–346, 1956.

Hyppönen, M., R. Pellinen, C. Sucksdorff, and R. Torniainen, Digital all-sky camera, *Tech. Rep. 9*, Finnish Meteorological Institute, Helsinki, 1974.

Höffner, J., and U. von Zahn, The 1996 Leonid shower as studied with a potassium lidar: Observations and inferred meteoroid sizes, *J. Geophys. Res.*, *104*, 2633–2643, 1999.

Ivanov, V. E., and T. I. Sergienko, Interaction of the auroral electrons with the atmospheric gases. (the Monte-Carlo modelling), 1992, Nakua, St. Petersburg, 1992.

Janesick, J. R., T. Elliott, S. Collins, M. M. Blouke, and J. Freeman, Scientific charge-coupled devices, *Optical Engineering*, *26*, 692–714, 1987.

Johansson, H., Station software for ALIS, *IRF Tech. Report 036*, Swedish Institute of Space Physics, 1991, ISSN 0284-1738.

Jones, A. R. V., R. L. Gattinger, F. Creutzberg, F. R. Harris, A. G. McNamara, A. W. Yau, E. J. Llewellyn, D. Lummerzheim, M. H. Rees, I. C. McDade, and J. Margot, The ARIES auroral modelling campaign: Characterization and modelling of an evening auroral arc observed from a rocket and a ground-based line of meridian scanners, *Planet Space Sci.*, *39*, 1677–1705, 1991.

Jones, A. V., *Aurora*, vol. 9 of *Geophysics and astrophysics monographs*, D. Reidel Publishing Company, 1974, ISBN: 90-277-0272-1.

Kaila, K., Optical instrumentation of Oulu, `http://spaceweb.oulu.fi/projects/optical` and Private communication, 2003a.

Kaila, K., Private communication, 2003b, data analysis and publication in progress.

Kaila, K., Private communication, 2003c, (See also `http://spaceweb.oulu.fi/projects/optical`).

Kaila, K. U., An iterative method for calculating the altitudes and positions of auroras along the arc, *Planet. Space Sci.*, *35*, 245–258, 1987.

Kaila, K. U., and H. J. Holma, Absolute calibration of photometer, *Phys. Chem. Earth*, *B(25)*, 467–470, 2000.

Keo Consultants, Kiruna telecentric lens systems, 1994, vendor-provided documentation.

Keo Consultants, Telecentric lens for Kyoto university, 1997, vendor-provided documentation.

Kinser, J. M., and T. Lindblad, Detection of microcalcifications by cortical stimulation, in *Proceedings EANN'97 Neural networks in engineering systems*, edited by A. Bulsari and S. Kallio, pp. 203–206, 1997, ISBN: 952908667-9.

Kosch, M. J., T. Rietveld, M., S. Å, and T. Hagfors, HF-Induced Airglow: Double Patches, *Phys. Chem. Earth*, *25*, 475–581, 2000a.

Kosch, M. J., T. Rietveld, M., T. Hagfors, and T. B. Leyser, High-latitude HF-induced airglow displaced equatorward of the pump beam, *Geophys. Res. Lett.*, *27*, 2817–2820, 2000b.

Kosch, M. J., M. T. Rietveld, A. J. Kavanagh, C. Davis, T. Yeoman, F. Honary, and T. Hagfors, High-latitude pump-induced optical emissions for frequencies close to th third electron gyro-harmonic, *Geophys. Res. Lett.*, *29*, 27–1–274, 2002a.

Kosch, M. J., M. T. Rietveld, T. Yeoman, K. Cierpka, and T. Hagfors, The high-latitude artificial aurora of 21 February 1999: An analysis, *Adv. Polar Upper Atmos. Res.*, 2002b, (in press).

Labsphere, *A guide to integrating sphere theory and applications*, Labsphere, 1997.

Lance, C., and R. H. Eather, High frequency active auroral research program (HAARP) imager, *Tech. rep.*, Air Force Geophysics laboratory, USAF, Hanscom AFB, Massachusetts USA, 1993, PL-TR-93-2219.

Lauche, H., and O. Widell, Intercalibration of low light level sources, letter from Hans Lauche, 2000a.

Lauche, H., and O. Widell, Intercalibration of low light level sources, in *Proc. of 27th Annual European Meeting on Atmospheric Studies by Optical Methods, Stockholm, Sweden*, Meteorological institution, Stockholm university, Sweden, 2000b.

Leyser, T. B., Parametric interactions between upper hybrid and lower hybrid waves in heating experiments, *Geophys. Res. Lett.*, *18*, 408–411, 1991.

Leyser, T. B., and B. Gustavsson, Private communication, 2003.

Leyser, T. B., B. Gustavsson, B. U. E. Brändström, F. H. Å. Steen, T. A. M. T. Rietveld, and M. Ejiri, Simultaneous measurements of high-frequency pump-enhanced airglow and ionospheric temperatures at auroral latitudes, *Adv. Polar Upper Atmos. Res.*, *14*, 1–11, 2000.

Leyser, T. B., B. U. E. Brändström, B. Gustavsson, T. Sergienko, and M. T. Rietveld, Enhanced airglow by high frequency electromagnetic pumping with the EISCAT heating facility and observed by the multi-station auroral large imaging system ALIS, in *URSI*, URSI, 2002, paper 815, 2002.

Lodin, H., The value of tomography in examination of the intrapulmonary bronchi, *Acta Radiol. Suppl.*, *101*, 1935.

Love, S. G., and D. E. Brownlee, A direct measurement of the terrestial mass accretion rate of cosmic dust, *Science*, *262*, 550–553, 1993.

Macleod, H. A., *Thin-film optical filters*, Macmillan, New York, 1986, ISBN: 0-02-948110-4.

Mantas, G. P., Large 6300 Å airglow intensity enhancements observed in ionosphere heating experiments are excited by thermal electrons, *J. Geophys. Res.*, *99*, 8993, 1994.

Mantas, G. P., and H. C. Carlson, Reinterpretation of the 6300 Å airglow enhancements observed in the ionosphere heating experiments based on analysis of Platteville Colorado, *J. Geophys. Res.*, *101*, 195–209, 1996.

Massey, P., *A User's guide to CCD Reductions with IRAF*, National Optical Astronomy Observatory, 1992, `http://iraf.noao.edu/docs`.

McDade, I. C., and E. J. Llewellyn, Satellite airglow limb tomography: Methods for recovering structured emission rates in the mesospheric airglow layer, *Canad. J. Phys.*, *71*, 552–563, 1994.

McNaught, R. H., and D. J. Asher, Variation of Leonid maximum times with location of observer, *Meteorit. Planet. Sci.*, *34*, 975–978, 1999.

McNeil, W. J., E. Murad, and S. T. Lai, Comprehensive model for the atmospheric sodium layer, *J. Geophys. Res.*, *100*, 16,847–16,855, 1995.

McNeil, W. J., S. T. Lai, and E. Murad, Models of thermospheric sodium, calcium and magnesium at the magnetic equator, *Adv. Space Res.*, *21*, 863–866, 1998.

McNeil, W. J., R. A. Dressler, and E. Murad, Impact of a major meteor storm on earth's ionosphere: A modeling study, *J. Geophys. Res.*, *106*, 10,447–10,465, 2001.

McWhirter, I., Imaging photon detectors and their use with single and multiple fabry-perot etalon systems for atmospheric wind measurements, Ph.D. thesis, University College London, London, 1993.

Meier, R. R., D. J. Strickland, J. H. Hecht, and A. B. Christensen, Deducing composition and incident electron spectra from ground-based auroral optical measurements: a study of auroral red line processes, *J. Geophys. Res.*, *94*, 13,541–13,552, 1989.

Mills, D. L., Network time protocol (version 3) specification, implementation and analysis, Request for Comments: 1305, 1992, ftp://ftp.rfc-editor.org/in-notes/rfc1305.txt.

Mohn, H., Perlemorskyer, in *Christiania Videnskabs-Selskabs Forhandlinger*, vol. 2, A. W. Brøggers bogtryckeri, Christiania (Oslo), Norway, 1893.

Na, H., and H. Lee, Orthogonal decomposition technique for ionospheric tomography, *Int. J. Imaging Syst. Technol.*, *3*, 354–365, 1991.

NASA, *Definition of the Flexible Image Transport System (FITS)*, NASA/Science Office of Standards and Technology, Code 633.2, NASA Goddard Space Flight Center, Greenbelt MD, USA, 1999, nOST 100-2.0, http://fits.gsfc.nasa.gov/fits_documentation.html.

Nilsson, L., OPERA operations program for ALIS version 1.0, *Internal Note 024*, Swedish Institute of Space Physics, Kiruna, Sweden, 1994.

Nilsson, L., and B. Nyström, OPERA operations program for ALIS version 1.0, *IRF Tech. Rep. 037*, Swedish Institute of Space Physics, Kiruna, Sweden, 1992, ISSN 0284-1738.

Noxon, J. F., and R. M. Goody, Observations of day airglow, *J. Atmos. Sci.*, *19*, 342–343, 1962.

Okano, S., S. Takeshita, and M. Taguchi, Absolute calibration system at NIPR for aurora/airglow measurements using an 1.9 m integrating sphere, in *Proceedings of the 24th annual European Meeting on Atmospheric Studies by Optical Methods*, Sentraltrykkeriet A/S Bodø, 1997, ISBN: 82-994583-0-7.

Pedersen, and Carlson, First observations of HF heater-produced airglow at the High Frequency Active Auroral Research Program facility: Thermal excitation and spatial structuring, *Radio Sci.*, *36*, 1013–1026, 2001.

Pellinen, R., and K. Kaila, Optical groundbased network, in *Proc. of the Cluster workshop, Svalbard, Norway 16–19 Sept.*, pp. 147–158, European Space Agency Publications Division, 1991, (ESA SP-330).

Pellinen-Wannberg, A., E. Murad, B. Gustavsson, U. Brändström, C.-F. Enell, C. Roth, I. P. Williams, and Å. Steen, Water in Leonid meteor trails, *(in preparation)*, 2003.

Perkins, F. W., and P. K. Kaw, On the role of plasma instabilities in ionospheric heating by radio waves, *J. Geophys. Res.*, *76*, 282–284, 1971.

Pliny, *Historiae Naturalis*, vol. II, chap. 27,33, (ancient text), ca. 77.

Pountain, D., The transputer strikes back, *Byte*, pp. 265–275, 1991.

Preston, T. J., *4400 Quad CCD Camera controller user guide. System description and operations manual*, AstroMed Ltd., Cambridge, 1993.

Preston, T. J., *4400 Quad CCD Camera controller user guide for motherboard issue B. System description and operations manual*, AstroCam Ltd., Cambridge, 1995.

Puccio, W., Private communication, 2002.

Pudovkin, M. I., Å. Steen, and U. Brändström, Vorticity in the magnetospheric plasma and its signature in the aurora dynamics., *Space Science Rev.*, *80*, 411–444, 1997.

Pudovkin, M. I., Å. Steen, N. V. Nikolaev, O. I. Kornilov, U. Brändström, B. Gustavsson, and P. Rydesäter, Automatic recognition of auroral forms, in *Ninth workshop on Virtual Intelligence / Dynamic neural networks*, edited by M. L. P. Thomas Lindbladh and J. Kinser, vol. 3728, pp. 121–127, Royal Institute of Technology, Stockholm, Sweden, The International Society for Optical Engineering, 1998, ISBN 0-8194-3202-4.

Raspopov, O. M., V. A. Dergachev, and E. G. Goos'kova, Ezekiel's vision: visual evidence of Sterno-Etrussia geomagnetic excursion?, *EOS, Transactions, American Geophysical Union*, *84*, 77, 2003.

Rayleigh, L., Absolute intensity of the aurora line in the night sky, and the number of atomic transitions required to maintain it, *Proc. Roy. Soc. London*, *A129*, 458, 1930.

Rees, D., I. McWhirter, P. B. Hays, and T. Dines, A stable rugged, capacitance-stabilised piezoelectric scanned Fabry-perot etalon, *J. Phys. E: Sci. Instrum.*, *14*, 1320–1325, 1981.

Rees, D., M. Vyssogorets, N. P. Meredith, E. Griffin, and Y. Chaxell, The doppler wind and temperature system for the ALOMAR observatory: Design and initial results, *J. Atmos. Terr. Phys.*, *58*, 1827–1842, 1996.

Rees, D., R. W. Smith, F. Sigernes, K. Henriksen, U. Brändström, W. B. Wickwar, N. D. Lloyd, and M. Harris, Observations of thermospheric wind patterns in the vicinity of the polar cusp from a doppler imaging system, in *Proceedings of the 24th annual European Meeting on Atmospheric Studies by Optical Methods*, Sentraltrykkeriet A/S Bodø, 1997, ISBN: 82-994583-0-7.

Rees, D., U. von Zahn, G. von Cossart, K.-H. Fricke, W. Eriksen, and J. A. McKay, Daytime LIDAR measurements of the stratosphere and mesosphere at the ALOMAR observatory, *Adv. Space Res.*, 1999, proc. COSPAR meeting, Nagoya, July 1998, accepted.

Rees, D., M. Conde, Å. Steen, and U. Brändström, The first daytime ground-based optical image of the aurora, *Geophys. Res. Lett.*, *27*, 313–316, 2000.

Rees, M. h., and D. Luckey, Auroral electron energy derived from ratio of spectroscopic emissions 1. model computations, *J. Geophys. Res.*, *79*, 5181, 1974.

Rietveld, M. T., H. Kohl, H. Kopka, and P. Stubbe, Introduction to ionospheric heating at Tromsø —I. Experimental overview, *J. Atmos. Terr. Phys.*, *55*, 577–599, 1993.

Romick, G. J., and A. E. Belon, The spatial variation of auroral luminosity—II, *Planet Space Sci.*, *15*, 1695–1716, 1967.

Rydesäter, P., and B. Gustavsson, Investigation of smooth basis functions and an approximated projection algorithm for faster tomography, *Int. J. Imaging Syst. Technol.*, *11*, 347–354, 2001.

Rydesäter, P., Processing of multi-station auroral image data, Lic. thesis, Applied Physics and Electronics, Umeå University, Umeå, Sweden, 2001, ISBN: 91-7305-149-7.

Rydesäter, P., Å. Steen, U. Brändström, and B. Gustavsson, Classifying auroras using artificial neural networks, in *Ninth workshop on Virtual Intelligence / Dynamic neural networks*, edited by M. L. P. Thomas Lindbladh and J. Kinser, vol. 3728, pp. 115–120, Royal Institute of Technology, Stockholm, Sweden, The International Society for Optical Engineering, 1998, ISBN 0-8194-3202-4.

Rydesäter, P., B. Gustavsson, U. Brändström, and Å. Steen, Lossy compression of scientific images of aurora, in *Proc. of 28th Annual European Meeting on Atmospheric Studies by Optical Methods*, Sodankylä Geophysical Observatory, 2001, (in press).

Scourfield, M. W. J., and N. R. Parsons, Auroral pulsations and flaming — Some initial results of a cinematographic study using an image intensifier, *Planet Space Sci.*, *17*, 1141, 1969.

Seneca, *Quaestiones Naturales*, vol. I, chap. 14–15, (ancient text), ca. 63.

Sergienko, T., Private communication, 2003.

Sergienko, T., B. Gustavsson, Å. Steen, U. Brändström, M. Rietveld, T. Leyser, and F. Honary, Analysis of excitation of the 630.0 nm airglow during heating experiment in Tromsø on February 16, 1999, *Phys. Chem. Earth*, *25*, 531–535, 2000.

Simpson, W., The point-to-point protocol (ppp), *Request For Comments: 1661*, 1994, ftp://ftp.rfc-editor.org/in-notes/rfc1661.txt.

Sipler, D. P., and M. A. Biondi, Measurements of $O(^1D)$ quenching rates in the F region, *J. Geophys. Res.*, *77*, 6202–6212, 1972.

Siscoe, G. L., A historical footnote on the origin of aurora borealis, *EOS, Transactions, American Geophysical Union*, *59*, 994, 1978.

Siscoe, G. L., S. M. Silverman, and K. D. Siebert, Ezekiel and the Northern lights: Biblical aurora seems plausible, *EOS, Transactions, American Geophysical Union*, *83*, 173, 2002.

Solomon, S., R. R. Garcia, F. S. Rowland, and D. J. Wuebbles, On the depletion of Antarctic ozone, *Nature*, *321*, 755–758, 1986.

Solomon, S. C., P. B. Hays, and V. J. Abreu, Tomographic inversion of satellite photometry, *Applied Optics*, *23*, 3409–3414, 1984.

Solomon, S. C., P. B. Hays, and V. J. Abreu, The auroral 6300 Å emisson: Observation and modelling, *J. Geophys. Res.*, *93*, 9867–9882, 1988.

Spurny, P., H. Betlem, K. Jobse, P. Koten, and J. van't Leven, New type of bright Leonid meteors above 130 km, *Meteorit. Planet. Sci.*, *35*, 1109–1115, 2000.

Steen, Å., The optical laboratory in Kiruna: A new research facility in the auroral zone, *KGI Tech. Report 033*, Kiruna Geophysical Institute, Kiruna, Sweden, Kiruna, Sweden, 1987, ISSN 0349-2672.

Steen, Å., Investigations of auroral dynamics, techniques and results, Ph.D. thesis, Swedish Institute of Space Physics, Kiruna, Sweden, 1988a, (KGI Scientific Report 1994), ISSN 0984-1703.

Steen, Å., An auroral height measuring system designed for real time operation, *Rev. Sci. Instrum.*, 1988b.

Steen, Å., An Auroral Large Imaging System in Northern Scandinavia, in *Proc. 9th Symposium on European rocket and ballon programmes and related research, Lahnstein, FRG*, pp. 299–303, European Space Agency, 1989, ESA SP-291.

Steen, Å., ed., *Auroral Tomography workshop proceedings*, IRF Scientific Report 213, Swedish Institute of Space Physics, 1993, ISSN 0284-1703.

Steen, Å., Application for equipment to an optical calibration facility in kiruna, Funding application to Forskningsrådsnämnden (FRN), 1998, (partly in Swedish, IRF Dnr 238-150/98).

Steen, Å., and P. N. Collis, High time-resolution imaging of auroral arc deformation at substorm onset, *Planet. Space Sci.*, *36*, 715–732, 1988.

Steen, Å., P. N. Collis, and I. Häggström, On the development of folds in auroral arcs, *J. Atmos. Terr. Phys.*, *50*, 301–313, 1988.

Steen, Å., U. Brändström, and K. Kaila, A scientific and technical description of ALIS, in *Proc. NSSR Annual meeting Bolkesjø, Norway*, pp. 153–164, Nordic Society for Space Research, 1990.

Steen, Å., U. Brändström, and B. Gustavsson, ALIS — a multi station imaging system at high latitude with multi disciplinary scientific objectives, in *Proceedings 13th ESA Symposium on European Rocket and Balloon Programmes and Related Research*, pp. 261–266, ESA, 1997a.

Steen, Å., B. Gustavsson, and U. Brändström, Temporal variation of 2D altitude distributions of lee-wave generated polar stratospheric clouds, in *Proceedings of the 4th European symposium of polar stratospheric ozone*, 1997b.

Steen, Å., B. Gustavsson, U. Brändström, T. Aso, and M. Ejiri, OI 846.6 nm auroral imaging, in *Proceedings of the 25th annual European Meeting on Atmospheric Studies by Optical Methods, Granada, Spain*, pp. 90–95, Instituto de Astrofísica de Andalucia, Granada, Spain, 1999a.

Steen, Å., B. Gustavsson, C.-F. Enell, and U. Brändström, PSC dynamics investigated by multi-station imaging — techniques, results and prospects, in *Air pollution research report. Mesoscale processes in the stratosphere*, edited by K. Carslaw and G. Amanatidis, vol. 69, pp. 239–242, European Comission, 1999b, ISBN 92-828-4629-6.

Stenbaek-Nielsen, H. C., and T. J. Hallinan, Pulsating auroras: Evidence for non-collisional thermalization of precipitating particles., *J. Geophys. Res.*, *84*, 3257–3271, 1979.

Stoffregen, W., All-sky camera auroral research during the third geophysical year 1957–1958, *Tellus*, *7*, 509–517, 1955.

Stoffregen, W., An all-sky camera for auroral research, description and operational manual, *Tech. rep.*, Uppsala Jonosfärsobservatorium, 1956.

Stoffregen, W., ed., *I.G.Y. ASCAPLOTS*, vol. XX (part 1) of *Annals of the international geophysical year*, Pergamon Press, Oxford, London, New York, Paris, 1962.

Størmer, C., Bericht über eine Expedition nach Bossekop etc., *Vid. Selsk. Skr. Math. Nat. Kl.*, 1911, Christiania (Oslo), Norway.

Størmer, C., Photogrammetrishe bestimmung der Höhe von irisierenden Wolken (Perlmutterwolken) am 30. Dezember 1926., *Geofysiske Publikasjoner*, *5*, 1–8, 1930.

Størmer, C., *The Polar Aurora*, Clarendon Press, Oxford, 1955.

Strickland, D. J., R. R. Meier, J. H. Hecht, and A. B. Christensen, Deducing composition and incident electron spectra from ground-based auroral optical measurements: theory and results, *J. Geophys. Res.*, *94*, 13,527–13,539, 1994.

Stubbe, P., H. Kopka, H. Lauche, M. T. Rietveld, A. Brekke, O. Holt, T. B. Jones, T. Robinson, A. Hedberg, B. Thidé, B. Crochet, and H. J. Lotz, Ionospheric modification experiments in northern Scandinavia, *J. Atmos. Terr. Phys.*, *44*, 1025–1041, 1982.

Syrjäsuo, M., New Finnish all-sky cameras, in *Proceedings of the 24th annual European meeting on atmospheric studies by optical methods*, pp. 247–251, Sentraltrykkeriet A/S Bodø, 1997, ISBN: 82-994583-0-7.

Syrjäsuo, M. T., All-sky camera, (master's-thesis), Helsinki Univ. of Technology, 1996.

Syrjäsuo, M. T., Auroral monitoring network: From all-sky camera system to automated image analysis, (D.Sc.(Tech.)-thesis), Finnish Meteorological Institute, Helsinki, Finland, 2001, Contribution series 32, ISBN: 951-697-551-8.

Theuwissen, A. J. P., *Solid-state imaging with charge-coupled devices*, vol. 1 of *Solid-state scenece and technology library*, Kluwer, 1995.

Tolbert, M. A., Polar clouds and sulfate aerosols, *Science*, *272*, 1597, 1996.

Toon, O. B., P. Hamill, R. P. Turco, and J. Pinto, Condensation of HNO_3 and HCl in the winter polar stratospheres, *Geophys. Res. Lett.*, *13*, 1284–1287, 1986.

Tornéus, A., GOSSIP a general information panel for ALIS, *IRF Tech. Rep. 040*, Swedish Institute of Space Physics, Kiruna, Sweden, 1992, ISSN 0284-1738.

Torr, M. R., and P. Espy, Intercalibration of instrumentation used in the observation of atmospheric emissions: Second progress report, *Tech. Rep. 101*, Utah State University, Center for atmospheric and space sciences, Logan Utah, 1981.

Trondsen, T. S., High spatial and temporal resolution auroral imaging, Ph.D. thesis, University of Tromsø, 1998.

Urashima, A., T. Aso, M. Ejiri, Å. Steen, U. Brändström, and B. Gustavsson, Camera calibration by integrating sphere for the auroral tomography observation, *Adv. Polar Upper Atmos. Res.*, *13*, 79–88, 1999.

Vaattovaara, M., and J. Enback, Development of a calibration system using a monochromator and an APD, *Internal Note 023*, Swedish Institute of Space Physics, 1993.

Vegard, L., Photographische Aufnahmen des Nordlichtspektrums mit einem Spectrographen von grosser Dispersion, *Phys. Zhur.*, *14*, 677–681, 1913.

Vegard, L., and O. Krogness, The position in space of the aurora polaris, in *Geofysiske Publikasjoner*, vol. 1 of *Geofysiske Publikasjoner*, pp. 1–170, A. W. Brøggers bogtryckeri, Christiania (Oslo), Norway, 1920.

Veklerov, E., and J. Llacer, Feasible images and practical stopping rules for iterative algorithms im emission tomography, *IEEE Trans. Medical Imaging*, *8*, 186–193, 1989.

von Zahn, U., M. Gerding, J. Höffner, W. J. M. Neil, and E. Murad, Fe, Ca and K atom densities in the trails of Leonids and other meteors: Strong evidence of differential ablation., *Meteorit. Planet. Sci.*, *34*, 1017–1027, 1999.

Waldemark, J., V. Becanovic, U. Brändström, C. Holmström, M. Larsson, T. Lindblad, C. S. Lindsay, and Å. Steen, Investigation of useful image preprocessing for analysis of aurora images, in *Proceedings EANN*, 1997.

Wannberg, G., The G2-system and general purpose alternating code experiments for EISCAT, *J. Atmos. Terr. Phys.*, *55*, 543–557, 1993.

Weinbren, M., *A manual of tomography*, H. K. Lewis & Co., 1946.

Weinstock, J., Theory of enhanced airglow during ionospheric modifications, *J. Geophys. Res.*, *80*, 4331, 1975.

Weinstock, J., and B. Bezzerides, Theory of electron acceleration during parametric instabilities, *Phys. Rev. Lett.*, *32*, 754–758, 1974.

Widell, O., and H. Henricson, Intercalibration of low light level sources, in *Proc. of 28th Annual European Meeting on Atmospheric Studies by Optical Methods, Oulu, Finland*, Sodankylä Geophysical Observatory, 2001, (in press).

Wilcke, J. C., *Tal om de nyaste förklaringar öfver Norr-Skenet, hållet, i Kongl. Maj:ts höga närvaro, för dess vetenskaps-academie, vid praesidii nedläggande, den 7 Febr. 1778*, Johan Georg Lange, Stockholm, 1778.

Yamauchi, M., Private communication, 1999, (see also `http://www.irf.se/pics/YamaAuroraVideo/`).

Index of acronyms

CTE Charge Transfer Efficiency, 26
pc photo-cathode, 28
FoV field-of-view, 5
IBC International Brightness Coefficients, 23

ADCs Analogue to Digital Converters, 36
AIDA Alis Internal Data Administration, 69
AIS ALIS Imager Subsystem, 123
ALIS Auroral Large Imaging System, I, 1, 2, 5
ANS Abisko Scientific Station, 15
API Application Program Interface, 79
ASC All-Sky Camera, 2
ASI all-sky optical imager, 2

BSC Bright Star Catalogue, 62

CC control centre, 17
CCD Charge Coupled Device, 25, 123
CCH CCD Camera Head, 47, 123
CCH CCD camera head, 35
CCU Camera Control Unit, 36, 47, 123
CCU CPS Control Unit, 48
CPC Camera Positioning system Control unit, 123
CPC CPS Control unit, 44
CPS Camera Positioning System, 13, 44, 47, 123
CT Computer Tomography, 83

DCS Double Correlated Sampling, 27
DDS Digital Data Storage, 16
DIS Doppler Imaging System, 110
DQE detective quantum efficiency, 25

ECU Environmental Control Unit, 123
EISCAT European Incoherent SCATter radar, 75
EPLD Erasable, Programmable Logic Device, 36
EPROM Erasable Programmable Read-Only Memory, 71
ERP Effective Radiated Power, 86
ESD electrostatic discharge, 36

FITS Flexible Image Transfer System, 16
FPN Fixed Pattern Noise, 27
FW Filter Wheel, 123
FWC Filter Wheel Control unit, 41
FWC Filter-Wheel Control Unit, 123
FWC Filter-Wheel Control unit, 47

GIP General Instrument Platform, 151
GLIP Ground-based Low-light Imaging Platform, 8, 121
GPS Global Positioning System, 123, 131

HAARP High Frequency Active Auroral Research Program facility, 96
HALIS Housing for ALIS, 122
HF high-frequency, 85
HU Housekeeping Unit, 123, 130

ICC Imager Control Computer, 148
ICCD Intensified CCD, 25
IGY International Geophysical Year, 2
IPC Image Processing Computer, 13

IRF Swedish Institute of Space Physics, I, 10
IT Information Technology, 11

LAN Local Area Network, 132, 148

MART Multiplicative Algebraic Reconstruction Technique, 83
MCP micro-channel plate, 28
MHD Magnetohydrodynamical, 107

NBS National Bureau of Standards, 54
NIPR National Institute for Polar Research, 84
NIPU Near-Sensor Interface and Processing Unit, 123
NIPU Near-sensor Interface and Processing Unit, 13
ntp network time protocol, 131

OC Operations Centre, 17
OPERA OPERations system for ALIS, 69

PAI Portable Auroral Imager, 3, 30
PCNN Pulse Coupled Neural Networks, 81
PDU Power Distribution Unit, 123, 127
PLL Phase-Locked Loop, 131
ppp Point-to-Point Protocol, 15
PPS Pulse Per Second, 131
PRNU Photo Response Non-Uniformities, 27
PSC Polar Stratospheric Clouds, 1, 2, 77
PSF point spread function, 64
PWR Power subsystem, the electrical installation of the GLIP, 123

RBNN Radial Basis Neural Network, 82
RFI Radio Frequency Interference, 96

SC Station Computer, 132
SC station computer, 71
SC Station Computer, the main computer at the GLIP, 123
SEE Saturation Equivalent Exposure, 29
SIRT Simultaneous Iterative Reconstruction Technique, 84
SIT Selective Imaging Technique, 82
SVD Singular Value Decomposition, 82
Swe-ALIS the Swedish part of ALIS, 5

UPS Uninterruptable Power Supply, 148
UPS Uninterrupted Power Supply, 130

WAN Wide Area Network (connected to the Internet), 148
WLI WAN/LAN Interface consisting of the WAN-Interface, a router, a switch and possibly also a firewall, 148
WTS Westward Travelling Surges, 76

Index of notation

(i, j) pixel indices., 62
A_{CCD} $[m^2]$ area of CCD-detector., 23
A_{app} $[m^2]$ effective aperture of the optics., 23
A_i $[m^2]$ image area., 23
A_{pix}, 28
A_{pix} $[m^2]$ area of a CCD pixel., 23
A_s $[m^2]$ source area., 21
A_s $[m^2]$ source of area., 24
B_{ADC} $[\mu V/\text{counts}]$ ADC bit weight (90.6 μV/counts)., 58
$C_{abs\lambda c,binxy}$ $[R/\mathring{A}]$ absolute calibration constant with binned pixels., 62
$C_{abs\lambda c}$ $[R/\text{counts}]$ absolute calibration constant., 58
E Spectral radiant incidence (irradiance)., 23
G_{CCD} $[\mu V/e^-_\gamma]$ CCD output sensitivity., 58
G_P [1] programmable gain setting (5 or 10)., 58
G_S $[\text{counts}/e^-_\gamma]$ imager system gain., 58
I, 23
I $[R]$ column emission rate., 24
$I_{bg,ij}$ $[R]$ sky background correction., 61
I_{cal} $[R]$ "known" column emission rate., 58
I_{ij} $[R]$ calibrated pixel-value., 61
$I_{ls}(\lambda)$ $[R/\mathring{A}]$ column emission rate of the light standard., 58
L spectral radiant sterance., 21
L_E, 23
L_E $[W\,m^{-2}\,\text{sr}^{-1}]$ spectral radiant sterance in energy units., 22
M_{FO} [1] fibre-optic minification ratio., 28
N, 26
N_e [1] effective index of refraction., 40
Q_{EI}, 25
$Q_{E_{CCD}}$, 30
T, 23, 24
$T'(\lambda)$ [1] normalised filter transmittance function., 59
$T(\lambda, ...)$ [1] transmittance., 23
$T_f(\lambda)$, 59
T_{CCD}, 25
T_{FO}, 28
T_X, 23
T_a, 23
$T_{dome}(\lambda)$, 124
T_f, 23
$T_f(i, j, \lambda)$ [1] transmittance of the filter., 62
T_o, 23
T_w, 25
CTE^N, 26
DN [counts] digital output., 27
DN_{Cij} [counts] uniformly illuminated central pixels of the CCD., 58
DN_{DC} [counts] DC-bias-level., 30
DN_{SEE} [counts] maximum charge-well capacity., 29
DN_{ij}, 58
DN_{ij} [counts] digital output., 49
DN'_{ij}, 61
DN'_{ij} [counts] corrected pixel value., 54
DN_{max}, 29
DN_{min} [counts] minimum ADC output., 30
DR $[dB]$ Dynamic Range., 30
$\Delta\lambda$ $[\mathring{A}]$ filter passband., 58

$\Delta\lambda$ [Å] filter-bandwidth., 40
$E_{\gamma_{app}}$ [photons $s^{-1}\,m^{-2}$] spectral radiant incidence at the aperture., 24
E_{γ_i} [photons $s^{-1}\,m^{-2}$] spectral radiant incidence at the image plane., 24
FR [images/s] frame rate., 34
FoV_o [angle] optical field-of-view., 50
FoV_p, 10
FoV_p [angle] field-of-view per pixel., 10
FoV_x [angle] field-of-view in x-direction., 50
FoV_y [angle] field-of-view in y-direction., 50
L_γ, 22, 23
NEE Noise Equivalent Exposure., 29
Ω [sr] solid angle., 22
Ω_{ds}, 24
$\Phi_{\gamma_{app}}$ [photons/s] photon flux., 24
Φ [W] radiant flux., 22
Q_E, 25
Q_E [e^-/photons] quantum efficiency., 25
SNR, 27–30, 32
SNR [1] signal-to-noise ratio., 25
SNR_{ICCD} SNR of an ICCD., 29
α, 44, 45
a_ϕ, 45
a_ϕ [angle] azimuth., 44
β, 44, 45
B_0 [counts] black-level (or preset bias)., 51
B_{Lj} [counts] overscan-strip correction., 51
$B_{\overline{Z}ij}$ [counts] averaged bias-correction image., 52
B_{ij} [$B_]$ bias (or DC-level)., 51
B_q [counts] quadrant bias., 51
$\cos^4\theta$, 53
$\cos^4\theta$ "natural vignetting"., 24
D_{ij} counts dark-current correction image., 52
h_θ, 44
$\epsilon(\mathbf{r}, t, \lambda)$ [photons $m^{-3}s^{-1}$] volume emission rate., 22
η_E, 25
η_P [1] phosphor efficiency., 28
$F_{Mij\lambda}$, 59
$F_{Mij\lambda}$ [1] modelled flat-field correction., 54
$F_{ij\lambda}$ [1] flat-field correction., 52
$f_\#$ [1] f-number., 24
λ, 22, 23, 58
λ index., 52
$\lambda_1 \cdots \lambda_2$ [$\mathring{A}$] filter passband., 58
λ_θ, 40
λ_{cw}, 59
λ_{cw} [Å] filter centre wavelength at normal incidence., 40
ζ, 107
$n_{e^-_\gamma}$, 26
$\overline{n}_{e^-_{\gamma MCP}}$ [e^-_{RMS}] average number of secondary photoelectrons., 28
$\overline{n}_{e^-_{\gamma,pc}}$ [e^-_{RMS}] average number of signal electrons generated by the photo-cathode., 28
$\overline{n}_{e^-_{\gamma ij}}$, 58
$n_{e^-_{max}}$ [e^-] charge well capacity., 29
$n_{\gamma_{CCD}}$ [photons] number of photons hitting the CCD., 25
n_{γ_i} , 28
n_{γ_i} [photons] number of photons reaching the image plane., 25
$n_{\gamma_{pix}}$ [photons] number of photons hitting an individual pixel., 25
ν, 22
$\overline{X}$, 26
$\overline{DN}'_C$, 60
$\overline{g}$, 29
$\overline{g}$ [1] average MCP gain., 28
$\overline{n}_{e^-_\gamma}$ [e^-_{RMS}] average number of photoelectrons., 26
e^-_{RMS}, 27
$\langle X \rangle$, 26
$\langle n_{e^-_{ICCD}} \rangle$ [e^-_{RMS}] total noise for the ICCD., 29
$\langle n_{e^-_\gamma} \rangle$ [e^-_{RMS}] standard deviation of the noise resulting from the

photoelectrons., 26
$\langle n_{e_d^-} \rangle$ $[e^-_{RMS}]$ dark-current noise., 26
$\langle n_{e_p^-} \rangle$ $[e^-_{RMS}]$ pattern noise., 27
$\langle n_{e_r^-} \rangle$ $[e^-_{RMS}]$ standard deviation of the noise floor (or read noise)., 27
$\langle n_{e_s^-} \rangle$ $[e^-_{RMS}]$ shot noise., 26
$\langle n_{e_{tot}^-} \rangle$ e^-_{RMS} total noise., 30
τ_{DCS} $[\mu s]$ DCS integrator time constant., 58
θ, 40
θ_{max}, 40
θ_{max} [angle] maximum ray-angle through the filter., 40
t_{int}, 25, 54, 62
t_{int} $[s]$ on-chip integration ("exposure") time., 34
t_{misc} $[s]$ misc. time before the next image can be read., 34
t_{read} $[s]$ read-out time., 34
$\langle X \rangle^2$, 26
z_θ, 45
z_θ zenith-angle., 44
c, 22
d_{app} $[m]$ aperture-stop., 24
f $[m]$ focal length., 24
$f_{\#fl}$ [1] f-number setting on the front lens., 40
h, 22
h_i, 24
h_s, 24
i $[1 \cdots m]$ pixel columns., 49
j $[1 \cdots n]$ pixel rows., 49
k_{MCP} microchannel excess noise., 29
l $[m]$ line of sight., 22
r_i, 24
r_s, 24
t_{DCS} $[\mu s]$ DCS integration time., 58
$t_{int,k}$ $[s]$ integration time for image k., 52
[R/Å], 56

x_{bin} [1] binning-factor in the x-direction., 62
y_{bin} [1] binning factor in the y-direction., 62

Index

CTE Charge Transfer Efficiency, 26
SNR of an ICCD SNR_{ICCD} , 29
pc photo-cathode, 28
HF pump-enhanced airglow, 145
FoV field-of-view, 5
IBC International Brightness Coefficients, 23
α-axis, 45
β-axis, 45
"known" column emission rate I_{cal} $[R]$, 58
"natural vignetting", 53
"natural vignetting" $\cos^4\theta$, 24

Abisko Scientific Station ANS, 15
absolute calibration constant $C_{abs\lambda c}$ $[R/\text{counts}]$, 58
absolute calibration constant with binned pixels $C_{abs\lambda c,binxy}$ $[R/\mathring{A}]$, 62
ADC bit weight (90.6 μV/counts) B_{ADC} $[\mu V/\text{counts}]$, 58
ADCs Analogue to Digital Converters, 36
AIDA, 71
AIDA Alis Internal Data Administration, 69
AIS ALIS Imager Subsystem, 123
ALIS Auroral Large Imaging System, I, 1, 2, 5
ALIS Imager Subsystem AIS, 123
Alis Internal Data Administration AIDA, 69
All-Sky Camera ASC, 2
all-sky optical imager ASI, 2
Analogue to Digital Converters ADCs, 36
aniara, 71, 72
ANS Abisko Scientific Station, 15
aperture-stop d_{app} $[m]$, 24
API Application Program Interface, 79
Application Program Interface API, 79
area of a CCD pixel A_{pix} $[m^2]$, 23
area of CCD-detector A_{CCD} $[m^2]$, 23
arnljot, 71
ASC All-Sky Camera, 2
ASI all-sky optical imager, 2
Auroral Large Imaging System ALIS, I, 1, 2, 5
average MCP gain $\overline{g}$ [1], 28
average number of photoelectrons $\overline{n}_{e_\gamma^-}$ $[e^-_{RMS}]$, 26
average number of secondary photoelectrons $\overline{n}_{e^-_{\gamma MCP}}$ $[e^-_{RMS}]$, 28
average number of signal electrons generated by the photocathode $\overline{n}_{e^-_{\gamma,pc}}$ $[e^-_{RMS}]$, 28
averaged bias-correction image $B_{\overline{Z}ij}$ [counts], 52
Azimuth, 44
azimuth a_ϕ [angle], 44
azimuth/elevation drive, 44

bias (or DC-level) B_{ij} $[B_]$, 51
bias-frame, 51
bias-pixels, 50
binning factor in the y-direction y_{bin} [1], 62
binning-factor in the x-direction x_{bin} [1], 62
black-level (or preset bias) B_0 [counts], 51
Bright Star Catalogue BSC, 62
BSC Bright Star Catalogue, 62

calibrated pixel-value I_{ij} $[R]$, 61
camera control unit, 45, 50

Camera Control Unit CCU, 36, 47, 123
Camera Positioning system Control unit CPC, 123
Camera Positioning System CPS, 13, 44, 47, 123
Camera stand, 48
CC control centre, 17
CCD Camera Head CCH, 47, 123
CCD camera head CCH, 35
CCD Charge Coupled Device, 25, 123
CCD output sensitivity G_{CCD} $[\mu V/e^-_\gamma]$, 58
CCH CCD Camera Head, 47, 123
CCH CCD camera head, 35
CCU, 58
CCU Camera Control Unit, 36, 47, 123
CCU CPS Control Unit, 48
Charge Coupled Device CCD, 25, 123
Charge Transfer Efficiency CTE, 26
charge well capacity $n_{e^-_{max}}$ $[e^-]$, 29
column emission, 22
column emission rate, 23
column emission rate I $[R]$, 24
column emission rate of the light standard $I_{ls}(\lambda)$ $[R/\mathring{A}]$, 58
Computer Tomography CT, 83
control centre, 18
control centre CC, 17
corrected pixel value DN'_{ij} [counts], 54
CPC, 44
CPC Camera Positioning system Control unit, 123
CPC CPS Control unit, 44
CPS, 71
CPS Camera Positioning System, 13, 44, 47, 123
CPS Control Unit CCU, 48
CPS Control unit CPC, 44
CT Computer Tomography, 83

dark-current correction image D_{ij} counts, 52
dark-current noise, 29
dark-current noise $\langle n_{e^-_d} \rangle$ $[e^-_{RMS}]$, 26
DC-bias-level DN_{DC} [counts], 30
DCS, 36
DCS Double Correlated Sampling, 27
DCS integration time t_{DCS} $[\mu s]$, 58
DCS integrator time constant τ_{DCS} $[\mu s]$, 58
DDS Digital Data Storage, 16
detective quantum efficiency DQE, 25
Digital Data Storage DDS, 16
digital output DN [counts], 27
digital output DN_{ij} [counts], 49
digital-output, 58
DIS Doppler Imaging System, 110
Doppler Imaging System DIS, 110
Double Correlated Sampling DCS, 27
DQE detective quantum efficiency, 25
Dynamic Range DR $[dB]$, 30

ECU Environmental Control Unit, 123
effective aperture of the optics A_{app} $[m^2]$, 23
effective index of refraction N_e [1], 40
effective quantum yield, 25
Effective Radiated Power ERP, 86
EISCAT, 76
EISCAT European Incoherent SCATter radar, 75
electron multiplication noise, 29
electrostatic discharge ESD, 36
Environmental Control Unit ECU, 123
EPLD Erasable, Programmable Logic Device, 36
EPROM, 72
EPROM Erasable Programmable Read-Only Memory, 71
Erasable Programmable Read-Only Memory EPROM, 71
Erasable, Programmable Logic Device EPLD, 36
ERP Effective Radiated Power, 86

ESD electrostatic discharge, 36
European Incoherent SCATter radar EISCAT, 75

f-number setting on the front lens $f_{\#fl}$ [1], 40
f-number $f_{\#}$ [1], 24
Fabry-Perot filters, 40
fibre-optic minification ratio M_{FO} [1], 28
field-of-view FoV, 5
field-of-view in x-direction FoV_x [angle], 50
field-of-view in y-direction FoV_y [angle], 50
field-of-view per pixel FoV_p [angle], 10
filter centre wavelength at normal incidence λ_{cw} [Å], 40
filter passband $\Delta\lambda$ [Å], 58
filter passband $\lambda_1 \cdots \lambda_2$ [Å], 58
Filter Wheel Control unit FWC, 41
Filter Wheel FW, 123
filter-bandwidth $\Delta\lambda$ [Å], 40
Filter-Wheel Control Unit FWC, 123
Filter-Wheel Control unit FWC, 47
FITS, 71
FITS Flexible Image Transfer System, 16
Fixed Pattern Noise FPN, 27
flat-field correction $F_{ij\lambda}$ [1], 52
Flexible Image Transfer System FITS, 16
focal length f [m], 24
FPN Fixed Pattern Noise, 27
FPS, 71
Frame rate, 34
frame rate FR [images/s], 34
frequency, 22
FW Filter Wheel, 123
FWC, 44
FWC Filter Wheel Control unit, 41
FWC Filter-Wheel Control Unit, 123
FWC Filter-Wheel Control unit, 47

General Instrument Platform GIP, 151
geometrical calibration, 62
GIP General Instrument Platform, 151
GLIP Ground-based Low-light Imaging Platform, 8, 121
Global Positioning System GPS, 123, 131
GOSSIP, 18
GPS Global Positioning System, 123, 131
Ground-based Low-light Imaging Platform GLIP, 8, 121

HAARP High Frequency Active Auroral Research Program facility, 96
HALIS Housing for ALIS, 122
HENRIK, 71
HF high-frequency, 85
High Frequency Active Auroral Research Program facility HAARP, 96
high-frequency HF, 85
high-speed link, 15
Housekeeping Unit, 71
Housekeeping Unit HU, 123, 130
Housing for ALIS HALIS, 122
http, 70
HU Housekeeping Unit, 123, 130

ICC Imager Control Computer, 148
ICCD Intensified CCD, 25
IGY International Geophysical Year, 2
image area A_i [m^2], 23
Image Processing Computer IPC, 13
image-intensifier, 28
Imager Control Computer ICC, 148
imager system gain G_S [counts/e^-_γ], 58
index λ , 52
Information Technology IT, 11
integrating sphere, 52
integration time, 25
integration time for image k $t_{int,k}$ [s], 52
Intensified CCD ICCD, 25
interference filter, 40

International Brightness Coefficients IBC, 23
International Geophysical Year IGY, 2
IPC Image Processing Computer, 13
IRF, 11, 15–18
IRF Swedish Institute of Space Physics, I, 10
IT Information Technology, 11

LAN Local Area Network, 132, 148
line of sight l $[m]$, 22
Local Area Network LAN, 132, 148

Magnetohydrodynamical MHD, 107
MART Multiplicative Algebraic Reconstruction Technique, 83
maximum ADC output, 29
maximum charge-well capacity DN_{SEE} [counts], 29
maximum ray-angle through the filter θ_{max} [angle], 40
MCP micro-channel plate, 28
mean value, 26
MHD Magnetohydrodynamical, 107
micro-channel plate MCP, 28
microchannel excess noise k_{MCP} , 29
mima, 71, 72
minimum ADC output DN_{min} [counts], 30
misc. time before the next image can be read t_{misc} $[s]$, 34
modelled flat-field correction, 59
modelled flat-field correction $F_{Mij\lambda}$ [1], 54
Multiplicative Algebraic Reconstruction Technique MART, 83

narrow-band interference filters, 40
National Bureau of Standards NBS, 54
National Institute for Polar Research NIPR, 84
NBS National Bureau of Standards, 54
Near-Sensor Interface and Processing Unit NIPU, 123
Near-sensor Interface and Processing Unit NIPU, 13
network time protocol ntp, 131
NIPR National Institute for Polar Research, 84
NIPU, 38, 44, 47, 48, 71
nipu, 71, 72
NIPU Near-Sensor Interface and Processing Unit, 123
NIPU Near-sensor Interface and Processing Unit, 13
Noise, 26
Noise Equivalent Exposure NEE , 29
normalised filter transmittance function $T'(\lambda)$ [1], 59
ntp network time protocol, 131
ntpd, 72
number of photons hitting an individual pixel $n_{\gamma_{pix}}$ [photons], 25
number of photons hitting the CCD $n_{\gamma_{CCD}}$ [photons], 25
number of photons reaching the image plane, 28
number of photons reaching the image plane n_{γ_i} [photons], 25
number of transfers, 26

OC Operations Centre, 17
on-chip integration ("exposure") time t_{int} $[s]$, 34
OPERA OPERations system for ALIS, 69
operations centre, 18
Operations Centre OC, 17
OPERations system for ALIS OPERA, 69
optical field-of-view FoV_o [angle], 50
overscan-strip, 50, 51
overscan-strip correction B_{Lj} [counts], 51

PAI Portable Auroral Imager, 3, 30
parsifal, 69, 70
passband, 40
pattern noise $\langle n_{e_p^-} \rangle$ $[e^-_{RMS}]$, 27
PCNN Pulse Coupled Neural Networks, 81
PDU Power Distribution Unit, 123, 127

Phase-Locked Loop PLL, 131
phosphor efficiency η_P [1], 28
Photo Response Non-Uniformities PRNU, 27
photo-cathode, 29
photo-cathode *pc*, 28
photo-cathode dark-current noise, 29
photometry, 21
photon flux $\Phi_{\gamma_{app}}$ [photons/s], 24
photon-noise, 29
pixel columns i $[1 \cdots m]$, 49
pixel indices (i, j) , 62
pixel rows j $[1 \cdots n]$, 49
Planck's constant, 22
PLL Phase-Locked Loop, 131
point spread function PSF, 64
Point-to-Point Protocol ppp, 15
Polar Stratospheric Clouds PSC, 1, 2, 77
polar-stratospheric clouds, 10
Portable Auroral Imager PAI, 3, 30
Power Distribution Unit PDU, 123, 127
Power subsystem, the electrical installation of the GLIP PWR, 123
ppp, 69
ppp Point-to-Point Protocol, 15
PPS Pulse Per Second, 131
PRNU Photo Response Non-Uniformities, 27
programmable gain setting (5 or 10) G_P [1], 58
PSC, 61
PSC Polar Stratospheric Clouds, 1, 2, 77
PSF point spread function, 64
Pulse Coupled Neural Networks PCNN, 81
Pulse Per Second PPS, 131
PWR Power subsystem, the electrical installation of the GLIP, 123

quadrant bias B_q [counts], 51
quantum efficiency Q_E [e^-/photons], 25
radames, 70
Radial Basis Neural Network RBNN, 82
radiance, 21
radiant flux Φ [W], 21
Radio Frequency Interference RFI, 96
radiometric unit for the aurora and airglow, 22
radiometry, 21
Rayleigh, 22
Rayleighs/Ångström, 56
RBNN Radial Basis Neural Network, 82
read noise, 27
read-noise, 34
read-out time t_{read} [s], 34
reference pixels, 51
reference-pixels, 50
Removing the instrument signature, 49
RFI Radio Frequency Interference, 96
rigoletto, 70
root-mean-square electrons, 27

Saturation Equivalent Exposure SEE, 29
SC Station Computer, 132
SC station computer, 71
SC Station Computer, the main computer at the GLIP, 123
SEE Saturation Equivalent Exposure, 29
Selective Imaging Technique SIT, 82
shot noise $\langle n_{e_s^-} \rangle$ [e^-_{RMS}], 26
Signal-to-noise ratio, 27
signal-to-noise ratio *SNR* [1], 25
signal-to-noise ratio of an ICCD, 28
Simultaneous Iterative Reconstruction Technique SIRT, 84
Singular Value Decomposition SVD, 82
SIRT Simultaneous Iterative Reconstruction Technique, 84
SIT Selective Imaging Technique, 82
sky background correction $I_{bg,ij}$ [R], 61

solid angle Ω [sr], 22
solid angle of the lens aperture as seen from the source, 24
source area A_s [m^2], 21
source of area A_s [m^2], 24
Spectral radiant incidence (irradiance) E , 23
spectral radiant incidence at the aperture $E_{\gamma_{app}}$ [photons $s^{-1}\,m^{-2}$], 24
spectral radiant incidence at the image plane E_{γ_i} [photons $s^{-1}\,m^{-2}$], 24
Spectral radiant sterance, 21
spectral radiant sterance, 23
spectral radiant sterance L , 21
spectral radiant sterance in energy units L_E [$W\,m^{-2}\,sr^{-1}$], 22
spectral radiant sterance in quantum units, 22
speed of light, 22
ssh, 70
standard deviation, 26
standard deviation of the noise floor (or read noise) $\langle n_{e_r^-}\rangle$ [e^-_{RMS}], 27
standard deviation of the noise resulting from the photoelectrons $\langle n_{e_\gamma^-}\rangle$ [e^-_{RMS}], 26
Station Computer SC, 132
station computer SC, 71
Station Computer, the main computer at the GLIP SC, 123
SVD Singular Value Decomposition, 82
Swe-ALIS the Swedish part of ALIS, 5
Swedish Institute of Space Physics IRF, I, 10

telnet, 69
the Swedish part of ALIS Swe-ALIS, 5
threshold of detection, 29
tosca, 69, 70
total noise $\langle n_{e^-_{tot}}\rangle$ e^-_{RMS}, 30
total noise for the ICCD $\langle n_{e^-_{ICCD}}\rangle$ [e^-_{RMS}], 29
Transmittance, 124
transmittance $T(\lambda, ...)$ [1], 23
transmittance of the atmosphere, 23
transmittance of the filter $T_f(i, j, \lambda)$ [1], 62

uniformly illuminated central pixels of the CCD DN_{Cij} [counts], 58
Uninterruptable Power Supply UPS, 148
Uninterrupted Power Supply UPS, 130
UPS Uninterruptable Power Supply, 148
UPS Uninterrupted Power Supply, 130

variance, 26
verdi, 70
vignetting, 24
volume emission rate $\epsilon(\mathbf{r}, t, \lambda)$ [photons $m^{-3}s^{-1}$], 22
Vorticity, 107

WAN Wide Area Network (connected to the Internet), 148
WAN/LAN Interface consisting of the WAN-Interface, a router, a switch and possibly also a firewall WLI, 148
wavelength, 22, 23
Westward Travelling Surges WTS, 76
Wide Area Network (connected to the Internet) WAN, 148
WLI WAN/LAN Interface consisting of the WAN-Interface, a router, a switch and possibly also a firewall, 148
WTS Westward Travelling Surges, 76

Zenith angle, 44
zenith-angle z_θ , 44
zero-exposure, 51